MESOGRANULATION AND SUPERGRANULATION IN THE SUN

by

Laurence Jay November

B.S., California Institute of Technology, 1973

A thesis submitted to the Faculty of the Graduate School of the University of Colorado in partial fulfillment of the requirements for the degree of

Doctor of Philosophy

Department of Astro-Geophysics

1980

Laurence J. November (Ph.D., Astro-Geophysics)

Mesogranulation and Supergranulation in the Sun

Thesis directed by Professor Juri Toomre and
Professor Adjoint Katharine B. Gebbie

Simultaneous satellite and ground-based observations of supergranular velocities in the Sun were made using the University of Colorado UV Spectrometer on OSO 8 and the Sacramento Peak Observatory diode array instrument. We compare our observations of the steady Doppler velocities seen toward the limb and at disk center in several spectral lines that span 1400 km in their heights of formation.

Our observations indicate that supergranular flows are able to penetrate at least 11 density scale heights in the atmosphere. Seen at radius vector 0.8, the dynamic range of these motions increases from about 800 ms^{-1} in the photosphere to about 3000 ms^{-1} in the middle chromosphere. At disk center, regions of downflow tend to correlate with the bright Ca II network, those of upflow with the darker areas. The dynamic range of these vertical motions is only about 200 ms^{-1} in the photosphere but increases in the middle chromosphere to a value comparable with that seen at radius vector 0.8. Thus a distinct change appears to occur in the flow structure: whereas the horizontal component of the velocity predominates in the low photosphere, suggesting strong braking of the

vertical momentum there, the motions higher in the atmosphere are more isotropic. These observations imply that supergranular velocities should be evident in the transition region.

In addition to supergranular scale flows, our observations at disk center show a 7000 km scale of motion, which may be convective in origin. We call this mesogranulation. Mesogranules are most apparent in the Mg I λ5173 spectral line formed in the lower chromosphere. In the low photosphere, they are masked to some extent by the large signals from granulation and five-minute oscillations. Our Si II λ1817 observations of the middle chromospheric motions indicate that a 7000 km scale of motion is also present there. If the scale of granulation is related to the depth of the HI ionization zone, and that of supergranulation to the HeII zone, then the mesogranules may represent the scale of motion driven in the HeI ionization zone. The decrease of the kinetic energy flux with height in the atmosphere suggests that major dissipation is occurring in these flows.

This abstract is approved as to form and content. We recommend its publication.

Signed Jim Toomre
Faculty Member in Charge of Thesis

Signed Katharine B. Gebbie
Faculty Member in Charge of Thesis

ACKNOWLEDGEMENTS

It has been both a pleasure and an inspiration for me to work closely with Dr. Juri Toomre during the course of this study. He is a friend but at the same has remained my most critical ally. His advice is never shallow but always cuts quickly to the root of a matter. The most valuable piece of knowledge I take with me as I complete these studies is a sense for the "sparkle" in a problem. It is the "sparkle" which allows us to distinguish between that which is exciting and opens up new avenues of thought from that which is mundane. Juri's keen sense for the "sparkle" has been my guide.

I also express my gratitude to Katharine Gebbie and to George Simon with whom I have closely worked. Katharine's careful reading of this text has both helped to make it more readable and scientifically better thought out. Her efforts and concern are truly appreciated. George Simon has provided a sense of wisdom that underlies these observations.

I express my appreciation to the High Altitude Observatory and members of its staff for providing the

computing facilities used for this work. In carrying out the OSO 8 observations, I received congenial cooperation from members of the staff of the Laboratory for Atmospheric and Space Physics. As well, I recognize the assistance provided by the observers at Sacramento Peak Observatory. I also express my thanks to the Joint Institute of Laboratory Astrophysics and its staff for the facilities provided and the effort expended toward completion of this work.

This research was supported in part by the National Aeronautics and Space Administration through Grants NGL-06-003-057 and NSG-7511, and by the Air Force Geophysics Laboratory through Contract F19628-77C-0104 to the University of Colorado.

THE GRADUATE SCHOOL

UNIVERSITY OF COLORADO

Report on Final Examination for the Ph.D. Degree

The committee appointed to examine Laurence Jay November for the Ph.D. Degree reports as follows: (Delete word which does not apply.)

Final examination. October 20, 1979 (date) Satisfactory; ~~unsatisfactory.~~

Examining committee:	Satisfactory Signed:	Unsatisfactory Signed:
Juri Toomre, Chm.	Juri Toomre	
Katharine Gebbie, Co-Chm.	Katharine Gebbie	
Peter A. Gilman	Peter A Gilman	
Oran R. White	Oran R. White	
Dimitri M. Mihalas	Dimitri Mihalas	
Frank Q. Orrall	Frank Q Orrall	
George W. Simon	George W Simon	
Robert Richtmyer	Robert D Richtmyer	

University of Colorado — FINAL GRADE CARD — Graduate School

572 66 8442 (Matric. No.)

(B) DC CSC MC (Campus: circle one)

November, Laurence Jay
(Last Name) (First Name) (Middle Name)

Dept. and Course No. AG 800

Title of Course Ph.D. Thesis

For the ____ semester 19 ____ quarter to count ____ semester hours ____ quarter hours

Thesis Defense 10/20/79

Final Grade A

20 OCT 1979
Date

Juri Toomre
Instructor's Signature

Return to Graduate School, 914 Broadway

No. GS-16B-76

TABLE OF CONTENTS

PAGE

PAGE

LIST OF FIGURES

PAGE

PAGE

CHAPTER 1

CONVECTIVE PROCESSES IN THE SOLAR ENVELOPE

1.1 Introduction

Very little is presently known about what is occurring in the 150,000 km below the solar surface (0.2 solar radii), where convection transports 99% of the energy flux. This region is probably the origin of many phenomena, such as the solar activity cycle, differential rotation, magnetic field motion and reconnection, and acoustic and gravity waves. The goal of this work is to determine the height variation of the larger scale convective motions as they penetrate into the solar atmosphere. Interpretation of these results in terms of dynamical convection models applicable to the Sun helps provide some feel for the nature of the motions below the surface and helps clarify the role that convection plays in affecting the solar atmosphere.

Two disparate scales of convection are observed in the Sun, granulation and supergranulation, with horizontal cell sizes of 1100 km and 32,000 km. In addition, there is strong evidence for giant cells with a convective scale of order 200,000 km. The granulation exhibits

a pronounced temperature variation across the cells as evidenced by its appearance in white light photographs. Doppler measurements in photospheric spectral lines indicate that relative upward and outward motions of comparable amplitude occur in the cells. Supergranulation is evident mainly in velocity measurements and shows a primarily horizontal outflow from cell centers in the photosphere. These cells are separated by magnetic fields which are associated with regions of bright network emission in chromospheric intensity pictures. Apparently magnetic fields are swept to the cell border by the underlying convective motions. The solar differential rotation and the magnetic activity cycle are the main evidence for giant cells. A large scale of convection that is modified by solar rotation may serve to produce the observed angular momentum transport toward the solar equator and to generate and move magnetic fields to create the solar dynamo.

Interior models for the Sun that rely on the mixing-length theory predict that the outer 150,000 km of the solar envelope is convectively unstable. The convective instability, as measured by the local Rayleigh number, is greatest in the three ionization zones of H I, He I, and He II. Figure 1.1 from Toomre (1979) schematically illustrates this with values given for the local density scale height ℓ_ρ and Rayleigh number R. Here R

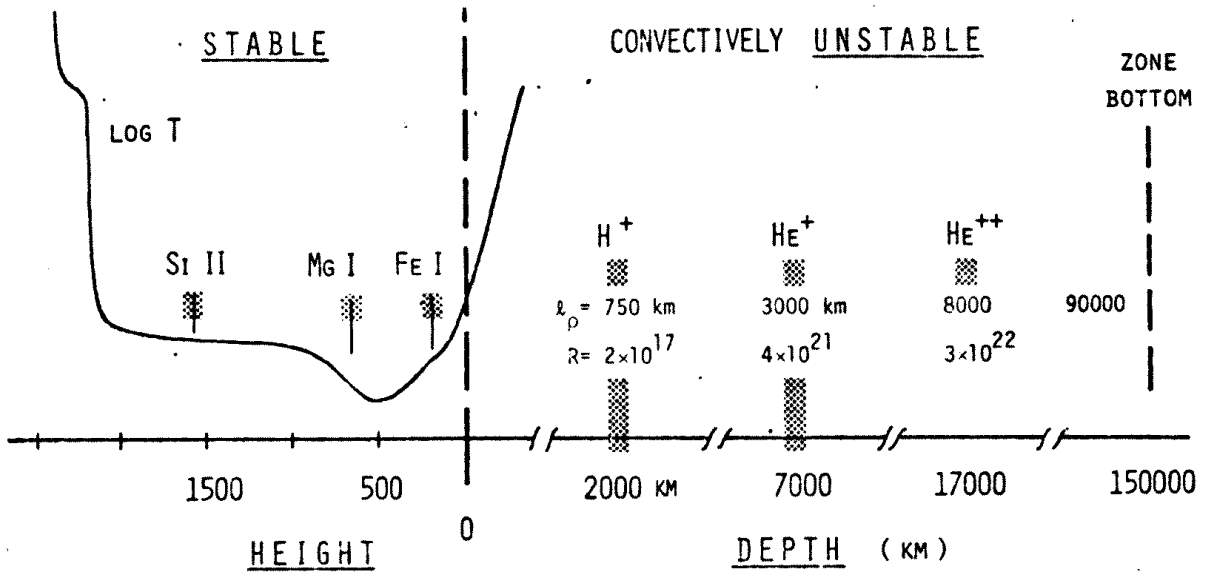

Figure 1.1

Map of the solar convection zone. This is a schematic illustration of the solar convection zone. The 150,000 km depth is predicted from mixing-length models (Gough and Weiss 1975). The ionization zones of H I, He I, and He II are places of increased instability as measured by the local Rayleigh number R. The disparate scales of convective motion that are seen as granulation and supergranulation probably receive most of their driving in the H I and He II zones. The density scale height h_ρ in these zones may be representative of the horizontal scales of the motions. The density scale height h_ρ and Rayleigh number R are based upon the mixing-length density, molecular viscosity, and radiative conductivity. (from Toomre 1979)

is based upon ℓ_ρ and the radiative opacity and viscosity. In laboratory convection, the cell size is found to be comparable to the depth of the unstable zone. Convection models for the Sun based on mixing-length treatments have not been able to explain the observed discrete scales of motion. The solar convection zone is difficult to model with more refined treatments for the dynamics because it is very unstable (large R) and shows a large variation in density, opacity, specific heat, and viscosity. It is reasonable to suppose that the discrete scales of convective motion that are observed are driven in the most unstable ionization zones. We therefore associate the H I ionization with granulation, and the He II ionization with supergranulation. Finally, the giant cells may reflect the overall 150,000 km depth of the convection zone.

The present work is concerned with observations of the supergranulation. Our extensive measurements may serve to: 1) clarify the role of convection in generating or modifying the phenonema seen in the solar atmosphere, 2) provide a probe of the mean structure of the solar envelope region. Supergranulation is particularly well suited for this since the motions originate at considerable depth but can still be readily observed in the atmosphere. Supergranulation may play an important role in the generation of the acoustic and gravity waves,

contribute to the coronal heating, affect the surface diffusion of network magnetic fields, and help determine strong magnetic field processes in active regions.

In this study we determine the amplitude of the supergranular flows as they penetrate into the solar atmosphere from the photosphere to the middle chromosphere. In the photosphere the motions are readily observed in a number of weak spectral lines found at visible wavelengths accessible with ground-based instruments. Above the temperature minimum, where most of the lines fall in the ultraviolet, Doppler measurements must be made from satellite. We have carried out simultaneous velocity measurements in a number of visible lines using the Sacramento Peak Observatory (SPO) diode array instrument and in ultra-violet lines using the University of Colorado Ultraviolet Spectrometer on the Orbiting Solar Observatory 8 (OSO 8).

Much of what is seen in the solar atmosphere must be related to convection in the solar envelope. However the explicit connection between the observed features and the convection is not yet well understood. Since radiative processes alone cannot explain the increase in temperature with height above the photosphere, some other energy source must be present. Acoustic and gravity waves, or Alfven waves and magnetic instabilities, or possibly supergranular convective motions may provide the

necessary additional upward flux of mechanical energy and contribute to the deposition of energy in the upper atmosphere. The role that supergranulation can play in this process, or in the generation of acoustic and gravity waves can be clarified by understanding the height variation of its deposition of mechanical energy flux. By mapping out the height variation of the motion field, we may determine how much energy is deposited and at what heights in the observed region.

These observations also provide a benchmark for nonlinear models of solar convection that are currently becoming available (Toomre, Zahn, Latour, and Spiegel 1976, Nelson and Musman 1977). The most useful diagnostic for this purpose is the measured height variation of the motions as they penetrate into the solar atmosphere. Models for stars and for convective penetration indicate that thermal fluctuations in the cellular motions do not penetrate as effectively as the motion field, so that only the velocity fluctuations will be evident at some distance in the adjoining stable region. There is certain evidence for this in the Sun in that supergranulation shows little convective thermal fluctuation, yet its motion field is indicative of active convection in the solar envelope. In this work we look for many of the properties of penetrating convective motions seen in other systems, such as a propensity of the motions to

drive counter cells, a scale height for braking of the vertical mass flux, and a preference for upflow or downflow in the cell center.

It is useful to review here some of the observed properties of supergranulation and the competing motion fields of granulation and the five-minute oscillation. Granulation is of interest here for two reasons: it is a well observed convective flow in the Sun that can be compared with the supergranulation, and it is the major source of noise in our Doppler velocity measurements. The five-minute oscillation is the largest component in our photospheric Doppler measurements and is a potential contributer to noise although it can be effectively filtered. Supergranulation may play an important role in generating these waves, and the possible interconnection of these processes is useful to discuss here.

1.2 The Motion Fields in the Solar Atmosphere

a) Granulation

i) history

The clearest evidence for convection in the Sun comes from the observation of granulation. William Herschel (1801) first discerned the granulation as "a very remarkable unevenness" which extends "over all the

surface of the globe of the Sun." The first detailed drawings, like the example shown in Figure 1.2, were made by Secchi (1875) who clearly recognized the cellular structure and the dark interlanes so characteristic of convection cells. He described the solar surface as covered by a multitude of small bright features, which he likened to grains. Huggins (1866) noted that the granules, as he called them, were usually round to oval although more irregular forms did occur. He accurately estimated their diameter to lie between 1.0" and 1.5". The first photographs of granulation were obtained by Janssen (1877). These are comparable in quality to the best modern day ground-based photographs.

Although granulation completely covers the solar surface and shows high contrast in white light intensity photographs, it has remained difficult to observe owing to its small spatial scale. Granules are of order 1" in size, which is the resolution limit in the best ground-based observations. The success of nineteenth century observations was not exceeded until observations could be made from balloons, from which photographs could be obtained under conditions of improved atmospheric seeing.

ii) spectrum of sizes and lifetimes

A major breakthrough occurred in the study of solar granulation with the project Stratoscope experiment (Schwarzschild 1959). A 12-inch solar telescope equipped

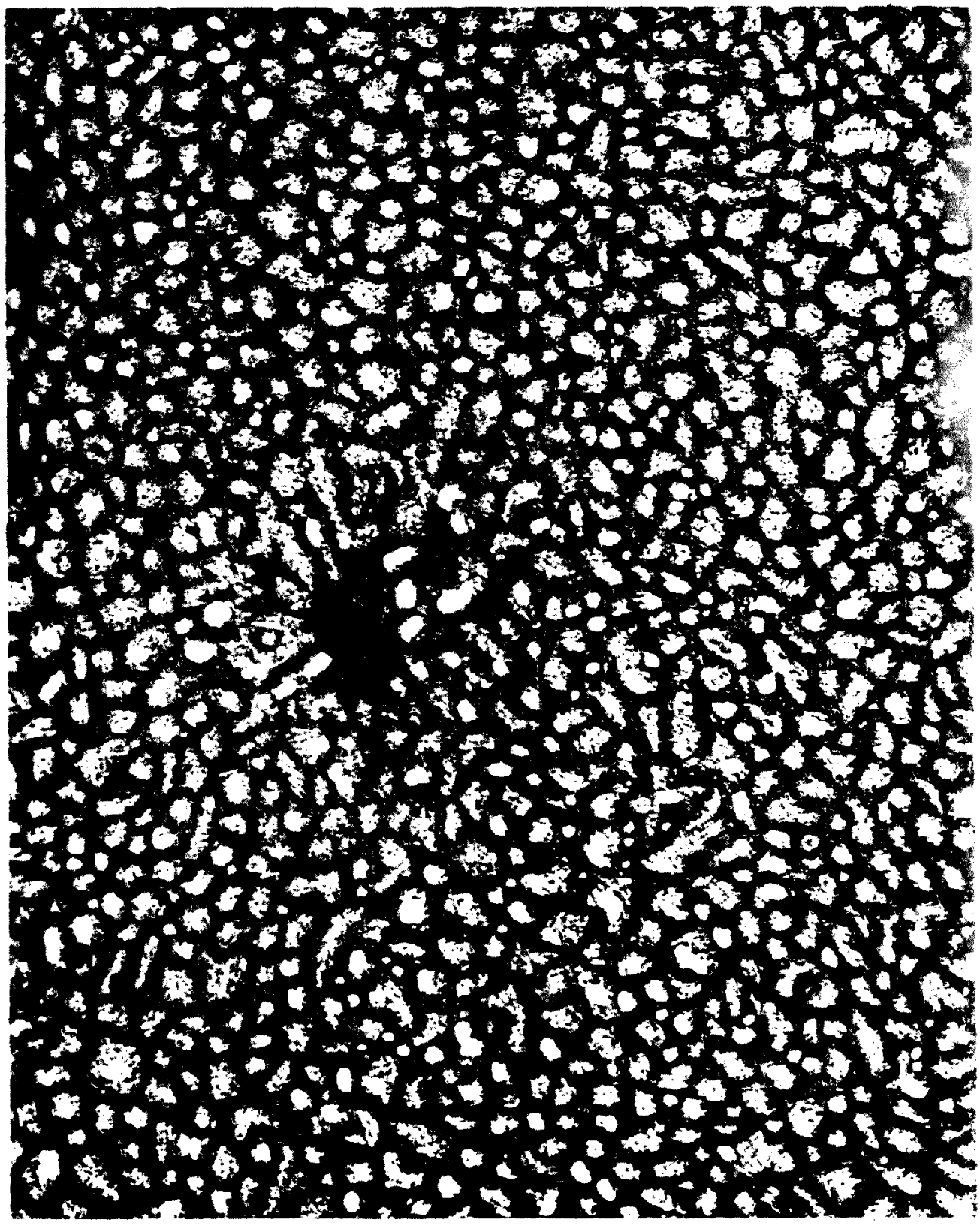

Figure 1.2

Secchi's drawing of the granulation. This white light drawing of the solar photosphere was made by A. Secchi and appears in his book Le Soleil (1875). This is the first observation which clearly shows the "grains" as Secchi called them. This drawing bears good resemblance to modern day photographs of the photospheric granulation pattern, nicely showing the small bright grains separated by the darker interlanes.

with a photoelectric pointing mechanism and an automatic camera was carried by balloon to an altitude of 80,000 feet. A number of photographs of the solar granulation were thereby obtained with a resolution of 0.3", the diffraction limit of the instrument. Figure 1.3 shows one example of these. The granules range in size from 300 km to 1800 km and are closely packed cells separated by dark, often very narrow lanes. Leighton (1963) and Namba and Diemel (1969) study the distribution of sizes in the Stratoscope photos and conclude that a granule cell has a mean size of 1100 km (lane to lane). Leighton's autocorrelation analysis indicates that this mean size is also a preferred scale characteristic of the granular packing. It is evident in the photographs that very small or very large granules are fairly rare and that the distribution of sizes is sharply peaked near the 1100 km scale.

Bahng and Schwarzschild (1961) measure the mean lifetime of granules in the Stratoscope photographs. Their cross correlation analysis shows that the correlation decays exponentially in time with a half-life of 4 minutes. Lifetimes are related to granule size, ranging from a half-life of 3.1 minutes for small granules to a 6.1 minutes for large granules.

iii) mean motion field

Ground-based observations of the velocity field in

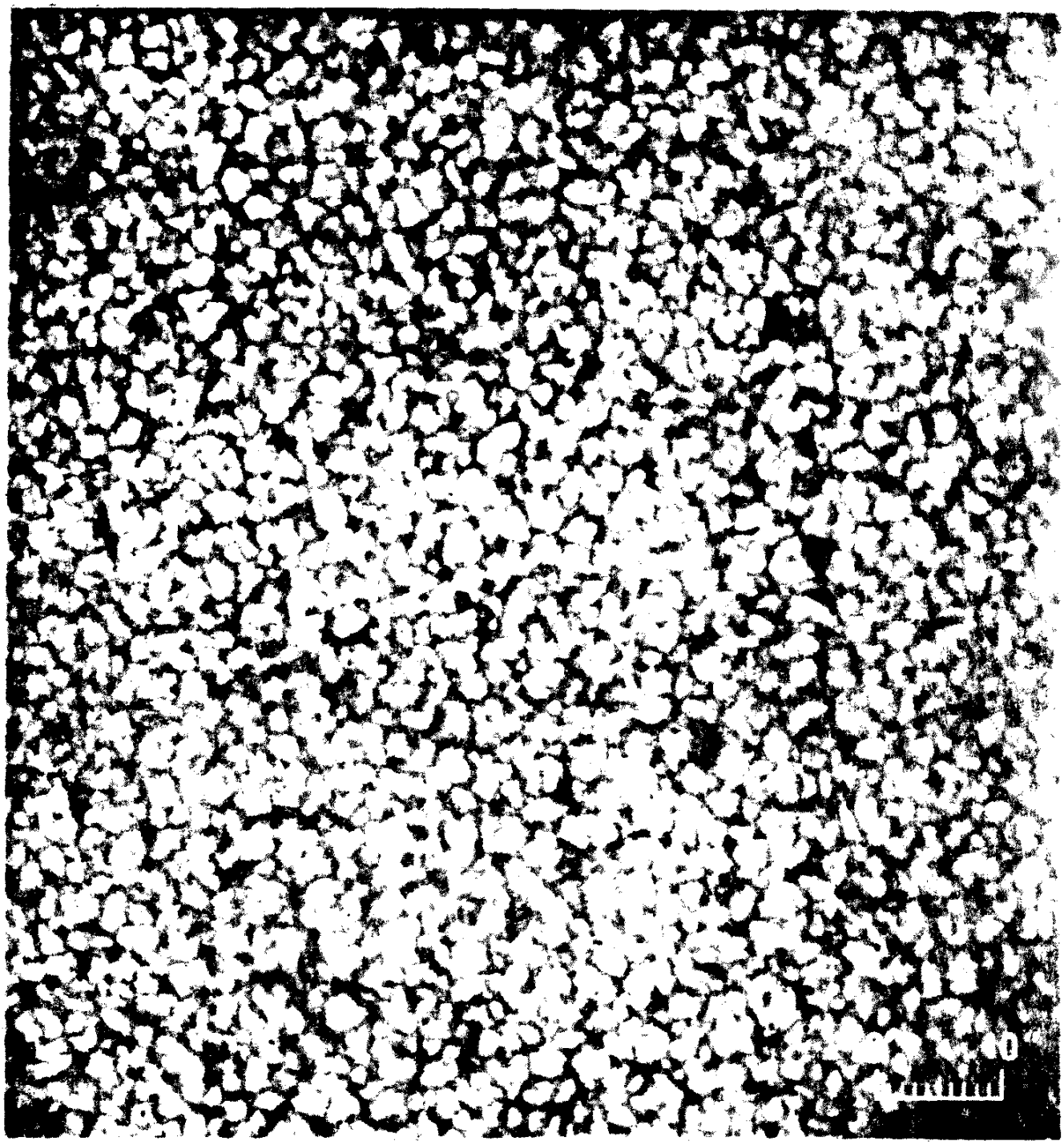

Figure 1.3

Stratoscope photograph. This photograph of the photospheric granulation was obtained with the 12 inch balloon borne telescope on project Stratoscope from an altitude of 80,000 feet in August 1959. The bright granulation and dark interlanes can be resolved to within 0.3" or 200 km on the Sun which is the diffraction limit of the instrument. From this and other photographs obtained by project Stratoscope it has been possible to deduce the characteristic scale and lifetime for the granulation. (Schwarzschild 1959)

a granule are difficult because features of less than 500 km cannot be resolved. Beckers and Morrison (1970) perform a statistical study of the granulation and map out the velocity field in the "average" cell. Their observations are made using pairs of filtergrams taken on either side of the photospheric line λ6569.2. The filtergram pairs are microdensitometered and differenced to determine the Doppler velocity. These measurements sample many disk positions from the center, $R_V = 0$, to near the limb, $R_V = 0.8$. Granule centers are identified visually, and the velocity is averaged by computer over many thousands of examples. These observations were made under very good seeing conditions with the Sacramento Peak Observatory Tower Telescope, and the data reduction method allows a mean motion field to be inferred beyond the normal atmospheric resolution limit. However, the finite atmospheric resolution systematically reduces the velocity amplitude so that the mean motion field is underestimated. Beckers and Morrison conclude that the mean granule exhibits an upward velocity component in its center with amplitude $\simeq 380$ ms^{-1} and a horizontal outflow with peak amplitude $\simeq 220$ ms^{-1}.

iv) height variation of motions.

There have been many attempts to study the height variation of the root mean square (rms) velocity associated with granulation (Canfield and Mehltretter 1973,

Canfield 1976, Keil and Canfield 1978). This is a difficult problem, again because granulation is at the limit of atmospheric resolution. A major uncertainty is introduced when trying to correct the velocity rms for conditions of perfect resolution. All these studies formulate a point spread function, which describes the atmosphere and telescope smearing function. The observed image is then the convolution of the perfect seeing image and the point spread function.

Line profiles are determined with an introduced spatial smearing function. The nominal width for the point spread function is determined by fitting the central intensity in the profile to the observed value for the spectral lines used in these studies. The rms oscillatory signal is removed using the power spectra determined as a function of height by Canfield and Musman (1973). These studies generally agree that the granulation velocity rms is about 1300 ms^{-1} at $\tau_{5000}= 1$ and decreases with an exponential scale height of 150 km. This corresponds to a mass flux rms of 4.4×10^{-2} g cm^{-2} s^{-1} at $\tau_{5000}= 1$ and a scale height for mass flux decrease of 64 km, given the densities from the Harvard Smithsonian Reference Atmosphere (HSRA of Gingerich et.al. 1971). This result is shown in Figure 1.4.

v) granulation noise

Owing to its large amplitude, granulation waves in

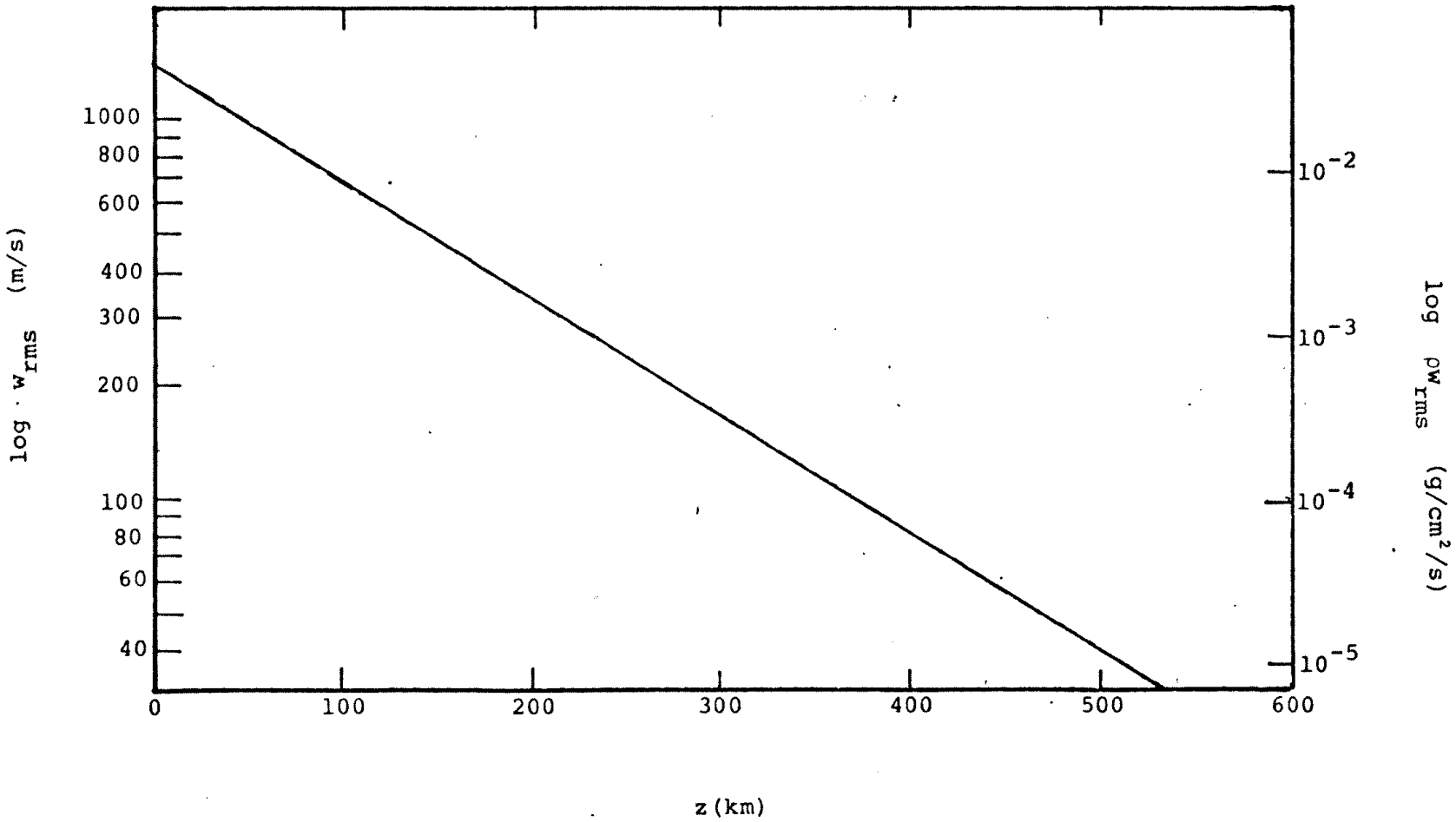

Figure 1.4

Height variation of the granulation velocity. This result is from the study of Keil and Canfield (1979). The velocity measurements are corrected to perfect resolution by comparing computed line profiles with those measured. In computing the line profiles an image point spread function is introduced to represent the total effect of atmospheric and instrumental degradation. The oscillations are removed from the measured rms fluctuations using the result of Canfield and Musman (1973).

introduces considerable noise into photospheric measurements of the vertical component of the steady motion. Further the granular signal is aperiodic so that time averaging of the measurements over a limited interval cannot effectively filter it out. We estimate a statistical noise component given that the mean amplitude for the granulation signal is V, that it varies on a spatial scale of 0.6", and that it exhibits a typical lifetime of 8 minutes. Granules have odd shapes and various sizes so a box r arcseconds on a side will randomly sample some upward and some downward components of the motion. If observations are designed with r" x r" spatial sampling, then $(r/0.6)^2$ granule velocity fluctuations will be sampled in each measurement. The rms error introduced in this sampling procedure is reduced from the mean amplitude of the individual elements by the square root of the number of elements that lie in the box so that the residual signal will be V/(r/0.6). Time averaging these observations for T minutes further reduces the granular contribution by a factor of $(T/8)^{0.5}$, provided the sampling time is less than the lifetime of a granule. In observations for which r= 1" and t= 20 minutes made in the middle photosphere where V= 500 ms^{-1} (Worden and Simon 1976), this formula gives a granular contribution of 190 ms^{-1}. Our measurements at disk center in Fe I lines (Chapter 3) are spatially averaged with r= 3" and

averaged in time with t= 60 minutes so that the granular contribution should be about 35 ms^{-1}.

A systematic error is also introduced in measurements that do not resolve the components of the granular velocity signal (Beckers and Nelson 1978). From spatial averaging due to less than perfect seeing or finite instrumental resolution, a single measurement of intensity in the line profile will include many features that exhibit upward or downward motion. The line shifts that are computed will not simply be the spatial average of these velocities. Rather this measurement must weight brighter features preferrentially. Since a granule exhibits upflow in the cell center where it is bright and downflow on the edge of the cell where it is dark, velocity determined from the spatially integrated intensity across a granule will show a net upflow. This effect will be most pronounced at disk center where we see only the vertical component in the granular flows and this can indeed account for the red shift that is seen toward the limb in photospheric velocity measurements. Similarly any intrinsic difference between granules that lie on the network boundary and those in the network interior could be reflected in velocity measurements as a net flow in the network boundary. For example, an apparent downflow will be observed in network regions if, as has been suggested by Beckers (1978), granules show less contrast

there.

b) Five-Minute Oscillation

In the photosphere the component of the motion generally measured to have the largest amplitude is the five-minute oscillation. It was first discovered independently by Leighton (1961) and by Evans and Michard (1961). Evans and Michard (1962) inferred motions in the solar atmosphere from a time sequence of spectrograms and found that the motions vary in time with the characteristic five-minute period. From the time analysis of displacements of several spectral lines they concluded that the mean period of the oscillation decreases with increasing height. For the periods near 300 seconds, the phase of the oscillation was found to be constant with height suggesting that this oscillation is due to evanescent or standing waves.

Leighton (1959) pioneered a new technique in solar observations after the work of Babcock (1953), permitting analysis of the velocity signal in two spatial dimensions. Leighton installed two exit slits on the spectrograph of the 60 foot tower at Mt. Wilson, one on either side of a spectral line center. As the entrance slit of the spectrograph was stepped across the solar image, the two exit slits were stepped across separate photographic plates, thereby creating two solar images at wavelengths

on either side of a spectral line. Positions in the solar image where material is moving relative to the observer appear brighter in one of the two photographs. By photographically subtracting the images, a velocity picture is produced on which bright features represent, e.g. motion away from, dark features motion toward, the observer, and neutral gray features are positions of no relative motion. Using the new technique Leighton was also able to identify the five-minute oscillation.

Leighton, Noyes, and Simon (1962) introduce the Doppler difference picture by photographically subtracting two velocity images separated in time by 2.5 minutes, in order to cancel the steady velocity component and accentuate those motions that change sign with this period. The five-minute oscillations appear as features that are about 7" in diameter and have amplitudes of 600 ms^{-1}. This study shows that oscillatory regions persist for about 20 minutes corresponding to about four oscillation cycles.

An early attempt to diagnose the dispersion of these waves was made by Frazier (1968a,b). He determines power as a function of horizontal wavenumber k and frequency ω, producing a so-called k-ω diagram. Unfortunately tracking errors in the observations and nonlinearities in the distance scale along the slit considerably complicate his analysis and its interpretation.

In all his spectral lines most of the power occurs in the high-frequency low-wavenumber domain, indicating that these are acoustic modes. Some power is also seen in the low-frequency high-wavenumber domain, which Frazier attributes to granulation. This signal noticably decreases with increasing atmospheric height.

Using data with greater resolution in both ω and k, Deubner (1975) was able to show that the oscillatory power is restricted to certain well defined 'ridges' in k-ω space. This had been originally predicted by Ulrich (1970a). His original observations that showed this were carried out for 3 h 55 min and along a 300" line centered on the solar disk. The velocity samples are Fourier transformed along the scan direction and in time, and a correction is applied that reduces the power due to waves traveling at an oblique angle to the scan direction. The resulting k-ω diagram has much greater resolution than Frazier's data. Deubner's observations were made with the relatively coarse sampling time of 110 seconds and spatial resolution element of 2.0" x 2.5", which permits the extensive spatial sampling necessary for improved k resolution. More recent observations by Deubner, Ulrich, and Rhodes (1979) are a time series of two-dimensional velocity images made from raster scans covering 192" x 944", lasting 7.11 hours, and obtained on the Sacramento Peak Diode Array in the non-magnetic photospheric

spectral line Fe I λ5576. The velocities computed are Fourier transformed in x, and averaged in y which selects the $k_y = 0$ component and physically isolates only those wave modes with phase velocity in the x direction. Fourier transforming this in time produces the desired k-ω diagram. Figure 1.5 shows the resulting k-ω diagram. The ridges are discrete and there is little power between them.

The presence of the ridges indicates that only certain wave modes are allowed and all others must be strongly filtered in the solar envelope. The narrowness of the ridges indicates that the modes that occur are long lived (at least several hours) and of large spatial extent (one-half a solar radius). The 20-minute lifetime of the five-minute oscillators measured in other studies apparently is the result of interference between the discrete modes and actually represents the beat frequency of that interference. This is corroborated in the k-ω observations since the separation in frequency between the first and second ridges is about $2\pi/(20\ \text{min})$. The existence of the ridges is confirmed by Rhodes, Ulrich, and Simon (1977).

The approximate position of the ridges can be interpreted by a simple model. To obtain some feel for the behavior of an acoustic wave in the solar envelope, let us examine properties of the dispersion relation for

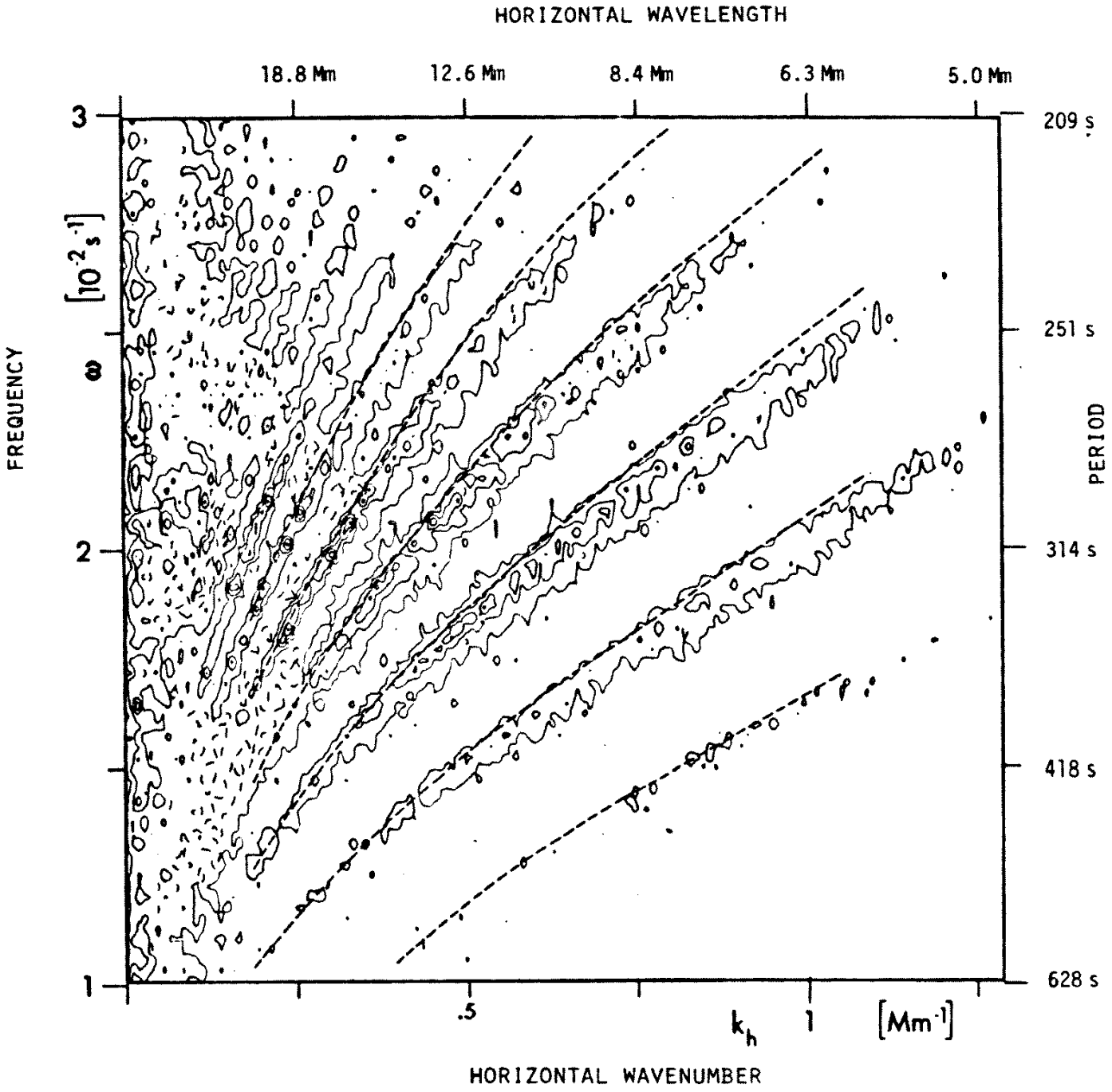

Figure 1.5

k-ω diagram. This contour plot shows power observed in the five-minute oscillation as a function of horizontal wavenumber k and frequency ω . The observations from which this diagram was obtained sampled photospheric velocities in Fe I λ5576 with 192" x 944" and 7.11 hours coverage. The velocities were Fourier transformed in the long spatial direction and in time and averaged in the short direction to obtain this k-ω diagram. This observation convincingly demonstrates that only certain wave modes occur. The vertical reflection properties for acoustic waves in the envelope nicely explains why only certain modes are allowed. The dashed lines show the predicted positions of the ridges using a solar interior model from Ulrich and Rhodes (1977). (Deubner, Ulrich, and Rhodes 1979)

a medium with a constant vertical gradient of temperature. The appropriate dispersion relation results from linearizing the inviscid equations of motion and using the adiabatic energy equation for a perfect gas. Separable solutions can be obtained that are sinusoidal in the horizontal coordinate x, in the vertical coordinate z, and in time t, and which involve a vertical wavenumber k_z, a horizontal wavenumber k_x, and a frequency ω. We assume that the mean conditions in the Sun remain constant in the horizontal x and in time t, but vary in the vertical z. A given wave will maintain constant k_x and ω, but will vary in k_z. The dispersion relation relates a local k_z to the waves k_x and ω, and allows us to track the wave propagation by ray tracing methods. We assume that the vertical wavelength for the waves is small compared to the scale height for the variation of the mean state.

Propagating waves occur between upper and lower temperature cutoffs; damped or evanescent solutions are found outside of this range. Physically the upper and lower temperature cutoffs correspond to wave reflection points. The high temperature reflection point results from the increase in sound speed c that occurs with increasing temperature and depth. Wave reflection occurs when c exceeds the maximum allowable phase speed for a given mode, ω/k_x. As the temperature in a perfect gas

in hydrostatic equilibrium decreases, the density scale height also decreases; the phase relation between the density and velocity fluctuations over a wavelength is affected, and at some lower temperature cutoff waves of a given mode become evanescent. In the solar envelope g constant, but T increases with depth at approximately the adiabatic rate. This creates a natural acoustic cavity in the envelope in which waves may be reflected upward at some depth $z_0(k, \omega)$. In the atmosphere, wave modes may be reflected downward either at a low temperature cutoff in the photosphere (when $\omega < 2\pi/300$ sec), or at a very high temperature cutoff in the transition zone. This defines the reflection point $z_1(k_x, \omega)$.

For a given wave mode k_x, ω, the upper and lower reflection points z_0 and z_1 define a harmonic cavity in the solar envelope. For illustrative purposes we consider the properties of such a cavity having infinite Q. If the time of travel of the wave across this cavity is exactly an integral number of oscillation periods π/ω, the wave will be an eigenmode; otherwise it will experience destructive interference. The wave travel time is written as an integral in z from z_0 to z_1 of the vertical phase speed of the wave $(k_x^2 + k_z^2)^{0.5} / ck_z$.

We have solved this integral numerically for a range of k_x, ω, given T(z) from a mixing-length model for the solar interior. The vertical wavenumber $k_z(z)$ is

defined in the dispersion relation discussed earlier, so it is determined completely by local conditions and the assumption that dT/dz is constant within at least one vertical wavelength for the wave. Figure 1.6 shows the resulting lines, each corresponding to the locus of eigenmodes for a given number of wave nodes j found within the cavity. In the figure four regions are labeled. Region I contains photospheric gravity wave modes, which have not been considered here. Region II contains those modes that have an upper reflection point in the solar atmosphere but that may travel freely into the interior. The trapped modes with an upper reflection point in the photosphere lie in region IV, and the trapped modes with an upper reflection point in the transition zone lie in region V. This result, although simply obtained, agrees well with the non-radial pulsation models for the Sun by Ulrich (1970a), and Ando and Osaki (1975). It also agrees qualitatively with the observations (compare with Figure 1.5), although the positions of the ridges are significantly displaced from their expected locations. By detailed comparison with the observations, Ulrich and Rhodes (1977) probe the internal T(z) in the envelope and discover that it has a shallower gradient than had been expected on the basis of mixing-length analysis.

The fact that narrow ridges are observed indicates

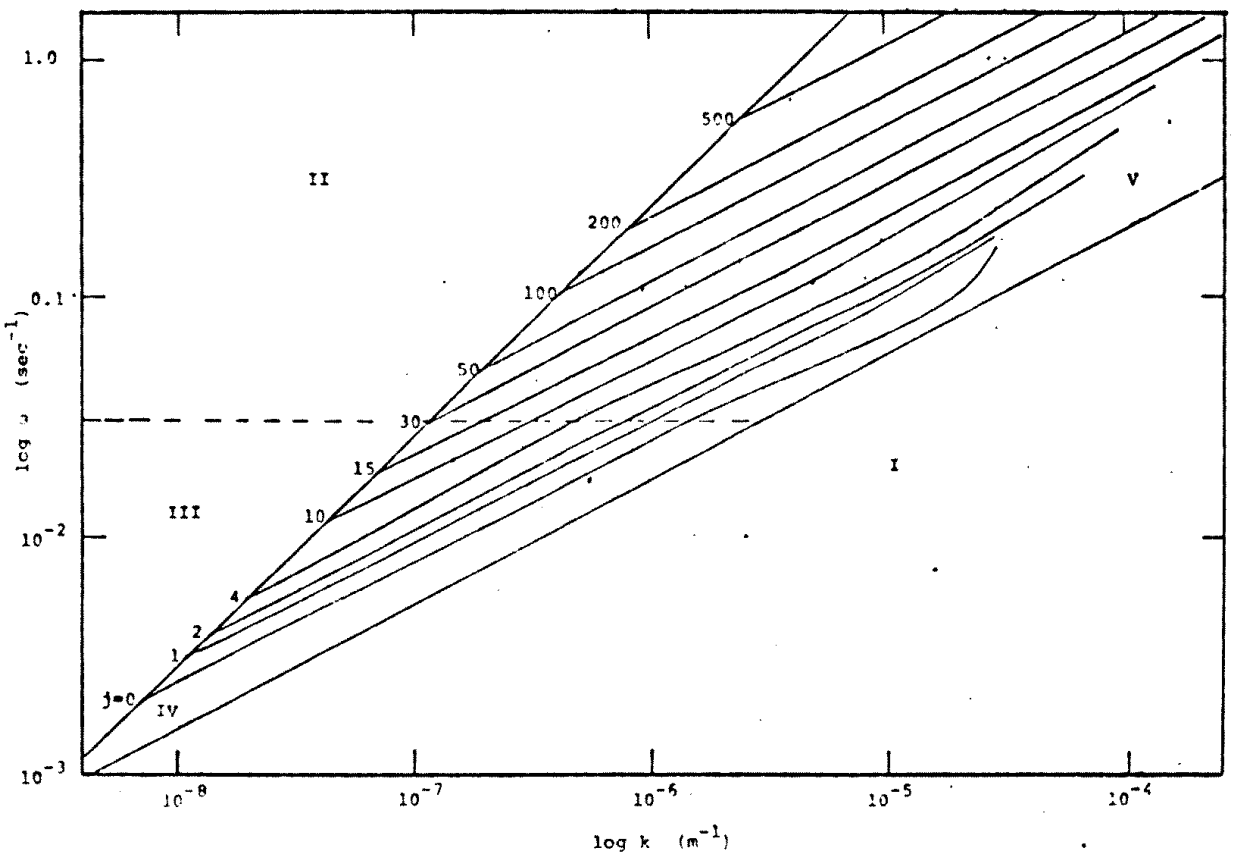

Figure 1.6

Model generated k–ω diagram. The solar envelope filtering properties are readily modeled using the linear wave dispersion relation for acoustic-gravity modes in a medium with constant density scale height. This diagram shows our prediction for the positions of the ridges using a mixing-length model for the solar envelope (Latour 1970). Region I contains those modes which are gravity waves in the photosphere. The dashed line separates waves reflected downward in the transition zone (above the line) from those reflected downward at the temperature minimum (below the line). Regions II and III contain wave modes which travel freely into the solar interior and not reflected upward. The trapped modes lie in regions IV and V where we expect power to occur only along the curves. The integer j denotes the number of nodes that occur in the standing wave between its upper and lower reflection points.

that the lifetimes of the wave modes are at least several hours and that the Q of the solar envelope cavity is high. Whatever drives the wave modes must produce a coherent oscillation over a large portion of the solar surface. Two driving mechanisms have been proposed: 1) Ando and Osaki (1975, 1977) have studied the possibility that overstable driving due to the variation of opacity with temperature may transfer energy from the radiation field into a standing wave. 2) Goldreich and Keeley (1977a,b) consider the interaction of convective overturning with wave modes suggesting that significant power may be put into a particular mode stocastically by turbulent eddies in the convective flow field.

Ando and Osaki formulate a linear model for the radiation driven waves, which shows marginal growth for some of the eigenmodes. The e-folding time for the fastest growing modes is about 1000 cycles. This model has two serious problems: First the predictions disagree with the observations. The fastest growing modes predicted in the model do not correspond to the regions of greatest power in ω, k_x, and some of the decaying solutions actually correspond to areas of maximum power in ω, k_x. Second, dissipation due to convective motion has not been included. It is hard to imagine that waves can maintain phase for 1000 cycles in a medium with such vigorous motion. We expect that adjacent columns of gas

flowing with opposite senses of vertical velocity are present in the convection zone where the waves are trapped. If the amplitude of this motion is, for example 0.1 c, then a given eigenmode in the region of upflow will differ in vertical wavelength by about 10% compared to the same eigenmode in the region of downflow. Thus the eigenmodes in the columns of upflow and downflow will exhibit opposite phase in less than 10 wave cycles. Since most of the observed eigenmodes have nonzero horizontal wavenumber k_x, these modes can interfere destructively. The only eigenmodes that might survive are those whose maximum displacement coincides spatially with regions of little motion in the convection zone.

Goldreich and Keeley (1977a) consider the influence of convection in a model similar to that of Ando and Osaki, but they introduce a Reynolds stress damping term into the equations of motion to simulate the gross effect that convection may have on damping the wave modes. They find that no radial eigenmodes feel net growth from the radiative driving. Unfortunately, their calculation does not consider this effect on the non-radial eigenmodes, which allow large k_x and are applicable to the five-minute oscillations. It is possible that convective overturning may generate an excess of acoustic noise and put power into the eigenmodes of the envelope cavity. Waves produced by such an energetic process should show

no preference for horizontal phase. Destructive interference results and much of the acoustic energy in a given eigenmode may be lost from the cavity. A certain component will however survive since complete destructive interference of the modes requires as much horizontal phase selection as complete constructive interference. Thus acoustic waves of a particular eigenmode that are produced at many places without regard to horizontal phase will leave a surviving stocastic component. The amplitude of the surviving component depends upon the vigor of each acoustic wave source and the total number of sources. This is difficult to model since we have no estimate of the vigor of the convection or of its horizontal variation over the Sun. In one approach Goldreich and Keeley (1977b) write the linear equations for the waves including a nonhomogeneous nonlinear driving term, which represents the convective motions (like Lighthill 1952, and Stein 1967). For a given spectrum of turbulent convection, they estimate the spectrum of waves produced, showing that this type of mechanism is unable to drive radial modes of pulsation with an observable amplitude. Before we can decide whether this is an effective mechanism for driving the five-minute oscillations, such arguments to non-radial modes. A large uncertainty remains due to the lack of an accurate spectrum for the turbulent convection.

c) Supergranulation

While attempting to measure the solar rotation by Doppler methods, Hart (1954, 1956) noticed a residual signal at radius vector 0.8 that had a spatial periodicity along the equator with a mean wavelength of 26,000 km and a velocity amplitude of 400 ms^{-1}. After investigating the possibility that this component was due to scattered light in the instrument, she concluded it was real and demonstrated its persistence during the several hours of the observations. This motion field was subsequently identified as supergranular flows.

i) horizontal component of motion

Leighton, Noyes, and Simon (1962) introduce a tilted pair of exit slits on the spectrograph of the 60 foot tower at Mt. Wilson, in order to cancel the effects of solar rotation and to measure the local velocity component in the solar photosphere. The most prominent feature in their observations is the five-minute oscillation, a temporally periodic motion field having a spatial scale of about 7". They photographically average velocity pictures taken 2.5 minutes apart to obtain a so-called Doppler sum picture. Figure 1.7 shows such a picture taken in the photospheric Ca I λ6103 line. Supergranule cells with a typical diameter of 32,000 km and a velocity dynamic range of about 1000 ms^{-1} fill the region

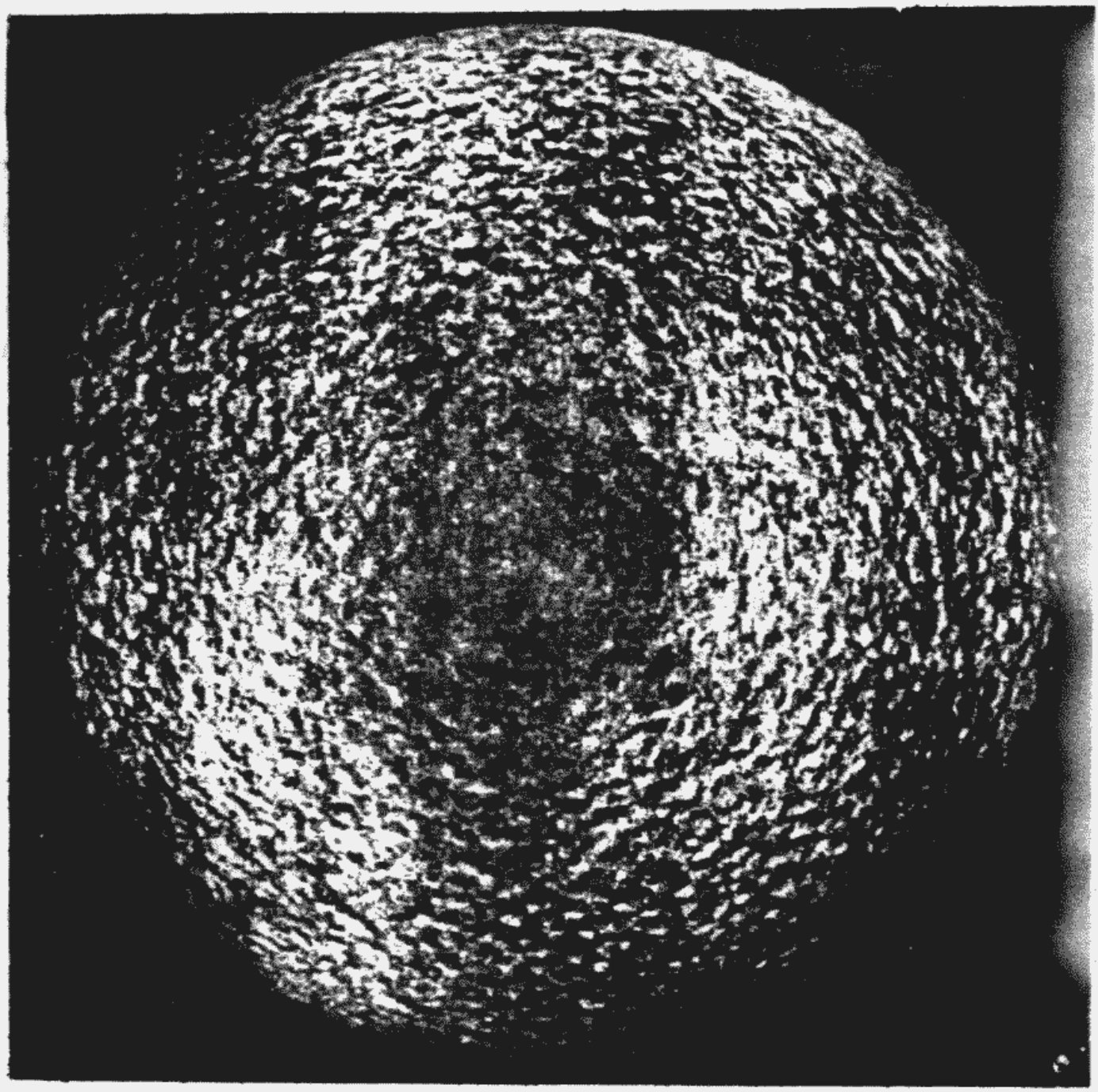

Figure 1.7

Supergranulation in full disk Doppler sum plate. This dramatic Doppler sum plate was obtained by G.W. Simon on 23 June 1962 using the Mount Wilson Magnetograph system operating in the Ca I λ6103 photospheric line. The supergranulation is apparent between radius vectors 0.4 and 0.9. A supergranular cell is characteristically 32,000 km = 0.05 radii across and shows horizontal outflow from the cell center. Dark features which represent flow toward the observer are generally situated on the disk center side of a cell and are adjacent to bright features representing flow away from the observer and toward the limb. The supergranular cells are defined by the their very prominent horizontal component which is evidenced in photospheric velocity pictures, like this one. Vertical flows in the cells show at least a factor of five less amplitude as evidenced by the lack of steady flows at disk center and probably cannot be resolved in photographically obtained Doppler sum pictures. (courtesy G.W. Simon)

from radius vector 0.4 to 0.9.

Simon and Leighton (1964) analyze the Doppler sum observations of the supergranulation in greater detail. They study the cells by autocorrelation analysis and find a high spatial correlation between the chromospheric magnetic network and the boundary between cells. These features are also correlated with the chromospheric network, best seen in Ca II λ3933. This suggests that the supergranular flow may sweep magnetic fields to the cell boundary.

Some attempt has been made to measure the horizontal motions in the supergranulation using tracer methods. Simon (1967) examines a sequence of very high resolution white light photographs obtained on the Sacramento Peak Tower Telescope. The granules that survive from one image to the next are identified as tracers, and their displacements are statistically analyzed. These observations, as well as an application of Fourier techniques to the problem (Harvey 1976), are marginally able to detect the supergranular motions. This is a very subtle effect, since a granule carried at the supergranular velocity of 800 ms^{-1} will move less than 0.5 arcseconds in its 8 minute lifetime.

ii) vertical component

Although much effort has been expended to measure the vertical component of the supergranular motion field,

these velocities remain at the limit of detectability. The main difficulties in making these observations are due to 1) granulation noise, 2) systematic velocities resulting from contrast variations possible in granules (Beckers and Nelson 1978), 3) spurious line shifts caused by line profile changes due to magnetic fields (Frazier 1974), and 4) residual oscillatory signals. Simon and Leighton (1964) report a correlation between cell boundaries and downflow observed in Hα and in Hβ with an amplitude of $\simeq 1000$ ms^{-1}, but they point out the hazards inherent in a simple velocity interpretation in these lines: Hα and Hβ feel contributions over a broad range of heights, and thus asymmetries in the line profile may occur that cannot be interpreted as an isolated motion field. Photospheric lines exhibit a small vertical component of the motion, which seems associated with the cell boundaries. Simon and Leighton correlate a small amplitude downflow with regions of enhanced magnetic field. Measurements of such small amplitude motions however are certainly at the limit of photographic methods.

Tanenbaum et.al. (1969) present one-dimensional spatial scans that are the average of 300 velocity determinations or several hours of observations. Some of their scans were made using the Mt. Wilson magnetograph system with 5 arcsecond resolution and sample an 11 arcminute line crossing the central meridian at 15

degrees latitude ($0.26 < R_V < 0.43$). These observations were made in the spectral lines Fe I λ5250, Fe I λ5906, and Na I λ5896. Although this study indicates that downflow sites occur on the cell boundary we must seriously question how much of the horizontal velocity signal may be present in the measurements. The supergranulation shows a component of horizontal velocity that may be an order of magnitude larger than the vertical component in the photosphere. Thus observations for $R_V > 0.2$ show a horizontal component at least comparable to the vertical. Those of Tanenbaum et.al.s Mt. Wilson measurements that were obtained near the center of the disk are not compared to the chromospheric intensity; no conclusions can be drawn from them other than that a vertical component may be present with 100 ms^{-1} amplitude. Their observations obtained on the Kitt Peak magnetograph system at disk center are compared with the Ca II network in their figure 11, but the authors fail to identify unambiguously the spectral line used or any of the details of the observing program, such as the time to make a scan or the resolution element size. Although these observations appear to show downflow correlated with enhanced chromospheric intensity, it is impossible to make any detailed evaluation of the data.

Frazier (1970) (see also Skumanich et.at. 1976) made observations with the Kitt Peak Magnetograph system

in order to obtain Doppler sum pictures with greater sensitivity than those used by Leighton et.al. These measurements were made in the upper photospheric Fe I λ5233 and lower photospheric Fe I λ5250 lines. The velocity measurements are digital and are derived from photodetector measurements of intensity on either side of the line center wavelength. The 67 x 90 Doppler sum raster with 2.4" x 2.4" resolution element was built out of seven line sections, each section being observed twice with a time interval of 150 seconds. Each Doppler sum picture was obtained after one hour of observation, and four of these were averaged to obtain the velocity pictures used in this study. The Fe I 5233 velocity picture shows a high degree of correlation with the magnetic field image obtained simultaneously, in the sense that points of downflow coincide with those of enhanced magnetic field. The Fe I λ5250 velocity picture, however, does not show a similar correlation, in conflict with the results of Tanenbaum et.al. Frazier averaged many one-dimensional scans across cells seen in the Fe I λ5233 velocity picture to produce a cross-section for the "average" supergranule cell. This shows a broad region of upflow in the cell interior with an amplitude of 40 ms^{-1} and typically a 5000 km wide band of downflow at the cell perimeter with amplitude of 80 ms^{-1}. We expect that oscillatory noise, however, contributes substantially to the observed

signal. In a Doppler sum plate made from a single pair of velocity images, oscillations with periods around 200 or 400 seconds may leave a residual noise component of about 50% amplitude or 200 ms^{-1}. In this study four Doppler sum plates were averaged in time reducing this oscillatory noise to about 100 ms^{-1}, comparable in amplitude to the reported downflows.

Musman and Rust (1970) show an example of a two-dimensional Doppler sum picture compared to a simultaneously obtained Ca II λ3933 negative. These observations were made on the Sacramento Peak Big Dome Doppler Zeeman Analyzer (DZA), which is a photoelectric instrument similar to the Mt. Wilson magnetograph. They averaged twenty-five 35 second scans to obtain the velocity image that is shown here in Figure 1.8. Their observations were made using a 6 arcsecond entrance window. More often than not, relative material downflow occurs on the network boundary and upflow is observed in the cell interior, but this is not strictly the rule. Unfortunately these observations are centered at $R_V = 0.47$, where we expect the motion to be dominated by the horizontal supergranular component.

Some observations have been carried out to determine the height variation of the vertical and horizontal motion fields associated with the supergranulation. Deubner (1971) examines the velocity rms in time averaged

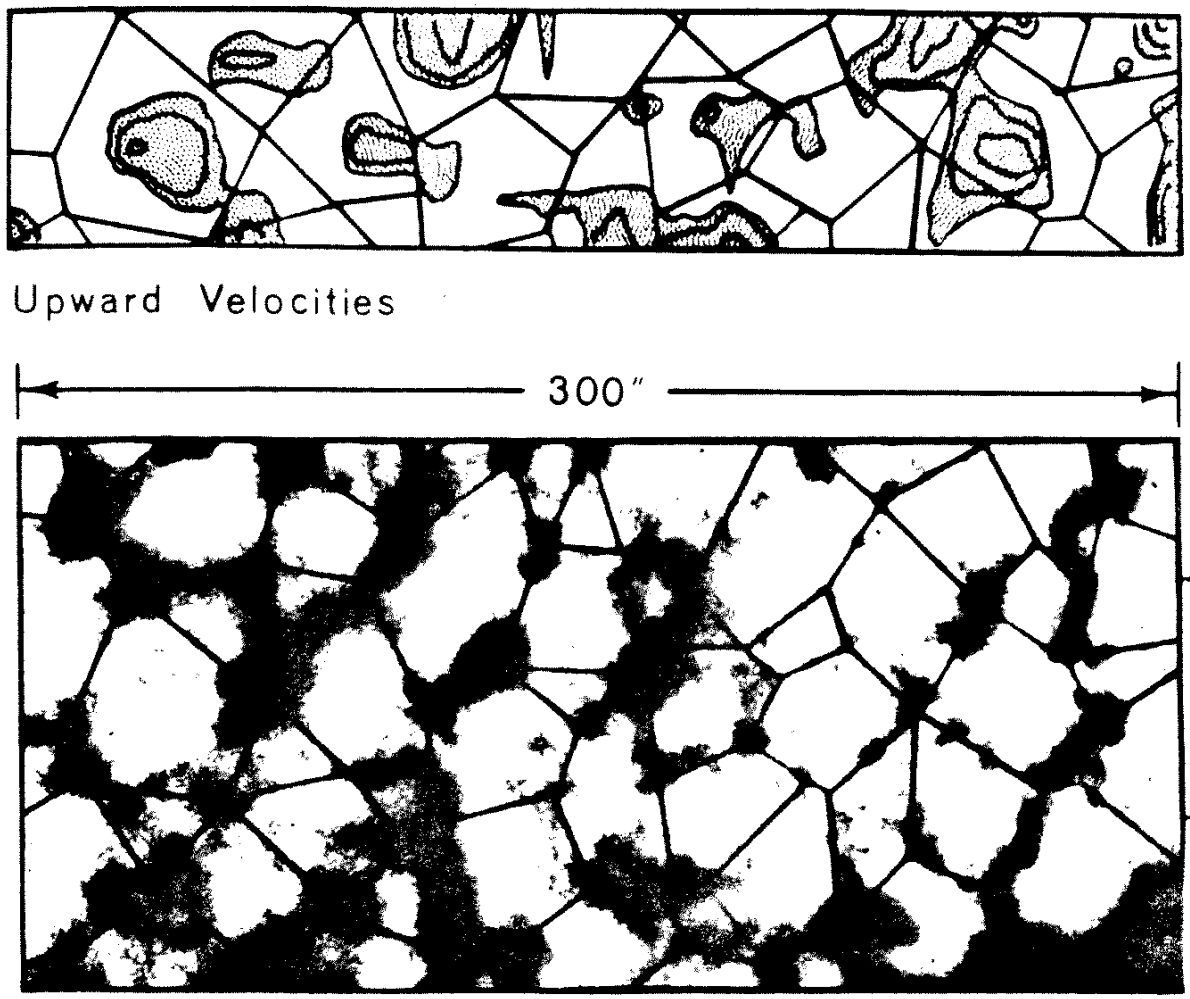

Figure 1.8

Possible vertical steady flows. The top and bottom contour plots show the line of sight velocity toward and away respectively as measured by Musman and Rust (1970) using the SPO Doppler Zeeman Analyzer operating in Fe I λ5250. The middle image shows the Ca II bright network in negative. Lines are drawn in all three images over the apparent network. These observations usually show apparent downflow in the network and upflow in the cells, however, the pointing was centered at $R_v = 0.47$ where there is a sizable contribution from the horizontal supergranular component.

linear scans as a function of radius vector. These observations were made in a number of spectral lines that sample from the deep photosphere (C I λ5380) to above the temperature minimum (Mg I λ5173). The observations are similar to those of Tanenbaum et.al. and use the Coude reflector at Anacapri with 4" x 4" resolution. The linear scans were made along the equator from limb to limb in a time of 150 seconds and six such scans were averaged to obtain the velocity measurements used in this study. In the deep line C I λ5380, the horizontal velocity amplitude is 210 ms^{-1} compared to a steady vertical velocity amplitude of about 25 ms^{-1}. High in the photosphere the vertical and horizontal components seen in Mg I λ5173 become comparable in amplitude and are roughly 130 ms^{-1}. Deubner's results show less rms amplitude than those of the other studies because they were made with lower spatial resolution. These observations indicate that the horizontal rms decreases with height whereas the vertical rms increases with height. It is uncertain however, that the rms velocity for the vertical component is associated with supergranulation. To settle this issue, Deubner compares linear scans with Hα spectroheliograms and points out that downflow sites seen in all these lines correlate with the chromospheric network. He also obtains two-dimensional raster scans and these confirm this result. Unfortunately, the spatial coverage in

these observations is less than one supergranular cell making statistical results uncertain.

Worden and Simon (1976) have carried out a similar study using three Fe I lines that sample heights from the deep photosphere to the temperature minimum. This is the first study using non-magnetic (g= 0) spectral lines, thereby avoiding the erroneous velocity measurements that can occur in regions of strong fields. Their observations were made on the Sacramento Peak diode array instrument, which provides two-dimensional photoelectric measurements in a number of spectral lines simultaneously. The rasters were obtained with 1" x 1" resolution, covering 128" x 128" in a total time of 1 minute. The observations were carried out at disk center in the velocity lines Fe I λ4065, Fe I λ5123, and Fe I λ5434, and in the magnetically sensitive line Fe I λ8468. Velocity and magnetic field images obtained from this data were averaged over 20 minutes to cancel the five-minute oscillation and some granulation residuals. Comparison of the velocity images with the magnetic field picture shows the surprising result that downflow is correlated with sites of enhanced magnetic field only in the deepest formed line Fe I λ4065. The other two lines even show a small net upflow at the magnetic field sites. Our estimates indicate, however, that granulation noise should be $\simeq$190 ms^{-1} in these data since 1" spatial resolution was

used and the averaging was over only about 2-3 granule lifetimes. The result from this study is in conflict with all the previous observations.

iii) temperature structure

A number of observational studies have searched for a temperature structure in the supergranulation analogous to that seen in the granulation and such as might be expected for vigorous convection. In the chromosphere there is a definite temperature increase associated with the cell boundary as evidenced by the Ca II λ3933 network. This is generally considered to result from the enhanced magnetic field strength and associated magneto-hydrodynamic waves; it is probably not directly associated with the convection. A number of investigators have looked for temperature structure at deeper levels in the atmosphere. Simon (1967) compares white light granulation photographs with H and Ca II λ3933 images. He points out that often there are bright and dark regions that vary with a scale of about 5000 km but that these are not well correlated with the Ca II network (see also Beckers 1968). A similar result is obtained by Worden (1975), who compares observations made in three infrared wavelengths, one formed 30 km below the $\tau_{5000}= 1$ level, one that samples at the $\tau_{5000}= 1$ level, and a strong Mg I line at 1.7108μ formed near the temperature minimum. The deep photospheric intensity measurements show

structure with 3% contrast but the patterns do not show a high correlation with the Ca II network.

The observations of temperature structure in the deep photosphere are at the limit of detectability, and the results are conflicting and difficult to interpret. It is not surprising that so small a temperature variation occurs between the supergranule cell and its boundary. If the cells are convective, originating deep in the solar envelope, the motions we see must have penetrated substantially beyond the region of convective driving; since thermal variations associated with convection do not penetrate as effectively as the motions themselves, we would not necessarily expect to see them. From the work of Simon (1967) and Worden (1975), there does appear to be some thermal structure in the deep photosphere, but it is at best weakly correlated with the chromospheric network or with the supergranulation.

1.3 Our Program of Observations

The goal of this program is to measure the height variation of the vertical and horizontal components of the supergranular motion. We make simultaneous velocity measurements in a number of spectral lines that sample from the photosphere to the middle chromosphere; the

observations are carried out both at disk center and R_V= 0.8 so that we can sample the vertical and horizontal components of the flow respectively. Our program requires measurements in the ultraviolet using satellites, for the visible portion of the spectrum does not contain lines formed in the middle chromosphere that are suitable for velocity studies. Our satellite observations using the University of Colorado Spectrometer on the Orbiting Solar Observatory 8 (OSO 8) are made in the Si II λ1817 line formed in the middle chromosphere. At the same time we make similar observations with the photospheric Fe I λ5576 or Fe I λ5434 lines and in the low chromospheric Mg I λ5173 line using the Sacramento Peak Observatory (SPO) Diode Array. Direct comparison of the velocities obtained in the separate spectral lines provides a method of identifying the supergranular flows at different heights. This also provides confidence in our ability to discern supergranular steady velocities in the chromosphere where they have never been identified and at disk center where there remains much disagreement in the results of previous observations.

This program of observations differs from previous work in three important ways: 1) We extend the measurements of supergranular flows to the middle chromosphere. This is a region that has never been explored and so these observations can serve to clarify the role of

supergranulation in chromospheric processes. 2) We directly compare our velocity measurements of the steady component with independent time averages and thereby distinguish the contribution due to noise. 3) We make detailed comparison of the motions that we measure in the different spectral lines. For the lines formed at similar heights this provides another check on the velocity measurements. Throughout the range of available heights this allows us to trace the motions directly and strengthens the inferences we can make from the relatively low resolution satellite observations.

The details of our observing program and data reduction techniques are described in Chapter 2, where we present results from our observations at radius vector $R_V = 0.8$. Our measurements of the vertical component seen in the ground-based observations at disk center are discussed in Chapter 3. Here we present our observations of mesogranulation, a steady motion field with a 10" scale between that of granulation and supergranulation. Chapter 4 discusses the corresponding OSO 8 observations of vertical steady flows seen in the chromosphere. The primary goal of this work, a map of the height variation of the vertical and horizontal flows in the supergranulation cells, is presented in Chapter 5. There much of the theoretical literature relevant to this work is reviewed in the context of the results of these observations.

Many of the qualitative features of the supergranular flow are compared with convection theories and laboratory experiments.

CHAPTER 2

THE HEIGHT VARIATION OF THE HORIZONTAL VELOCITY FIELD

2.1 Introduction

With Doppler measurements of velocity we are able to examine separately the horizontal and vertical components of the supergranular motion by making measurements near the limb and at disk center. The problems encountered in either of these measurements are somewhat different since the character of the flow changes significantly from the vertical to the horizontal component. In this chapter we examine observations of the horizontal component of the supergranular motion with measurements made near radius vector $R_V = 0.8$. At that position on the disk the line-of-sight velocity V, which we measure by Doppler shifts in spectral lines, is composed of a horizontal component u and a vertical component w, with $V = 0.8u + 0.6w$. Although a position closer to the limb would yield Doppler velocities that more nearly sample just the horizontal flows, the features there would be too foreshortened for us to resolve an individual supergranule cell with our satellite observations. Thus the radius vector 0.8 location gives a fair representation of

the horizontal motions, though there may be a significant blending of both u and w in the Doppler signal. Separate observations at disk center will directly measure the vertical flow in supergranulation. These will permit us to resolve some of the ambiguity in our radius vector 0.8 observations of the horizontal flow.

Our observations are made in a number of spectral lines so that we can analyze the height variation of the motions from photospheric to chromospheric levels. Doppler velocity measurements at chromospheric levels require satellite measurements since spectral lines suitable for this are accessible only in the ultraviolet. We have carried out coordinated satellite and ground-based observations using the University of Colorado Ultraviolet Spectrometer on Orbiting Solar Observatory 8 (OSO 8) and the diode array instrument at the tower telescope at Sacramento Peak Observatory (SPO). The velocities are determined from Doppler shifts of a middle chromospheric Si II line accessible with OSO 8 and from Fe I and Mg I photospheric lines observed at SPO. The heights of formation of these spectral lines span 1400 km or nearly 11 density scale heights. These observations are complemented by SPO intensity and magnetic field measurements in other spectral lines.

2.2 Observations and Reduction

Our ground-based observations are made with the SPO diode-array, which operates at the exit slit of the echelle spectrograph attached to the vacuum tower telescope (Dunn, Rust, and Spence 1974; Worden and Simon 1976). Five strings of 32 diodes each are arranged parallel to the slit: pairs of diode strings are located on either side of the Fe I λ 5576 line (for measuring Doppler velocities) and the Fe I λ8468 line (for magnetic intensities), and the final string is centered on the Ca II K line at λ3933 (for determining network patterns). The entire system is then spatially rastered to provide two-dimensional intensity, velocity, and magnetic images at each of the selected wavelengths. One complete raster covers a nominal area of 240" x 260", with a spatial resolution of 2" x 2". Such rasters are repeated every 84 s, allowing us to develop statistics for waves with periods in excess of about 180 s. Typical observing runs last about 3 hours.

The Ca II intensity image of the chromospheric network is used primarily to establish the relative pointing between the ground-based and satellite observations, and it also provides a means of identifying the supergranule

cell boundaries. Regrettably the Ca II chromospheric lines are not well suited for explicit velocity measurements because both the H and K profiles are heavily saturated and have very low slopes in their cores. We have selected the Fe I line at λ5576.10 as suitable for photospheric velocity measurements, primarily because it is not subject to Zeeman splitting (g= 0). Narrow enough to provide adequate velocity sensitivity, this Fe I line is formed over a sufficiently small height range to provide good vertical resolution as well. In addition, it is not seriously blended with other lines. According to calculations of Altrock et.al. (1975), the steepest portion of the λ5576 profile, as seen at radius vector 0.8, is formed at a mean height of about 200 km above τ_{5000}= 1. Regions of enhanced magnetic field strength in the photosphere are identified from measurements in the magnetically sensitive Fe I λ8468 line (g= 2.5).

Our satellite observations are made with the OSO 8 Ultraviolet Spectrometer (Bruner et.al. 1976). While we had hoped to make our EUV observations in a number of different chromospheric and transition-region spectral lines, the sensitivity of the detector has limited us in practice to the Si II λ1816.93 line, formed in the upper chromosphere at about 6500°K (Tripp, Athay, and Peterson 1979) at a height of about 1600 km (Chipman et.al. 1976). Two sampling modes are used to obtain the Si II λ1817

data: (1) In its fast raster-mode, the detector samples 7 x 8 spatial points with 20" x 20" resolution, in a time interval of 42 s. By performing spatial rasters successively on either side of the line profile, we obtain a sequence of two-dimensional intensity and velocity frames. Given the available photon counts, this compromise between spatial coverage and temporal resolution allows us to sample an area equivalent to that of about 10 supergranule cells, and to do so with a repeat time rapid enough to resolve those oscillatory and impulsive components that have been seen to possess substantial power. The available observing time on OSO 8's 96 minute orbit is at best 57 minutes: by utilizing up to five successive orbits, we are able to obtain observations spanning periods of as much as 7.5 hours. (2) Better spatial resolution is obtained by the point mode in which a one-dimensional array of 20 spatial points is sampled, each with 2" x 20" spatial resolution. At each spatial point, six measurements are made across the line profile, thus providing a more sensitive velocity determination. These observations are completed in a time interval of 150 s and then repeated for the duration of the orbit.

The large field-of-view (nominally 140" x 160") in the OSO 8 raster-mode intensity observations is used to determine the co-alignment with the SPO instrument. Further, the accompanying velocity patterns allow us to

establish the persistence of the large-scale steady velocity fields over many orbits. However, the 20" x 20" spatial resolution in this mode is not sufficient to permit detailed comparison between the OSO 8 and SPO velocity observations. Such comparisons are carried out mainly with the OSO 8 point-mode data, and our strategy has been to make raster-mode and point-mode observations on alternate orbits.

a) Determining the Velocities

At each spatial position, we obtain the instantaneous Doppler velocity by comparing our observed ratio $r = (I_R - I_B)/(I_R + I_B)$ with a grid of values computed as a function of the Doppler shift $\Delta\lambda_V$. For the OSO 8 and SPO raster-modes I_R and I_B are the intensities measured on the red and blue sides of line center at a distance $\Delta\lambda_M$ where the slope of the profile is approximately steepest. For the higher-resolution point mode on OSO 8, I_R and I_B are weighted means of the three measurements on each side of the line profile, the weighting factor being the slope of the unshifted profile. As long as the shape of the line profile does not change, r depends only on the Doppler shift of the line.

In order to compute a grid of ratios r we adopt a mean line profile $\phi(\Delta\lambda)$ for each spectral line, where $\Delta\lambda$ is the distance from line center. Detailed observations

of the Si II λ1817 profile in both quiet and moderately active regions indicate that it is a Gaussian with a constant width of 0.08Å. A background due to scattered light from the line itself and from the λ1900 continuum appears to vary in proportion to the central intensity in the line. For the Fe I 5576 line, an out-of-focus image is used to measure the mean profile $\phi(\Delta\lambda)$ prior to each observing run. This technique is subject to certain systematic errors if there are spatially unresolved velocities like those due to granulation. These motions may introduce asymmetries into the mean line profile or if present during the observations may lead to a misinterpretation of the line shift. Estimates for the nature and amplitude of this effect are a current research topic (Keil 1976), but probably are less than 50 ms^{-1} (see Worden 1975).

From $\phi(\Delta\lambda)$ we compute a table of ratios,

$$r(\Delta\lambda) = \frac{\phi_+' - \phi_-'}{\phi_+' + \phi_-'} \quad , \tag{2.1}$$

where $\phi_\pm = (\Delta\lambda_M \mp \Delta\lambda_V)$, and ϕ' is the mean profile ϕ convolved with the spectral window of the red or blue detector. The Doppler shifts $\Delta\lambda_V$, and hence the velocities V corresponding to values of r obtained from observation, are found by interpolation.

We have tested this method using artificially

generated data for which the line profile was sampled in a number of different modes. We find that the method can be at least as reliable as either Gaussian-fit procedures, which often diverge, or moment methods, which are strongly affected by background intensity.

b) Time Averaging the Velocities

We determine the persistent velocities associated with supergranulation by forming long time averages of the data, thereby attempting to filter out the various wave modes, granulation, impulsive events, and other non-steady motions. The dominant time-varying velocities that can be spatially resolved by our observations are the five-minute oscillations. In the Fe I line these oscillations have typical amplitudes of order 400 ms^{-1} at disk center and show power in a broad band of frequencies from about 2.5 mHz (400 s period) to 5 mHz (200 s). The typical oscillation element has a horizontal coherence scale of about 7". From the narrow ridges of power evident in k-ω (temporal and spatial frequency) diagrams, the individual oscillating elements appear to be the result of interference patterns associated with global oscillatory modes (Deubner 1977; Rhodes, Ulrich, and Simon 1977, Deubner, Ulrich, and Rhodes 1979). The velocity amplitude of these Fe I oscillations decreases noticeably toward the limb, being only about 250 ms^{-1} at

radius vector 0.8. The OSO 8 observations of oscillations in Si II have much the same character. Line profiles are usually measured with a 2" x 20" sampling element and repeated at a single location every 51 s to form time series spanning about 50 minutes in each orbit. Power spectra of the Doppler velocities show quasi-periodic oscillations in a band centered at 3.3 mHz (300 s period), with substantial power in the interval from 2.5 mHz to 5 mHz (Chipman 1977; Athay and White 1979). The oscillating velocities have peak amplitudes of about 2000 ms^{-1}. This broad band of oscillations shows up in about half of the data sets. The power spectra also show a flat plateau in power from 10 mHz to the 34 mHz Nyquist frequency; this noise-like component is thought to be of solar origin, but instrumental image jitter has not been ruled out. Toward the limb, the velocity amplitude in the Si II quasi-periodic oscillations drops off more rapidly than the intensity fluctuations, reaching a typical value of 1000 ms^{-1} at radius vector 0.8. This oscillatory component in our observations is effectively filtered out by averaging data over entire satellite orbits, or roughly 10 oscillation periods.

The velocity signal from granulation is greater in the SPO photospheric observations than in the OSO 8 chromospheric studies because these motions appear to decay rapidly with height. In the SPO data, we estimate that

granular residual motions will contribute about 100 ms^{-1} to each velocity measurement, since the SPO spatial resolution of 2" x 2" is insufficient to resolve the individual cells. By time-averaging over periods long (of order 50 minutes) compared with the characteristic granule lifetime of about 10 minutes, we sample a number of different granulation patterns, thereby reducing the effect of these residual motions.

Even our time-averaged velocity fields may, however, contain a spurious signal from spatially unresolved motions of granules and waves. Since regions of ascending motion in granules emit more photons than the cooler descending regions, they produce a blue shift in measurements of Doppler velocities near disk center. Further, any change in the character of the granulation in regions of enhanced magnetic fields could result in an apparent large-scale steady velocity pattern that is just an artifact of the unresolved motions (Beckers and Nelson 1978).

Similar bogus or unresolved velocities could be produced by wave modes that exist only in certain regions or whose character is modulated by underlying structure. If the unresolved velocities are predominantly radial, these effects will decrease toward the limb, making the study of the horizontal flows associated with supergranulation more tractable than that of the vertical motions

at disk center. In the upper chromosphere, spatially unresolved velocities in spicules may influence our observations, as may the wave modes with velocity amplitudes that increase with height, provided the velocities are correlated with intensity fluctuations. These issues could best be clarified by velocity observations with spatial resolution better than 0.5" x 0.5" and with 10 s time sampling. Until such data become available, we must be cautious in interpreting large-scale velocity patterns.

c) Instrumental Errors in Measurement

Our time averaging over many individual observations also substantially reduces errors in measurement that are instrumental in origin. These errors arise from detector shot noise, spectrograph drift, image jitter, relocation of the wavelength drive, and lack of absolute spectral reference for the spectrographs.

Shot noise is due primarily to the limited sensitivity of the detectors. The diode detectors in the SPO instrument have a measured error of ±1.0 % at the operating light levels. At half-maximum intensity in the unshifted Fe I λ5576 profile, this corresponds to an error of 30 ms^{-1}. Since our velocities are obtained by differencing two such measurements, the statistical error in any single velocity determination is about ±40 ms^{-1}.

Statistical uncertainties add by the square of the noise amplitudes since the noise increase is a random walk process. Averaging over 10 time frames reduces this to about 15 ms^{-1}, which must be added to the estimated 50 ms^{-1} uncertainty introduced by asymmetries in the mean line profile.

The situation is quite different for the OSO 8 measurements. The typical number of photon counts in our Si II λ1817 observations is about 65, corresponding to an error of 12% in each intensity measurement. Given the Si II line shape, this translates to an error of about 1000 ms^{-1} in a single determination of velocity. Averaging over the 45 pairs or rasters obtained in one orbit reduces the shot-noise error to about ±150 ms^{-1}. Image motion across the slit due to pointing jitter, with resulting intensity variations, introduces a false velocity signal that is stochastic in character. We estimate that with the 2" wide slit this error is about ±50 ms^{-1} in the orbital averages. Laboratory calibration of the wavelength drive prior to launch showed that the drive could be relocated to within ±0.03 in second order after repeated cycling. This corresponds to an additional uncertainty of about 100 ms^{-1} in our averaged velocities, increasing the total statistical error to ±300 ms^{-1} in the OSO 8 raster-mode data averaged over one orbit. In the higher-resolution point mode, this total error

reduces to ±200 ms^{-1}. The velocity rms will be increased by this amount due to the noise. When we quantitatively interpret our results we subtract this level of rms noise to estimate the signal rms.

Both the SPO and OSO 8 instruments have problems with spectrograph stability. During a typical 3 hour observing run, the SPO spectrograph may drift by 45 mÅ, introducing line shifts of 2400 ms^{-1} in Fe I λ5576. On OSO 8 the problem is accentuated by the slowly varying thermal stresses in the spectrograph, which can result in shifts of about 15,000 ms^{-1} in Si II λ1817 during the course of an orbit. In order to ensure that the detectors follow the general shift in the line, active feedback systems have been incorporated into the software. After each SPO raster and after each pair of OSO 8 rasters, the spatially averaged intensities on either side of line center are compared and the grating angle updated to compensate for any net drift.

Since no absolute spectral standard is available for either instrument, we must use empirical means to convert apparent Doppler shifts into velocities relative to the solar surface. For this we adjust the spatial averages of the Doppler velocities in each time frame to be the same constant, thereby correcting for departure due to changes in the orbital motion or residual effects of thermal drift. To ensure that any error in our

velocity determination at a single spatial point does not unduly affect the average of an entire frame, we insist that our adjustments vary smoothly through the course of an orbit. Clearly this procedure may be biased by large-scale, long-period oscillations or net flows, but it appears to be adequate for the study of supergranular flows seen. The uncertainties in velocities arising from the thermal drift are of order 50 ms^{-1} when the raster-mode data are averaged over one orbit.

d) Stability of the Diodes

Individual diodes in the SPO diode array slowly drift in sensitivity as a function of time. The diodes always respond linearly within the signal error but change in gain and dark current (zero light level). This introduces streaks in the intensity (and velocity) images which run perpendicular to the slit and with the spatial raster direction.

In order to correct this problem after the data acquisition we use an algorithm, described in Appendix A, which determines a table of gain factors g_i and dark current levels d_i for the diodes i from the raw data in one sample raster. We then apply these correction factors to subsequent 15 minutes of observations after which a new table is generated. The g_i and d_i are used to define a corrected intensity I_i' from the observed

intensity I_i for diode i, with

$$I_i' = g_i I_i + d_i \ . \qquad (2.2)$$

The algorithm we use is local, in the sense that diode measurements are compared to those of adjacent diodes and no condition is applied over the entire raster. This effectively removes the streaks without introducing any physically unrealistic intensity or velocity signal. Systematic variations like limb darkening and solar rotation are accurately reproduced, since the last diode in the string is compared with the first diode on the next swath. Results from using this method have been encouraging.

We attribute much of our success in measuring the small amplitude vertical flows to this correction (see Chapter 3). Previous attempts to identify the vertical photospheric flows have been greatly limited by the data acquisition rates available with most telescopes. Although diode array systems with many detectors usually surmount this difficulty, such systems remain underutilized because of the difficulty to establish and maintain an accurate calibration.

e) Coordination of Satellite and Ground-based Observations

With adequate preparation, we find that we have little difficulty in establishing and identifying the areas of overlap between the OSO 8 and SPO observations. Predictions of the satellite orientation supplied by Goddard Space Flight Center (GSFC) are translated into Standard Stonyhurst coordinates and transmitted to SPO several days prior to the observations. These predictions allow us to establish the satellite pointing to within ±60", well within the SPO spatial coverage, which was designed to accommodate a possible 90" pointing error. Once the data are collected, GSFC provides more precise satellite pointing information, which enables us to relocate the OSO 8 raster within the larger one from SPO. The final correlation is then established by comparing the OSO 8 Si II λ1817 and SPO Ca II λ3933 intensity pictures and is invariably found to be within 40" of the expected pointing position.

2.3 Results

Our observational program was comprised of 42 OSO 8 orbits during 12 observing days over a 9 month period starting in April 1976; 28 of the orbits were devoted to raster-mode and 14 to point-mode observations. These

observations were successfully coordinated with SPO on eight of these days. Preliminary data from OSO 8 were available for analysis shortly after the conclusion of each observing day, thus permitting us to respond to the results in planning the next sequence of observations. The goal of this work is broadly stated in these scientific questions: (a) Do persistent motions of a supergranular scale exist in the chromosphere? (b) What spatial scales and velocity amplitudes characterize these motion fields? (c) How do supergranular velocities seen in Fe I in the photosphere correlate with those observed in Si II in the chromosphere? We address each of these issues in turn.

a) Persistence of the Motions

Figure 2.1 shows Si II λ1817 intensity pictures, and the corresponding velocity averages, for three successive orbits of the OSO 8 satellite. The observations were averaged in time over each orbit. The instrument was operated in its fast raster mode, so these pictures are formed from arrays of 7 x 8 spatial points, each with a spatial resolution of 20" x 20". In order to aid our visual interpretation and comparison with ground-based observations, we display each 7 x 8 raster as a picture in which the gray shade varies continuously between the centers of the raster elements. In the velocity image we

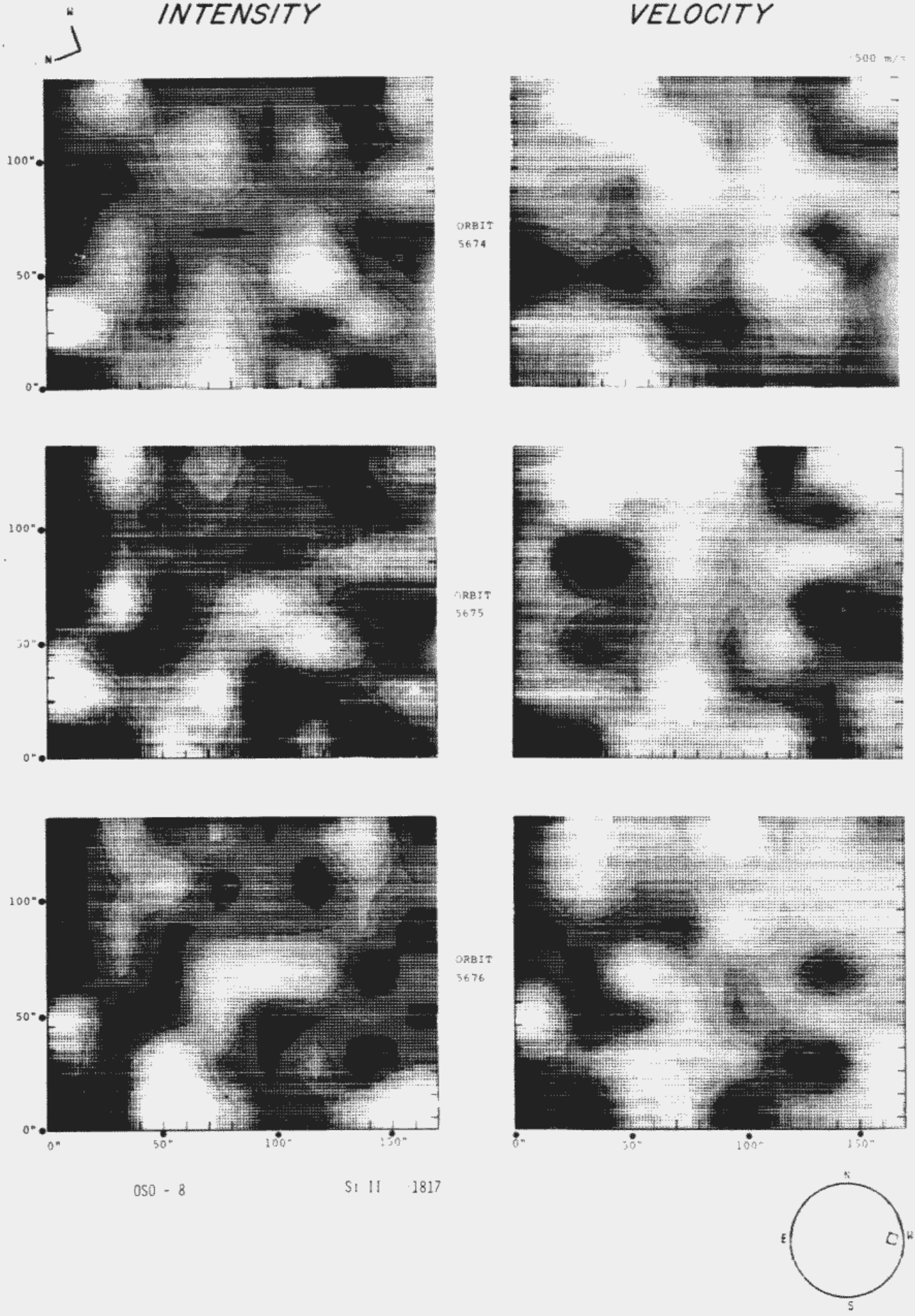
INTENSITY
VELOCITY
N
500 m/s
100"
50"
0"
ORBIT
5674
ORBIT
5675
ORBIT
5676
0"
50"
100"
150"
OSO - 8
S: II 1817
N
E
W
S

Figure 2.1

Persistence of the OSO 8 observations at R_V= 0.8 day 6183. These are time-averaged intensity and Doppler velocity images formed from OSO 8 raster-mode observations in Si II λ1817. The observations cover an area 132" x 168" at radius vector 0.8 on the quiet Sun near the west limb on day 6183 (1 July 1976). The pointing of the instrument was not updated to compensate for the effect of solar rotation so we expect a roughly 10" drift toward the west between the successive orbits. The left side shows the intensity pictures, each an average over one full orbit's observations. Although this data is composed of only 8 x 7 sampling points, we interpolate between with continuous gray tones. The intensity pictures show the same bright features in the three separate images indicating reproducability of the measurements and accuracy of the pointing. The first two velocity averages on the right show the same upflow and downflow features indicating that there are steady flows present in the middle chromosphere. Persistence in the third velocity image is less certain.

use the convention that approaching motion is dark and receding motion bright. Like all the observations discussed in this chapter, these rasters were made on the quiet Sun at a radius vector 0.8 in order to sample a substantial component of the horizontal velocities in the supergranular flows.

The observations shown in Figure 2.1 were made toward the west limb, which is to the upper left in these pictures. Averaged over our 20" x 20" observing window, the dynamic range in these motions is about 1000 ms^{-1}, although the statistical error in the measurements is as much as ± 300 ms^{-1}. Comparison of these pictures shows that the same patterns of time-averaged intensity and velocity were present during the three orbits, which amounts to a total time interval of about 3.5 hours. This data set represents one of our better examples of flows that are seen to persist. The dynamic range of the velocity signal in the chromospheric Si II line is large compared to amplitudes measured in the photosphere. These OSO 8 observations establish that large scale steady velocity fields exist in the upper solar atmosphere at many scale heights above those observed in the photosphere.

In comparing the images the eye automatically looks for spatial patterns, but such patterns are often merely an artifact of the interpolation used which provides

smooth variation of brightness over the image. It is more useful to examine individual features to ascertain their persistence in the orbit sequence. In Figure 2.1, for example, the shape of the dark feature to the left of center in the velocity image changes somewhat between the first and second orbits but its approximate position and amplitude remain unchanged. In the third orbit this feature is still partially present. The third orbit in the series agrees with the first in many places although there are also points of difference. This all suggests a persistence of the flow pattern.

Our data base for studying the persistence of these motions is comprised of a total of five sequences of raster-mode observations, each spanning from three to five orbits. Within each sequence, orbital averages of the intensity picture show that the patterns of bright and dark features are clearly distinguishable from one orbit to the next, although the velocity time averages are less consistently reproduced. Some of these sequences are shown in Appendix C. Figure C.1 presents three orbits which span 5.5 hours. This was the only day of persistence studies on which the satellite pointing was updated to compensate for the rotation of the Sun. Without correction for solar rotation the image drifts about 10" per orbit toward the west. The intensity images show a very remarkable degree of persistence in

this set. Although the pattern in velocities varies somewhat, individual features remain present in all three images.

In the orbit sets presented as Figures C.2, C.3, and C.4, no correction was made for solar rotation. Since every odd orbit is skipped in these sets there is a 20" shift between subsequent images. This is readily apparent in the intensity pictures as features drift toward the west. In these three examples the motion field exhibits persistence of individual features when proper compensation is made for this drift.

One quantitative measure of the correlation we use is the linear regression coefficient r_ℓ. The parameter r_ℓ varies from 0. to 1. depending upon the degree of correlation. For the set of orbits in Figure 2.1, for example, the velocities have $r_\ell \simeq 0.4$ between separate pairs, which for the data base of 56 points implies more than a 90% probability of correlation (Bevington 1969). Figure C.1 also shows $r_\ell \simeq 0.4$ between separate pairs.

The occasional lack of persistence we see in these data sets may be due in part to an evolution of the solar velocity patterns during the observing period, nonlinear effects in the velocity determination, or statistical noise in our raster-mode observations. We expect that even a small drift of the image can adversely affect the velocity determination. The velocity we measure for each

raster element is not merely the spatial average of velocities but represents an average over the 20" x 20" raster element which weights velocities associated with brighter features preferentially. Shifting of the raster elements by say 10" may move brighter features from one raster element to the next and thereby affect the velocity determination in a nonlinear way. The largest contribution to the error, however, must be from the statistical noise in the velocity determination.

b) The Coordinated Observations

Figure 2.2 shows an example of our coordinated satellite and ground-based observations. In the upper frames we compare an OSO 8 time averaged Si II λ1817 intensity picture (orbit 7636) with one formed from Ca II λ3933 data taken simultaneously at SPO. The two instruments were pointed at a quiet region on the Sun near the northwest limb. The OSO 8 Si II picture at the left is again a full orbital average of raster-mode observations with 20" x 20" resolution, similar to those shown in Figure 2.1. The SPO Ca II picture at the right, with 2" x 2" resolution, is a section from the larger spatial raster, time-averaged over 30 minutes during the four orbit OSO 8 observing run. The limb is directly to the left in these pictures: limb darkening has been removed from the Ca II data in order to facilitate comparison with Si II,

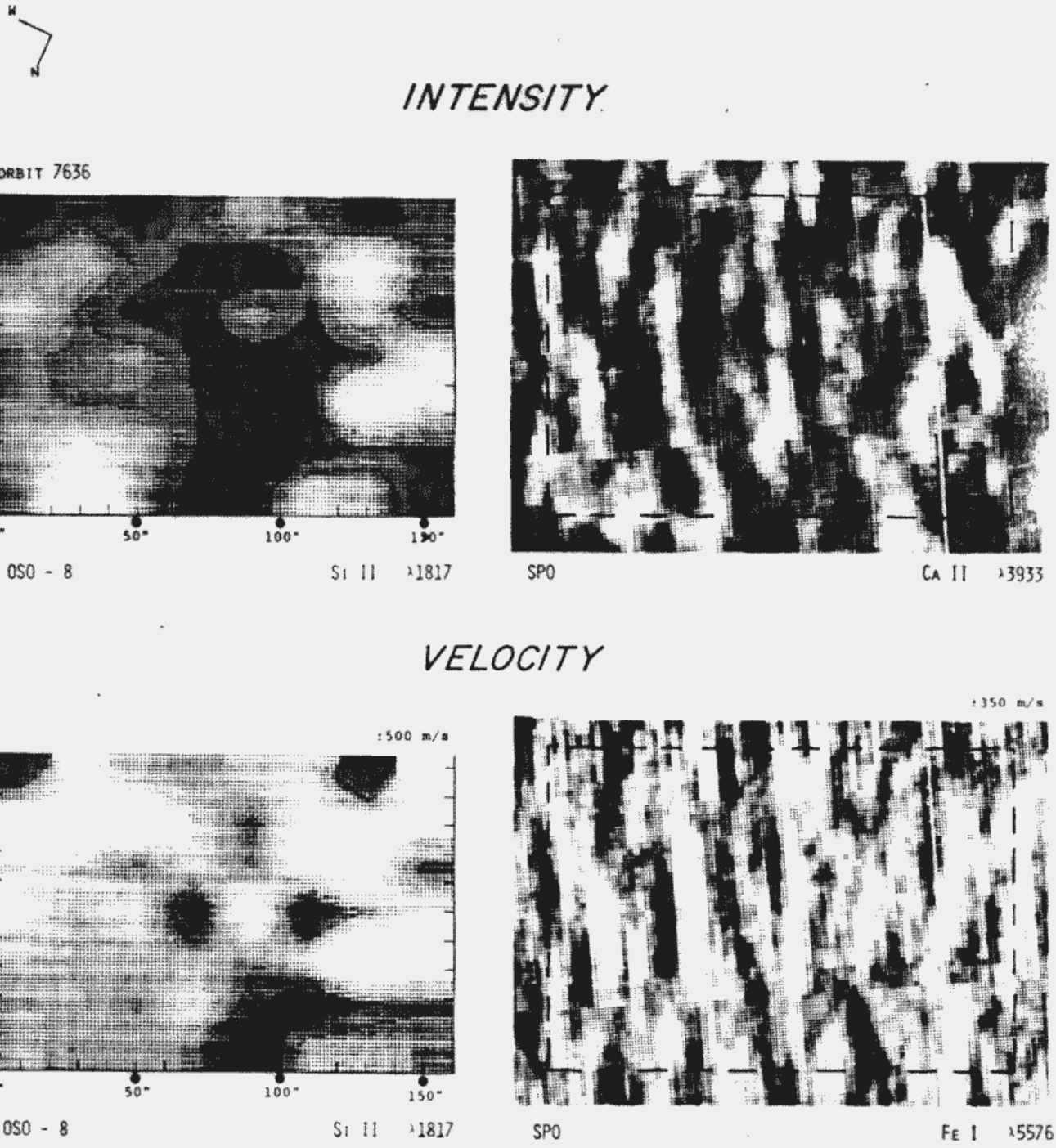

Figure 2.2

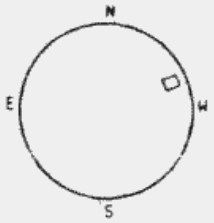

SPO and OSO 8 coordinated observations from day 6313. This compares the SPO time-averaged intensity and Doppler velocity images with those obtained simultaneously with OSO 8 in its fast raster mode. The dashed outlines on the SPO pictures at the right show the region of overlap in the pointing of the two instruments, a 132" x 168" area at radius vector 0.8 on the quiet Sun near the northwest limb on day 6313 (8 November 1976). In the upper frames, the SPO intensity picture in Ca II λ3933 is compared with the OSO 8 Si II λ1817 picture. The lower frames show the corresponding velocity averages formed from SPO Fe I λ5576 photospheric observations at the right and OSO 8 Si II data from orbit 7636 on the left. The Fe I velocity image clearly shows the foreshortened supergranular cells aligned perpendicular to the limb direction. The spatial resolution in the OSO 8 velocity image is inadequate to resolve this effect.

which shows little center-to-limb variation.

Although the instruments have quite disparate spatial resolutions, we are very certain of the pointing overlap in this comparison. There are five exceptionally bright regions in the Si II intensity and these all can be readily identified in the Ca II intensity image. Using the satellite and ground-based pointing information alone we are able to locate the images to within 40". The similarity in the Ca II and Si II intensity patterns gives us a means of refining the actual pointing of the two instruments: we do so by maximizing the computed cross-correlations between the SPO Ca II and the OSO 8 Si II intensity images as their relative positions are shifted. This permits us to co-locate the SPO and OSO 8 data sets to within the 20" x 20" resolution of the OSO 8 instrument. If higher resolution observations are available further correction is made to within the 2" x 20" pointing of this data.

In Figure 2.3 the brightest chromospheric emission features in Ca II are identified by contouring a 10" x 10" running mean of the Ca II data. We chose this sampling window as the most satisfactory compromise between the 20" x 20" resolution of the OSO 8 picture and the 2" x 2" resolution of the SPO observations. The resulting contours are overlaid on both the Ca II and Si II intensity images, where it is seen that, allowing for the

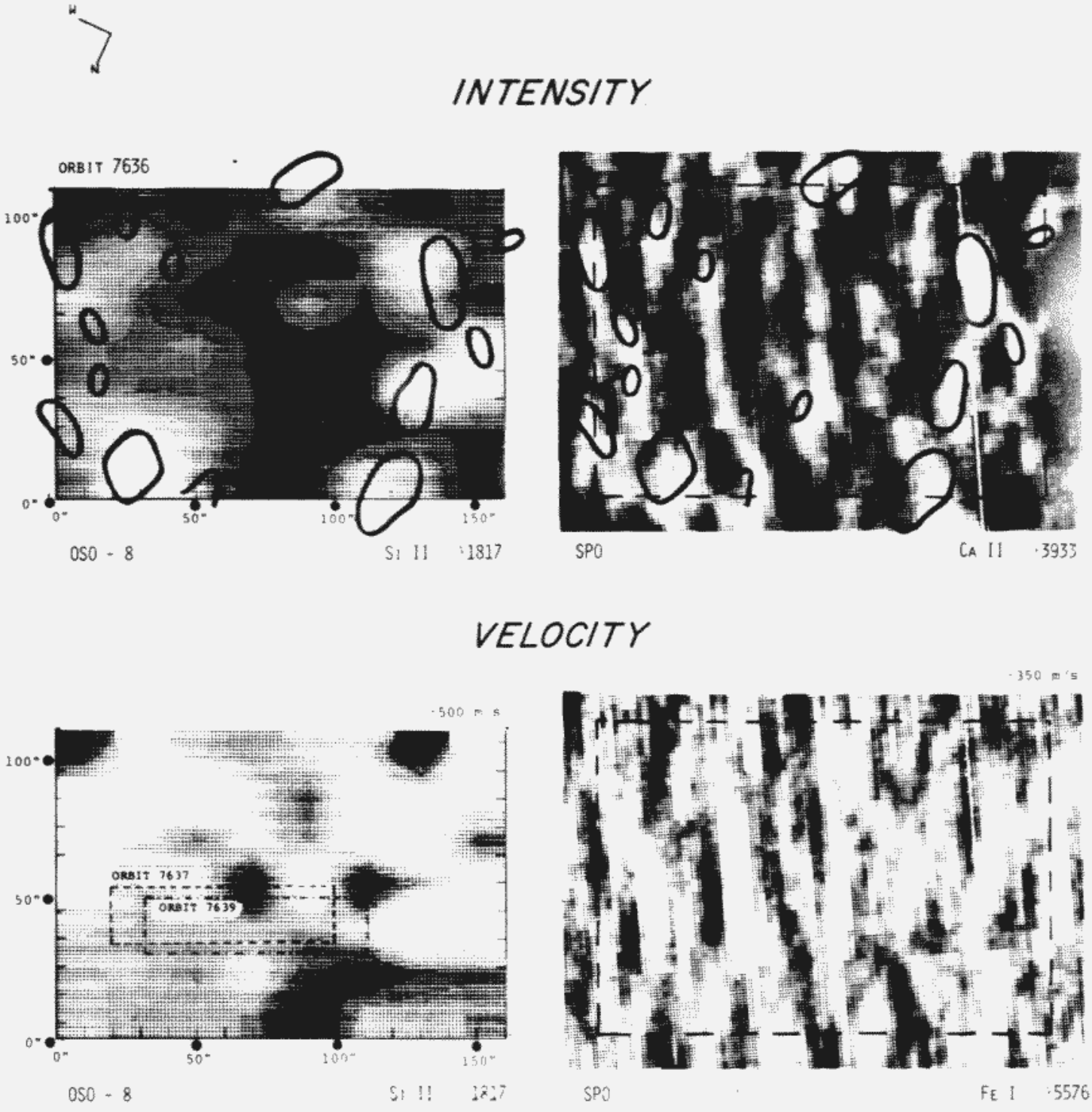

Figure 2.3

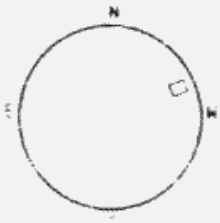

Confirmation of pointing on day 6313. This repeats Figure 2.2 with contours of the bright Ca II emission features at the right overlaid on the Si II intensity picture at the left. The contours are drawn from a 10" x 10" spatial average of the Ca II intensity image. It is evident with this intermediate resolution that bright features are well correlated. The boxes which are overlaid on the OSO 8 velocity image show the coverage of the higher-resolution point-mode experiments run during orbits 7637 and 7639.

difference in spatial resolution, the Si II bright features are well correlated with the gross pattern of network emission in Ca II.

Implicit in the correlation of this comparison is the fact that both lines show the same bright features. This is not surprising since Ca II λ3933 and Si II λ1817 are both chromospheric lines, Ca II K being formed at about 2000 km (Linsky and Avrett 1970) or only some 400 km above the estimated height of Si II λ1817. Network patterns have in fact been observed even in the transition region in Ne VIII (Tousey et.al. 1973) and in O VI (Reeves et.al. 1974). Nor is it surprising that our SPO measurements in Fe I λ8468 show that regions of high magnetic field in the photosphere coincide with areas of enhanced Si II emission: such a correspondence between magnetic fields and Ca II emission is well known.

The lower frames in Figure 2.2 show the corresponding time-averaged velocity pictures formed from Si II chromospheric data on the left, and from Fe I photospheric observations on the right. Although the zero of velocity is still somewhat uncertain, the dynamic range of the OSO 8 raster-mode velocities is again about 1000 ms^{-1}, as in the previous figures. In the SPO picture, with its higher spatial resolution, the dynamic range is about 800 ms^{-1}, comparable with that found in earlier work (Simon and Leighton 1964). Here the horizontal

components of the supergranule motions are clearly seen as line-of-sight velocities alternating in sign as the elongated cells become increasingly foreshortened toward the limb. The same cellular structure is not however apparent in the OSO 8 picture, which appears to have little immediate resemblance to the Fe I velocities.

One possible reason for the lack of correspondence between the Si II and Fe I velocity pictures may be the low spatial resolution in the OSO 8 raster-mode observations. The 20" x 20" sampling window results in quite drastic spatial averaging of the velocity fields, since it encompasses a significant portion of a single supergranulation cell. In order to understand how the sampling window affects the resulting patterns, we have used our 2" x 2" SPO data to simulate low-resolution Si II intensity and velocity pictures. For each 2" x 2" spatial element, the Si II profile is represented by a Gaussian with a central intensity proportional to the Ca II intensity and a spectral shift given by the Fe I velocity. These profiles are then spatially averaged, not by forming a running mean but by assigning a single value to each averaging box, as is done with OSO 8. We find that the effects of spatial averaging depend strongly on the functional form of the pattern and on its scale relative to that of the averaging box. Figure 2.4 illustrates a sequence of different spatial averages of the SPO data

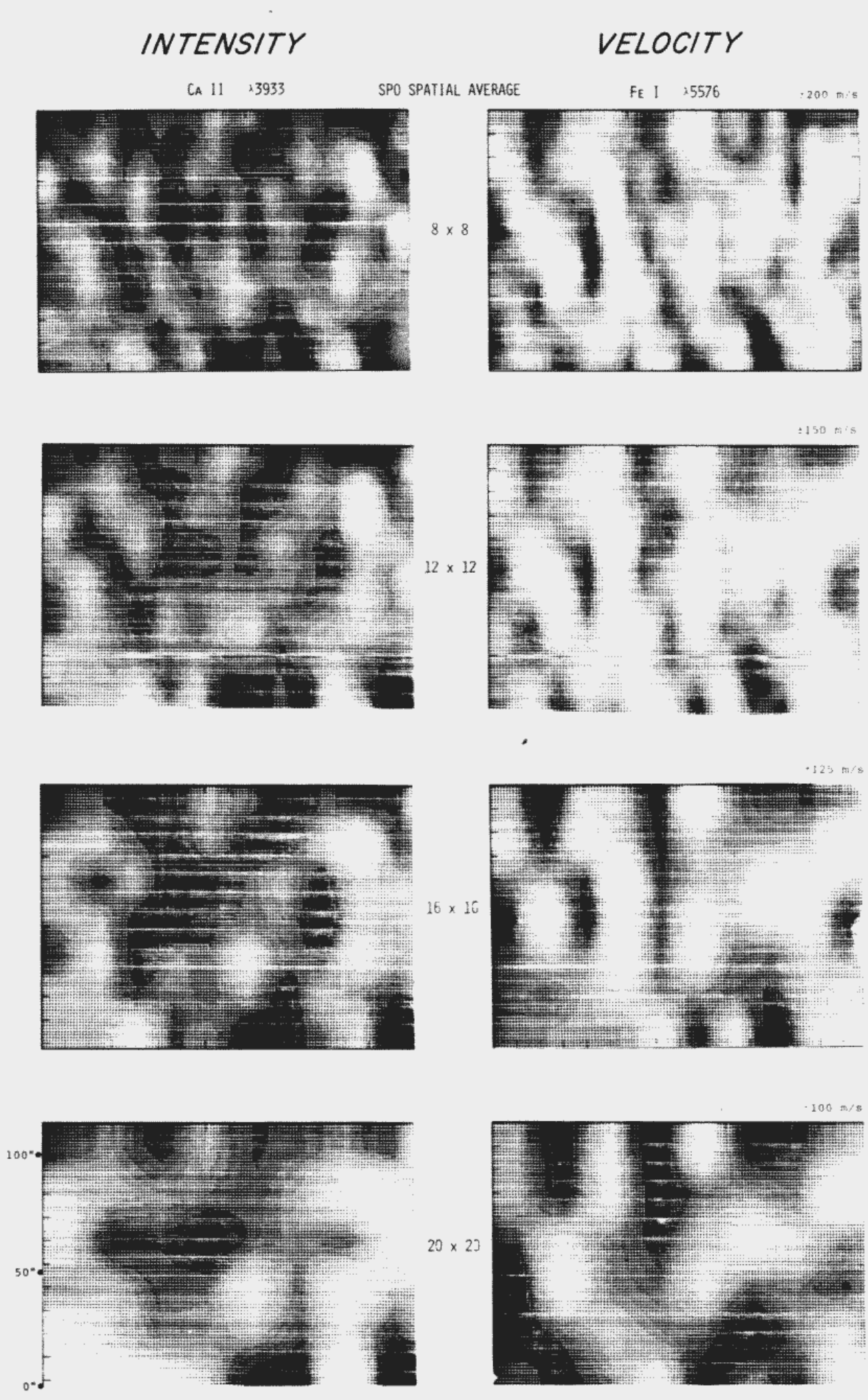
INTENSITY
VELOCITY
Ca II λ3933
SPO SPATIAL AVERAGE
Fe I λ5576
±200 m/s
8 x 8
±150 m/s
12 x 12
±125 m/s
16 x 16
±100 m/s
20 x 20
100"
50"
0"

Figure 2.4

Spatial averaging of the SPO data from day 6313. This sequence of four images was made from the SPO time-averaged Ca II intensity and Fe I velocity images shown in Figure 2.2. Each intensity-velocity pair shows what an OSO 8 obtained image with r x r resolution might look like. The elongated supergranular cells are still apparent in velocity even with 16" x 16" sampling, but in the 20" x 20" images they are difficult to discern. The centroids of the brightest features in intensity can be recognized even with 20" x 20" spatial averaging, however, many bright elements have blended together. The spatial averaging in the OSO 8 observations obliterates the cellular structure so clearly apparent in the SPO picture.

formed in this way, using SPO raster data previously shown in Figure 2.2. With 8" x 8" spatial averaging, the original intensity and velocity patterns are reproduced independently of any shift in the position of the image. With 12" x 12" averaging, the intensity patterns are still apparent, but the striated cellular patterns of horizontal motion begin to be obliterated. With the severe 20" x 20" averaging of the OSO 8 satellite, the brightest intensity features continue to be recognizable, but the velocities lose all cellular appearance, much as in all the OSO 8 low-resolution raster pictures. This comes about because the velocities alternate in sign, approaching and receding motion occupying about equal areas, whereas intensities are positive, with isolated sites of enhanced emission dominating the network pattern. If the averaging grid is displaced laterally, the resulting velocity patterns are somewhat modified in detail, being most sensitive to displacements in the direction of the image foreshortening. The resulting velocity pattern is not however arbitrary: broad features evident after the 8" x 8" averaging of the simulated data are still visible with the 20" x 20" averaging. In our raster-mode observations, the same time-averaged velocity patterns are often present over a number of satellite orbits, and we believe that this persistence reflects the actual behavior of the unresolved velocity fields. From

the simulations, we estimate that the velocity amplitude in 2" x 2" Si II data might be a factor of 3.5 greater than the 100 ms^{-1} obtained with our 20" x 20" sampling. However, the spatial degradation in the raster-mode data is such that we cannot infer much about the steady velocity fields other than that they do display persistence.

Detailed comparison of the OSO 8 and SPO velocities clearly requires the higher spatial resolution available with the point-mode observations, which sample a one-dimensional array of 20 spatial points, each with 2" x 20" spatial resolution. We have therefore made raster-mode and point-mode observations on alternate orbits in many of our coordinated SPO and OSO 8 experiments, including the one shown in Figure 2.2. The 20" x 80" areas covered by point-mode observations during two subsequent satellite orbits 7637 and 7639 are shown in Figure 2.3, displaced due to the effects of solar rotation. As can be seen from the the orientation of these boxes, the 80" spatial scan in all the point-mode observations is made nearly perpendicular to the limb, with the 2" x 20" sampling window parallel to the limb. This serves to minimize spatial averaging of the supergranular pattern in these velocity measurements, provided the velocity fields in the middle chromosphere appear as foreshortened cellular patterns similar to those in the photosphere.

c) Comparison with OSO-8 Higher Resolution Observations

The comparison of these point-mode observations with the SPO data is made in Figures 2.5 and 2.6 for data spanning the two orbits 7637 and 7639. Here the 2" x 2" resolution data from SPO, shown in panel (a) of both figures, has been spatially averaged to mimic the 2" x 20" resolution obtained with OSO 8. The resulting time-averaged Ca II intensity picture and Fe I velocity picture from SPO are shown in the (b) panels as line drawings. The corresponding OSO 8 Si II intensity and velocity pictures, time-averaged over one full orbit, are shown in the (c) panels as line drawings. The intensities in Ca II and Si II are plotted on a linear scale but in arbitrary units, chosen so that the images have comparable contrasts. With this higher spatial resolution, the bright features seen in the Si II intensity picture again correlate well with those in Ca II.

To facilitate comparison of the Fe I and Si II velocities, the solar rotation component has been removed from the Fe I velocity data shown here and in Figure 2.2, since it would otherwise contribute a noticeable 160 ms^{-1} across the 80" segment shown. The Si II velocity data have not been so modified, for the rotational gradient is very small in these data with their fourfold greater dynamic range. Because of foreshortening, we would

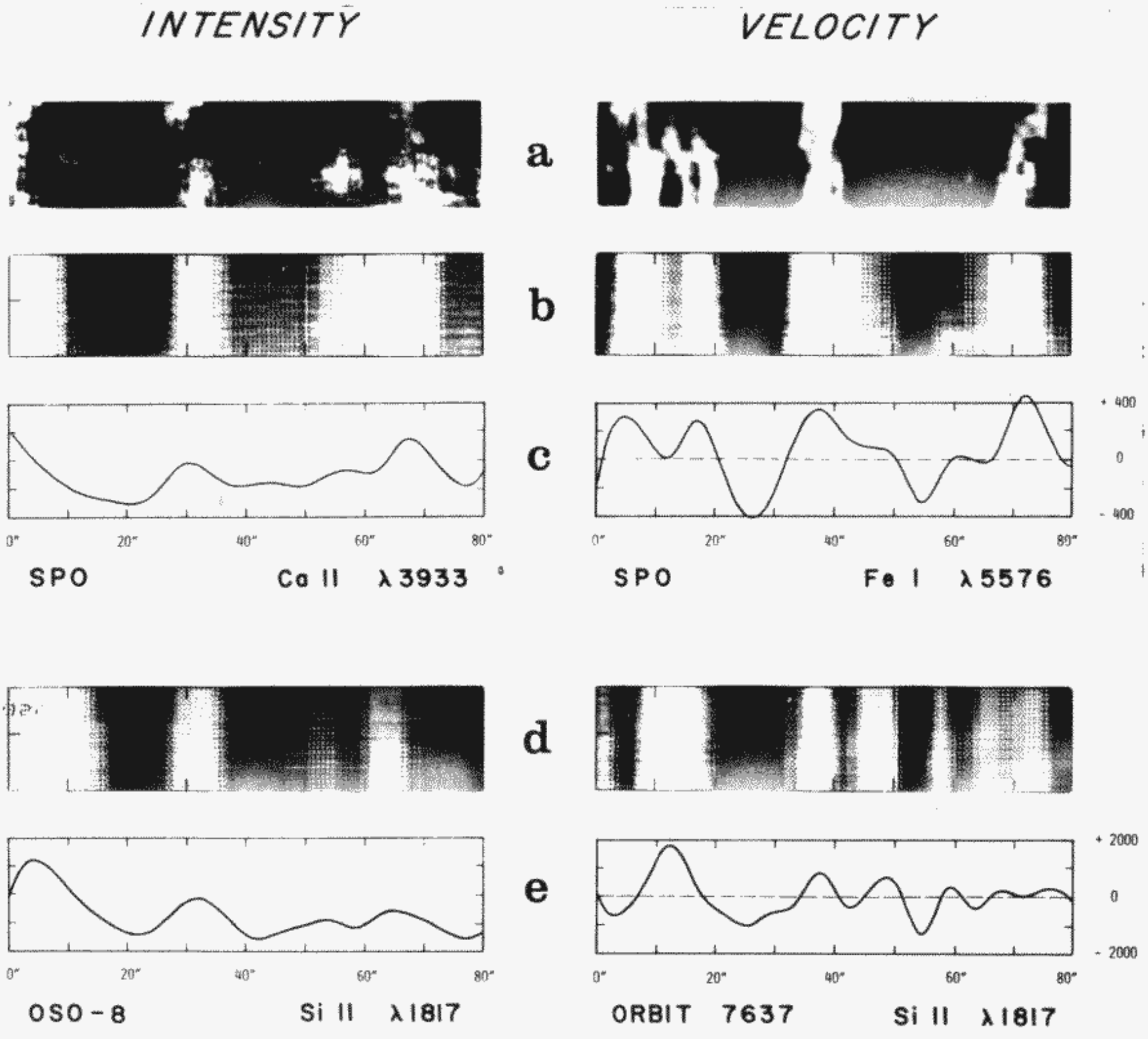
INTENSITY
VELOCITY
a
b
c
d
e
0"
20"
40"
60"
80"
+ 400
0
- 400
+ 2000
0
- 2000
SPO Ca II λ3933
SPO Fe I λ5576
OSO-8 Si II λ1817
ORBIT 7637 Si II λ1817

Figure 2.5

Comparison of SPO with higher-resolution OSO 8 observations from orbit 7637 day 6313. The region covered is a 20" x 80" area at radius vector 0.8 on the quiet Sun, denoted by a box in Figure 2.4. The SPO diode array provides data with a spatial resolution of 2" x 2"; the Ca II λ3933 intensity picture and Fe I λ5576 velocity pictures are shown in the top row (a). The same images, spatially averaged to correspond to the OSO 8 resolution of 2" x 20", are shown as one-dimensional images in (b) and as line drawings in (c). The OSO 8 observations in Si II λ1817 are shown in (d) as intensity and velocity images and in (e) as line drawings. The Si II velocities in this orbit have an rms of 610 ms^{-1}. The Ca II and Si II intensity pictures in panels (b) and (d) display similar spatial variations; the brighter emission features are well correlated. Comparison of the FeI and Si II velocity images in panels (b) and (d) reveals that the same general patterns of steady supergranular motion are present in both the photosphere and the middle chromosphere. The line drawings (c) and (e) show that the motion fields usually have the same sense at the two heights in the atmosphere, although the dynamic range in the horizontal flows increases from 800 ms^{-1} in Fe I to at least 3000 ms^{-1} in Si II.

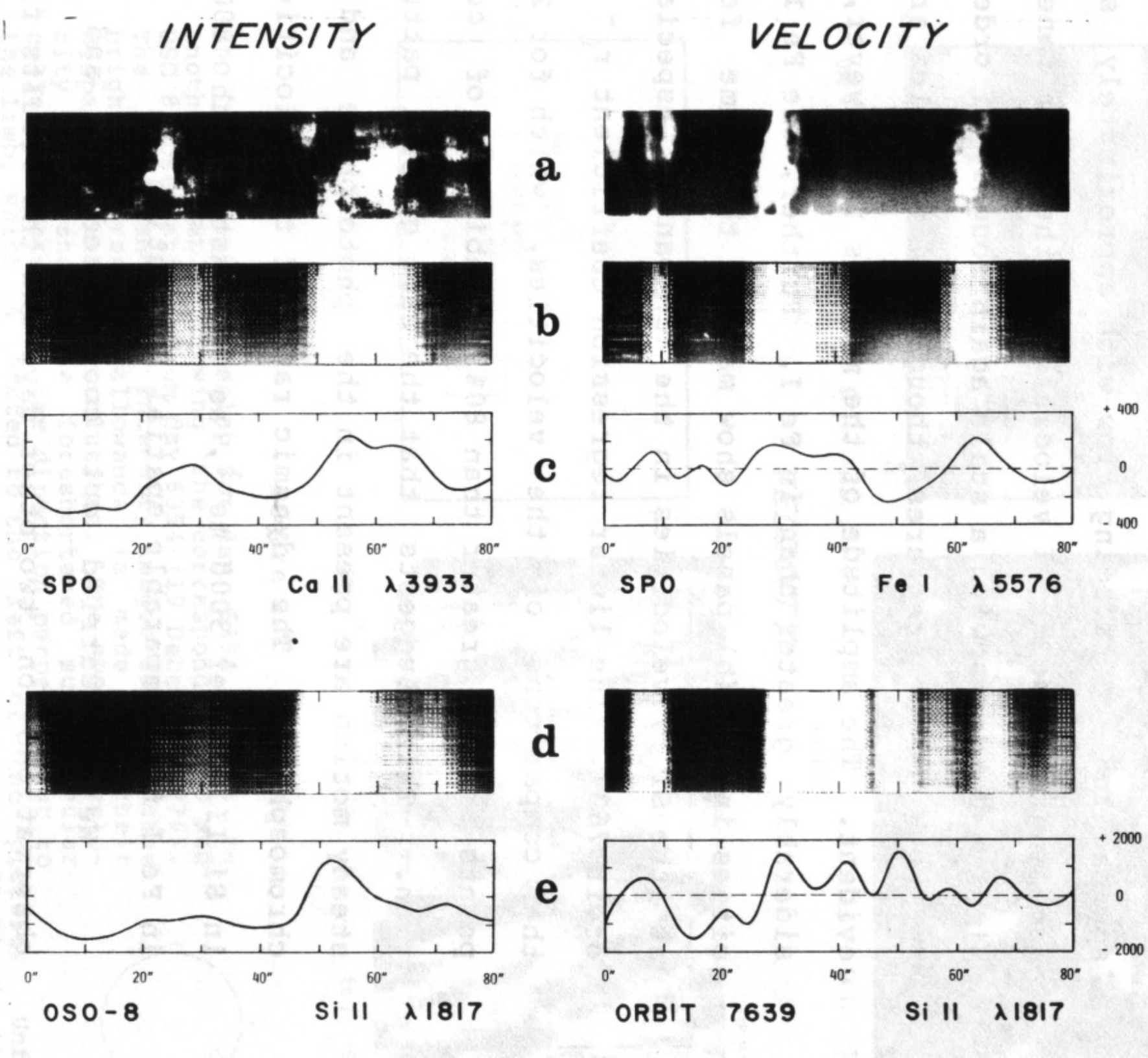
INTENSITY
VELOCITY
a
b
c
d
e
+ 400
0
- 400
0"
20"
40"
60"
80"
SPO
Ca II λ3933
SPO
Fe I λ5576
+ 2000
0
- 2000
OSO-8
Si II λ1817
ORBIT 7639
Si II λ1817

Figure 2.6

Comparison of SPO with higher-resolution OSO 8 observations from orbit 7639 day 6313. This companion to Figure 2.5 shows the time-averaged supergranular flows and intensity patterns observed from SPO and with OSO 8 during orbit 7639. The area covered is labeled as a box in Figure 2.4. The abscissa spans 80" on the Sun, in a direction perpendicular to the limb. This orbit also illustrates a remarkable intensity correlation between the two instruments which confirms the pointing. The velocities correlate well indicating that the horizontal flows we see in the photosphere are preserved in the middle chromosphere in sign but the amplitude increases by about a factor of five between the two heights. The velocity rms is 715 ms^{-1} in this orbit.

expect the typical horizontal scale in the direction of the limb to be about 15" for the photospheric supergranulation. The Fe I velocity data in the upper two panels of Figures 2.5 and 2.6 show alternating patterns of approaching and receding flow with approximately such a wavelength. The Si II velocities in the lower panel show similar patterns with a scale again roughly of order 20" for the major features, though smaller scales are also evident. The amplitude of the motions is, however, considerably greater than in Fe I. Further, the Fe I velocities in the (b) panels show many of the same features as the Si II velocities in the (c) panels, especially in orbit 7637. The linear regression coefficient $r_\ell \sim 0.4$ in the comparisons of the velocities, which for 20 data points implies greater than 80% probability of correlation. This suggests that the same general patterns of steady motion are present in the photosphere and upper chromosphere. The dynamic range of the velocities seen in Si II is over 3000 ms^{-1}, as contrasted with 800 ms^{-1} in Fe I for comparable spatial resolution.

We have carried out coordinated SPO and OSO 8 observations on two other days and the results from one of these is shown in Figures 2.7 and 2.8. We are able to establish overlap of the Si II and Ca II intensity images as illustrated in Figure 2.7; all the bright and dark features in the Si II images can be recognized in the Ca

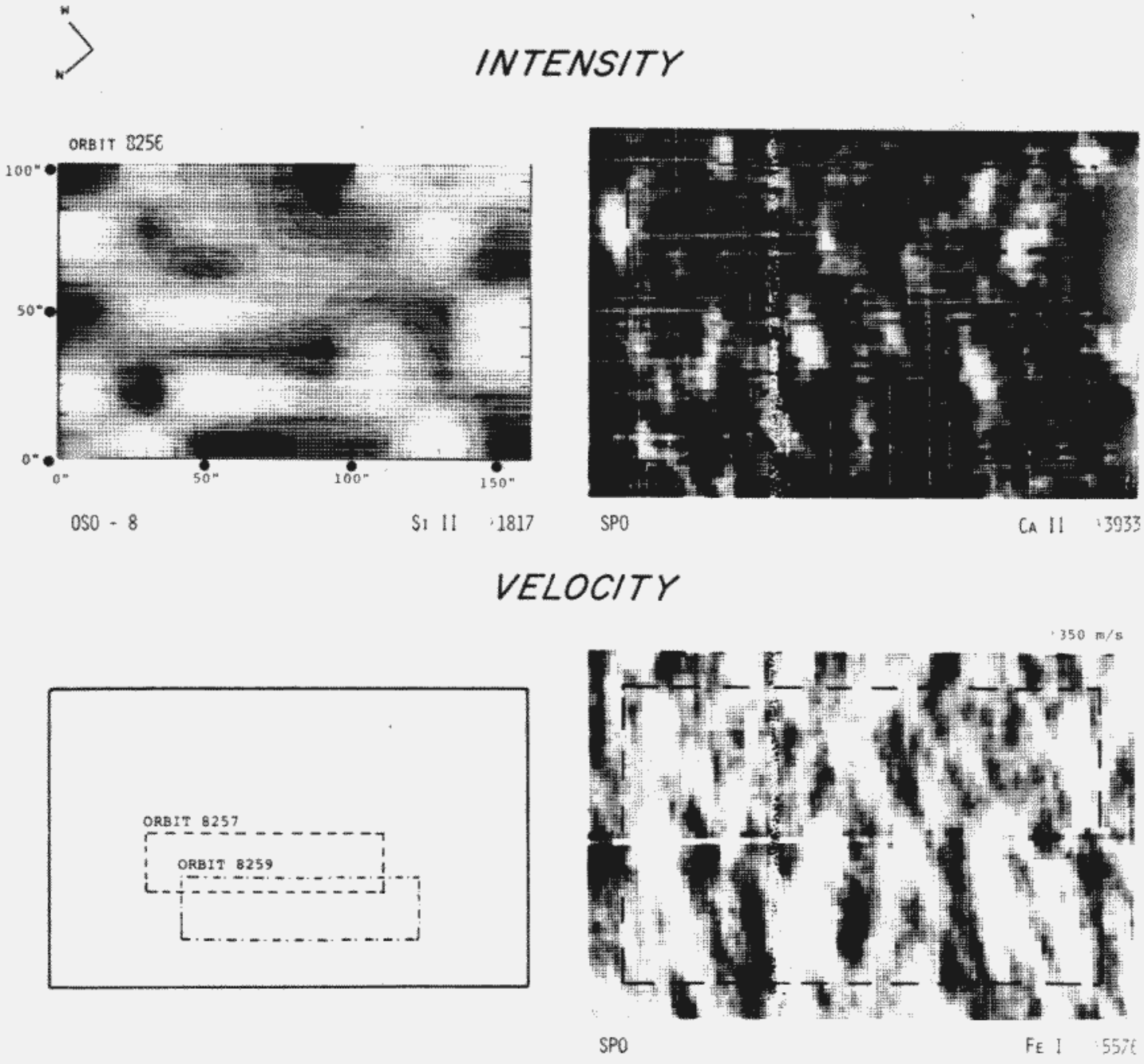

Figure 2.7

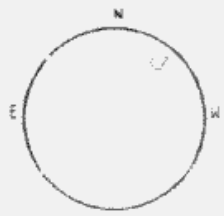

SPO OSO 8 pointing overlap for day 6354. This is another example showing the corresponding SPO and OSO 8 observations from day 6354 (19 December 1976). The Si II and Ca II intensity images show the same bright features when allowance is made for their disparate spatial resolutions. The SPO Fe I velocity image shows the foreshortened supergranular cells elongated in the direction perpendicular to the limb, which is located to the left of the picture. Unfortunately corresponding velocity images were not available in these observations as the OSO 8 experiment failed to track the instrumental drift of the Si II spectral line. The relative pointing boxes for high resolution experiments run during subsequent orbits 8257 and 8259 are outlined by dashed lines in the lower left outline.

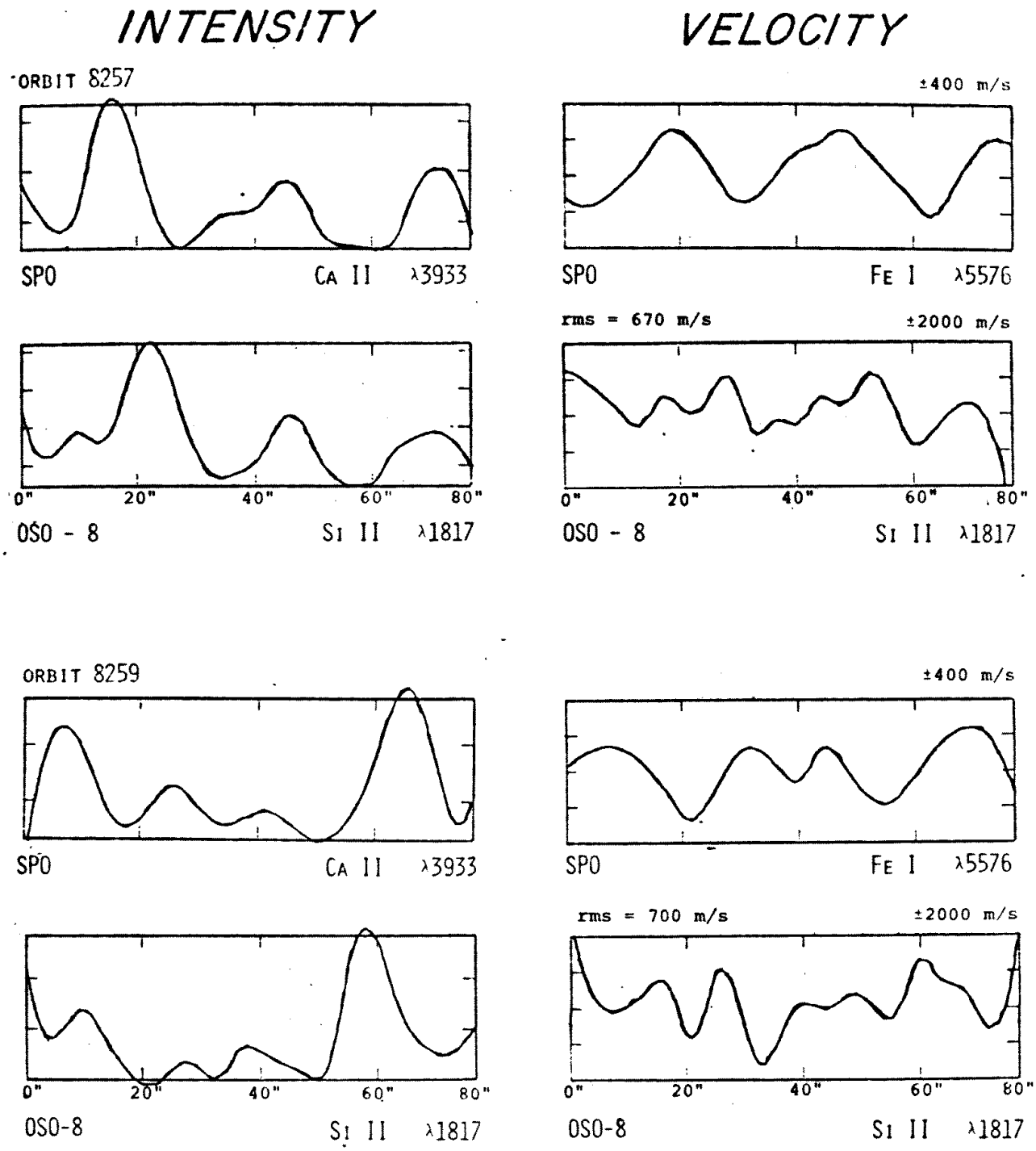

Figure 2.8

Comparison of SPO with higher-resolution OSO 8 observations from day 6354. Here we show SPO intensities from Ca II λ3933 and velocities from Fe I λ5576 spatially averaged to 2" x 20" resolution and located by the dashed outlines in Figure 2.7. The corresponding Si II intensity and velocity line drawings are shown directly beneath these. As in the previous examples (Figure 2.5 and 2.6), these orbits show a very convincing Ca II and Si II intensity correlation which confirms the accuracy of the relative pointing of the two instruments. The velocities, for the most part, show the same receding and approaching flows although the amplitude of the motion in Si II is a factor of five larger than that seen in Fe I. This indicates that supergranular flows seen in the photosphere direct correlate with the steady flows that occur in middle chromosphere but with increased amplitude.

II image making proper allowance for the disparate spatial resolutions. Unfortunately due to an error in the satellite pre-programmed instructions the OSO 8 instrument failed to follow the spectral line drift and so we were unable to compute the corresponding Si II velocity image. The Fe I velocity image nicely illustrates the foreshortened supergranular motion field. The limb is to the left in these pictures.

The pointing locations of the subsequent high-resolution experiments from orbits 8257 and 8259 are shown in Figure 2.7 below the Si II intensity image. Figure 2.8 shows line drawings of the intensity and velocity measurements from these orbits, accompanied by the corresponding line drawings for the spatially averaged SPO data. These SPO images were formed from the Ca II intensity and Fe I velocity data with 2" x 20" averaging in the manner of Figure 2.5. The correlation between Ca II and Si II intensity in both examples is excellent, which reflects the similarity in the behavior of the Si II and Ca II lines. Although the velocity correlation is not as striking, many of the individual features (particularly in orbit 8257) can be recognized between the Fe I and Si II images. This may indicate that the steady supergranular motions seen in the photosphere probably penetrate into the chromosphere. The motion field appears to change only in amplitude as the sign and

relative strength of the motion field are preserved between the two heights. The remarkable thing here is that the dynamic range of the 2" x 20" observations increases from 400 ms^{-1} in the photosphere to over 3000 ms^{-1} in the chromosphere. The linear regression coefficient of $r_{\ell} \simeq 0.35$ for the SPO and OSO 8 velocity in these data sets.

An additional 6 high resolution point-mode orbits were carried out independently of SPO at radius vector $R_V = 0.8$. The intensity and velocity images in these point-mode orbits are shown in Figures 2.9 and C.5, where we also list the values for the rms velocity amplitude. Photospheric velocities near the limb typically show both flow toward and flow away within each supergranule cell, and the bright chromospheric network is confined to the region between cells. Our OSO 8 observations are consistent with this behavior as generally the sign of the velocity does not correlate with the intensity level. The Si II velocities vary on a spatial scale of about 10" and the intensity on a scale of 20" as do photospheric velocities and intensities at large radius vector (see Figures 2.2, 2.7 for example).

A possible interpretation of these point-mode observations is that the steady motions we see in the photosphere penetrate into the chromosphere and in so doing increase in dynamic range from 700 ms^{-1} to over

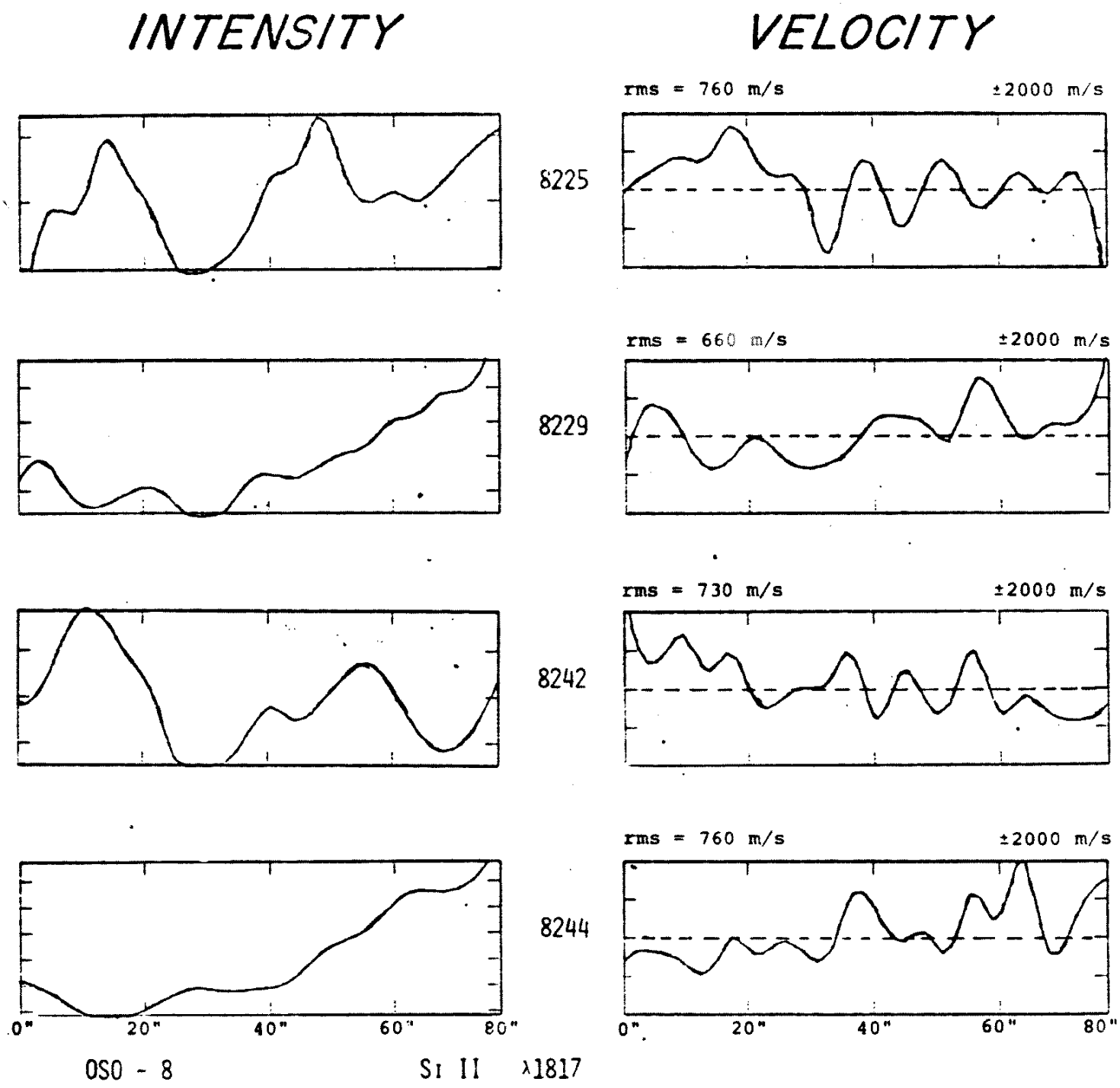

Figure 2.9

Examples of other OSO 8 higher-resolution point-mode orbits. These are additional examples of point-mode observations in Si II showing the intensity and velocity line drawings. All these orbits were run with the slit oriented perpendicular to the direction toward the limb. The intensities vary on a scale of ~30" corresponding to roughly the scale of the chromospheric network. The velocities show considerably more substructure and vary on a scale of roughly 15". This is consistent with our observations in photospheric lines as the chromospheric emission borders the approaching and receding flows in the cell. The dynamic range in the velocity in these examples is roughly 1500 ms^{-1} and and the rms is about 700 ms^{-1}.

3000 ms^{-1}. The average rms velocity from all the available high resolution observations at R_V= 0.8 is 700 ms^{-1}. However, we associate considerable uncertainty with this value. The mean rms on different days varies from 500 ms^{-1} to over 800 ms^{-1}. This may be due to statistical fluctuations possible in our small sampling or it may also be the result of error in the velocity determination. The velocity uses the step size of the wavelength drive on the OSO 8 instrument as its calibration standard, and this is subject to some degree of uncertainty.

2.4 Conclusions

Our coordinated OSO 8 and SPO observations of persistent flows show that steady motions are present in the middle chromosphere. The motions persist for at least 7.5 hours and vary on a spatial scale of about 15" in the direction perpendicular to the limb. This is also the scale of variation that supergranule flows in the photosphere exhibit.

We are able to accurately co-locate the pointing of the two instruments as evidenced by the very good intensity correlation seen in the Si II and Ca II measurements. This allows us to directly compare the velocities

at the two heights. Our impression is that quite a number of flow features are evident at the two heights, however, we have no reason to expect that the motions at the two heights should be correlated. Besides the lack of any physical basis for correlation there are even a number of factors which can degrade this correlation if it does exist. One factor is that the steady Doppler velocity at R_V= 0.8 may be largely vertical. In the low photosphere, the Doppler velocity is observed to increase by a factor of at least 5 from disk center to limb, indicating that the supergranular motions are predominately horizontal there. Near the temperature minimum, however, the steady velocities measured in Mg I show little center-to-limb variation (Deubner 1971), suggesting that here the horizontal and vertical components of supergranular motion have comparable amplitudes. A distinct change appears to occur in the flow structure of the supergranulation between the low photosphere and the temperature minimum. Our OSO 8 results show that this tendency toward isotropy is accentuated higher in the atmosphere. The Si II observations at disk center which are discussed in Chapter 4, show a dynamic range in the vertical velocity of about 3000 ms^{-1}, comparable with that at radius vector 0.8. Thus the steady Doppler velocities at radius vector 0.8 probably contain significant contributions from both the vertical and horizontal components of

supergranular motion.

While penetration to these heights is not inconsistent with theoretical considerations, the motions are more vigorous than might have been anticipated based on similar ground-based studies. Deubner (1971) reports that at radius vector 0.8 the spatial rms of the supergranular motions decreases systematically with height from 170 ms^{-1} seen in C I λ5052 in the low photosphere to 110 ms^{-1} in Mg I λ5173 above the temperature minimum. Contrary to this apparent trend in the lower atmosphere, our OSO 8 observations of Si II in the middle chromosphere yield an rms value of 700 ms^{-1} and a dynamic range of 3000 ms^{-1} for these steady flows. To interpret these observations physically it is first important to determine the mass flux in this flow since the density changes so dramatically with height. There are 6 density scale heights between C I λ5052 and the height of formation of Mg I λ5173, which represents a decrease in the mass flux by a factor of 150. The heights at which the Fe I 5576 and Si II λ1817 spectral lines are formed differ by about 1400 km or nearly 11 density scale heights. In our observations, while the steady horizontal velocities increase by a factor of 5 between the photospheric Fe I λ5576 and the chromospheric Si II λ1817, the mass flux in this flow has decreased by a factor of 10^4. Thus the horizontal mass flux in the flow simply decreases with

height. To understand the amount of braking of the vertical component to which this horizontal mass flux corresponds requires further knowledge of the amplitude of the vertical component. We turn to this basic issue in the next three chapters.

CHAPTER 3

THE VERTICAL FLOWS IN SUPERGRANULATION AND MESOGRANULATION

3.1 Introduction

The vertical component of the supergranular motion field is far more difficult to observe than the horizontal component. Its amplitude in the photosphere is less than 100 ms^{-1}, which corresponds to a line shift of less than 2m$\mathring{A}$ in the visible. There are several sources of noise that complicate and limit these observations: instrumentation, granulation, solar oscillations, and supergranular horizontal motions may all introduce a noise signal greater in amplitude than the vertical component we wish to measure.

Most previous attempts to study the vertical component of the supergranular motion field have been seriously hindered by some or all of these problems, and results from these studies must be interpreted with care. Photographic techniques like those used by Leighton, Noyes, and Simon (1962) or Simon and Leighton (1964) introduce large errors since the film response is nonlinear, and velocities are systematically introduced in

regions of large intensity contrast. These observations were the first to suggest that small amplitude downflow is correlated with the chromospheric network and the boundary of the supergranular cells, but this result is somewhat uncertain.

Many previous observations have been inadequately averaged in time leaving residual noise from the oscillations. The Doppler sum plate used by Leighton and associates is the average of two Doppler pictures separated in time by 150 seconds. Oscillatory residuals as large as 200 ms^{-1} may occur for 200 or 400 second periods in photospheric observations. Frazier (1971) (see also Skumanich 1976) averages four Doppler sum plates to arrive at the velocity picture used in his study. This reduces the oscillatory signal by a further 50%, but the amplitude of the residual is still comparable to that of the supergranular vertical motions.

Observations of high spatial resolution experience considerable noise arising from granulation. The granulation has a very large amplitude in the photosphere, and its variation is aperiodic in time. The observations of Worden and Simon (1976) sample with 1" spatial resolution and average for 20 minutes. We estimate that in their study the granulation residual is about 190 ms^{-1} for the observed Fe I lines, which are formed in the low to middle photosphere. This residual is far in excess of the

vertical supergranular component they wish to resolve. Observations made in photospheric lines must be averaged spatially over at least 2.5" x 2.5" and temporally for 30 minutes in order to reduce the granulation residual to less than 75 ms^{-1}.

The horizontal supergranular component is another source of noise. Tanenbaum et.al. (1967) and Musman and Rust (1970) present observations that sample at relatively large radius vector where the horizontal supergranular component is at least comparable to the vertical. The steady motion fields they identify may result from horizontal supergranular flows and their results should be treated with some caution.

Only Tanenbaum et.al. (1967) and Deubner (1971) present observations made with spatial and temporal averaging adequate to reduce these sources of noise below the amplitudes expected for the supergranular vertical component. Downflow sites are found to be correlated with the chromospheric network. Tanenbaum et.al. present one-dimensional scans centered on the solar disk, although important details needed to evaluate these observations are not presented. The bright Ca II features are found to correlate with points of maximum downflow, though many sites of upflow and downflow are evident away from the bright network. Deubner's measurements are one-dimensional scans with 4" x 4" spatial

resolution and are averaged over 30 minutes in time. These are compared with H filtergrams; downflow sites are found to correlate with the chromospheric network. Deubner also obtains two-dimensional raster scans which confirm this correlation, but the spatial extent of these observations is less than one supergranular cell.

In this chapter we present our two-dimensional observations of the steady vertical motions obtained with the SPO diode array (see November et.al. 1976, 1977a, 1977b, 1979, Gebbie et.al. 1979). These observations offer improvements over the previous work in four ways: 1) The diode array provides a very high data acquisition rate, so we are able to sample a fairly large area of sun (256" x 192") with 1" x 1" resolution in a time small compared to a cycle of the five-minute oscillation. This allows us to cancel quite effectively the oscillatory signal. 2) In our data reduction we are able to successfully recalibrate changes in the sensitivity and zero light level of the diodes and thus can infer small amplitude velocities that have large spatial extent (see section 2.2d and Appendix A). This problem has greatly limited observations of this sort using the diode array in the past. 3) Besides averaging the data in time, we apply a 3" x 3" spatial running mean, thus reducing the intrinsic granulation noise. 4) We obtain velocity measurements in several spectral lines simultaneously,

including Mg I λ5173 which is formed near the temperature minimum. In the low chromosphere the granulation signal is very small so these observation will show less noise. In these observations we are able to recognize steady flows with amplitude ~50 ms^{-1} which appear in each of the spectral lines and persist throughout independent averages of the data (section 3.2).

Our success in this type of observation makes it possible to explore a number of issues which have previously been beyond our reach. The main objective is to examine the supergranular flows and thus we compare our velocity measurements to the Ca II network which defines the cell boundaries (section 3.3). In addition our examination of the morphology of the flows indicates that a ~10" scale of steady motion is present which possesses velocity amplitudes greater than that of the ~45" supergranulation. This we call mesogranulation and we explore some of the properties of this flow field in section 3.4.

3.2 The Observations

a) SPO Velocity Measurements

We obtained SPO velocity measurements at disk center on five days in our program of coordinated

satellite and ground-based observations. These runs lasted from one-half hour to two hours being limited by clouds, atmospheric seeing conditions, and operational constraints on the use of the instrument. On three of these days velocity measurements were available in Mg I λ5173. This chapter reports primarily the results from one of these days observations, although we have examined the data from the other days and find that those measurements corroborate the results reported here.

Seven strings of 64 diodes were arranged parallel to the slit with 1" x 1" resolution. Pairs of diodes were located on either side of Fe I λ5434, Mg I λ5173 (for velocities), Fe I λ8468 (for magnetic fields), and one string was centered on the Ca II λ8542 infrared line. With this setup the slit is scanned over 256" in three lateral swaths spanning 192", in a total time of 75 seconds.

The two lines Fe I λ5434 and Mg I λ5173 were selected because they provide velocity measurements at two separate heights, one in the photosphere and one in the low chromosphere. The line λ5434 is well suited for velocity studies: it is relatively narrow, is of low contrast, and is not affected by magnetic fields (g= 0); it is formed at a height of 250 km above τ_{5000}= 1 (Altrock et.al. 1975). Mg I is the most suitable line in the visible for measuring velocities above the temperature

minimum. It is relatively narrow near its core and is unblended by nearby lines. We are careful in our interpretations however, since the line does show some intensity contrast and is affected by magnetic fields.

Previous programs using the diode array have had difficulty detecting steady velocities as low as 50 ms^{-1} reliably. The main problem is that diodes change sensitivity and background levels significantly on a time scale of approximately 30 minutes. We attempt to overcome this problem by preprocessing a raster as described in Chapter 2 and in Appendix A, determining gain and dark current levels for each diode. Velocities are then calculated using the techniques described in section 2.2a. To isolate only the steady velocity component, we average the data over at least 30 minutes. Successive averages are then compared to establish persistence of the steady motions and to test the reliability of the gain and dark current levels that were adopted.

Figure 3.1 shows an example Mg I velocity picture obtained by averaging one hour of velocity measurements from day 8164 (1978 day 164 = 13 June 1978). The data which are 1" x 1" in spatial resolution have been softened by a 3" x 3" running mean to reduce noise. This figure shows several ~25" sites of material upflow like the one at x= 100", y= 130". These features we associate with the supergranulation and will later compare to the

VELOCITY

SPO DAY 8164 16:18:10

±110 m/s 60 MIN AVE

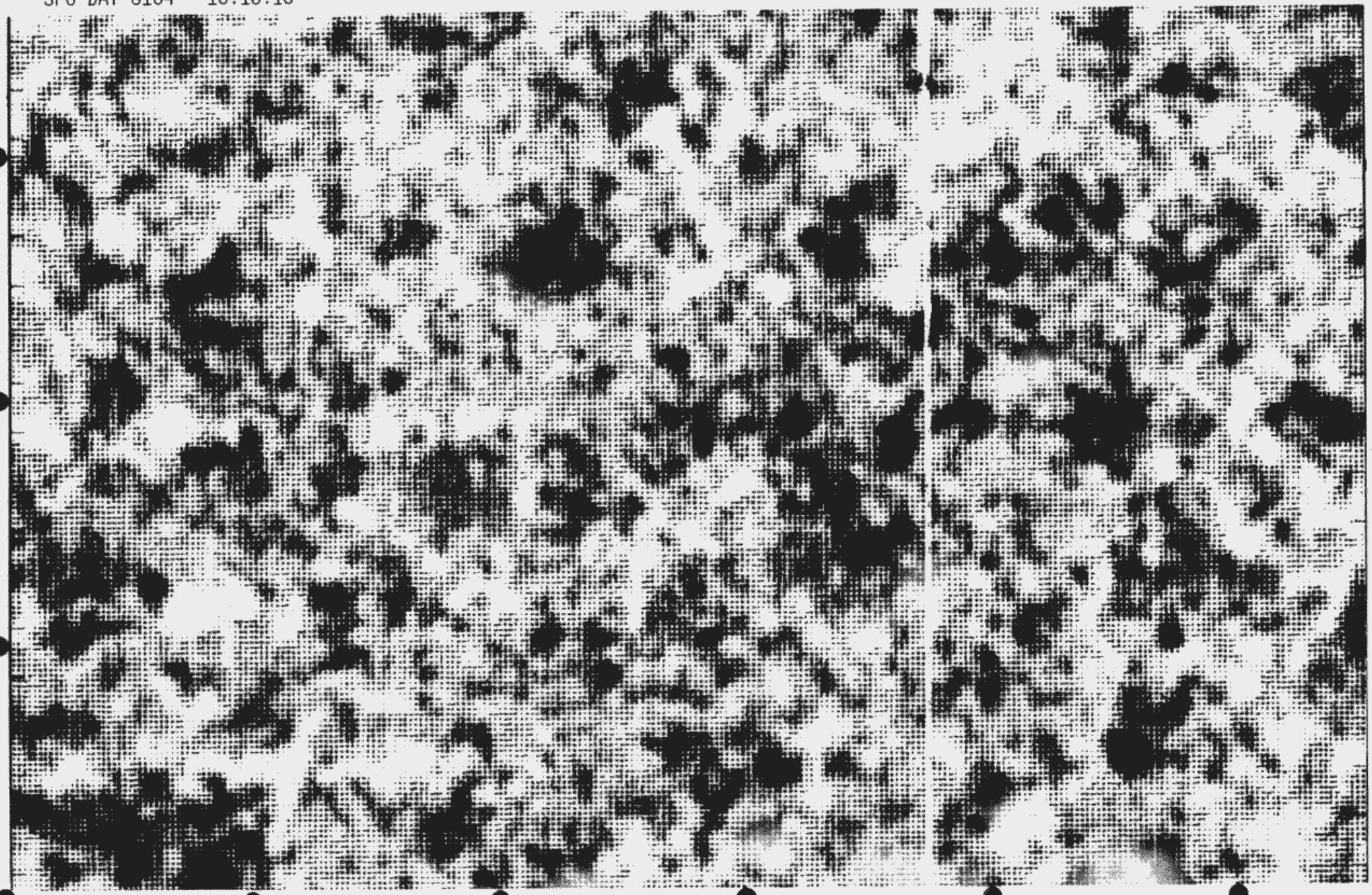

Mg I λ5173

Figure 3.1

The photospheric vertical velocities. This is a single Mg I λ 5173 velocity image obtained by averaging the measurements over one hour taken on day 8164 = 13 June 1978. These 1" x 1" observations have been spatially averaged using a running mean to 3" x 3". This reduces noise and any granulation residual signal. The range of velocities is from 110 ms^{-1} downflow (bright) to -100 ms^{-1} upflow (dark). We see many ~25" sites of material upflow like the one at x= 115", y= 120" surrounded by a network of downflow of comparable amplitude; these flows we attribute to supergranulation. Superposed on these motions are many small (~10") features showing ~100 ms^{-1} upflow or downflow like the upflow site (dark) at x= 135", y= 145"; these flows we call mesogranules.

Ca II λ8542 intensity measurements. In addition, this image shows considerable "spottiness". An apparent noise is present throughout the image with a spatial scale of 6" to 12". This we call mesogranulation.

b) Persistence

One important test of how real these steady flows are is how well they are reproduced in independent measurements. We compare separate one-half hour Mg I velocity averages examining both the larger scale supergranulation and smaller scale mesogranulation to test this persistence. In addition we compare the full one-hour Mg I velocity average to the similar average obtained in Fe I λ5434.

Figure 3.2 shows the two consecutive 30 minute time-averaged velocity images in Mg I λ5173 from our observations on day 8164 with the corresponding one-hour average. As in all these diode array measurements the effect of solar rotation has been removed. For each image the dynamic range of the displayed velocities has been selected to bring out the steady motions; we use the usual convention that material upflow is dark and downflow is bright.

The most prominent upflow and downflow features in Figure 3.2 are present in all three averages. Note for

SPO DAY 8164 **VELOCITY** Mg I 5173

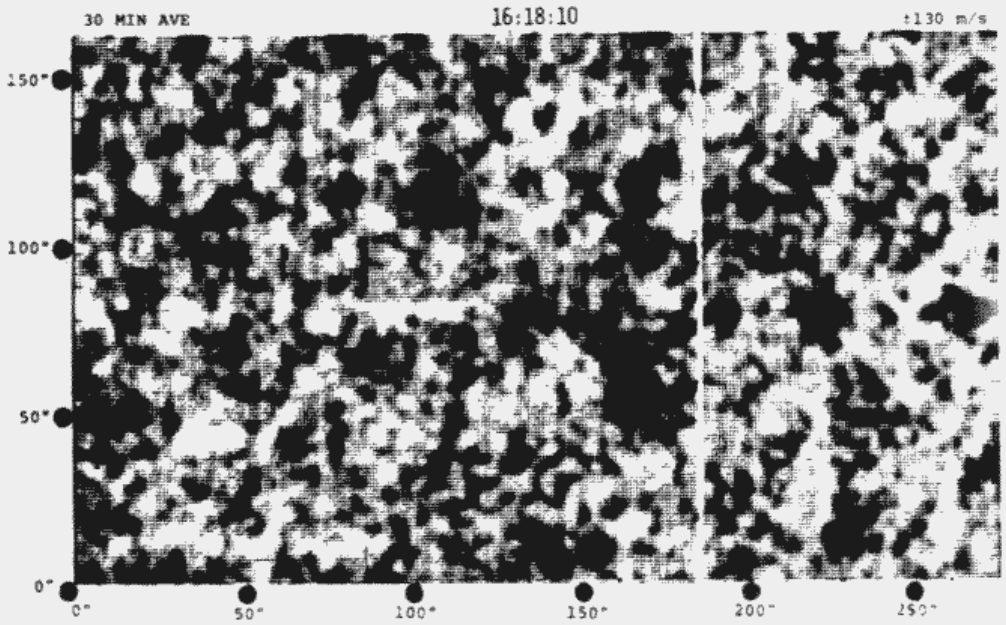

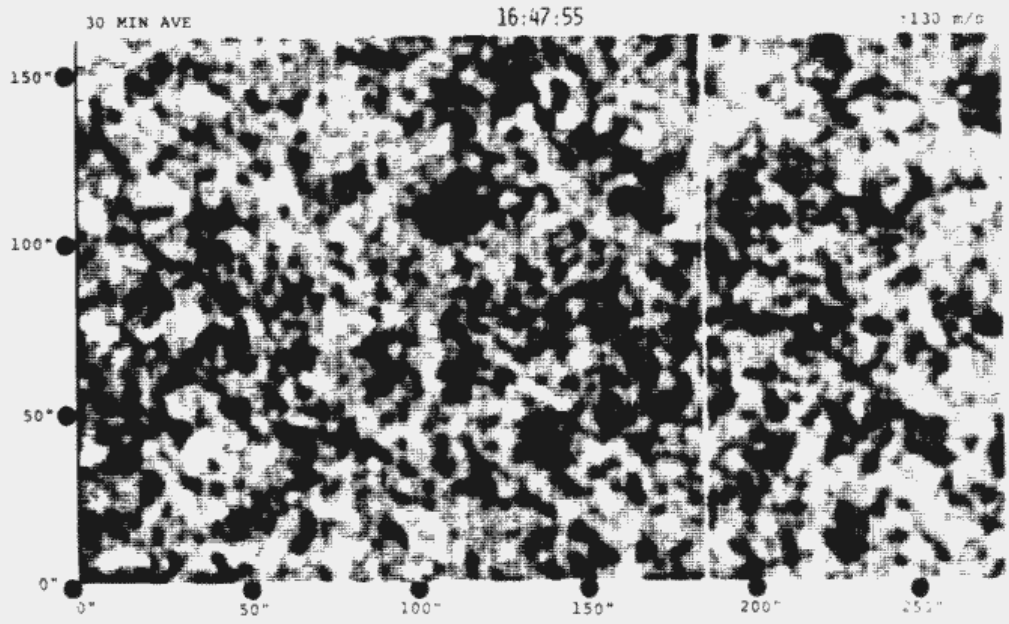

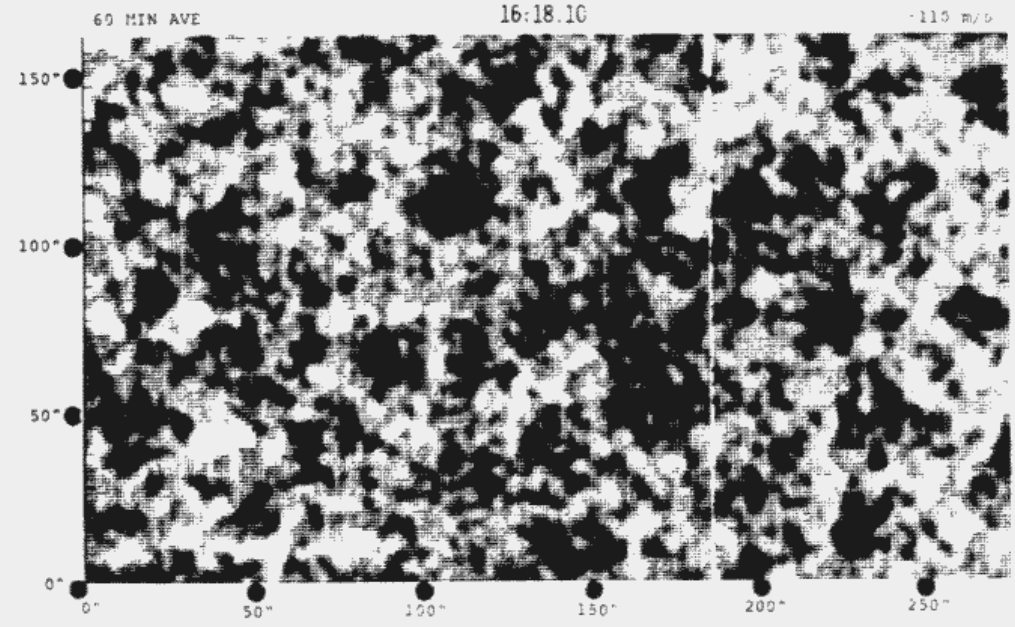

Figure 3.2

Persistence in the SPO velocity measurements day 8164. This figure shows successive 30 minute averages of the Mg I velocity measurements obtained at disk center on day 8164 (12 June 1978) accompanied by the full 60 minute average. The 30 minute averages show relatively little noise, and most features, even those with a scale ~10" can be recognized in the two images. This figure illustrates the persistence of the larger scale flows which we associate with the supergranulation. The large sites of material upflow, like the one at x= 115", y= 120" are clearly evident in both 30 minute averages and in the 60 minute average as are large areas of downflow like the complicated structure at x= 260", y= 25". These observations imply the existence of steady vertical flows in the photosphere with a supergranular scale.

example the ~25" upflow feature at x= 170", y= 70". In the second half-hour average the velocity zero seems shifted reducing the apparent contrast of this and other features but its presence in all the images is still reasonably certain. Note also the large region of upflow at x= 110", y= 130" clearly present in all three images.

Figure 3.3 shows an enlargement of a small portion of Figure 3.2 with an overlay identifying a few of the ~10" scale features that we call mesogranules. The coordinate scale shown in these images maps onto the coordinates of Figures 3.1 and 3.2 directly, so it easy to identify from where in the original raster does this enlargement. All the identified features can be clearly recognized in all three images at these spatial locations. We have identified only a few mesogranules and many others may be found upon further examination of the figure. The circled features can be used as reference locations in comparing other features in the images.

Almost every mesogranule that we identify in the full one-hour average can be recognized in both half-hour averages. There are, however, mesogranule-like features that are not present in both half-hour averages. These features must be due to the increased level of noise we expect in the shorter time averages.

The scale of the mesogranules appears to vary somewhat from ~5" (as at x= 78", y= 105") to ~12" (x= 80", y=

SPO DAY 8164

VELOCITY

Mg I λ5173

30 MIN AVE 16:18:10 ±130 m/s

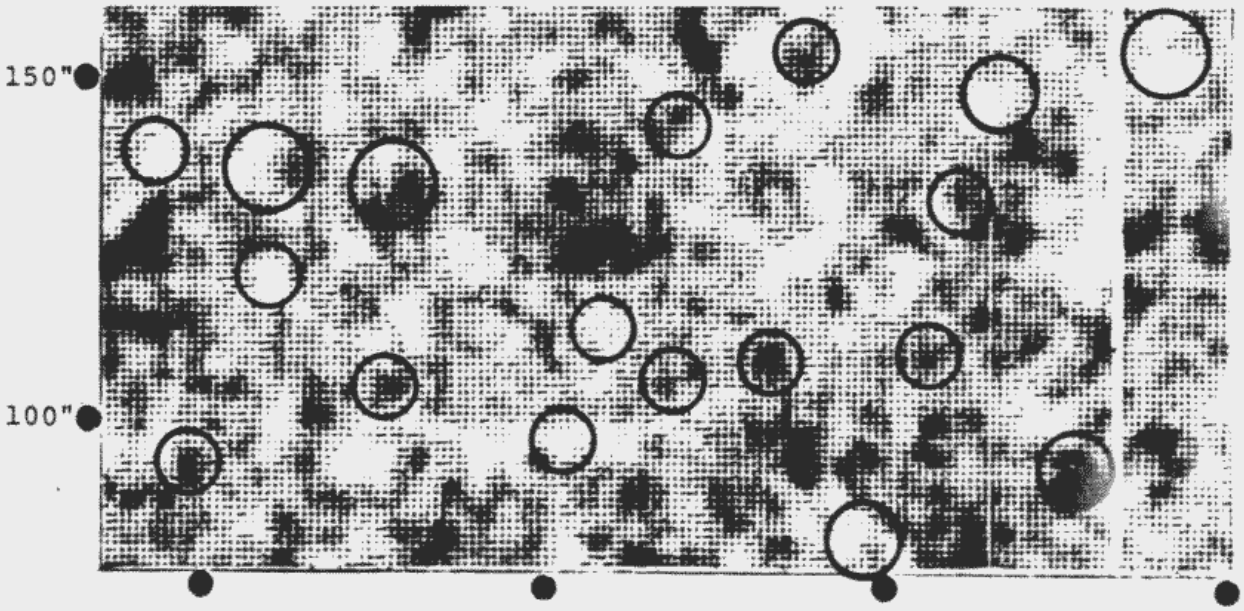

30 MIN AVE 16:47:55 ±130 m/s

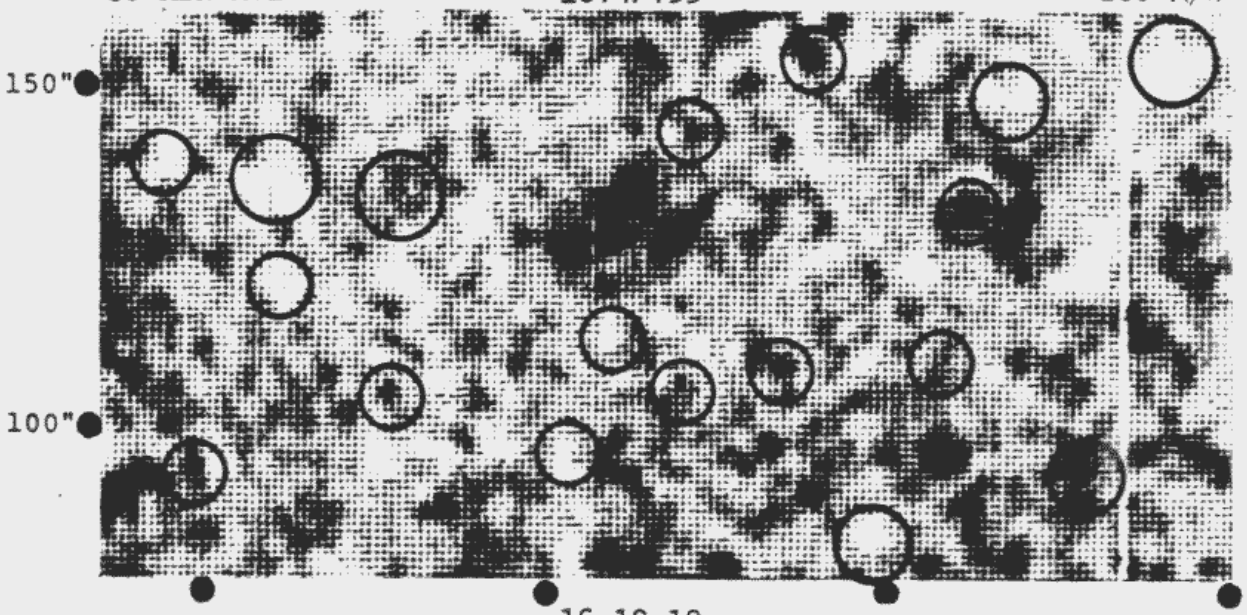

60 MIN AVE 16:18:10 ±110 m/s

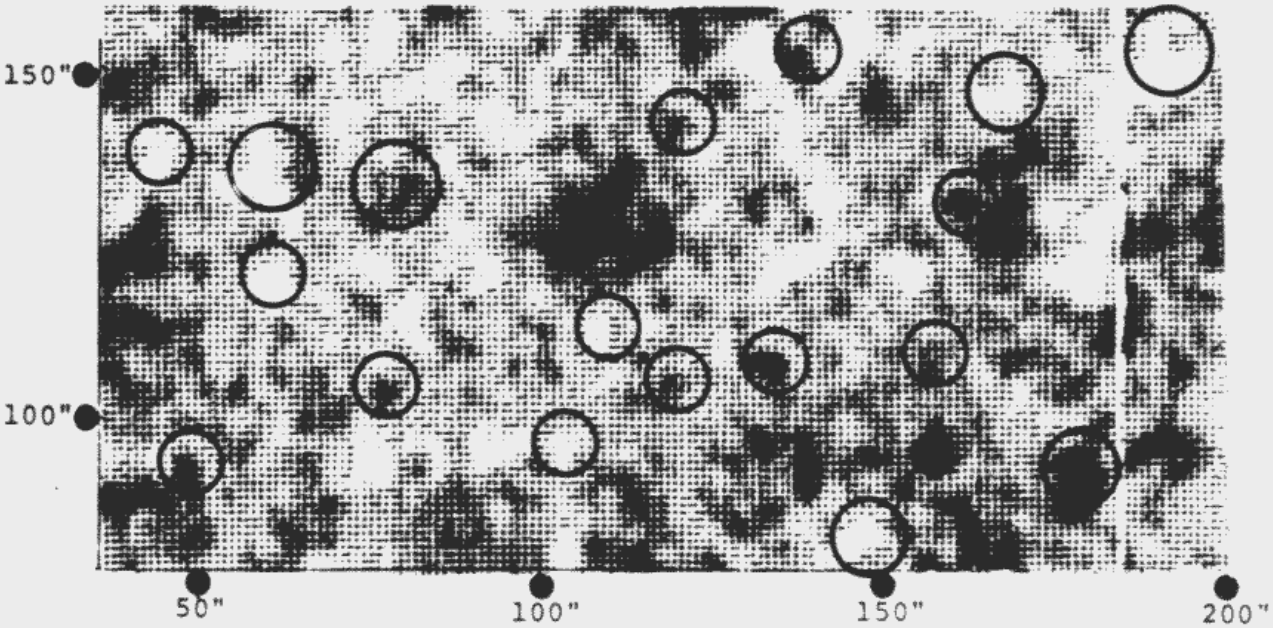

Figure 3.3

Persistence in the ~10" scale flows. A small portion of the two 30 minute and combined 60 minute averages of Mg I velocity data from Figure 3.2 are shown here on an enlarged scale. This portion of the larger image is identified by the scales in x and y which correspond to the same positions on the Sun as in Figure 3.2. Many isolated sites of upflow and downflow of ~10" are circled in the three averages illustrating the persistence of this scale of motion; these features we call mesogranules. The circled mesogranules help locate many others in the surrounding field which also persist.

135"). Some of the larger features, however, are probably made up of several mesogranules like the one at x= 180", y= 90". These ~10" features are apparent fairly uniformly over the image.

Our observations in Fe I λ5434 show greater noise. This is consistent with our estimates for the granulation amplitude at depth in the atmosphere. Figure 3.4 shows the one-hour Mg I velocity picture with the corresponding average in Fe I. Even with the increased noise there is still good correspondence between most of the ~25" features. Note for example the large site of upflow at x= 110", y= 130" and the site of downflow at x= 40", y= 50".

The smaller (~10") features are also present in the Fe I image and these correlate well with those seen in Mg I. Figure 3.5 shows the enlarged portion of the Mg I one-hour average velocity image from Figure 3.3 with the corresponding Fe I one-hour average. The circles identify the same mesogranules from Figure 3.3. Again most of these features are readily identified in both one-hour averages. Also the regions surrounding these mesogranules show other mesogranules apparent in both images.

The decreased noise in Mg I probably results both from the increase in supergranulation signal seen in this line and from an actual decrease of the noise with height, as may result from the decrease in the

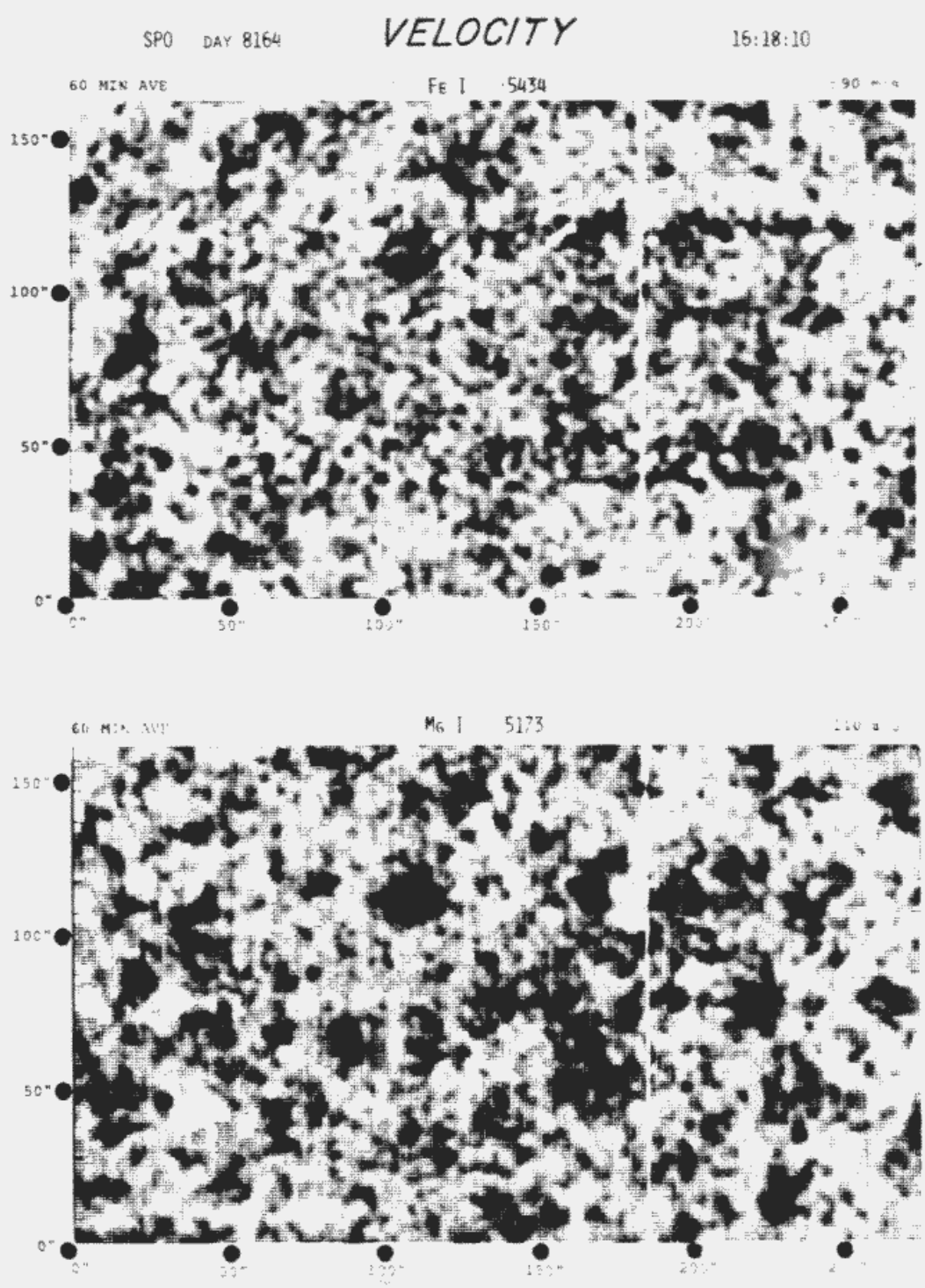

Figure 3.4

Correlation in velocities between Fe I and Mg I. The 60 minute Mg I λ5173 average of velocity is repeated from Figure 3.1 in the lower image. The upper image shows the simultaneously obtained 60 minute velocity average in Fe I λ5434. Although the Fe I velocities show much more noise most of the large scale sites of upflow and downflow correlate well between the two images. Note as in Figure 3.2 the ~25" site of material upflow (dark) at x= 195", y= 120" and the complicated downflow (bright) at x= 260", y= 25". This figure illustrates that the large scale steady flows we see in Mg I which is formed near the temperature minimum are also present in Fe I formed in the middle photosphere. The amplitude of the flow is greater in Mg I as the range of velocities represented in the lower image is somewhat greater than in the upper image.

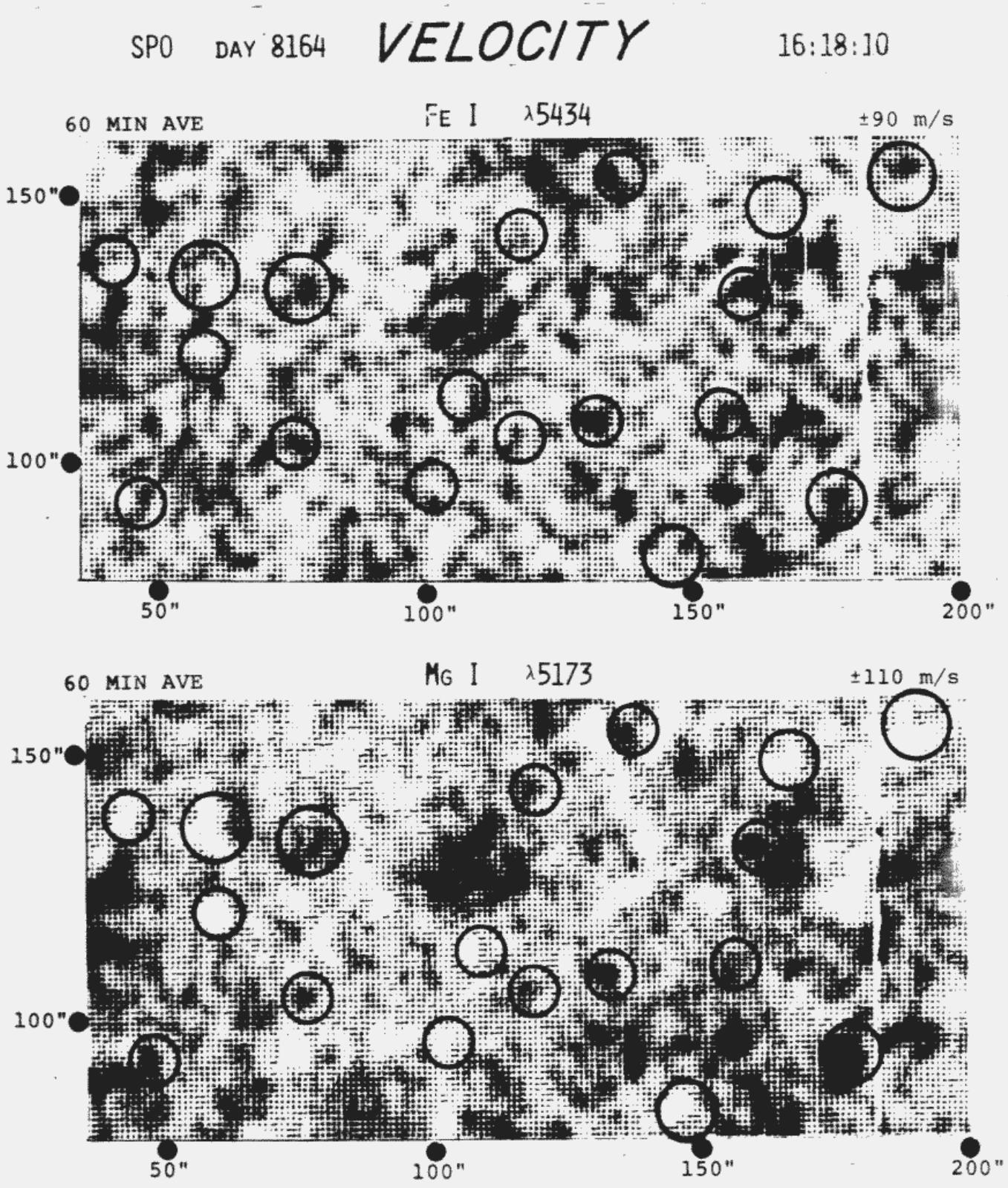

Figure 3.5

Correlation of the small scale flows. The same enlarged portion of Sun shown in Figure 3.3 is shown here for the one-hour averages of velocity in Mg I and in Fe I. The same mesogranules that were circled in Figure 3.3 are circled here. Many of these features are evident in both images as well as many others which have not been circled. The circles are useful as a reference in locating features between the two images. This correlation indicates that mesogranules are present at the two heights in the atmosphere sampled in these observations. As with the supergranulation, mesogranulation shows increased amplitude at the greater height.

granulation signal. At the height of formation of Mg I the granulation amplitude is about 25 ms^{-1} (see Figure 1.4). As discussed in Chapter 1, this signal is effectively filtered by the spatial averaging of 3" x 3" and the time averaging of 30 minutes. We estimate that the residual noise due to granulation at z= 580 km is less than 10 ms^{-1}. Both supergranulation and mesogranulation show increased amplitude with height in the atmosphere. We see this by comparing the amplitudes of the Fe I and Mg I velocities feature for feature in Figures 3.4 and 3.5.

3.3 Supergranulation

Figure 3.6 shows a 60 minute average of intensity in Ca II λ3933 together with the corresponding velocity in Mg I λ5173. The lowest image in this figure repeats the Mg I velocity picture with an overlay showing a contour of the Ca II intensity; the contour level was chosen so that the network is outlined.

Our impression is that most sites of large amplitude downflow (~100 ms^{-1}) coincide exactly with the bright chromospheric intensity seen in Ca II. For example, the complicated spatial structure of the downflow site at x= 190", y= 110" in the Mg I image correlates

SPO DAY 8164

INTENSITY

16:18:10

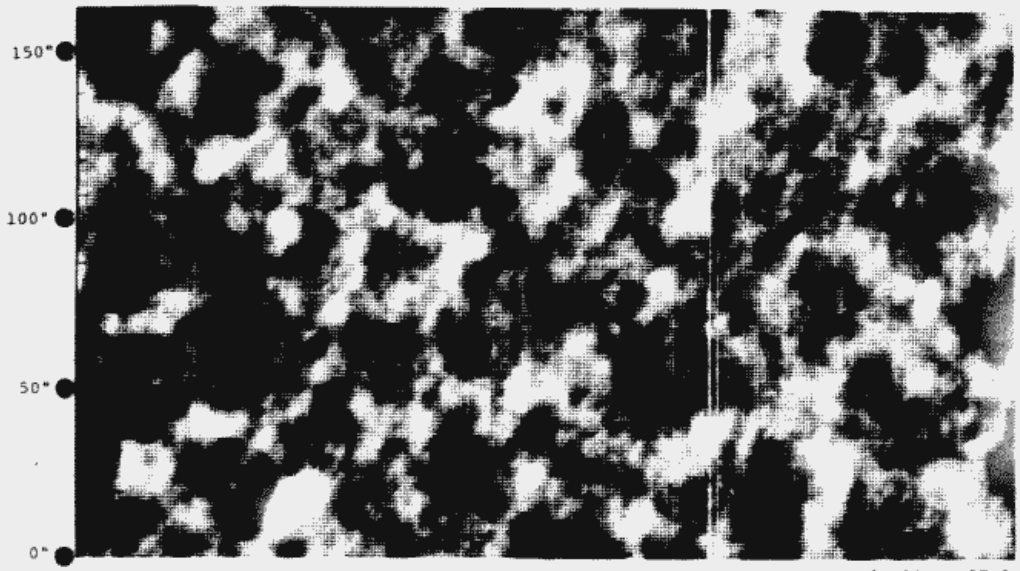

Ca II λ8542

VELOCITY

60 MIN AVE

±110 m/s

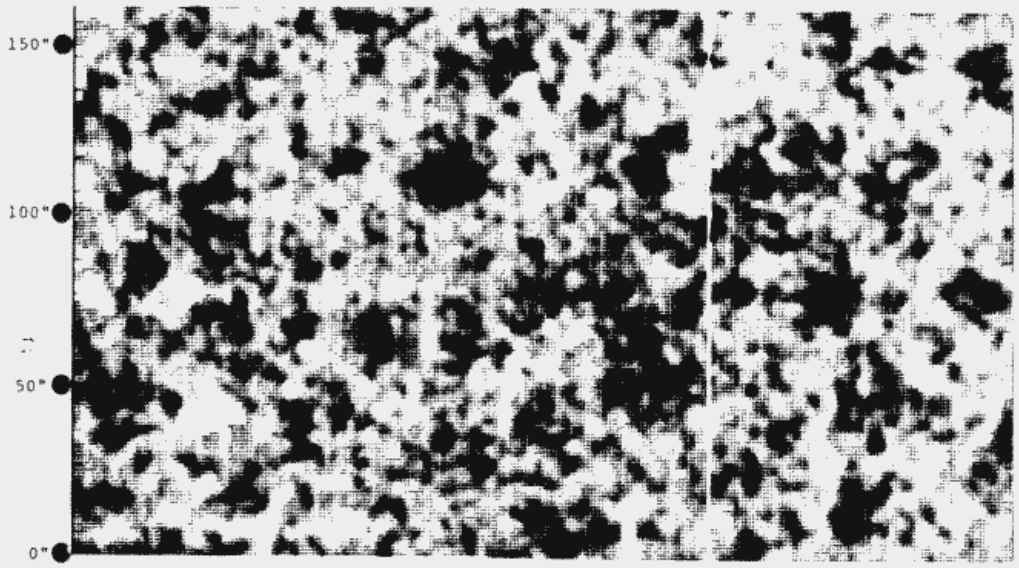

Mg I λ5173

60 MIN AVE

±110 m/s

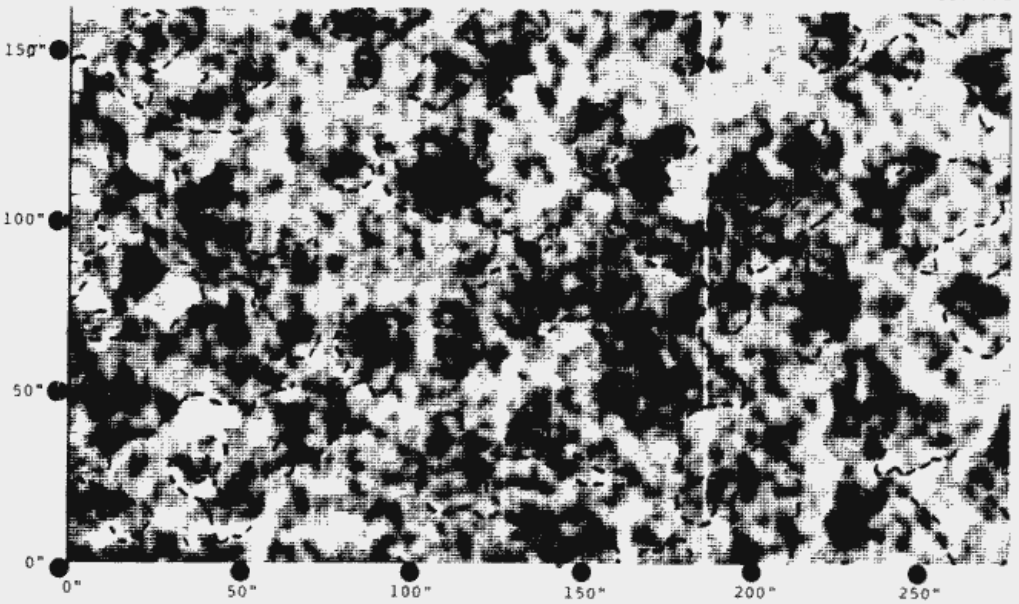

Figure 3.6

The vertical supergranular component day 8164. The 60 minute average velocity image obtained in Mg I on day 8164 is reproduced here (middle picture) with the corresponding intensity image in Ca II 8542 (top picture). The flow field shows features which vary on a scale of ~25" and correlate well with the chromospheric network. Areas of general downflow (bright in Mg I) are associated with brightness in Ca II, and areas of upflow (dark in Mg I) are usually found off the network. This is demonstrated in the lowest picture which repeats the Mg I velocity image overlaid with contours of constant Ca II intensity. This correlation indicates that these large scale steady flows are supergranular in origin.

well with the pattern of enhanced emission in Ca II. Also some of the sites of material downflow (bright) circled in Figure 3.2 are associated with magnetic fields. The features at x= 195", y= 155", and at x= 60", y= 140" for example are apparent as relative bright features in the Ca II intensity image in Figure 3.6. These features are accurately reproduced in the velocity in both position and shape. The well established correlation between Ca II bright features and increased magnetic field strength indicates that these flows are associated with the local fields.

The pattern of downflow with lesser amplitude (~40 ms^{-1}) does not specifically correlate with the Ca II bright features but does generally follow the network. This is illustrated in the lowest image in Figure 3.6 where downflow does usually occur within the network. This is not always the case; note the broad region of downflow at x=260", y=110".

In addition, sites of relative upflow do occur with amplitude comparable to the general downflow and are of supergranular scale. These features are always located in the cell interior as defined by the Ca II bright network. Note for example the upflow site (dark) at x= 100", y= 115" in Figure 6.

Thus we recognize three types of steady vertical flow fields associated with supergranulation. First is

the ~100 ms^{-1} downflows that are restricted to regions of enhanced magnetic field and are found only at bright points in the Ca II network. Second is the general tendency for lesser amplitude downflows to occur associated approximately with the Ca II network. Third we identify sites of ~50 ms^{-1} relative upflow that occupy the cell interiors as defined by the network. The space occupied by the lesser amplitude downflows and upflows is approximately equal although the zero of velocity may not be accurate as it is assigned assuming the frame average to be zero. These lesser amplitude flows are probably convective in origin and should be distinguished from ~100 ms^{-1} downflows which may be magnetically controlled.

3.4 Mesogranulation

The fine structures that persist in the velocity images (cf. Figure 3.3) are especially interesting. The picture of photospheric vertical flows derived from earlier work shows a broad region of material upflow in the cell center and downflow on the cell boundary. Although this is the general tendency for supergranulation, superposed on this flow is a smaller scale and greater amplitude motion field that we call mesogranulation.

The existence of mesogranules is confirmed by the

persistence we see for these features in the independent time averages of the velocity. This however says little about their origin. The other steady flow fields that exist in the sun -- granulation and supergranulation -- both appear to be convective in origin. These two flow fields show very disparate properties most clearly delineated by their very distinct scales. Those distinct scales may arise by the disparate depths at which these flows originate. Granulation probably feels its greatest driving in the H I ionization zone near the solar surface, whereas supergranulation may be driven in the He II zone at ~17,000 km depth. If mesogranules are convective in origin we may expect them to also adhere to some narrow range of scales indicative of conditions in the region where they receive their greatest driving - possibly the He I ionization zone. One clue as to the origin of the mesogranules can come from spatial power spectrum analysis which may be capable of identifying the range of scales that occur. Here we examine the time-averaged velocity images using two-dimensional Fourier power spectra and autocorrelation pictures.

Two-dimensional Fourier transforms are preferable to one-dimensional transforms since the two-dimensional transform is sensitive to size regardless of the orientation of a pattern. A sine wave of wavenumber $k = (k_x, k_y)$ in the data may introduce considerable power in the one-

dimensional transform at possible wavenumbers k to ∞ depending upon the wave orientation in the original data. The two-dimensional transform on the other hand, will always pick out the wavenumber k and the wave orientation. A sine wave, for example, shows power at two points in two-dimensional transform space: at k= (k_x, k_y), and at k= $(-k_x, -k_y)$. Similarly a square composed of two orthogonally directed sine waves will show power at four points in transform space that locate the corners of a square. Any N regular polygon similarly constructed will show power at 2N points in transform space. In the limit of large N a single circle centered about $k_x = k_y = 0$ and of radius k will appear in transform space. If isotropic patterns on the Sun adhere to one wavenumber k than they will show power in k_x, k_y in an annulus of radius k.

Our analysis of the two-dimensional transform of the Ca II λ8542 image indicates that considerable power occurs at spatial wavenumbers smaller than $2\pi/15{,}000$ km, whereas there is little power at larger wavenumbers. The Mg I and Fe I velocity images show considerable power out to wavenumber $2\pi/4000$ km indicating the existence of smaller than supergranular scales of motion in agreement with our impression. In these two-dimensional transforms there is considerable power near zero and this appears to decrease nearly monotonically with increasing wavenumber. Neither the Ca II

intensity nor Mg I and Fe I velocity transform images show concentric rings of power about $k_x = k_y = 0$ as we expect for an isotropic distribution of features with regular scale. Apparently both supergranulation and mesogranulation exhibit power over some range of scales.

The autocorrelation function is another useful diagnostic of spatial scales and patterns. The autocorrelation is defined for each possible spatial displacement Δx, Δy of the data on top of itself; it is the integral over the entire spatial domain of the data times the appropriately shifted data. This is equivalent to the inverse transform of the square of the two-dimensional power spectrum squared. It is a pure real function that varies from 0 to a maximum value in the range of complete anticorrelation to complete correlation. The autocorrelation of a sine wave will be a sine wave whose orientation in Δx, Δy is like that in the original data. The phase of the sine wave, however, is lost and will always occur with a maximum at the origin, $x = \Delta y = 0$. Other periodic functions are similarly reproduced but with a similar loss of phase information.

Figure 3.7 shows autocorrelation pictures for Ca II intensity and Mg I velocity from the 60 minute averages. Dark in these images occurs at shifts where the autocorrelation is large. The scale is labeled in arcseconds in the two directions Δx, Δy. Both images have a maximum

AUTOCORRELATION

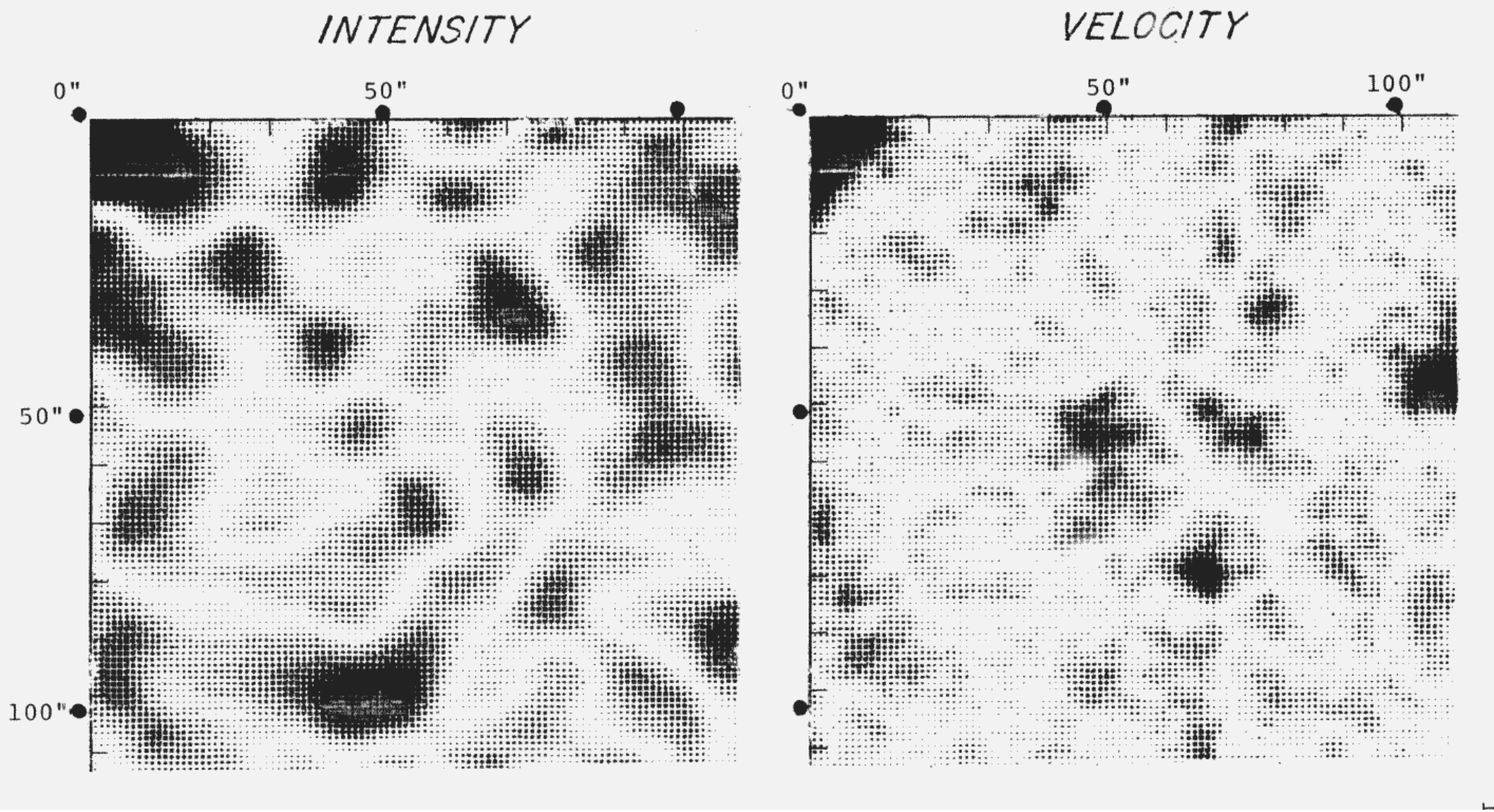

Figure 3.7

Autocorrelation images. The two pictures shown here are the two-dimensional autocorrelation functions of the Ca II λ8542 intensity on the left and of the Mg I λ 5173 velocity on the right. They are formed by taking the inverse Fourier transform of the two-dimensional power spectrum of the images that are shown in Figure 3.6. The autocorrelation at each point x, y is equal to the integral over the image of the data times the shifted data. Maxima in the autocorrelation are dark. The greatest maximum occurs at the origin x= y= 0 where the data are unshifted and show self correlation. There is evidence here for the supergranulation in both intensity and velocity. The mesogranular scale is indicated in the velocity autocorrelation by the width of the central maximum and by the recurrance of maxima with ~10" scales at various positions in the image.

autocorrelation at zero shift which is shown as saturated dark. For shifts out to ~10" both autocorrelations have an approximately monotonic decrease in all directions.

In Ca II the first minimum occurs closer to ~25" and varies depending upon the shift direction. This is very well defined as a narrow (bright) ribbon surrounding the central maximum. A second maximum occurs at 40" from the origin in all directions. This indicates preference for this scale in the Ca II intensities and is not surprising since it is the characteristic scale of network cells. We see considerable power at shifts much greater than supergranular scales indicating that features repeat throughout the original data. The Ca II autocorrelation image shows many ~30" rounded maxima separated by very narrow continuous ribbons of minima. This is somewhat reminiscent of the original Ca II intensity image with a scale like that of the network however somewhat smoother in appearance.

In Mg I the first minimum occurs at $\Delta x = \Delta y = 15"$ and is quite symmetric about zero. An apparent annulus of increased power is evident at radius 40". This is indicative of a spatially periodic velocity field of supergranular scale. The most prominant maximum outside the one at the origin occurs at $\Delta x = 110"$, $\Delta y = 50"$. This feature correlates with a maximum in the Ca II autocorrelation image and may be indicative of supergranular flows

correlated with the network. Other than this feature, the maxima that are present in this Mg I autocorrelation image are smaller and more ragged than those that occur in the Ca II autocorrelation image. Many 6" to 12" maxima occur throughout the image: some of these are superposed upon the larger maxima as in the feature at $\Delta x = 50"$, $\Delta y = 60"$; and some are individual maxima like the one at $\Delta x = 70"$, $\Delta y = 0"$. These features must be due to the mesogranulation.

The autocorrelation images seem to be less complicated than the original data. The Mg I velocity autocorrelation in Figure 3.7 shows fewer mesogranule-like features than the original data and lends itself to counting or measuring the individual features. Our general impression from this data is that most structures in the flow have scales of 6" to 12". Individual maxima of size greater than 12" are rare -- most maxima that occur with these scales are conglomerates of smaller maxima. The supergranulation scale of motion is evident primarily by the locations of the first and second minima that occur concentric about the origin and by the large scale variations seen throughout the image.

3.3 Conclusion

Our observations of the vertical velocity component in the photosphere indicate the existence of a scale of steady motion intermediate between that of the granulation and supergranulation, which we call mesogranulation. The mesogranules show scales between 6" and 12" and exhibit amplitudes of about 25 ms^{-1} in Fe I λ5434 and 40 ms^{-1} in Mg I λ5173. This motion field is apparent everywhere, both on and off the bright Ca II network and appears superposed upon a generally lesser-amplitude larger-scale vertical flow field. No corresponding intermediate scale of motion has been recognized in R_V= 0.8 observations.

Supergranular scale flows are present in these observations appearing as a general ~50 ms^{-1} downflow which is associated with the Ca II network and an equal amplitude relative upflow occurring in the cell interiors. These flows do not correlate specifically with Ca II bright features, indicating that they are associated with supergranulation and not with the chromospheric intensity. This is the first observation that appears to identify specific upflow features in the cell interior. These sites of upflow vary in size but often occupy a large portion of the supergranular cell interior (away from the bright Ca II network). Detail in the morphology of these flows is difficult to discern due to the superposed mesogranule flows.

In addition, we also recognize many sites of larger amplitude downflow (~100 ms^{-1}) specifically correlated with bright elements in Ca II. The well established correlation between Ca II bright features and magnetic fields indicates that these downflow sites are associated with increased magnetic fields. Previous observations of vertical flows have recognized this correlation (Frazier 1971), but have generally failed to detect the supergranular and mesogranular components of the vertical motions.

CHAPTER 4

THE HEIGHT VARIATION OF THE VERTICAL VELOCITY FIELD

4.1 Introduction

In this chapter we are primarily concerned with the height variation of the steady vertical motions of supergranular scale. Our program makes use of the University of Colorado UV Spectrometer on OSO 8 in conjunction with the SPO diode array. The technique used to measure the steady flows are as described for the horizontal motions in Chapter 2.

We begin by analyzing the lower-resolution raster-mode observations to obtain some feeling for the persistence of the measured flows. The raster-mode observations have the advantage that they sample the flows more frequently and are therefore less affected by oscillation noise. In addition the raster-mode pointing could be updated every orbit to follow features as they drift due to the solar rotation. This makes it possible to examine the same areas on the sun over very long periods of time. With these observations we are able to examine the large-scale flows which may be supergranular in origin.

Our higher-resolution observations permit us to

study smaller than supergranular scales of motion. We incorporate a new mode of observation in this work: the higher-resolution raster mode. This is the same as the raster mode except that the sampling is done more frequently so that rasters with more than 8 elements per line are obtained. With 30 x 7 raster-mode measurements we sample with nearly the spatial resolution of the point mode but with considerably better time sampling. The noise in these observations is considerably greater than with the point mode so we must average the data from several orbits to obtain useful information. With our higher-resolution raster-mode and point-mode observations we are able to examine features of smaller than supergranular scale. Features as small as mesogranules (~10") however, are at the 2" x 20" resolution limit of the instrument.

As in our R_V= 0.8 observations these OSO 8 measurements are accompanied by SPO diode array observations. The spectral lines have been chosen to sample motions spanning the photosphere to the middle chromosphere. In this work we incorporate the Mg I λ5173 line in addition to the diode array observations in Fe I. This line is formed near the temperature minimum and provides a third independent height from which we sample the steady flows.

4.2 Persistence in the OSO 8 Raster Mode

OSO 8 raster-mode observations that can be used to examine persistence of the motions were carried out near disk center on 15 satellite orbits during five different days. In this mode the UV spectrometer sweeps out 7 rows of 8 elements, each element having a spatial resolution of 20" x 20". By making pairs of rasters, one on each side of the SiII λ1817 line, we are able to compute an intensity and a velocity for each raster element, using the technique described in Chapter 2. About 40 raster pairs are obtained during a single 60 minute orbit, and the intensities and velocities are averaged to reduce the oscillatory signal and instrumental noise. It is the resulting time-averaged intensity and velocity images that are used here.

Figure 4.1 shows time-averaged intensity and velocity images for six consecutive orbits on day 6102 (11 April 1976). During this series the pointing of the satellite was updated to compensate for the drift due to solar rotation. To aide our visual interpretation, we portray the intensity and velocity as shades of gray and spatially interpolate between the 7 rows and 8 columns. We have found that this form of presentation eases the

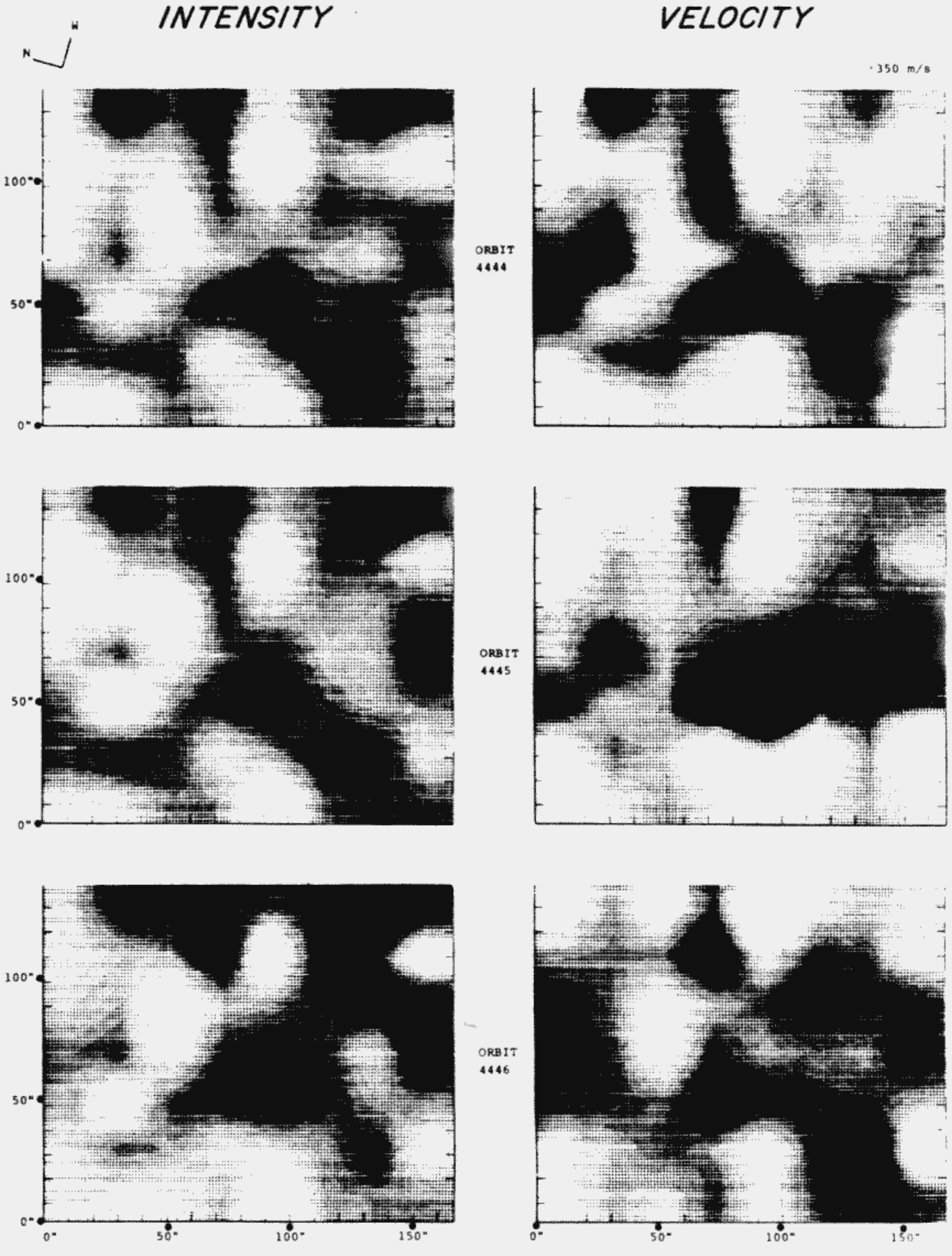

OSO - 8

S1 II 1817

INTENSITY

VELOCITY

±350 m/s

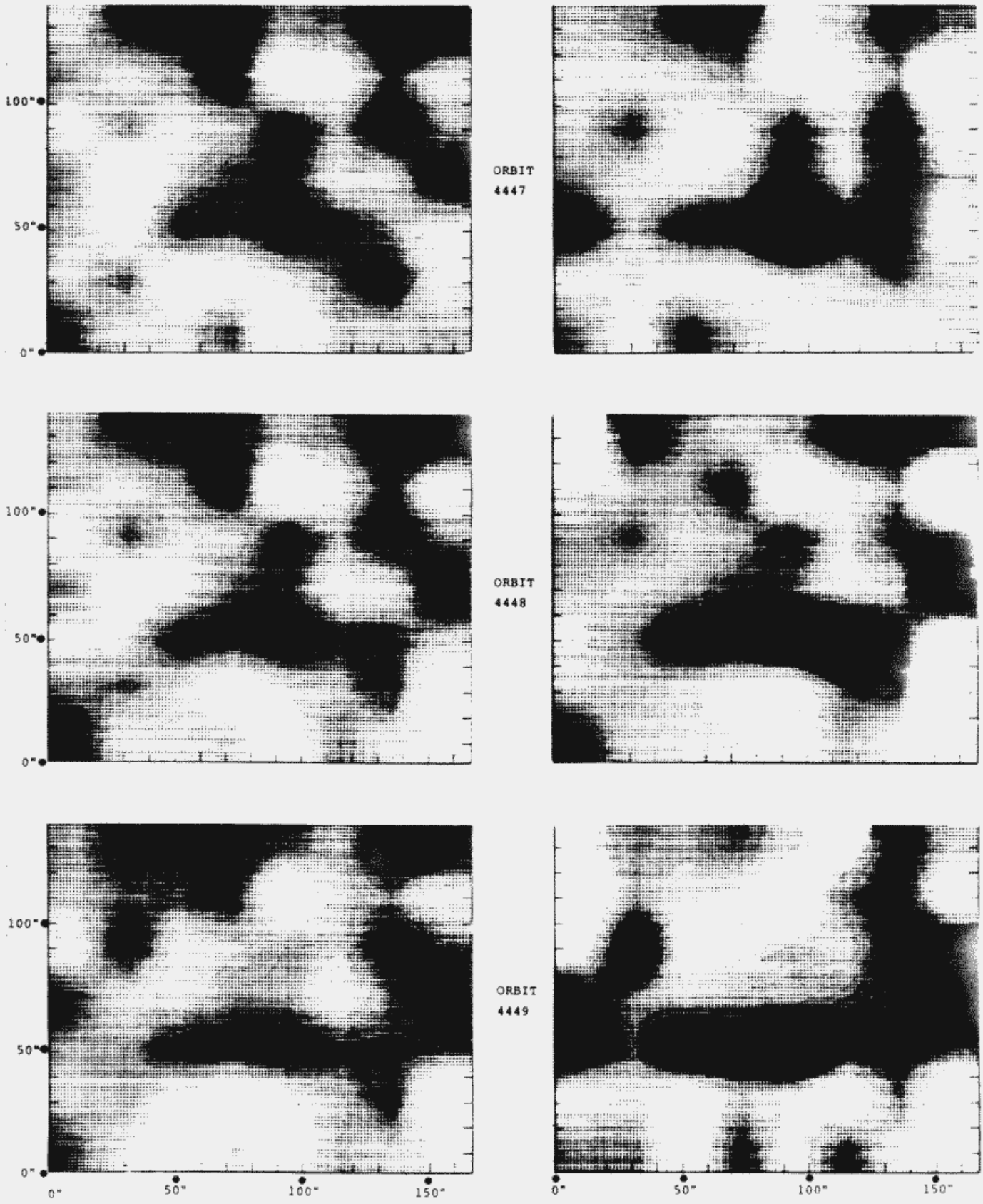

OSO - 8 S1 II 1817

Figure 4.1

Persistence of the OSO 8 velocities at R_V = 0.0 from day 6102. This is a sequence of six consecutive orbits showing the time-averaged intensity and Doppler velocity images formed from OSO 8 raster-mode observations obtained in Si II λ1817. The observations cover an area 140" x 166" at disk center in the quiet Sun and were obtained on day 6102 (11 April 1976). The left side shows the intensity pictures, each an average over one full orbit's observations. The intensity pictures show the same bright features in all six orbits. The pointing of the instrument was updated at the beginning of each orbit to compensate for the effect of solar rotation. The velocity images also show a very good correlation from one to the next with the exception of 4446. This demonstrates that there is a vertical steady motion field in the chromosphere with a scale of spatial variation roughly comparable to the supergranular scale. Also, this data demonstrates a remarkable correlation between bright features in the Si II intensity images and sites of velocity downflow. A similar behavior is not seen at large radius vector indicating that the horizontal and vertical flows have different spatial structure.

comparison between different observations and introduces little bias to the information content. Comparing each orbit against the next, we see that most features remain in both the intensity and the velocity images.

Emphasis in this comparison should be placed on the locations of large bright and dark features rather than on small spatial patterns. Substructures in the pictures are often artifacts of the interpolation procedure. In the sequence in Figure 4.1, all the intensity images show much the same bright features. The velocity images are dominated by a few flow fields. The large upflow site (dark) at x= 100", y= 50" for example is apparent in all the velocity images. Our impression is that most of the other prominant features persist as well.

One quantitative measure of the correlation between data sets is the linear regression coefficient r_ℓ (Bevington 1969). The parameter r_ℓ varies between 0 and 1 depending upon the degree of correlation, r_ℓ=0 implying no statistically significant correlation or anticorrelation. Successive orbits in the series (Figure 4.1) exhibit a very high degree of correlation both in intensity ($r_\ell \sim 0.8$) and in velocity ($r_\ell \sim 0.65$). We have further measured r_ℓ for pairs of orbits as a function of the time of separation, with the hope of understanding the evolution of features during the nine hours observing sequence. Although r_ℓ does decrease as a function of the

time between orbits, the scatter is quite large. Orbit 4445, for example, shows a very high degree of velocity correlation with orbit 4449, but orbit 4446 has a low velocity correlation with 4447. A similar impression is also evident in Figure 4.1 as we compare the images feature for feature. The noise in the data appears to be too large to allow any significant measure of pattern evolution.

Figure 4.1 also displays a striking correlation between intensity and velocity, unlike our measurements at R_V=0.8. This is a conspicuous feature in all our raster-mode experiments at disk center. With the exception of 4448, all the orbits in Figure 4.1 have a correlation of intensity with velocity of $r_\ell > 0.4$. The regression coefficient is one means we have for evaluating the data. The value r_ℓ=0.4 is quite statistically significant for this number of data points according to the T-test for the independence of measurements (Pough and Winslow 19 , Bevington 1969). This is consistent with our impressions drawn from the data.

We have carried out and evaluated four comparable studies on other days and these show a similar persistence in the velocities corroborating the spatial correlation between sites of material downflow and enhanced Si II intensity. Two of these are presented in Figures D.1 and D.2. On all four days the intensity

correlation between successive images is greater than 0.68 in all but one example, orbits 7869, 7870 (Figure D.2) where it is 0.52. Successive velocity images similarly correlate with $r_\ell > 0.48$ in all but this pair. Lites et.al. (1976) reaches the same conclusion, namely that disk center observations in chromospheric lines show a striking correlation between bright features and sites of velocity downflow in the steady component when viewed in the Si II line.

4.3 Higher-Resolution OSO 8 Observations

On three days we carried out raster-mode observations designed to give better spatial resolution but with increased noise. This was accomplished by sampling the intensity more frequently as the satellite pointing was scanned back and forth.

In these higher resolution, time-averaged OSO 8 observations we no longer see as striking a correlation between Si II bright features and regions of velocity downflow. On one day we carried out raster mode experiments that sample 30 spatial elements in each of 7 rows, each element having a spatial resolution of 5" x 20". Like the 8 x 7 rasters, these 30 x 7 rasters are run one on either side of the Si II λ1817 line in a total time of 82 seconds. We compute the intensities and velocities

for each pair of rasters and average over 40 repeats per orbit for a total of three orbits to produce the time-averaged images used here.

The lower two images in Figure 4.2 show intensity and velocity images for the 30 x 7 rasters run on day 8071 (year 1978, day 71). These data are an average in time over the three orbits 15020, 15021, and 15022. Since the sampling with the OSO 8 instrument in this 30 x 7 raster mode has greater resolution in x, features are artificially elongated in y. In the upper images each 3 adjacent spatial elements have been averaged leaving 10 x 7 samples in the raster. Notice that the resulting 10 x 7 intensity and velocity images show a striking correlation, in agreement with our impressions for the 8 x 7 raster data. The 30 x 7 intensity image appear to be nearly identical with the lower resolution 10 x 7, but the corresponding velocities show considerable spatial substructure.

This impression is corroborated in two other days of observations when we sampled 16 elements per raster line in the raster mode. The velocity signal changes on a spatial scale of about 10" and exhibits a dynamic range of 3000 ms^{-1}. After spatial averaging to 20" x 20" resolution a significant correlation between intensity and velocity is seen. Unfortunately the noise in this data is large, a result of the short sampling time necessary

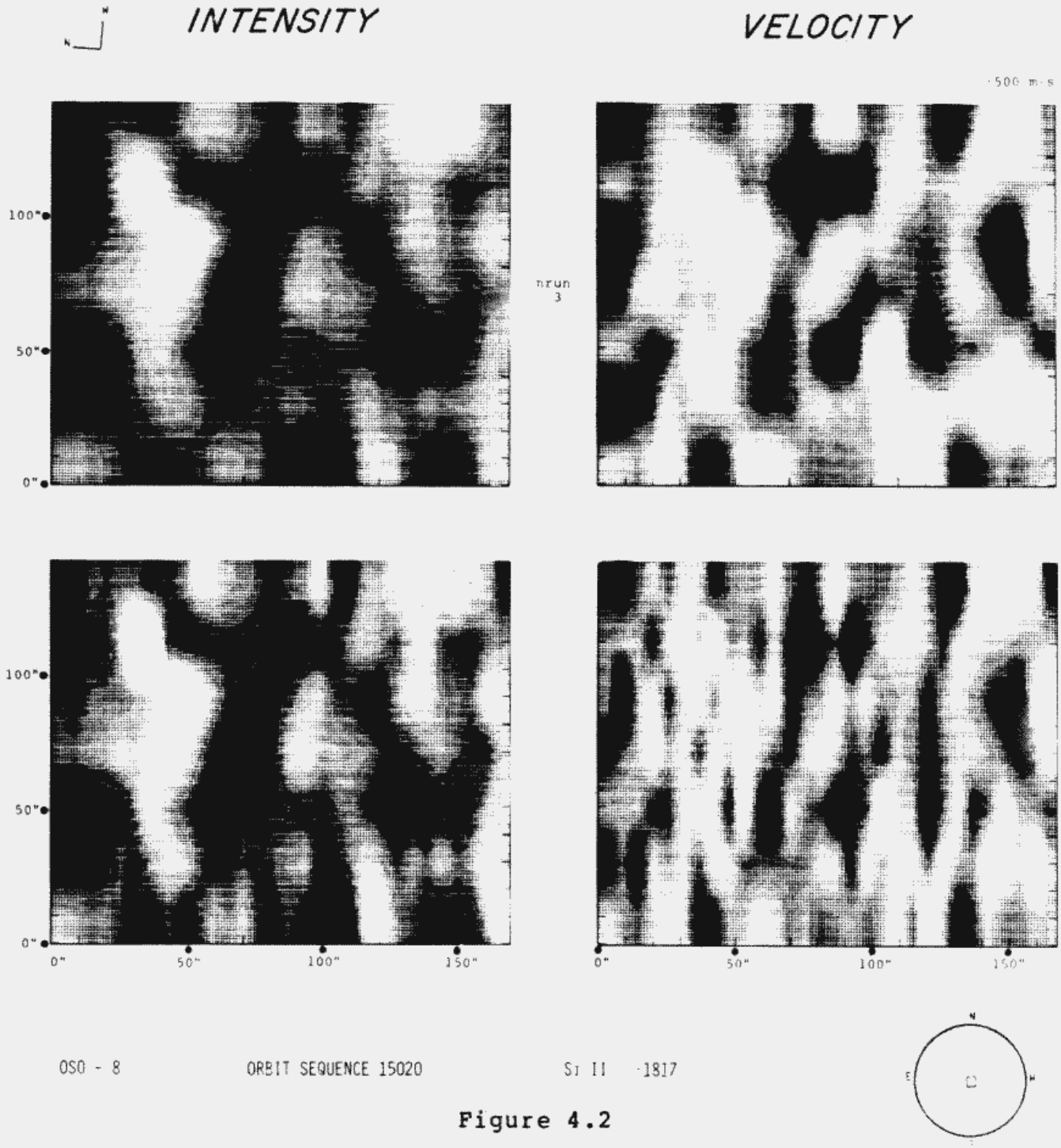

Figure 4.2

Higher-resolution raster-mode observations from day 8071. On day 8071 (12 March 1978) we ran three consecutive orbits of raster-mode experiments with an increased data acquisition rate so that 30 x 7 spatial elements were sampled in each repeat. The resulting intensity and velocity images made by averaging the observations over the entire three orbits are shown as the lower pair. The elongated pattern in the velocities is an artifact of the 5" x 20" rectangular sampling box. We have softened these measurements by applying a running mean of 3 elements and this result is shown in the upper pair. The spatial resolution of the upper pair is comparable to that of our previous raster-mode measurements and shows the remarkable correlation between intensity and velocity found previously. With higher spatial resolution, however, this correlation is less apparent. Although the intensity images look almost identical, the higher resolution velocity image shows considerable substructure which tends to diminish the correlation.

in making this observation.

In addition to these measurements, we obtained observations at disk center in the higher resolution point mode described in Chapter 2. In this mode the 2" x 20" slit samples a linear array of 20 spatial locations with a center to center separation of 4". At each spatial location, the Si II line profile is sampled at six wavelengths. One entire scan requires 160 seconds, which allows us to complete about 23 scans during an orbit. This observing mode provides more signal than raster mode observations since we spend our sampling time looking at a much smaller piece of the Sun. Unfortunately the satellite preprogrammed instructions do not allow us to update the pointing to compensate for solar rotation. Thus we cannot compare observations from separate orbits and must test for persistence by comparing half-orbit averages.

We have made these higher resolution point-mode observations during 27 orbits on six days. Twenty-six of the orbits show a significant intensity persistence in the two half-orbit averages ($r_\ell > 0.53$). Only 9 of the orbits show velocity persistence ($r_\ell > 0.3$), and some of these are shown in Figure 4.3. These nine orbits all display the general characteristic that the velocity changes on a horizontal scale of 10" and exhibits a dynamic range of 3000 ms^{-1}.

INTENSITY

VELOCITY

ORBIT 15023

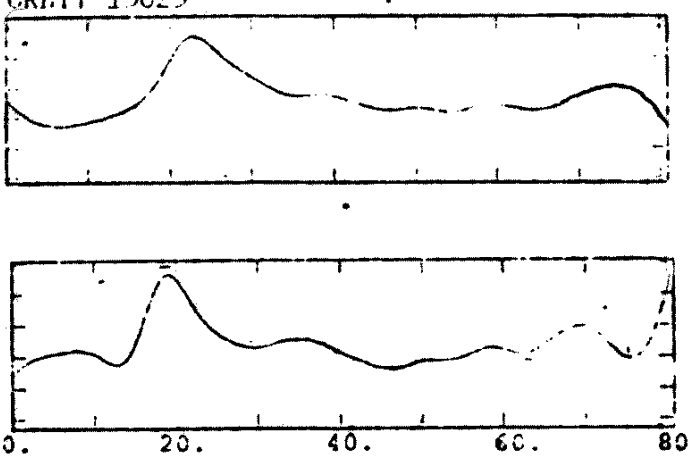

$r_1 = 0.538$

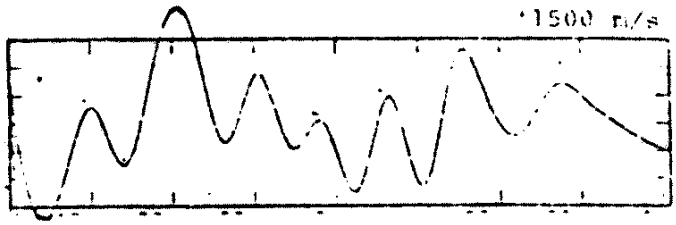

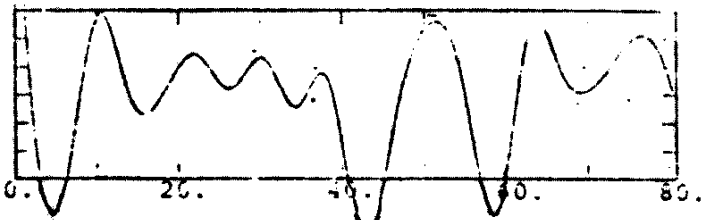

$r_1 = 0.468$

ORBIT 15024

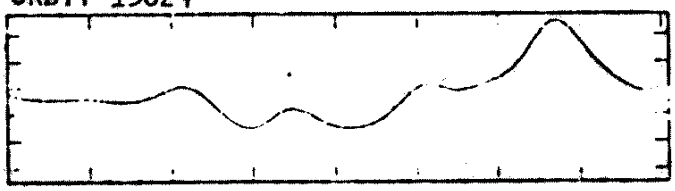

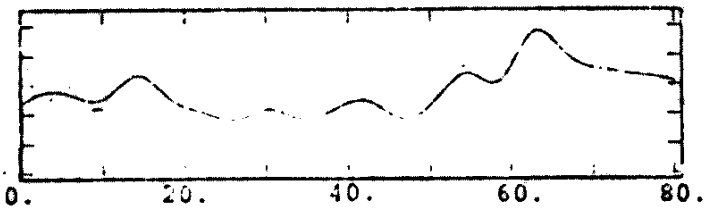

$r_1 = 0.778$

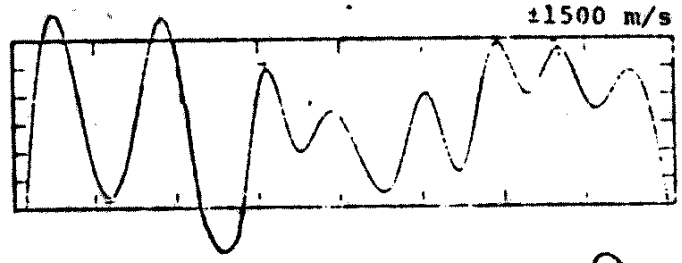

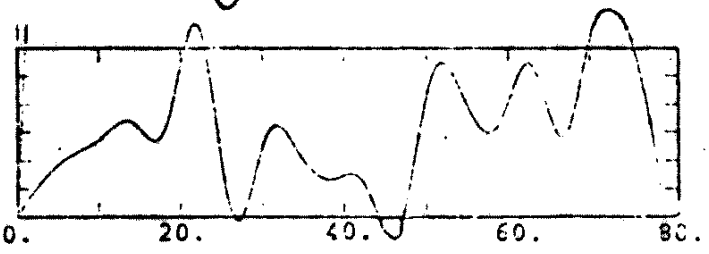

$r_1 = 0.271$

ORBIT 15026

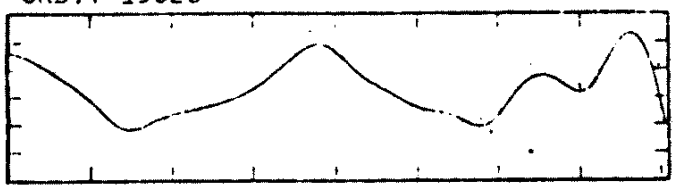

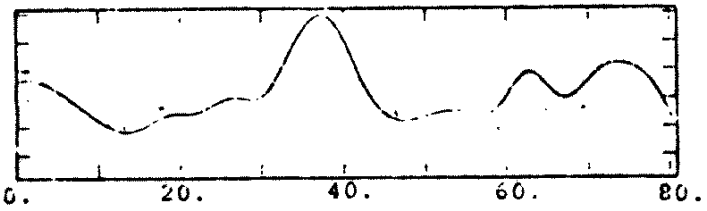

$r_1 = 0.800$

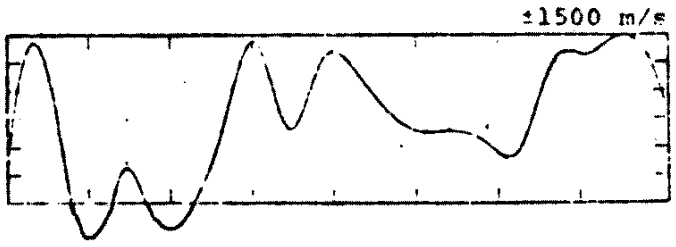

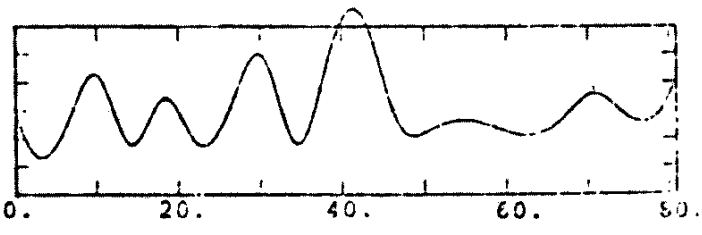

$r_1 = 0.175$

OSO - 8 St 11 A1817 . HALF ORBIT AVERAGES

Figure 4.3

Persistence in the point-mode observations from day 8071. Here we show three pairs of half-orbit averages for the point-mode observations on day 8071. Unfortunately the OSO 8 pointing cannot be updated in these point-mode experiments so we are unable to compensate for the effect of solar rotation. Thus we are unable to compare the measurements in successive orbits. Although these are among our best examples showing the highest level of persistence in the velocities, the degree of correlation is still rather low as indicated by the linear regression coefficients r_ℓ given with the data.

We attribute the general lack of persistence to three effects. 1) The estimated instrumental noise in the half-orbit averages is about ± 500 ms^{-1}, or roughly a third of the signal. 2) The velocity field appears to vary with a spatial scale less than that of the sampling particularly along the slit. 3) Solar rotation moves the image about 4" between separate half orbit averages, and this can significantly influence the average if the solar velocity field does indeed change on a small scale.

As in the previous raster-mode observations when we average this data with various running means we find that the intensity to velocity correlation is maximized with about 20" spatial sampling. This suggests that a supergranular scale of motion is present having relatively small amplitude and showing a correlation between sites of velocity downflow and the bright chromospheric network. The larger amplitude signal which appears in the higher resolution observations is most likely due to a smaller scale of motion superimposed on these supergranular flows. Unfortunately, it is beyond the resolution or sensitivity of these observations to understand the character of this flow field.

It is possible that the apparent variation of velocity with a scale of 10" may be due to the large noise component present in our Si II measurements. For two reasons this seems unlikely: First, our sampling

frequency in the 30 x 7 rasters was 5" and in the higher-resolution point mode it was 4". The small scale features vary with a scale of about twice this sampling frequency, whereas the noise will introduce large variations at this sampling frequency. Second, the evidence for persistence in a few of the point-mode orbits tends to rule out noise as the only source of the small spatial variations that we see. Noise is certainly a problem, but since a number of half-orbit average pairs show the same features these are probably solar in origin.

4.4 SPO OSO 8 Coordinated Observations

We have carried out simultaneous OSO 8 and SPO observations on three days making continuous diode array observations for at least 30 minutes. As many as eight orbits of satellite observations were carried out using both the raster-mode and the point-mode experiments. As in our studies at R_V=0.8 we use the raster-mode observations to check the relative pointing of the instruments and the point-mode observations for detailed velocity comparison.

We display the OSO 8 observations from day 8071 in Figure 4.2. Figure 4.4 repeats the 30 x 7 Si II images and compares these with the co-located Ca II 8542 intensity and Fe I λ5576 photospheric velocity images from

INTENSITY

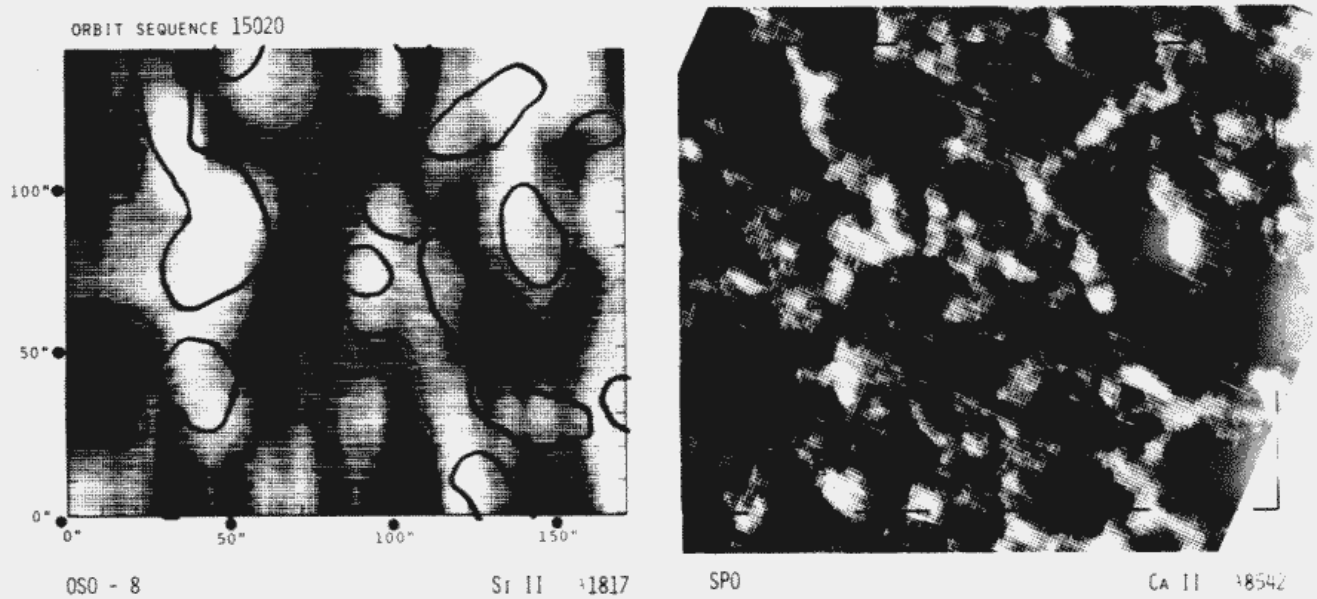

VELOCITY

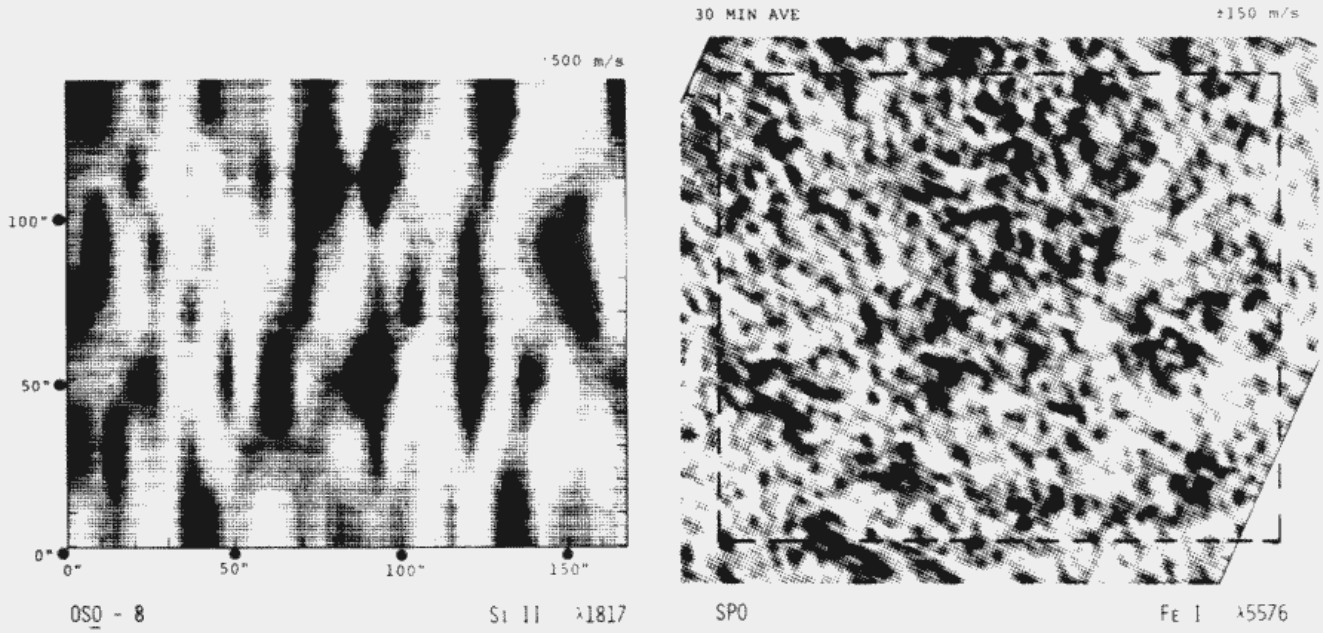

Figure 4.4

SPO OSO 8 overlap for day 8071. The 30 x 7 intensity and velocity images obtained by averaging three orbits of higher-resolution raster-mode observations on day 8071 are shown on the left with the accompanying SPO Ca II intensity and Fe I velocity pictures. The brightest features in the Ca II image are recognized in the Si II intensity image as indicated by the contours that appear on the Si II picture. These contours come from a 10" x 10" spatial average of the the Ca II intensities and help facilitate comparison of the two disparate instrumental resolutions. The velocity images are less easily compared as the scale for variation of the motions in the Fe I image is considerably smaller than the resolution available in the Si II measurements. We have the impression that sites of large amplitude flows in Si II occur in regions which have the same sign of the motion in Fe I.

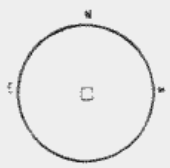

SPO. Velocity measurements in Mg I λ5173 were not made on this day.

The Si II and Ca II intensity images show excellent correlation considering the disparate spatial resolutions of the OSO 8 and SPO instruments. Contours drawn from the Ca II image spatially averaged with a 10" x 10" running mean are overlaid on the Si II image to illustrate this. All the brightest and darkest features in Ca II are evident in the Si II image. The Fe I velocity image has been spatially averaged by a running mean of 3" x 3" resolution to reduce the noise due to granulation. As in all our examples of disk center velocity measurements in photospheric lines, features on a scale of about 10" dominate the observed vertical velocities. This scale of motion is present with the larger-scale lesser-amplitude supergranular flow found correlated with the chromospheric network. Unfortunately, the OSO 8 observations do not provide adequate resolution to identify small scales of motion or to make a detailed comparison of the Si II chromospheric and Fe I photospheric velocity pictures. However, the two images do show some correlation in the sign of the larger scale motions. For example, the two prominant upflow (dark) sites near the top center of the Si II velocity image lie inside a large field of net upflow in Fe I. The possible presence and role of mesogranulation at this height will remain unresolved until

chromospheric velocity measurements are available having higher spatial resolution.

In addition observations using the OSO 8 point mode were obtained on the same day as these 30 x 7 rasters. These provide velocity measurements with better signal to noise and higher spatial resolution than is possible with the raster mode. Figure 4.5 shows the relative pointing for the point-mode experiments for day 8071 within the raster-mode pointing box for orbit 15020. Line drawings of the time-averaged intensities and velocities obtained in the five orbits of this series are shown in Figure 4.9 together with the corresponding SPO measurements in Ca II and Fe I. The SPO data is spatially averaged to simulate the OSO 8 observing procedure, like we have done in Chapter 2. The spatial position of the OSO 8 data relative to the SPO average is determined initially from the available pointing information and finally by comparing the Si II and the Ca II intensities. The striking correlation between the Si II and Ca II intensity patterns in all these orbits confirms the co-located pointing.

The SPO and OSO 8 time averaged velocities show less correlation than the intensities for the orbits in Figure 4.6. This may be due to: 1) the high level of noise in the OSO 8 velocity measurements, 2) spatial substructures in the velocity signal, or 3) a real absence of physical correlation between the photospheric and

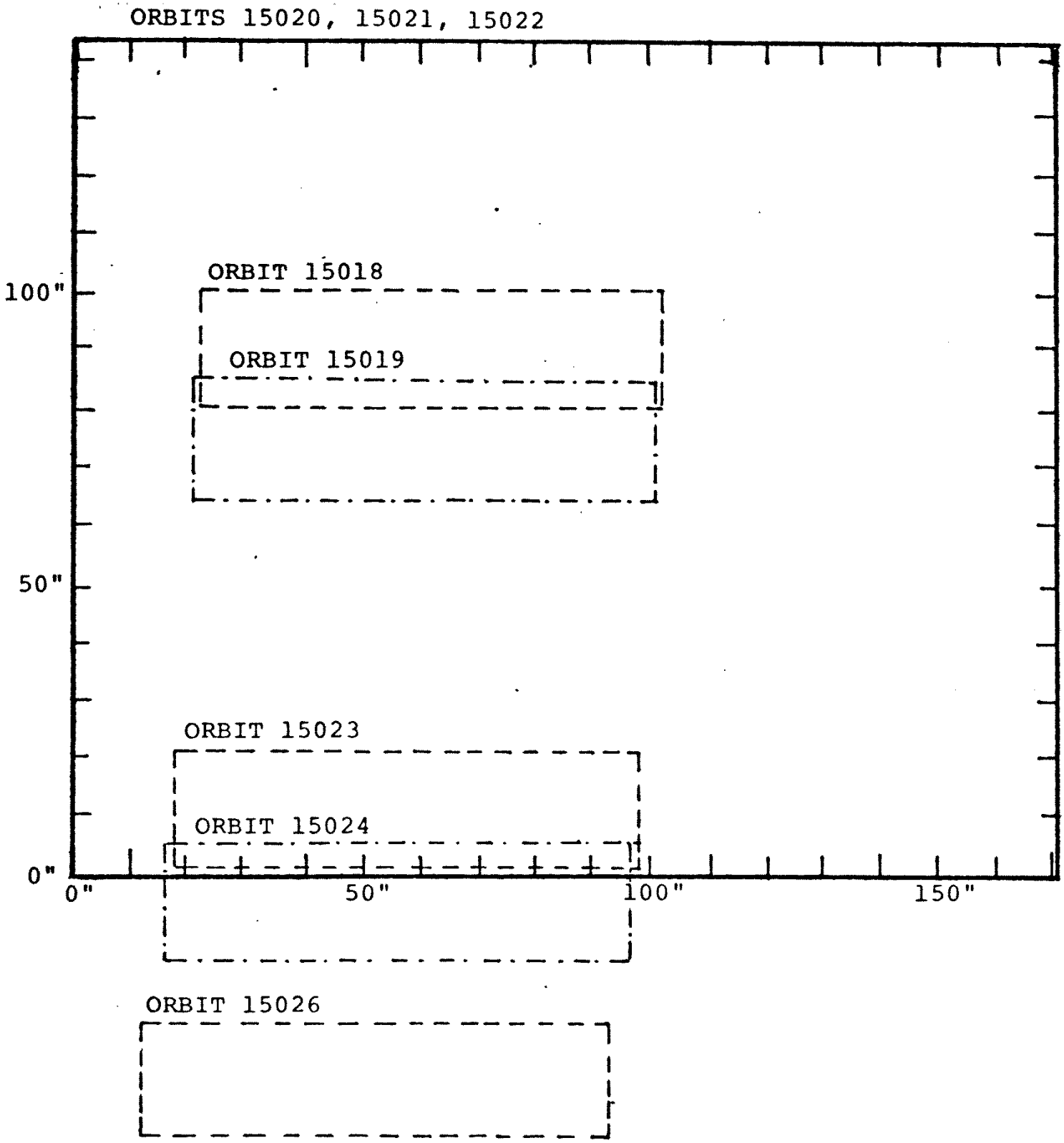

Figure 4.5

Relative pointing locations for experiments run on day 8071. This shows the positions for the five point-mode experiments run on day 8071 within the pointing box for the raster-mode orbits shown in Figure 4.4.

INTENSITY

VELOCITY

ORBIT 15023

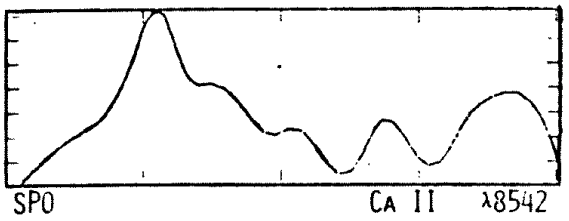

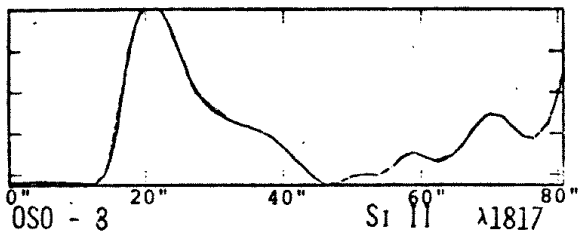

±100 m/s

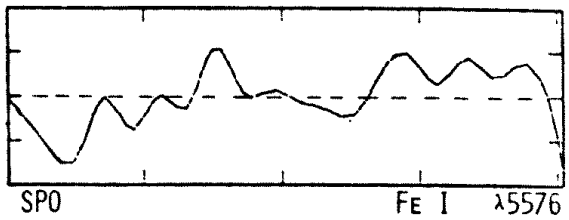

rms = 780 m/s ±2000 m/s

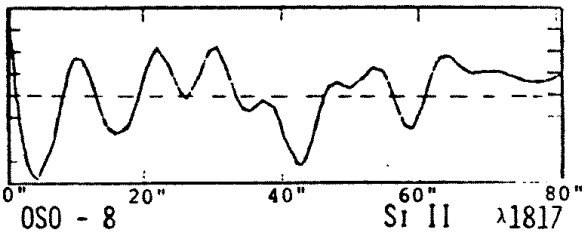

ORBIT 15024

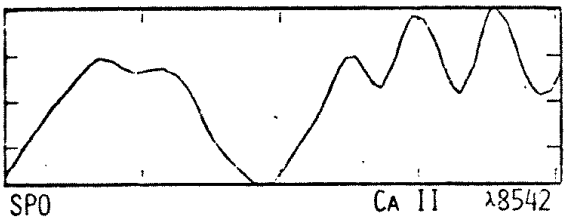

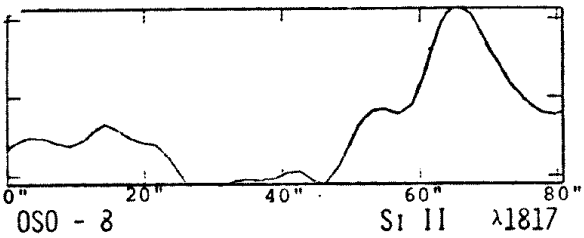

±100 m/s

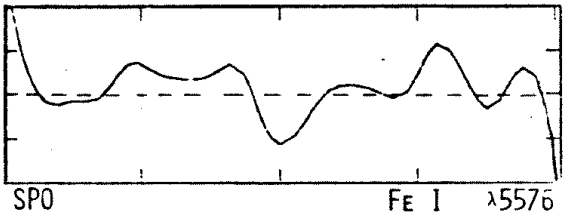

rms = 940 m/s ±2000 m/s

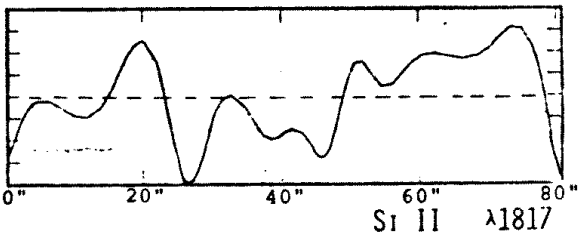

ORBIT 15026

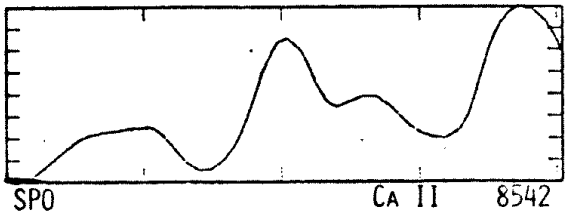

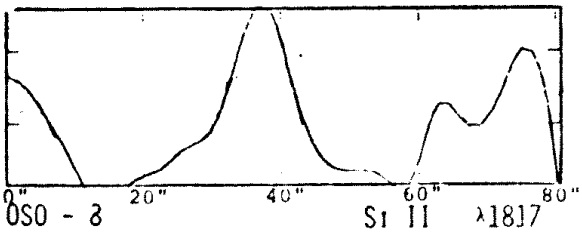

±100 m/s

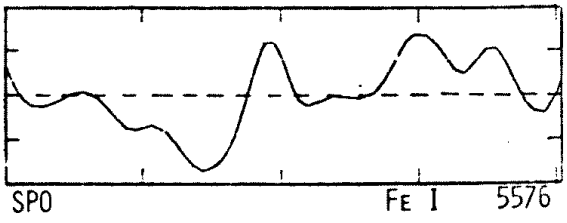

rms = 750 m/s ±2000 m/s

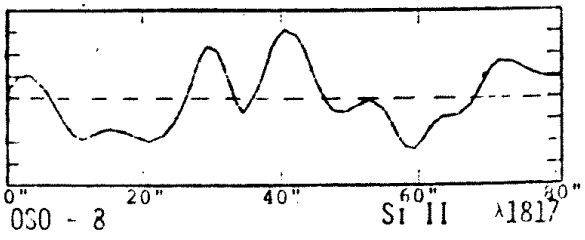

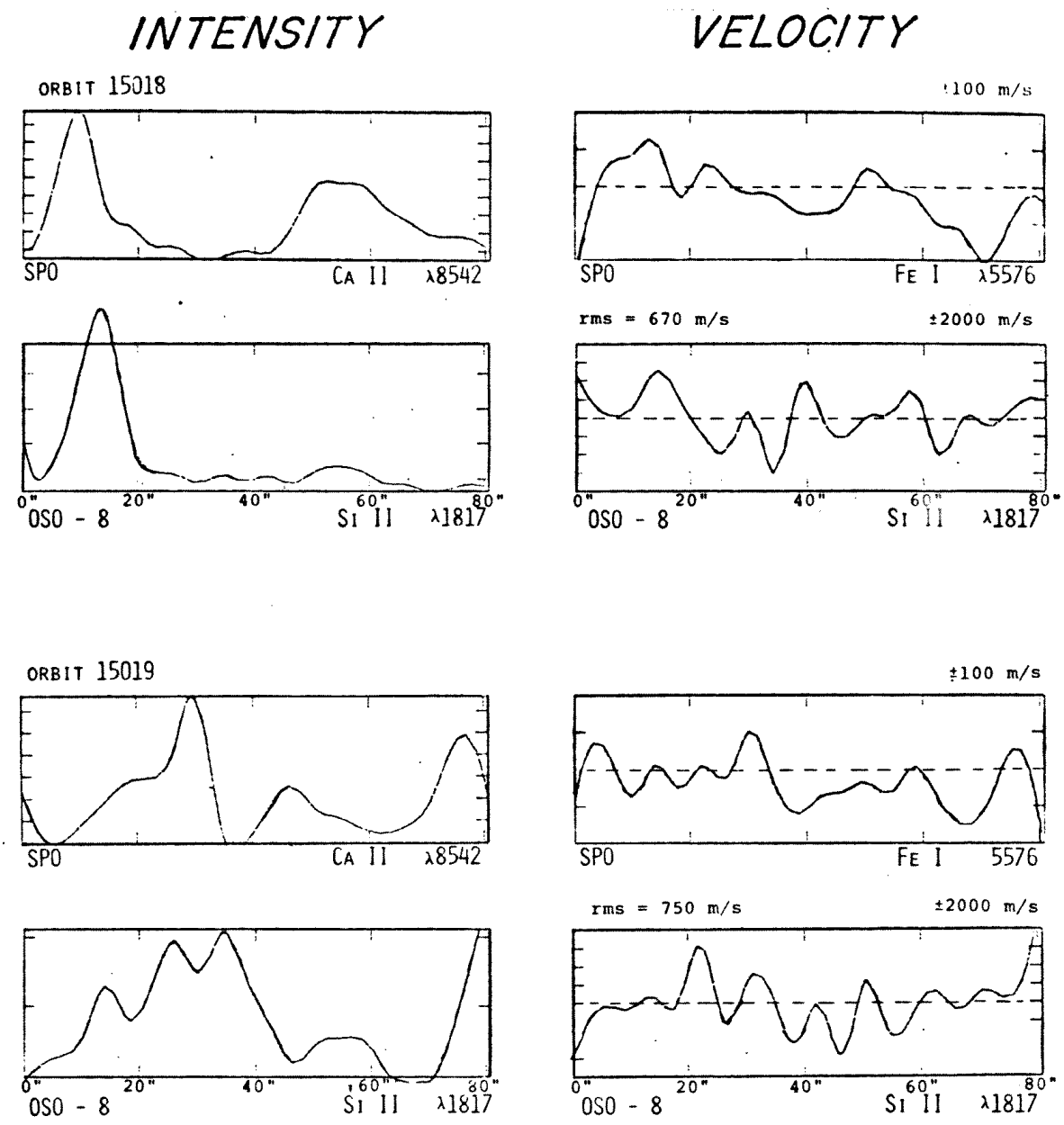

Figure 4.6

Comparison of SPO with higher-resolution OSO 8 observations from day 8071. The SPO intensity and velocity images shown here are made by spatially averaging the Ca II λ8542 and Fe I λ5576 images from Figure 3.7 to simulate the satellite sampling. These are shown with the corresponding Si II intensity and velocity line drawings. In all five orbits we find excellent agreement between the intensities, indicating that the relative pointing between the instruments is accurately determined. The velocities, however, do not show a convincing correlation in most of these examples. This may be the result of large noise in the measurements, spatial substructure in the Si II velocities that cannot be resolved, or the lack of an actual physical correlation between the motion fields.

chromospheric steady motions. Considerable noise is present in these OSO 8 observations as is evident from the degree of persistence between separate half-orbit averages. Spatial substructure is apparent in these OSO 8 velocity measurements consistent both with our 30 x 7 raster-mode observations and with the SPO photospheric velocity images. The predominant scale of motion is about 10" in all these measurements. Substructures in the velocity field degrade the comparison between SPO and OSO 8 observations in two ways. First, each velocity determination may sample several features along the 20" slit. Second, there may be small errors in the pointing overlap of the two instruments since this is confirmed by comparing the relatively large bright features in the chromospheric network.

Our impression from the 30 x 7 velocity comparison is that sites of velocity upflow or downflow in Si II are associated with larger regions of similar flow in Fe I. Also, both the OSO 8 and SPO observations show a correlation between places of large scale downflow and the chromospheric network. These suggest that there is some degree of similarity in the physical structure of the flows at the two heights. Unfortunately these point-mode observations appear to be inadequate to check this tendency or further clarify the nature of chromospheric motions.

We have carried out similar raster-mode and point-mode observations on two further days. Figures 4.7 and 4.8 show the OSO 8 raster-mode observations compared with the SPO Ca II intensity and Mg I velocity images for day 8164 orbits 16421 - 16426, and day 8165 orbits 16436 - 16440. These raster-mode observations sample 16 x 7 elements. The rectangular 10" x 20" sampling box causes the artificial elongation of the solar features apparent here. Contours drawn for 10" x 10" spatial averages of the Ca II intensity images are overlaid on the corresponding Si II intensity images. On both these days quite excellent agreement is found between the Si II and Ca II intensities. We have no doubt that the instruments were actually co-pointed. As in the previous example from day 8071 the velocities do not show a high degree of correlation.

On each of these days, three full orbits of point-mode observations were obtained. Figures 4.9 and 4.10 show line drawings of the Si II intensity and velocity with accompanying Ca II intensity and Mg I velocity line drawings made from spatial averages of the SPO data. The Si II and Ca II intensities are in excellent agreement in all six orbits. Although the velocity correlation is uncertain, as in the previous sequence of orbits in Figure 4.6, the Si II and Mg I velocities do vary with the same spatial frequency and show a number of sites with

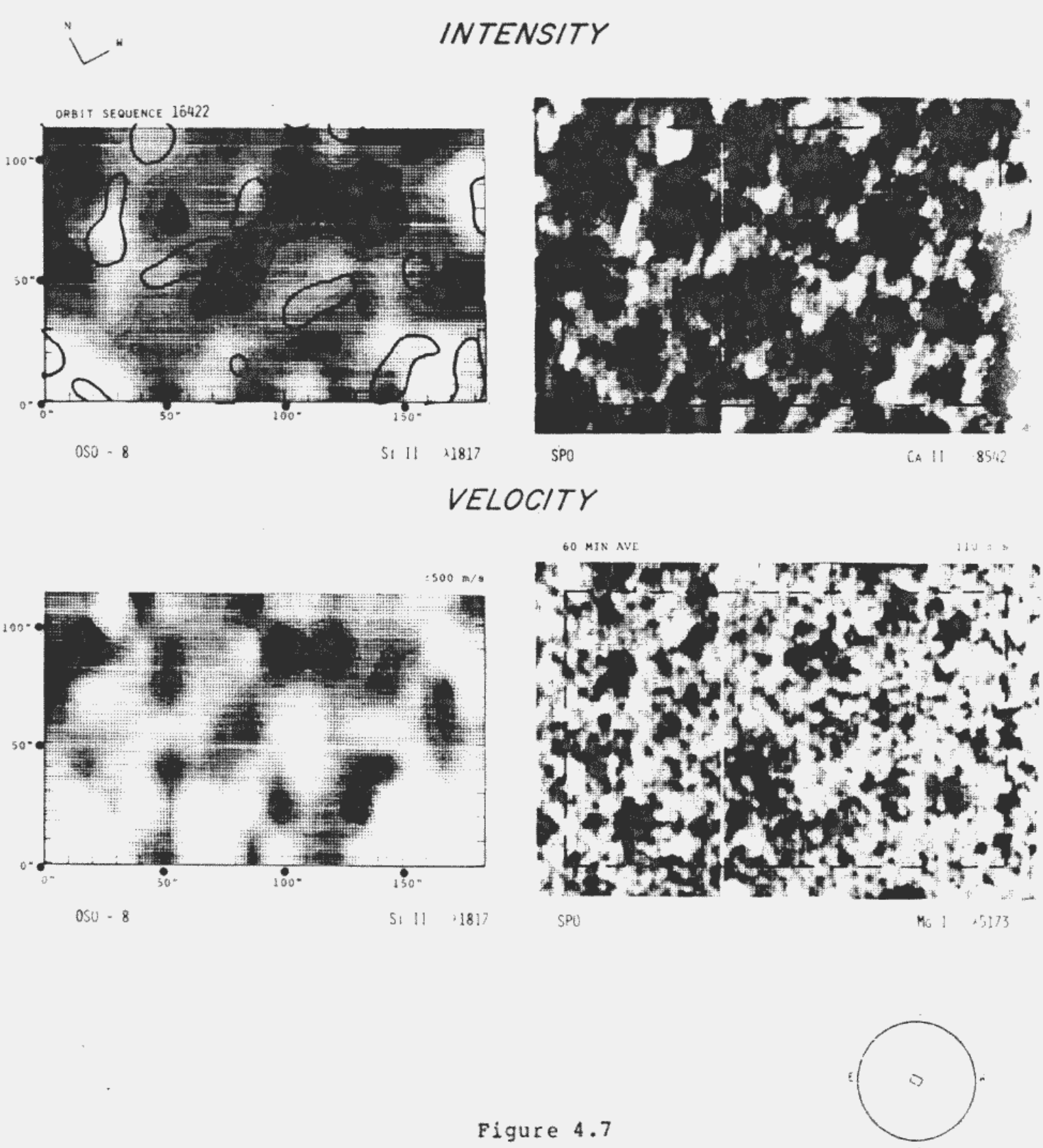

Figure 4.7

SPO OSO 8 overlap for day 8164. This is a second example of coordinated SPO OSO 8 observations (see Figure 4.4). The 16 x 7 OSO 8 intensity and velocity images obtained by averaging two orbits of higher-resolution raster-mode observations from day 8164 are shown on the left with the accompanying SPO Ca II intensity and Mg I velocity pictures. The brightest features in the Ca II image are recognized in the Si II intensities as indicated by the contours that appear on the Si II picture. It is difficult to identify features in common between the two velocity images perhaps because of the disparate resolutions of the instruments.

INTENSITY

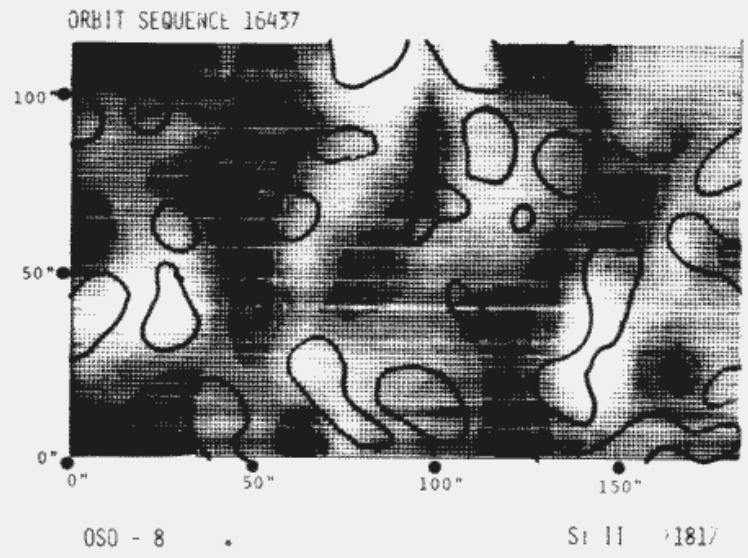

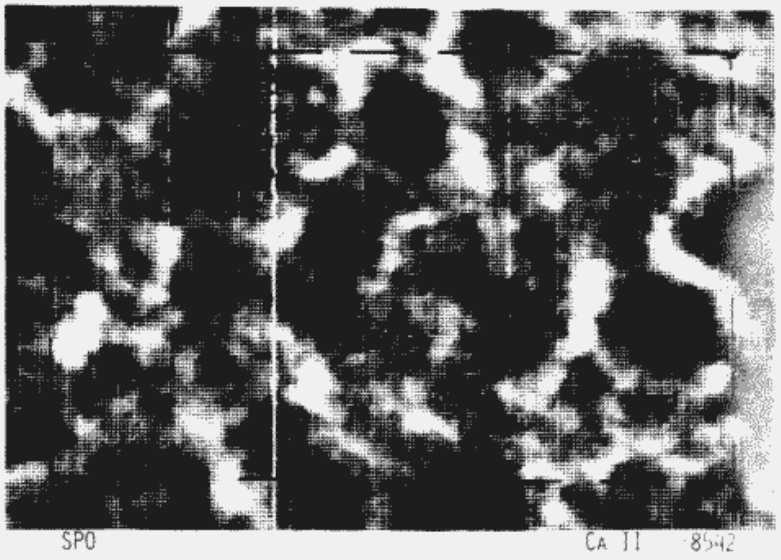

VELOCITY

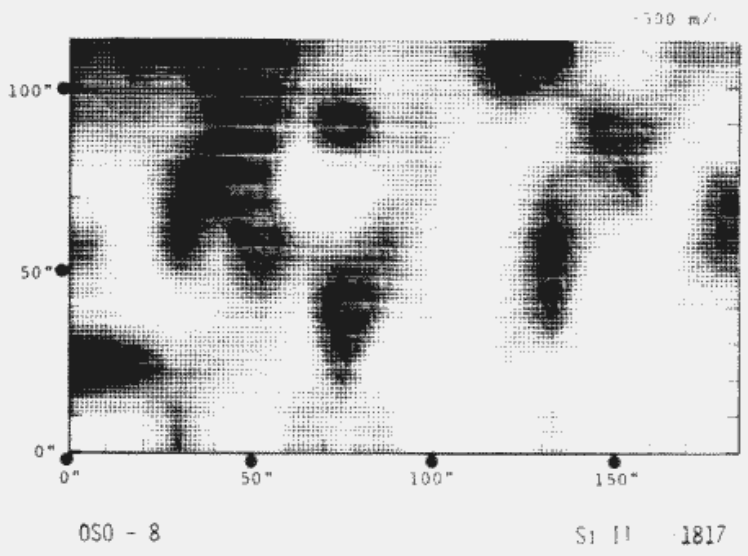

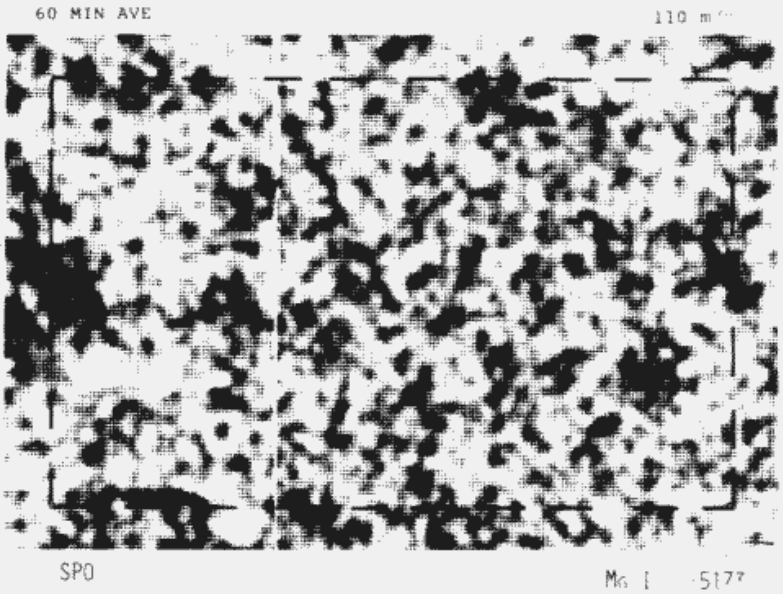

Figure 4.8

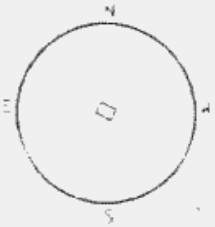

SPO OSO 8 overlap for day 8165. This is a third example of coordinated SPO OSO 8 observations (see Figures 3.7 and 3.10). These 16 x 7 OSO 8 intensity and velocity images obtained by averaging two orbits of higher-resolution raster-mode observations from day 8165 are shown on the left with the accompanying SPO Ca II intensity and Mg I velocity pictures. The brightest features in the Ca II image are again recognized in the Si II intensities as indicated by the 10" x 10" Ca II contours that appear on the Si II picture. It is difficult to identify common features between the two velocity images.

INTENSITY

VELOCITY

ORBIT 16421

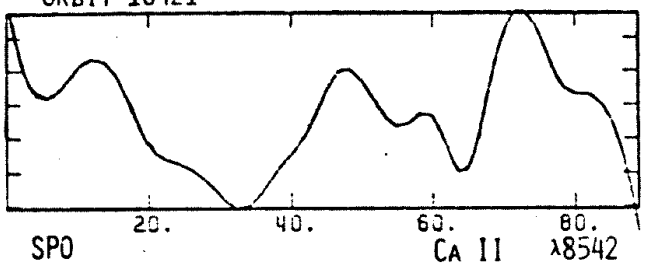

SPO — Ca II λ8542

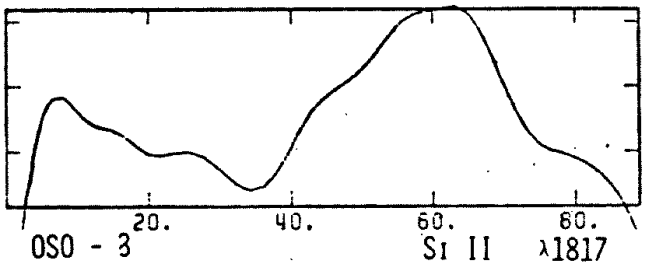

OSO - 3 — Si II λ1817

±100 m/s

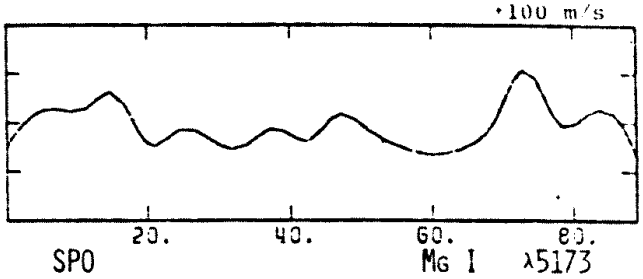

SPO — Mg I λ5173

rms = 580 m/s ±2000 m/s

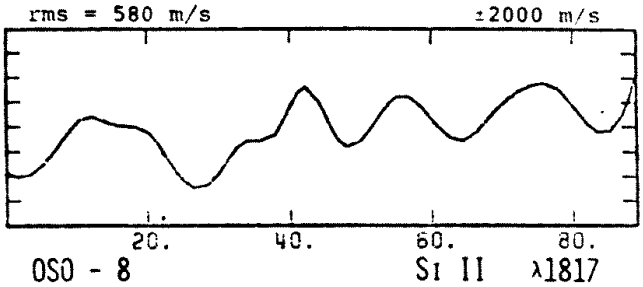

OSO - 8 — Si II λ1817

ORBIT 16425

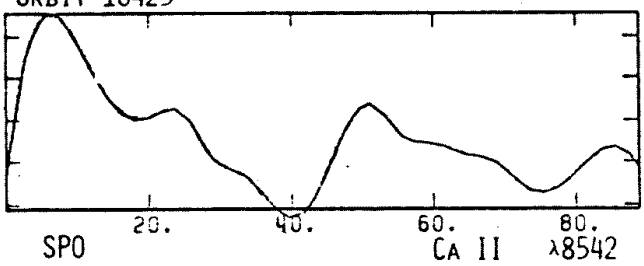

SPO — Ca II λ8542

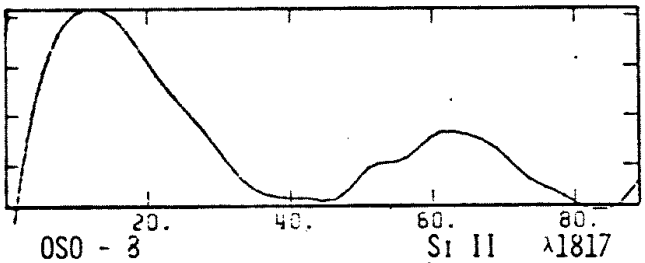

OSO - 3 — Si II λ1817

±100 m/s

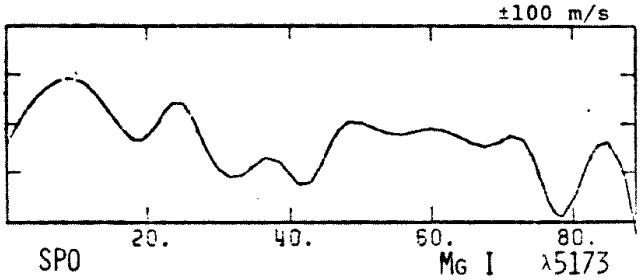

SPO — Mg I λ5173

rms = 390 m/s ±2000 m/s

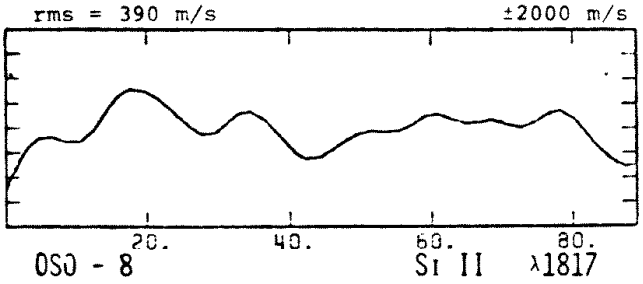

OSO - 8 — Si II λ1817

ORBIT 16426

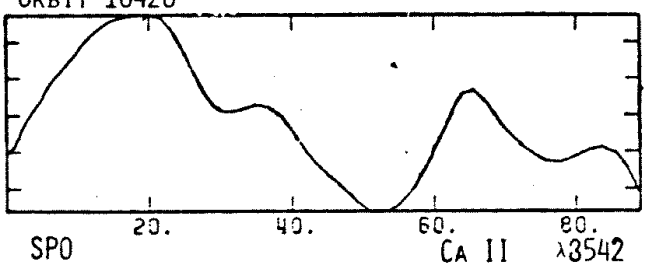

SPO — Ca II λ3542

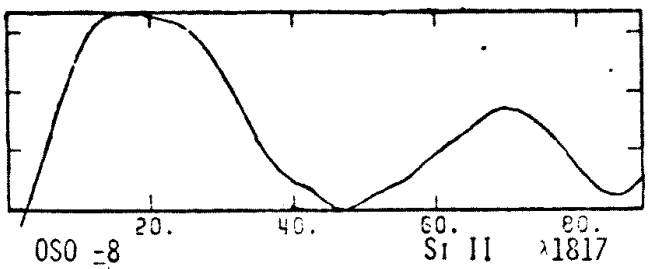

OSO -8 — Si II λ1817

±100 m/s

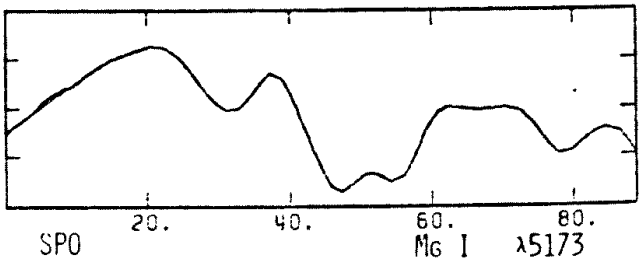

SPO — Mg I λ5173

rms = 390 m/s ±2000 m/s

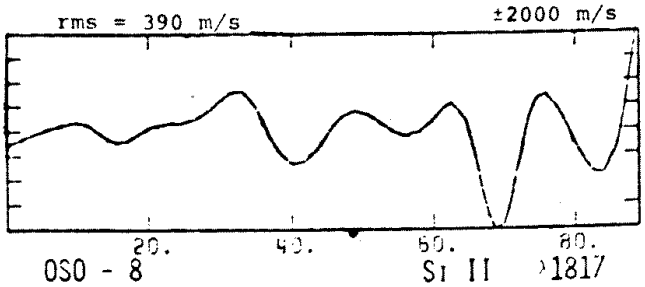

OSO - 8 — Si II λ1817

Figure 4.9

Comparison of SPO with higher-resolution OSO 8 observations for day 8164. The SPO intensity and velocity images shown here are made by spatially averaging the Ca II λ8542 and Mg I λ5173 images from Figure 4.7 as in the previous example from day 8071. These are shown with the corresponding Si II intensity and velocity line drawings. As before we see excellent agreement in the intensity correlation in all the orbits, but the velocities show little correlation.

INTENSITY

VELOCITY

ORBIT 16436

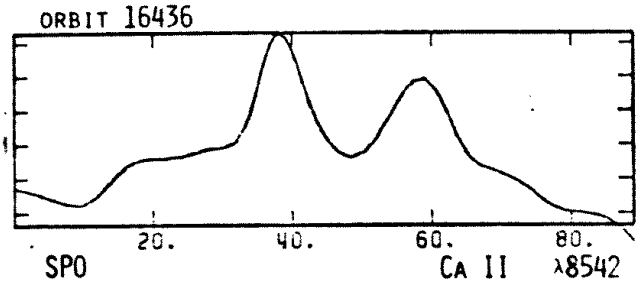

SPO — Ca II λ8542

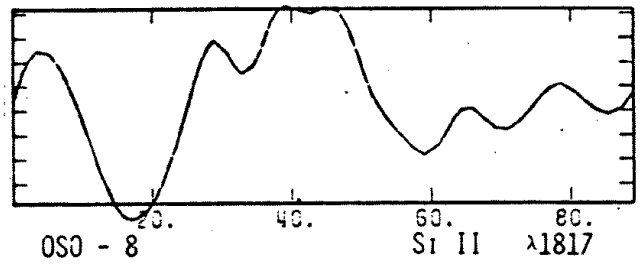

OSO - 8 — Si II λ1817

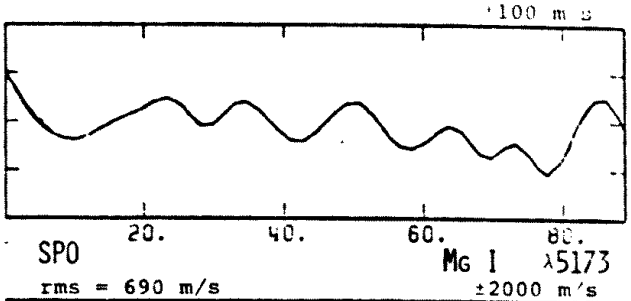

SPO — Mg I λ5173

rms = 690 m/s ±2000 m/s

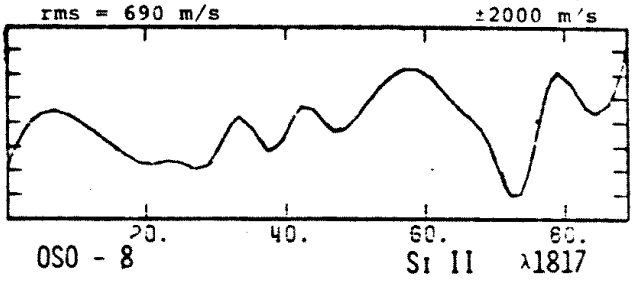

OSO - 8 — Si II λ1817

ORBIT 16439

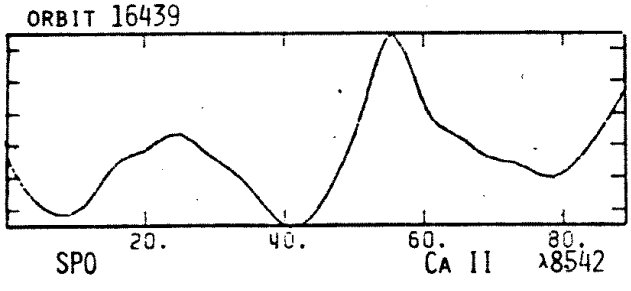

SPO — Ca II λ8542

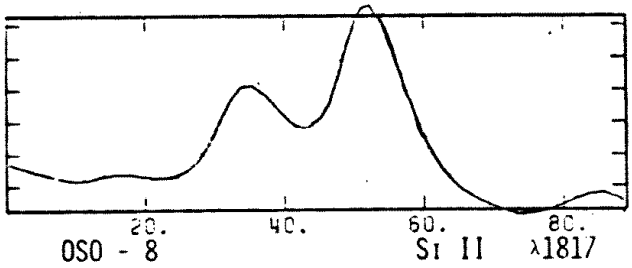

OSO - 8 — Si II λ1817

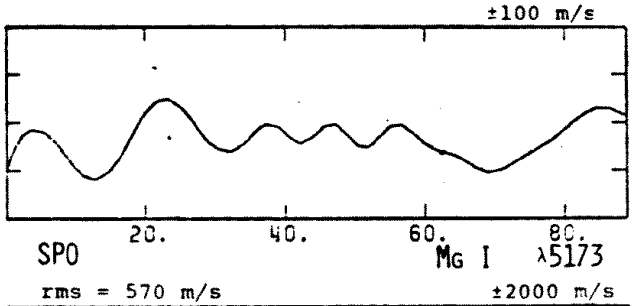

SPO — Mg I λ5173

rms = 570 m/s ±2000 m/s

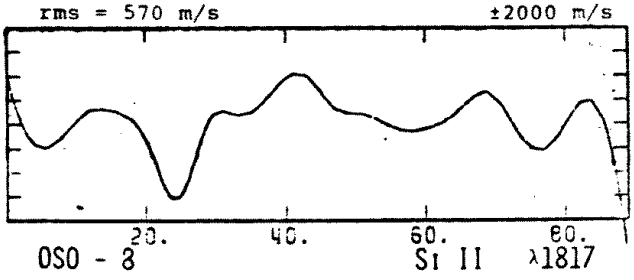

OSO - 8 — Si II λ1817

ORBIT 16440

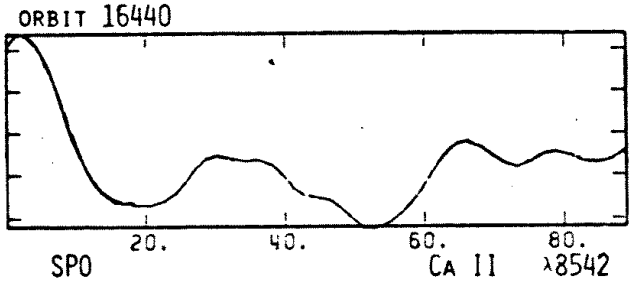

SPO — Ca II λ8542

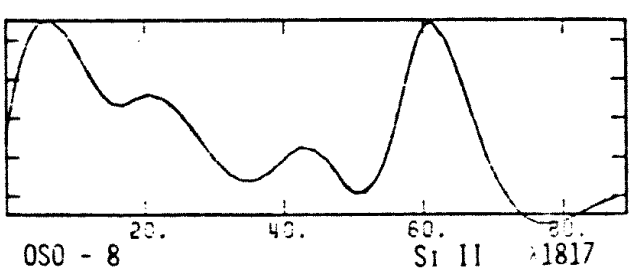

OSO - 8 — Si II λ1817

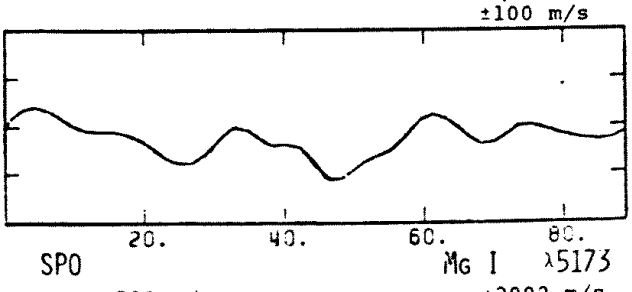

SPO — Mg I λ5173

rms = 520 m/s ±2000 m/s

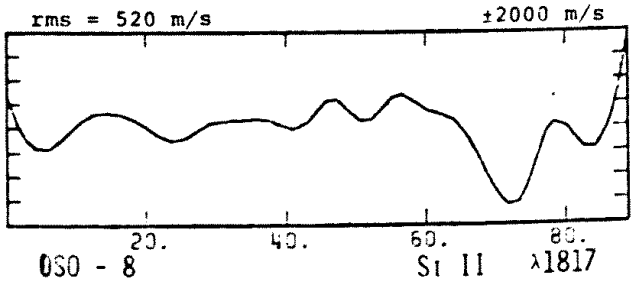

OSO - 8 — Si II λ1817

Figure 4.10

Comparison of SPO with higher-resolution OSO 8 observations for day 8165. The SPO intensity and velocity images shown here are made by spatially averaging the Ca II λ8542 and Mg I λ5173 images from Figure 4.8 as in the previous examples (Figures 4.6 and 4.9). These are shown with the corresponding Si II intensity and velocity line drawings. As before we see excellent agreement in the intensity correlation in all the orbits, but the velocities show little correlation.

the same relative magnitude of the flow. There are, however, many points of discrepancy. While these observations may tend to indicate that vertical motions associated with supergranulation are present in the chromosphere, the exact overlap in the motion fields cannot be well demonstrated. Further satellite observations with increased spatial resolution and lower noise are required.

4.5 Conclusion

Our observations made with the OSO 8 satellite lack the spatial resolution and areal coverage of the SPO data. The higher resolution observations in both the raster-mode and point-mode (about 4" x 20") show velocity variations on a scale of 10" with an rms amplitude of about 650 ms^{-1}. Lower resolution OSO 8 observations or data obtained by spatially averaging the higher resolution observations, show a good correlation between the Si II chromospheric network and sites of material downflow. This correlation is best seen with about 20" averaging and indicates that lesser amplitude motions are present in the chromosphere that are associated with the chromospheric network. Our measurements indicate that in the chromosphere there is also a 10" scale of motion

superposed upon the lesser amplitude supergranular scale of motion.

We have no doubt that the instruments were co-pointed accurately as there is good agreement between the OSO 8 satellite Si II and SPO ground-based Ca II intensity measurements. The velocites, however, do not show a convincing correlation. This work is greatly limited by the considerable noise and the low spatial resolution in the OSO 8 observations. This important comparison can only be made with higher-resolution ultraviolet observations.

CHAPTER 5

THE PENETRATION PROPERTIES OF THE MOTIONS

5.1 Introduction

Our observations of steady motions span the range of heights from the lower photosphere to the middle chromosphere. Here we address the following issues: What kinetic energy flux is present in these flows and what role may these motions play in the generation of acoustic and gravity waves, and in the contribution to chromospheric heating? This problem is discussed in section 5.2. What are we able to infer about the solar envelope structure by comparing our observations to solar convection models? We consider this issue in section 5.3.

Our observations indicate the existence of a scale of steady motion between the granulation and the supergranulation which we call mesogranulation. We detect mesogranules in our SPO diode array measurements at disk center. They have rms amplitudes of roughly 50 ms^{-1} and range in size from 6" to 12". Previous measurements of the vertical steady flows have apparently been unable to adequately reduce the granulation and oscillatory noise in order to discern the mesogranules. Our vertical

velocity measurements made in Mg I λ5173 most readily show this component since this line is formed at a height in the atmosphere where the granulation amplitude is negligable.

Mesogranules have not been detected at large radius vector where the motion field is apparently dominated by the supergranulation. The horizontal component of the velocity in the convective cells is proportional to the scale of convection and to the rate of decrease of the vertical component with height, as discussed in Appendix B. On the basis of its larger size we expect supergranulation to show a more pronounced horizontal component. A more extensive investigation of the structure in the horizontal motion field is required to ascertain the braking properties of the mesogranulation and supergranulation independently. Further ground-based observations with longer time averages, higher spatial resolution, and more extensive data analysis of the $R_V = 0.8$ observations are required to resolve this issue.

Mesogranulation may be convective in origin, and if so this indicates that there are three discrete scales of convective motion in the sun suggesting that these scales arise at the distinct depths at which H I, He I, and He II are ionized. For the most part, models for the solar convection zone have been based upon mixing-length analysis which is unable to make any estimate for

preferred scales of motion. Some procedures (Hart 1973, Bogart 1979, and Bohm 1979) have tried to match the mixing-length heat transport by defining the convection dynamics in terms of the eigensolutions that come from linear theory. This type of procedure is rather ad-hoc and physically questionable. A reasonably successful treatment of this sort by Bogart does indicate that three distinct scales of motion arise like the granulation, mesogranulation, and supergranulation. Non-linear convection models for A-type stars that use the anelastic-modal equations (Toomre et.al. 1976, Zahn et.al. 1979) indicate greatest convective instability in each of the ionization zones. The Rayleigh number, which may be thought of as the undimensional temperature gradient, is greatly enhanced in each of these zones. Although more detailed physical descriptions of the solar convection zone have proven difficult, a similar sort of behavior is most likely.

5.2 Effects on the Solar Atmosphere

a) Height Variation of the Convective Flows

Our observations indicate that supergranular scale steady flows are present in the chromosphere with substantial vertical and horizontal components. The smaller

scale mesogranules, present in the photosphere, cannot be specifically correlated with flows in the middle chromosphere, but a similar scale of motion does appear to be present at the greater height. The amplitude of these flows changes two orders of magnitude with height. Here we summarize our results for the vertical and horizontal components of mass flux $\rho w(z)$ and $\rho u(z)$ and estimate the kinetic energy flux $K(z)$ present in this flow using methods described in Appendix B. These are the quantities particularly relevant in trying to understand the role of the steady flows in the solar atmosphere. Unfortunately, we are unable to explicitly separate the mesogranular and supergranular components, and so most of our present analysis will pertain to their combined effect.

The observations consist of the rms velocity seen at disk center V(0.0), and at radius vector 0.8 V(0.8) for each of the spectral lines considered. These rms velocities V(0.0) and V(0.8) must be: 1) corrected for noise in the measurement, and 2) adjusted because of the different instrumental resolutions. The spectral line, the line profile sampling function, and the position on the disk where the measurements were obtained determine the height from which this velocity signal originates. This result can be translated into vertical and horizon-

tal components $w_{rms}(z)$ and $u_{rms}(z)$.

i) heights of formation of the spectral lines

There is considerable uncertainty as to the height at which some of the spectral lines are formed. The height of formation as defined by the response function for the line (Beckers and Milkey 1975) is considered the closest approximation to the place where the measured velocity originates. Altrock et.al. (1975) perform calculations for a number of nonmagnetic lines formed in the photosphere. The spectral lines Fe I λ5576 and Fe I 5434 used in our SPO observations are from this list. Since we also know the placement of the detectors in the line profile for our diode setup, we are able to determine the heights of formation of these lines fairly accurately.

Athay and Canfield (1969) and Altrock and Canfield (1974) calculate the source function for Mg I λ5173 which best reproduces the observed profile on the quiet Sun. We estimate the line center opacity τ_0 that corresponds to $\tau = 1$ in that portion of the line and at that radius vector where our observations are made. Altrock et.al. (1975) point out that for chromospheric lines the response function for velocities is approximately the intensity source function and $\tau = 1$ is about the height of greatest contribution. Our measuring window is centered at $\Delta\lambda = 0.05$Å from line center. This corresponds

to 0.80 line center depth at disk center and to 0.85 line center depth at R_V= 0.8. The optical depths at line center for τ = 1 in this part of the line and radius vector are roughly τ_0= 1.25 at R_V= 0.0 and τ_0= 0.71 at R_V= 0.8. These correspond to continuum optical depths of $\log(\tau_{5000})$= -4.65 and $\log(\tau_{5000})$= -4.89. Using the Harvard Smithsonian Reference Atmosphere (HSRA Gingerich et al. 1971) we find that these optical depths for the Mg I line are equivalent to z= 580 km at R_V= 0.0 and z= 785 km at R_V= 0.8.

Calculations for the source function in the Si II 1817 line have carried out by Finn and McAllister (1978) and by Tripp, Athay, and Peterson (1978). We estimate the height of formation for this line much as Mg I. Our observations were made with the detector placed at $\Delta\lambda$ = 0.04 Å which corresponds to approximately 80% line center intensity at both R_V= 0.0 and R_V= 0.8. Optical depth τ = 1 corresponds to line center τ_0= 1.25 at R_V= 0.0 and τ_0= 0.75 at R_V= 0.8. This maps into heights z= 1360 km at R_V= 0.0 and z= 1600 km at R_V= 0.8 for Si II in the model of Tripp et.al.

ii) the change in velocity with height

Table 5.1 summarizes the results of our observing program. The rms velocities given here represent the average of the available measurements. The photospheric velocity measurements at disk center have a large noise

Table 5.1

R_V= 0.0

wavelength	time	slit	height	V	Vn	V1	V2
Fe I 5576	30 m	3"x3"	200 km	68 m/s	60 m/s	30 m/s	19 m/s
Fe I 5434	60 m	3"x3"	250 km	45 m/s	37 m/s	26 m/s	16 m/s
Mg I 5173	60 m	3"x3"	580 km	50 m/s	3 m/s	49 m/s	30 m/s
Si II 1817	60 m	2"x20"	1360 km	639 m/s	200 m/s	607 m/s	607 m/s

R_V= 0.8

wavelength	time	slit	height	V	Vn	V1	V2
Fe I 5576	30 m	1"x1"	270 km	145 m/s	-	145 m/s	106 m/s
Fe I 5434	30 m	1"x1"	300 km	102 m/s	-	102 m/s	75 m/s
Mg I 5173	30 m	1"x1"	785 km	124 m/s	-	124 m/s	91 m/s
Si II 1817	60 m	2"x20"	1600 km	611 m/s	200 m/s	577 m/s	577 m/s

rms due to granulation, the amplitude of which we estimate using the result of Keil and Canfield (1979) summarized in Figure 1.4. The granulation residual that survives is given for the height of formation of the line reduced by the spatial and time averaging of the observations. We estimate this residual assuming that granules appear randomly on a scale (half wavelength) of 0.6" and survive 8 minutes, as discussed in Chapter 1. Noise in the horizontal component as seen in the Fe I data is negligable since the amplitude of the motion is so much larger there. In the Si II measurements, the noise is primarily due to instrumental errors, with an amplitude determined by the shot noise discussed in Chapter 2. We correct V(0.0) and V(0.8) for noise using the relation:

$$V_1^2(R_V) = V^2(R_V) - V_n^2 \quad . \tag{5.1}$$

This relation assumes statistical independence between the noise and the steady velocities. Table 5.1 lists the estimated noise V_n and the corrected $V_1(R_V)$ for each spectral line.

Due to the disparate spatial resolutions in the two instruments and in the modes of observation used, a correction must be applied to $V_1(0.0)$ and $V_1(0.8)$ before we are able to compare the velocity measurements. With decreased spatial resolution and increased observing window size r, $V_1(R_V)$ will decrease in amplitude in a way

which reflects properties of the unresolved velocity field. To determine the variation of $V_1(R_V)$ with r we have spatially averaged the SPO 1" x 1" resolution velocity measurements using the running mean of size r x r. For this we use the velocity measurements in Mg I λ 5173 from a 60 minute time average at disk center (R_V= 0.0 on day 8164) and a 60 minute average at R_V= 0.8 (day 8166). The Mg I measurements are most suitable for this since they show very little granulation noise. Figure 5.1 shows the resulting $V_1(0.0)$ and $V_1(0.8)$ as they vary with spatial resolution r. The OSO 8 observations discussed here were made using the rectangular 2" x 20" slit, so Figure 5.1 also shows the rms at the two radius vectors corresponding to this spatial averaging. For $V_1(0.8)$ at 2" x 20" the slit was aligned parallel to the limb as was the case in all our OSO 8 point-mode observations.

In Figure 5.1 $V_1(0.0)$ drops more rapidly than $V_1(0.8)$ for small r indicating that smaller scales are associated with the vertical motions. This is probably the result of mesogranulation. For comparison of these disparate scales of resolution used we extrapolate each rms velocity determination to a common 2" x 20" resolution: this defines $V_2(R_V)$.

The rms velocities $V_2(0.0)$ and $V_2(0.8)$ are shown in Figure 5.2 as a function of height z. These measurements are corrected for noise and extrapolated to the common

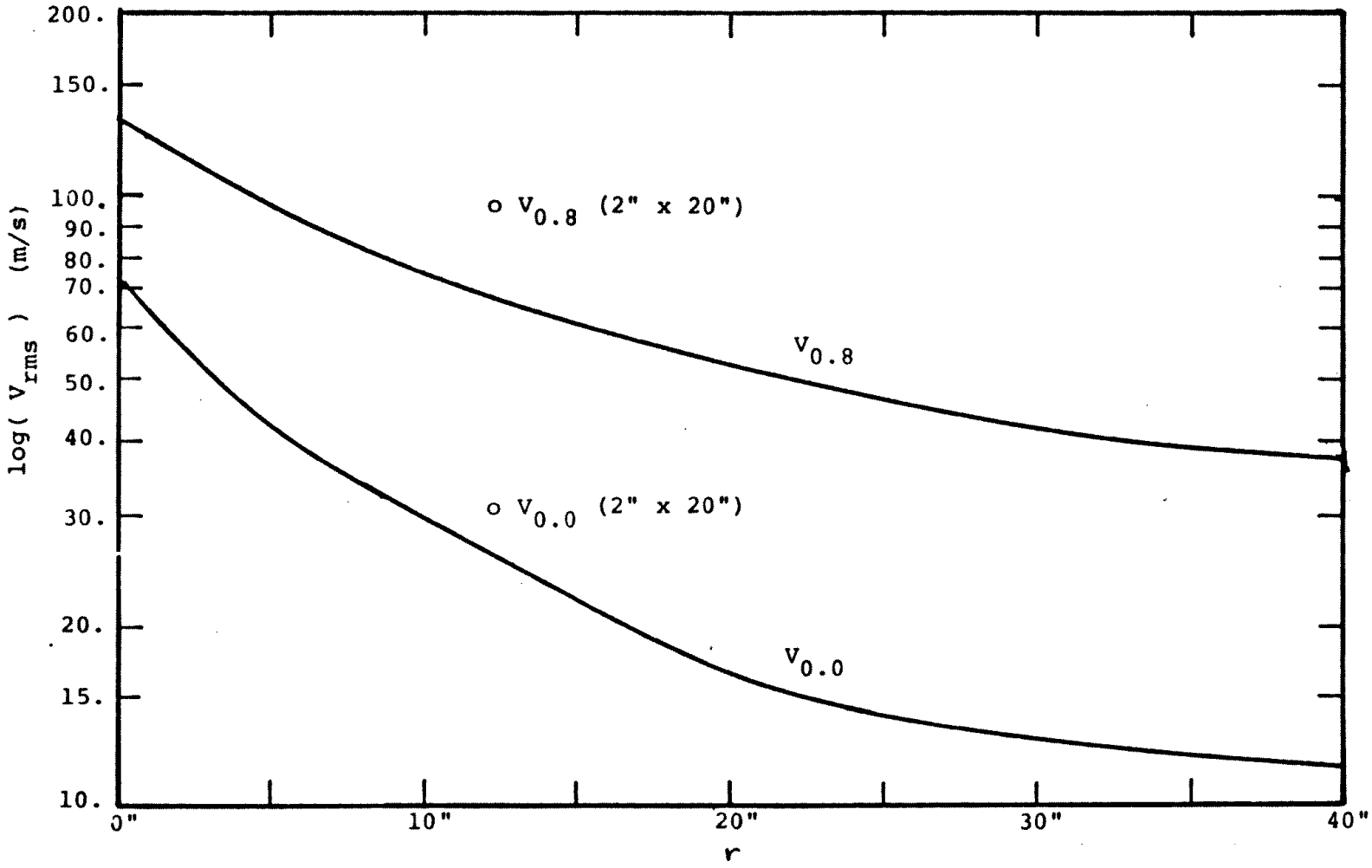

Figure 5.1

Effect of decreased resolution on the velocity rms. We spatially average 60 minute velocity observations in Mg I at disk center (day 8164) and at radius vector 0.8 (day 8166) to understand what effect varying the instrumental resolution may have on the velocity rms. The Mg I data shows mainly the mesogranulation and supergranulation and little noise and is most representative of the spatial structure we find in the velocities throughout the atmosphere. With increased spatial averaging box r x r, the vertical rms decreases more rapidly indicating the presence of the smaller scale mesogranulation. The two points (O) show the vertical and horizontal rms with 2" x 20" spatial averaging of the data.

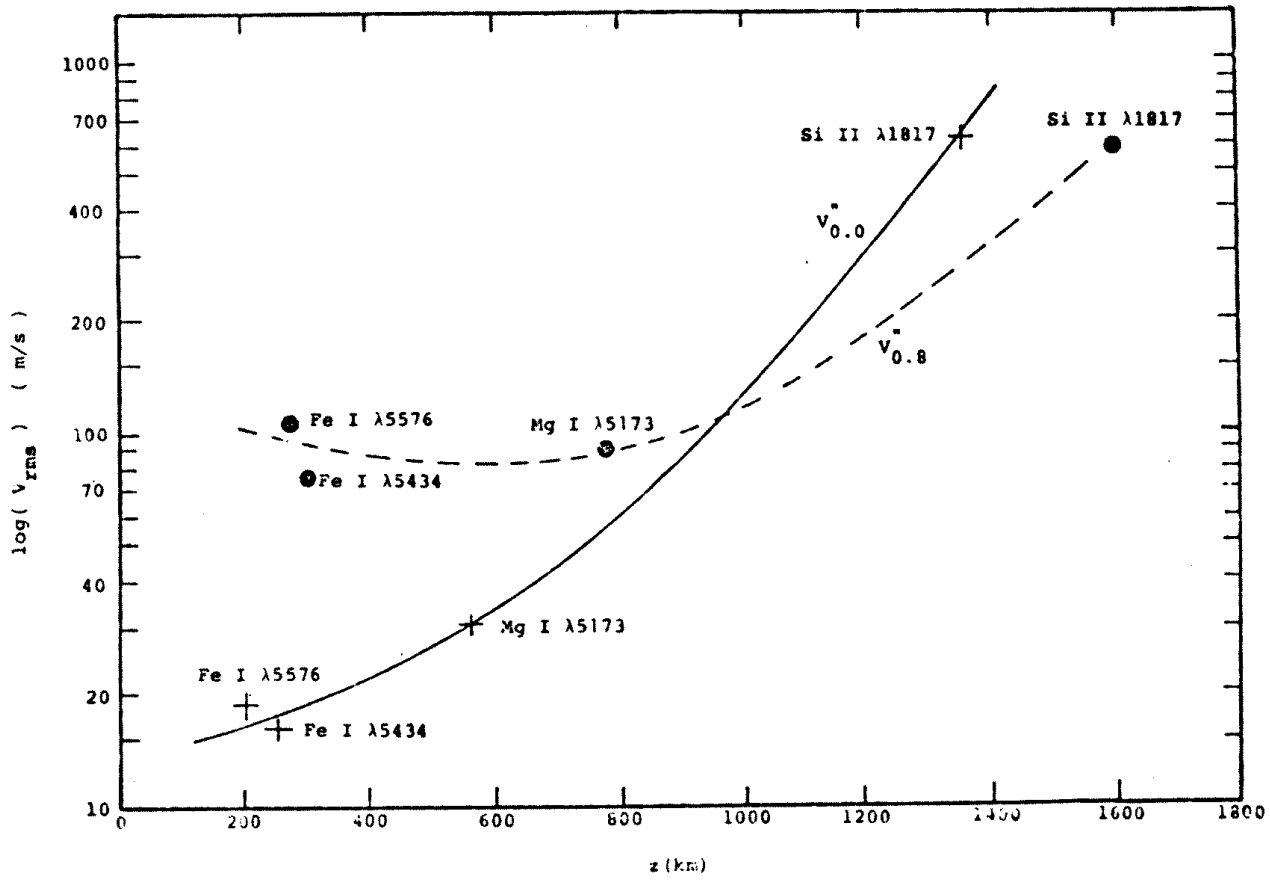

Figure 5.2

Height variation of the vertical and horizontal components The rms velocities measured in each spectral line have been corrected for noise and interpolated to the common 2" x 20" spatial resolution using Figure 5.1. The resulting velocity rms should be due primarily to the mesogranular and supergranular flows. The points (+) locate our four measurements of the vertical velocity rms which we see steadily increases throughout the atmosphere. The points (.) similarly locate the horizontal rms measurements. This component, which is denoted by the dashed line, remains fairly constant or decreases slightly below the temperature minimum and then increases with height in the chromosphere. Low in the atmosphere the two flow components differ by nearly an order of magnitude with the horizontal the dominant, but with increased height they become comparable with the vertical slightly larger.

instrumental resolution of 2" x 20". There is some uncertainty in the estimated vertical velocities for Fe I λ5576 and Fe I λ5434 since the largest component in this data is due to granulation noise. These velocities, however, are certainly less than that measured for Mg I λ5173. Also, there is some uncertainty in the estimated heights of formation of Mg I λ5173 and Si II λ1817. This may be as large as ±150 km on the basis of other studies for Mg I (Chipman 1978) and as evidenced by the lack of agreement between the actual and the modeled Si II line profile (Tripp et.al. 1978). These uncertainties, however, do not strongly affect our estimates for the kinetic energy flux K(z) as a function of height in the atmosphere z. The velocity of the flow at a given height that we interpolate between our measurements will change by less than a factor of two with these errors in the determined spectral line formation heights, which translates into half an order of magnitude in the determination of K(z).

In Figure 5.2 the vertical velocity rms shows a monotonic increase with height in the atmosphere. The horizontal velocity rms may actually decrease with height between the low photosphere and temperature minimum, as is also suggested in the observations of Deubner (1971), although above the temperature minimum this component rapidly increases with height. The mass flux of the flow

for both flow fields still decreases with z at all heights because of the rapid decrease of density that occurs with height.

iii) comparing the horizontal and vertical components

One of the properties of a cellular flow field that conserves mass is that the amplitude of the horizontal momentum is proportional to the rate of decrease of the vertical momentum with height and proportional to the cell radius. This is easily visualized in that a column of vertical upflow having a decreasing amplitude with height must turn the flow in the only direction available to it, the horizontal. The average horizontal flow amplitude at some radius in the cell is the surface integral of the derivative of the vertical momentum with height carried out over the cell interior area.

Our observations sample both the horizontal and vertical components in the supergranular and mesogranular flows. Unfortunately, the heights at which we sample the two flow components are quite different due to the increased path length that occurs at the large radius vector. Interpolation between heights is possible but this assumes that the flows are physically connected between the two heights. In addition this procedure will be quite sensitive to the fact that the velocity may be changing quite rapidly with height, so that a small error in determination of the formation height can lead to a

large error in the velocity determination.

For the idealized hexagonal planform function we have:

$$u_{rms} = \frac{\sqrt{2}}{a} \frac{w_{rms}}{h} , \qquad (5.2)$$

where h is the scale height for momentum decrease and a is the horizontal wavenumber of the planform function (see Appendix B). The cell wavenumber $a \sim \pi/d$, where d is the apparent cell diameter.

The vertical flows that are represented in Figure 5.2 show a mixture of mesogranulation and supergranulation and so we are only able to estimate the vertical scale heights and horizontal amplitudes of both motion fields separately. The largest component in the vertical motion field below z= 800 km is due to mesogranulation. Supergranular flows show approximately half this amplitude throughout this region as evidenced in our Fe I and Mg I disk center observations. Above this level we are unable to resolve the two components and the mixture in the vertical flow remains uncertain. Our SPO R_V= 0.8 observations show mainly the 32,000 km scale of motion and no apparent mesogranular component. Above z= 800 km the horizontal flows are similar and show a direct correlation with the underlying motion field, so that the horizontal flow amplitude there must be due to supergranulation.

At z= 300 km the scale height for vertical velocity decrease is h_v= 590 km which must be roughly the same for both the mesogranulation and supergranulation, since we see both scales of motion in our Fe I and Mg I measurements. At this height the density scale height is h_ρ= 110 km from Figure 5.3 which shows the density in the HSRA (Gingerich et.al. 1971). The combined scale height for mass flux decrease is h= 135 km. Supergranulation shows roughly w_{rms}= $V_2(0.0)$= 10 ms^{-1} and u_{rms}~ $V_2(0.8)$= 100 ms^{-1} at this height. We estimate a horizontal rms of about 1000 ms^{-1} from the relation (5.2), using the horizontal scale of 32,000 km. At this height, the mesogranular vertical component is w_{rms}= 18 ms^{-1}. With a horizontal scale of 7000 km and h= 135 km, we predict u_{rms}= 400 ms^{-1}.

Our estimates for the horizontal flow amplitudes are much larger than those that could be present. For the supergranular horizontal flows it is about a factor of ten too large. Also the mesogranule cells certainly could not have a horizontal flow amplitude of 400 ms^{-1} since these motions are masked by the 100 ms^{-1} supergranular flows. It is puzzling that in the lower atmosphere the horizontal flow amplitude for both mesogranulation and supergranulation is much less than our estimate which is based simply upon these continuity arguments. At this level in the atmosphere there is good

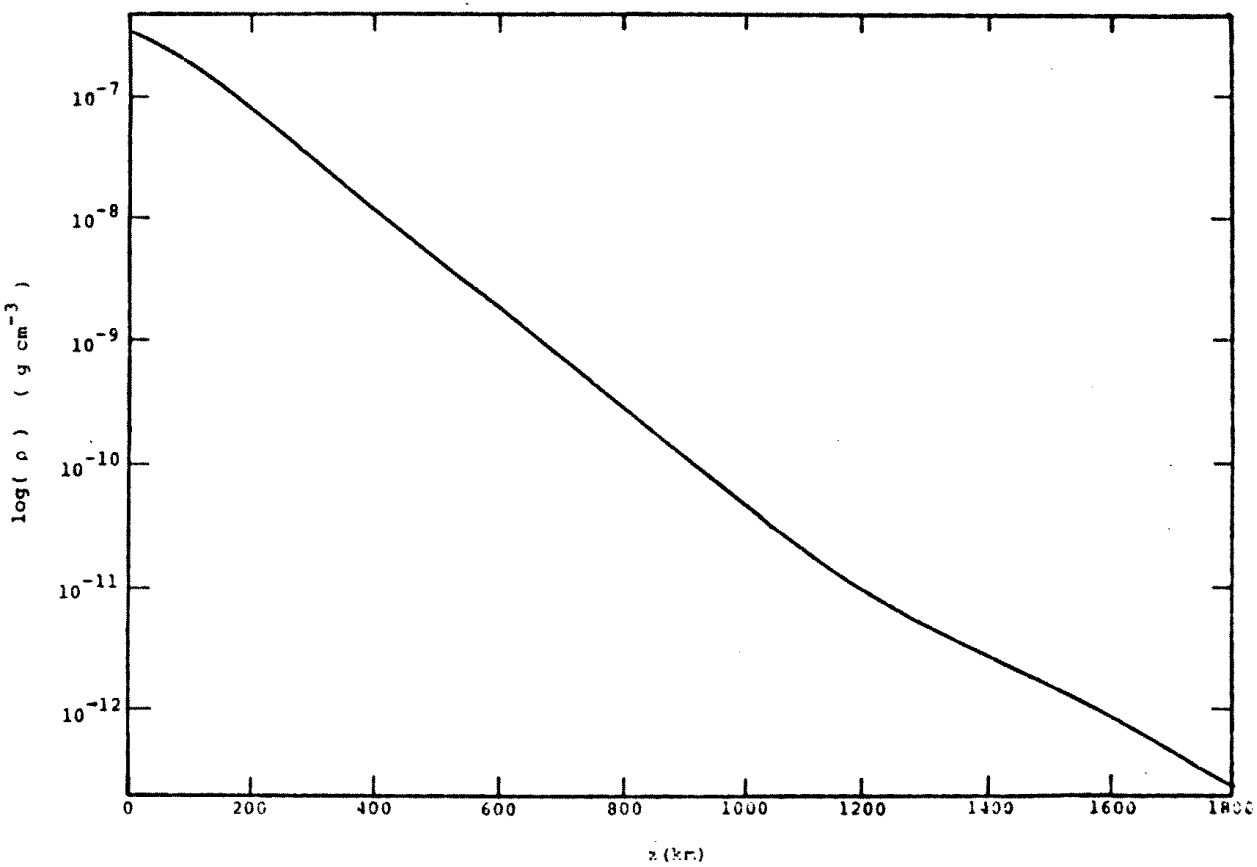

Figure 5.3

Density variation with height $\rho(z)$. This curve shows the mean solar density ρ as a function of atmospheric height z above $\tau_{5000} = 1$ from the HSRA solar model (Gingerich et.al. 1971). The density scale height remains fairly constant from the low photosphere (z= 0) to the middle chromosphere (z= 1400 km) and e folds with a scale of h_ρ = 110 km.

reason to expect continuity in the flows since we recognize the same flows at several heights in the region. Thus interpolation in height is probably a sound procedure. Difficulty may arise if the planform function is not hexagonal. If, for example, a cell consists of a few restricted sites of material upflow than the horizontal flow will not be proportional to the cell size but rather to the number of sites of upflow.

At z~ 950 km the horizontal and vertical flow components become comparable so that $u_{rms} = w_{rms}$ as indicated in Figure 5.2. Using a mean cell size of d= 7000 km, isotropy in the flow field indicates that h= 3200 km >> h_ρ, and we estimate the vertical flow amplitude to increase with a scale height of h_v= 110 km ~ h_ρ. We measure a scale height for velocity decrease of h_v= 240 km from Figure 5.2 in this region but there is large uncertainty in this value since it falls midway between the largely separated heights of formation for Mg I and Si II. It is possible that the scale height for velocity increase may be as small as 110 km in this region, consistent with our estimate.

In a qualitative sense the scale height for velocity increase must be almost as small as the scale height for density decrease for z> 1200 km, based upon our observation of the relatively small horizontal flows in this region. Extrapolating this behavior from the

chromosphere, we expect that these motions must penetrate into the transition zone with ever increasing velocity.

iv) the kinetic energy flux

The kinetic energy flux K present in this flow is determined from the horizontal and vertical flow components as in Appendix B,

$$K = \sqrt{\frac{2}{3}}\,\rho\, w_{rms}\, u_{rms}^2 + \sqrt{\frac{2}{3}}\,\rho\, w_{rms}^3 \quad . \tag{5.3}$$

In this we do not distinguish the mesogranulation and supergranulation; K is independent of the cell size and only weakly reflects the cell planform function. We correct our observations to perfect instrumental resolution from the present 2" x 20" using Figure 5.1. This assumes that the substructure of the flow field seen in Si II in the vertical is like what we see in the photosphere. Figure 5.4 shows a continuous function K(z), which is found by interpolating between the actual velocity measurements shown in Figure 5.1. This curve is essentially determined by three independent velocity measurements taken from the photospheric Fe I lines, the low chromospheric Mg I line, and the middle chromospheric Si II line. The flux K(z) shows a rapid decrease throughout the photosphere and is approximately constant in the chromosphere. The relatively large horizontal flow in the photosphere indicates that a great deal of braking of the motion is occurring. In the chromosphere

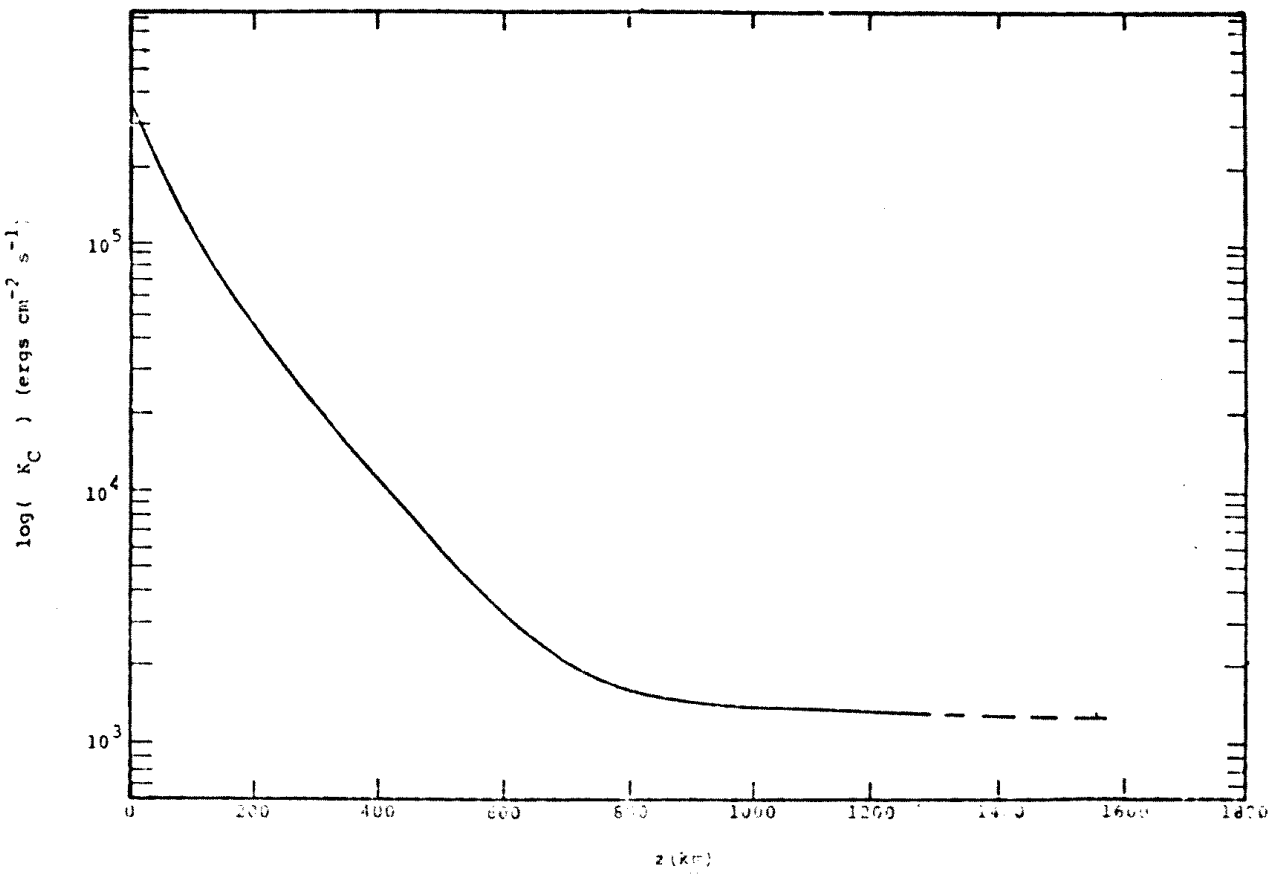

Figure 5.4

Kinetic energy flux K(z). The kinetic energy flux is determined from the vertical and horizontal velocity rms's from Figure 5.2, extrapolated to perfect spatial resolution (r= 0") using Figure 5.1. The continuous curve results because we use the curves drawn through the data points in Figure 5.2. Essentially K(z) is determined from independent observations of the vertical and horizontal flows at three levels in the atmosphere: in the low photosphere with Fe I λ5576 and Fe I λ5434, at the temperature minimum (z= 500 km) with Mg I λ5173, and in the middle chromosphere (z= 1400 km) with Si II λ1817. The rapid decrease in K(z) low in the atmosphere and its constancy at height reflects the tendency for the flows to become isotropic with increasing height.

the horizontal and vertical components are comparable and increasing with height. Little decrease in the vertical mass flux is occurring and the upward energy flux K is nearly constant.

b) Chromospheric Heating

In the low photosphere the Doppler velocity is observed to increase by a factor of at least 5 from disk center to the limb, indicating that the motions are predominately horizontal. Near the temperature minimum, however, the steady velocities measured in Mg I show little center-to-limb variation, suggesting that here the horizontal and vertical components of the the motion have comparable amplitudes. Our OSO 8 results now show that this tendency toward isotropy is accentuated higher in the atmosphere: At disk center the dynamic range is about 3000 ms^{-1} in the vertical, comparable with the horizontal component. This implies that substantial braking occurs in the photosphere, but much less occurs near the temperature minimum and in the chromosphere. We expect that motions penetrating into a very stable, stratified atmosphere may exhibit the large braking that occurs in the photosphere. It comes as a real surprise that this does not seem to be the case at higher levels in the atmosphere.

The extensive penetration of supergranulation into

the atmosphere raises the possibility that these motions have associated with them a kinetic energy flux that could help to resolve some of the dilemmas of chromospheric heating. Our estimate for the height variation of this flux K(z) is shown in Figure 5.4. The kinetic energy flux is approximately 10^5 ergs cm^{-2} s^{-1} in the low photosphere and 10^3 ergs cm^{-2} s^{-1} in the middle chromosphere. Chromospheric radiative losses appear to require a flux of order 4×10^6 ergs cm^{-2} s^{-1} (Athay 1976, p. 423), which cannot be explicitly satisfied by these supergranular scale motions even at the 200 km level. But such a flux is probably present somewhat deeper in the photosphere or below. The apparent decrease in mechanical flux with height must be accounted for by the production of turbulence and internal gravity waves. These motion fields couple well to convective flows so they are the likely channels for the required dissipation. We expect that these small scales of motion can be produced from dynamical instabilities of the strong horizontal shear layers present in the supergranular motions in the photosphere. The production of internal gravity waves at heights of 300 km and upward is especially interesting, for at these heights such waves would not be dissipated by the cooling effects of the H^- ion lower in the photosphere. Our estimates for internal gravity wave fluxes are very uncertain. However, the production of

these waves by shear instabilities is probable, and their flux should bear some relation to the rapid decrease of the mechanical flux with height in supergranular flows. The possibility thus exists that internal gravity waves produced by mesogranular and supergranular motions can lead to a nonnegligible flux of mechanical waves into the upper atmosphere.

At the 200 km level, the mechanical flux attributable to the velocity fields of granulation and the five-minute oscillations is estimated to be at least an order of magnitude greater than that reported here for the mesogranulation and supergranulation, and thus approaches the value required for chromospheric heating. However, major difficulties are encountered in trying to explain how such a mechanical flux gets to the required heights in the chromosphere. Gravity waves influenced by magnetic fields, however, may be capable of reaching these heights (Stein 1979). Their presence in the atmosphere has not been confirmed but there are basic difficulties in making these measurements. Gravity waves will not simply produce line shifts, but the pressure and velocity fluctuations in the wave conspire to produce an apparent line broadening (Mihalas 1979). The anomalous line broadening called microturbulence may indicate the presence of gravity waves.

5.3 Comparison to Solar Envelope Models

Although our observations offer only a sparse sampling of the height variation of mesogranular and supergranular motions, they do place certain quite strong constraints on theories for penetrative convection in the Sun. First they show the existence of three discrete scales of steady motion which may be convective in origin. Second, the mesogranulation and the supergranulation show very pronounced vertical braking low in the atmosphere and probably even more so in the underlying hydrogen ionization zone. If the latter were not true then it would be difficult to account for the small vertical velocities observed in the photosphere given any reasonable estimate of the mass flux in these cellular flows deeper in the convection zone. Third, these observations show that above the temperature minimum the vertical and horizontal motions in these large scale convective flows become comparable in amplitude, indicating that very much less braking is occurring at these higher levels. This is a surprising property of the motion field, and one that we cannot understand on the basis of convective penetration experiments or theory. Apparently these motions feel very strong braking in the hydrogen ionization zone which is convectively unstable, and less

in the stably stratified solar atmosphere!

The descriptions of convection which provide some estimates for the penetration properties of the motions come from a) the mixing-length theory, b) ice-water convection experiments, c) linear convection theory, and d) non-linear computation models based upon the anelastic modal equations. In this section we consider each of these examples and its relation to our observations.

Mixing-length analysis is probably limited to stellar interior calculations since it is unable to predict a motion field that conserves mass. This description is based upon scaling arguments and lacks certain of the main features we associate with convective processes, such as any reference to the horizontal scale of motion or to the penetration of flows into the stable regions which bound the convection zone. Mixing-length analysis is successful in stellar interior models because it is able to accurately determine the temperature structure throughout most of the unstable zone. There has been some attempt to introduce a preference mechanism for the scale of motion but these have been rather ad hoc. With some variations, this description is able to predict properties of the penetrating motions. We describe the mixing-length theory as a basis for other models as it does provide at least some semblance of a physical description of convection.

Ice-water experiments provide an interesting analogy for the Sun since these examine properties of a stably stratified fluid that lies immediately above a convectively unstable zone. Some of the properties observed in these systems can be compared with our observations. This comparison is qualitative and must be reviewed in light of the enormous difference between the two systems - stars show an enormous variation of conditions through the convection and penetration zones.

Fluid theories based upon the equations of motion are able to model the motion field in a physically consistent manner. The linear solution, however, is only generally applicable to systems near the onset of convection. Even though a system like the Sun is highly unstable, many of the properties of its motion field may be recognized in the linear example. The linear solution predicts the relative scale heights for velocity penetration and this we compare to the observations of granulation, mesogranulation, and supergranulation.

Recently non-linear theoretical models have become available using the anelastic modal equations, and these appear to be successful in describing convection in some stellar systems (Latour et.al. 1976). The anelastic approximation says that the heat transported by acoustic waves is negligible and time derivatives of density fluctuations in the continuity equation can be ignored. The

modal approximation assumes that only certain horizontal planform functions are available to describe the variation of the motions across a cell. The planform function that is realized is some linear combination of the original orthogonal set. We discuss some calculations of this sort for an A-type star (Toomre et.al. 1976). The A-type star is more tractable than the Sun since its mean structure is not highly modified by the non-linear processes. Although these studies do not model the meso-granulation and supergranulation in the Sun, we expect that the results may provide some intuition about the flows there, since the essential properties of the convection zones are the same - showing a large variation in conditions from bottom to top.

a) Mixing-Length Formalism

The earliest models for stellar interiors were by Robert Emden (1907). He assumed that convection was the sole mechanism which brings the energy that is produced in the deep interior to the surface. Based on this hypothesis he constructed his famous family of polytropic models. Schwarzschild (1906), however, finding that radiation is also an extremely efficient mechanism for carrying energy, developed the concept of radiative equilibrium and applied it to the atmospheric layers of the Sun. Schwarzschild also developed the general

criterion by which we can decide whether a layer in a star is in a convective state or in a radiative state.

Twenty years later Eddington (1926) applied the condition of radiative equilibrium in every star from the center to the surface, with no convection whatsoever in his treatment. Albrecht Unsöld (1930) showed that there must exist a zone of convective instability directly beneath the visible photospheric layer as a consequence of hydrogen ionization. Siedentopf (1932,1933,1935) described the granulation as the surface manifestation of those convective motions. Biermann (1932) introduced the mixing-length formalism as a description of stellar convection. He discovered that in some types of stars an appreciable portion of the envelope may be in convective equilibrium.

Mixing-length theory is the most familiar description of convection, and since it provides a framework we include some discussion of it here. If a region is convectively unstable then when a fluid parcel is displaced upward it finds itself buoyantly forced further upward. If a gas parcel is displaced upward a small amount Δr this will result in its adiabatic expansion and cause a temperature reduction $(dT/dr|_{ad})\ \Delta r$. If the temperature of the local medium cools more rapidly with height, then the parcel will find itself warmer than its surroundings by an amount $(dT/dr|_{ad} - dT/dr)\ \Delta r$, and consequently

feel buoyant (Schwarzschild 1958, Cox and Giuli 1968).

The heat flux H_C carried by this parcel is written in terms of its ascending velocity w:

$$H_C = \int_0^r c_p \rho w \left(\left.\frac{\partial T}{\partial r}\right|_{ad} - \frac{\partial T}{\partial r} \right) \partial r \quad , \tag{5.4}$$

where c_p is the gas specific heat, and ρ the gas density. The integral is taken over the path of travel for the parcel from the point of initial displacement r= 0 to the dissolvement r. From the first law of thermodynamics we write the adiabatic temperature gradient $dT/dr|_{ad}$ for a perfect gas in terms of the local pressure gradient dP/dr:

$$\left.\frac{\partial T}{\partial r}\right|_{ad} = \left(1 - \frac{1}{\gamma}\right) \frac{T}{P} \frac{\partial p}{\partial r} \quad , \tag{5.5}$$

where γ is the ratio of specific heats for the gas.

We estimate the velocity w of the accelerating gas parcel by balancing its kinetic energy with the buoyant potential energy.

$$\frac{1}{2} \rho w^2 = \int_0^r g(r') \int_0^{r'} \left(\left.\frac{\partial \rho}{\partial r'}\right|_{ad} - \frac{\partial \rho}{\partial r} \right) \partial r' \partial r \tag{5.6}$$

The integrals are taken over the parcel's path of acceleration from the point of initial displacement r= 0, and g(r) is the force of gravity. The first integration gives the density excess as a function of r and the second integration is over the upward buoyancy force. This equation assumes that the only force which affects

the fluid parcel is buoyancy, and that the velocity fluctuations are local, that is unable to feed back on the overall dynamics of the fluid.

The mixing-length assumption is that there exists a scale ℓ in the motion over which a parcel retains its identity, i.e. its thermal excess. Half the mixing length $\ell/2$ is taken as the average length scale for survival of a gas parcel. Thus this becomes the upper limit of the integrals in our estimate of the flux H_C and the velocity w. Further, if we assume that conditions in the medium do not change significantly over $\ell/2$ we arrive at an estimate for H_C and w in terms of the mixing length.

$$w = \frac{\ell}{2} \left(\frac{g}{T}\right)^{\frac{1}{2}} \left(\left.\frac{\partial T}{\partial r}\right|_{ad} - \frac{\partial T}{\partial r}\right)^{\frac{1}{2}}$$

$$H_C = c_p \rho \left(\frac{g}{T}\right)^{\frac{1}{2}} \left(\left.\frac{\partial T}{\partial r}\right|_{ad} - \frac{\partial T}{\partial r}\right)^{3/2} \frac{\ell^2}{4} \quad . \qquad (5.7)$$

In the description given here we have assumed that the fluid parcels rise adiabatically over their travel length ℓ. This is the assumption used in the theory of Böhm Vitense (1958) and represents the limit of efficient convection. Öpik (1950) develops a similar theory but in the limit that convection is inefficient and that the thermal diffusion time is shorter than the parcel travel time. In his theory a radiative heat loss term must be included in equation (5.5) and this changes the definition of the temperature and density excesses which

appear in (5.6) and (5.7).

To these equations we add the energy conservation equation:

$$H = H_C + H_R \ , \tag{5.8}$$

where H is the total heat flux and H_R is the radiative flux. In a star H is a constant outside the nuclear generation region and H_R is defined in terms of the temperature gradient:

$$H_R = -\rho c_p \kappa \frac{\partial T}{\partial r}$$

where

$$K = \frac{16\sigma_b T^3}{3\chi\rho^2 c_p} \ . \tag{5.9}$$

Here χ is the Rosseland mean opacity, and σ_b the Stefan-Boltzman constant. Equations (5.6) through (5.9) are complete and allow us to calculate T(z) given H, an expression for ℓ, and the hydrostatic equilibrium condition. This has been done in many stellar interior calculations (Schwarzschild et.al. 1957, Schwarzschild 1958, Demarque 1960, Baker and Kippenhahn 1962, Hofmeister et.al. 1964, Iben 1963, Henyey et.al. 1965, Cox A.N. et.al. 1966, Cox J.P. et.al. 1966, Mullan 1971)

Gough and Weiss (1976) calibrate the two mixing-length formalisms by evolving models to the present age, fitting the luminosity, radius, and effective temperature of the sun. They show that for a wide range of

compositions (metal abundance from 0.02 to 0.04) and for choices of the mixing-length (1 to 3 density scale heights) the evolved solar models for both formalisms show a single region of convective instability which extends from 150,000 km depth to the surface. Their solar models remain insensitive to large changes in the parameters in both the efficient and inefficient limits for the convection. Throughout most of the convection zone the thermal structure is adiabatic regardless of the model, and variations in the details of the description affect only the boundary regions above and below the zone. The connection between the radiative interior and the convection zone reflects only the gross properties of the zone. Although the mixing-length formalisms disagree in their predictions for the heat flux and the internal velocity structure, they are all still adequate for solar evolution models.

i) the scales of motion

Although no explicit provision for the horizontal scale of motion is included in the mixing-length analysis some workers have attempted to allow for different scales in order to explain the discrete scales that are seen in the Sun. Convection exhibits the property that the horizontal scale of motion is comparable to the vertical scale. In an early mixing-length treatment, Biermann (1932) assumed that ℓ is constant throughout the unstable

zone, and took it to be the size of the granulation. This procedure introduces difficulties deep in the zone where the density scale height is much larger than ℓ and may lead to an unreasonably low estimate for the convective velocity there. In later work Biermann (1943) regards the mixing-length as a scale for turbulent eddies which remains sensitive only to the local conditions and the local density scale height. This type of treatment has been generally adopted in most mixing-length formulations.

A number of early studies investigate the growth of inviscid, adiabatic modes in a polytropic sun (Skumanich 1955) or in the more realistic mixing-length model sun (Böhm 1963). These studies show that the growth rate among modes of a given horizontal wave number is a maximum for the fundamental, the solution which has no nodes in the vertical. The growth rate increases with decreasing horizontal scale which indicates that the smallest scales are preferred. Skumanich suggests that the predominant size might be fixed by radiative conduction.

Several studies (Hart 1973, Bogart 1978, Bohm 1979) explore the solutions from linear analysis using the model sun from mixing-length analysis. The linear problem is an eigenvalue problem with eigenfunctions for the vertical velocity (or vorticity, or mass flux) in depth z, and eigenvalues for their growth rates. Each

eigensolution determines the convective flux variation with height through the zone. Conservation of energy, required by these solutions, may be present in the form of kinetic energy of the motion and not be included in convective flux. In the spirit of mixing-length analysis these studies seek some linear combination of eigensolutions which conserves the total convective plus radiative flux through the zone.

If the set of eigensolutions were complete and orthogonal then a linear combination could be found for which the radial variation of the convective flux matches that of the mixing-length solution. The fundamental eigensolutions for the high horizontal wavenumber solutions have maximum mass flux near the solar surface and form a fairly orthogonal basis set. Only a few eigensolutions exist which have maximum mass flux at deeper levels and these have small horizontal wavenumber. These solutions greatly limit the functional forms for the convective flux that may be fit. This is one reason why this fitting procedure is successful only near the surface of the star.

In these studies the combination of eigensolutions is selected on the basis of some procedure. Hart chooses the amplitudes of the modes by the criterion that the maximum flux carried by a mode not exceed the convective flux calculated from the mixing-length analysis for that

point in the envelope. This in effect normalizes each mode to carry almost a solar luminosity at its maximum. He is unable to find a linear combination which could adequately reproduce the mixing-length convective flux. Bogart adopts the somewhat physical criterion that the maximum vorticity in the mode is proportional to its growth rate. Modes which grow more rapidly may be more likely to overcome the retardation of the flow due to eddy viscosity and these are likely to be the ones which survive. This selects the amplitudes for the eigenmodes so that the convective flux from an adjusted mixing-length model is reasonably reproduced in the outer envelope region of the star. The adjusted mixing-length model allows for variation of the superadiabaticity through the zone, which is essentially equivalent to variation of the mixing length ℓ.

Bogart is able to show that certain linear combinations of modes can adequately match the mixing-length determined convective flux near the top of the zone. He uses different normalization procedures such as the selection of a scaling factor between the maximum vorticity and the growth rate for the mode. One model that shows close approximation to the mixing-length convective flux near the surface of the sun, indicates that two modes carry most of the energy flux; their scales correspond closely to those of the granulation and

mesogranulation. Several models which do better at greater depth indicate that one mode carries most of the energy flux there; this mode corresponds in horizontal scale to the supergranulation. Bogart points out that the very large scale modes, which primarily carry the convective flux very deep in the zone, probably bear little resemblance to the linear eigenmodes he uses; these modes are highly modified by the rotation of the sun. Also, in the very large scale modes the maximum vorticity occurs near the solar surface far removed from the region where the motions carry their convective flux, so it difficult to accurately fit the mixing-length convective flux by applying some constraint to the vorticity of the flow.

It is difficult to understand what scales of convective motion we expect to find in the sun since modeling of these flows is most difficult. This mixing-length procedure for determining the scales of motion adopts a certain ad hoc method for determining the amplitudes of the different linear eigenmodes. Bogart's success in this work implies the existence of three discrete scales of motion corresponding to the granulation, mesogranulation, and supergranulation. The existence of a very large scale of convective motion is also possible but the amplitudes of the large scale modes are not adequately determined in this procedure. These scales arise, no

doubt, because of the change in superadiabaticity that occurs in the three zones of ionization. Much work needs to be done however to clarify this matter.

ii) penetration of the motions

The success of the mixing-length theory in solar model calculations reflects the insensitivity of these models to the convection description. Unfortunately, the choice of description most profoundly affects the predicted motion field and its possible penetration into the atmosphere. Some of the gross features for the convection, its preference for discrete scales of motion, its heat flux, the velocity structure near the boundary of the zone, vary from model to model. The predicted vertical velocity field in the description does not conserve mass and so shows a large and unphysical variation throughout the zone. The greatest inaccuracy seems to be that the dynamics are determined completely on the basis of the local conditions and are not tied to the motions in the rest of the star. The estimates for the velocity are not constrained by the condition of mass continuity. Spiegel (1963) examines this difficulty and presents a different version of the mixing-length theory. He introduces a bubble conservation equation which imposes the constraint that the convecting elements at each depth are generated at a rate q and survive over the mean free path ℓ= the mixing length. This expression resembles the

classical radiative transfer equation and permits a solution for the convective heat flux and upward velocity in terms of the integral of a convecting element "source function" $\mathcal{D}$. $\mathcal{D}$ is a function of q and is evaluated in the limit of a small mixing length ℓ. This heat flux and velocity replace (5.7) and, coupled with the condition of conservation of the total heat flux, determine the temperature gradient in the convection zone.

An interesting consequence of this formulation is that it makes a prediction for the convection at the boundary of the unstable region. This boundary is not sharp as the local mixing-length model suggests but represents a gradual transition between the radiative and convective zones. At the boundary the thermal excess $(dT/dr|_{ad} - dT/dr)$ becomes negative. This results in a complex source function $\mathcal{D}$ whose real part is negative. The convective heat flux and upward velocity that are calculated from this are oscillatory and exponentially decaying through the boundary zone.

A different approach to correct the local approximation has been through the use of an iterative procedure to introduce non-local corrections to the mixing-length calculation. Shaviv and Salpeter (1973, see also Roxburgh 1965) apply this to stellar core convection zones. They formulate the mixing-length equations precisely as we have done here for the efficient limit of convection.

The equations (5.7) and (5.8) provide information for an initial guess to the temperature structure $T_0(r)$. A first correction to $T_0(r)$ is found by solving the integral equations (5.4) and (5.6) for $H_C(r)$ and $w(r)$ and by substituting these into equation (5.8) (with (5.9)). Equation (5.8) is rewritten as a differential equation in $T_1(r)$:

$$\frac{4\sigma_b}{3\chi\rho}\frac{\partial T_1^4}{\partial r} = H_C(r) - H \ . \qquad (5.10)$$

Shaviv and Salpeter find that this method converges rapidly to T(r). Physically this procedure introduces non-local corrections in the calculation of $H_C(r)$, since $H_C(r)$ is calculated by integration over some finite domain. The calculation is not restricted to the unstable region but must extend into the boundary regions above and below. As with Spiegel's non-local treatment, this method provides some estimate for the scale of convective penetration. The authors find a non-negligible overshoot in stellar cores for parameters typical of stars with greater than one solar mass.

Ulrich (1970b,c, 1976) formulates a similar type of non-local theory, but in his model he includes an Eddington approximation to the radiative heat loss and a fluid entrainment term in the energy equation. This form of the theory may better estimate the efficiency of the convection and be suitable for stellar atmosphere

calculations. Ulrich models solar convection around the hydrogen ionization zone and makes a number of interesting predictions: The vertical motions exponentially decay as they pass into the photosphere with a scale height of about 300 km, but the temperature excess abruptly falls to nearly zero at the top of the unstable zone. The rms velocity is predicted to be 1400 m/s at the height τ_{5000}= 0.2. He finds that the interior adiabat is fairly insensitive to the choice of free parameters consistent with the result of Gough and Weiss (1976).

b) Ice-Water Experiments

The convective motions we are able to observe in the solar atmosphere have penetrated from the unstable region below the surface into the stable photosphere. Interpretation drawn from photospheric measurements of the dynamics or temperatures can come from models for an unstable layer of fluid bounded above and below by stable fluid. This is analogous to the classical laboratory experiment for convection in ice water. Water below 4°C has the property that its density increases with decreasing temperature. A tank containing water with increasing temperature from 0°C on the bottom to >>4°C on the top will be convectively unstable below the 4°C level and stable above.

A number of laboratory experiments have been

carried out for convection in ice water (Townsend 1964, 1966, Adrian 1975). As the bottom of the tank is cooled, convective motions begin in the unstable region. The initial temperature gradient is constant through the fluid - the result of thermal conductivity. After the onset of convection the unstable region grows in size, taking over much of the initially stable region. When convection reaches a steady state a large temperature gradient occurs at the bottom and top of the unstable region and is fairly constant in the middle where the convection is most vigorous. Above the convection zone the temperature gradient remains constant. Fluid motions are observed to penetrate vigorously into the stable region and the observations indicate that these produce gravity waves (Townsend 1966).

Musman (1968) and Moore and Weiss (1973) pose the problem as a numerical experiment. They trace the evolution of w, θ, and $\bar{T}$ for various Rayleigh numbers. Many of the solutions reach a steady state of vigorous motion in the unstable region and drive countercells in the stable region and show a residual oscillatory component in the penetration region due to gravity waves. Countercells are driven by viscous interaction between the horizontal motions at the top of the convection cell and stable fluid above. Upflow in the center of the convection cell and outflow at the top can drive a cell with

outflow underneath and upflow along the edges - thus a countercell.

In our observations we directly compare the motion field seen in the photosphere with that in the chromosphere. Thus we are able to distinguish mesogranular or supergranular motions from other sources and look for possible countercells. The horizontal motions, which are primarily supergranular in origin, show the same sign throughout the atmosphere. The observations of vertical motions indicate that the same sign occurs in the mesogranulation and supergranulation from the deep photosphere into the lower chromosphere. Our OSO 8 observations at disk center, which sample these vertical flows in the middle chromosphere, have inadequate spatial resolution to settle this issue, but suggest that the same sign for the motion field is present there.

Countercells are indicated by a change in sign of the vertical flow component with height; the horizontal flow mass flux is proportional to the derivative with height of the vertical mass flux. Our observations indicate that there are no countercells driven in either the mesogranular or the supergranular flows as both show the same vertical flows at all atmospheric heights.

The rapid decrease in the kinetic energy flux $K(z)$ low in the atmosphere (Figure 5.4) may imply a very significant production of gravity waves there. Gravity

waves are difficult to observe directly because of the phasing between the temperature and velocity fluctuations and may be manifest only as a line broadening (Mihalas 1979). The role of large scale convective flows in this process must be clarified.

c) Linear Analysis

The extent to which the fluid motions penetrate into the stable region scales as the stabilizing buoyancy force (or the negative Rayleigh number) $|R|^{-1/6}$, and as the cell wavenumber $a^{-1/3}$ (Latour and Zahn 1978). This can be seen by linearizing the equations of motion and by examining solutions for the motion in the convectively stable region. When the steady state equations of motion are linearized, a sixth order equation in W(z) results, where W(z) is the upward vertical velocity in the cell center.

The equations which describe this motion were first posed by Lord Rayleigh (1916). The equations of conservation of mass, momentum, energy, and an equation of state are written using the Boussinesq approximation. This assumes that variations in density are only significant in the buoyancy term ρg and are ignored everywhere else. The Boussinesq approximation is valid if the vertical extent of the layer is less than a density scale height (Spiegel and Veronis 1960). The equation of state

ignores pressure variation and is accurate for most fluids if the total temperature variation across the layer is small.

It is convenient to introduce some horizontal structure in the representation like by the modal representation and take horizontal averages of the equations (Gough et.al. 1975). The equations are linearized by expanding the variables for the problem in terms of mean and fluctuating parts and by retaining only terms which involve just one fluctuating quantity. This assumes that the fluctuating quantities are small compared to the mean state. The time independent solution is written in terms of W(z), the flow amplitude in the center of the cell.

$$\left(\frac{\partial^2}{\partial z^2} - a^2\right)^3 W(z) = Ra^2 \beta W(z) \quad . \tag{5.11}$$

Here $\beta = d\,\bar{T}/dz$ and is constant in the linear problem. The Rayleigh number R is an undimensional measure of the temperature difference across the layer and corresponds to the amplitude of the destabilizing buoyancy force. The horizontal wavenumber a specifies the scale for the cellular planform.

$$R = \frac{\alpha g \Delta T d^3}{\kappa \nu} \quad . \tag{5.12}$$

Here ΔT is the temperature difference across the layer, g the acceleration of gravity, d the distance across the

layer, $\nu(x,y,z)$ the kinematic viscosity, κ the thermometric conductivity, and α the thermometric expansion coefficient.

Three solutions to (5.11) have a negative real root and can satisfy the boundary condition that W(z) vanish at infinity. All three roots scale as $(R\beta)^{1/6}\, a^{1/3}$ for $|R| >> 0$, implying that the scale height for penetration goes like $(R\beta)^{-1/6}\, a^{-1/3}$.

i) in the Sun

The possibility that convection in the Sun exhibits this property of the linear solutions is intriguing. The solar penetration, however, may be considerably different from the prediction of a linear theory applicable to laboratory-like conditions. In a star properties of the fluid, such as its specific heat, density, and opacity change greatly with height. Further, the measure of instability, the Rayleigh number, is large and the convection is quite beyond the linear regime. Most significantly, the atmosphere of the star is optically thin, and the temperature contrast across a cell may readily leak away into space.

The source of braking in the linear system is anti-buoyancy, which is driven by the thermal variation across the cell. In the optically thin stellar atmosphere this force is significantly reduced, and the deceleration of the upward flows must be due to eddy viscosity or

pressure forces. A restoring pressure force can result out of the equation of state, which in a star is non-Boussinesq (Spiegel 1971, 1972).

Our observations of mesogranulation and supergranulation show a scale height for mass flux decrease of $h_m = h_s = 135$ km in the middle photosphere. Granulation at this height shows a velocity scale height of 150 km from the observations of Keil and Canfield (1978). This indicates a scale height for mass flux decrease of $h_g = 63$ km. Granulation have a characteristic wavenumber $a_g = \pi/(1100 \text{ km})$. The power law relation suggested by the scaling of the linear solution is:

$$\frac{h_g}{h} = \left(\frac{a_g}{a}\right)^{-1/3} . \qquad (5.13)$$

The power law which fits this relation for mesogranulation with its $a_m = \pi/(7000 \text{ km})$ is -0.412; for supergranulation with its larger scale $a_s = \pi/(30{,}000 \text{ km})$ and the power is -0.231. The apparent agreement between our observations and this scaling relation however may be fortuitous. It is interesting that the larger scales do show more extensive penetration but this may not reflect properties of the antibuoyancy force.

d) Nonlinear Analysis Applicable to Penetration in Stars

Properties of convective penetration in stars may be quite different. Stellar convection zones generally

span a number of scale heights, and so the Boussinesq approximation is no longer valid. The stable zones which bound the unstable region also exhibit considerable variation in conditions and in thermal dissipation properties, such as the transition from optically thin to optically thick radiative transfer in the stellar atmosphere. Toomre et.al. (1976) apply a modal description of convection to the envelope of a model A-type star (see also Nelson and Musman 1977). They apply the anelastic approximation to the general fluid equations which is not quite as severe as the Boussinesq approximation (Latour et.al. 1976). The anelastic approximation filters out all acoustic wave modes and is effected by setting $d\rho/dt = 0$ in the continuity equation. Thermal dissipation due to radiative transfer is considered by using the Eddington approximation in the energy equation, which is valid in both the optically thick and thin limits. The results, however, may be sensitive to the fact that the atmospheric conditions are in between. In this application a single mode is retained in the expansion for w. The system of equations is solved numerically for conditions in the envelope of an A-type star. Penetrative boundary conditions are imposed in the stable regions above and below the convectively unstable region.

An A-type star was chosen for this application because the convection does not greatly modify the mean

state. Figure 5.5 shows a mixing-length model prediction for $dT/dz|_{ad}$-dT/dz as a function of depth z. Two unstable regions occur which are separated by stable fluid. The lower region is unstable because of He II ionization - this is the region of maximum driving as measured by the local Rayleigh number, and it is also the region investigated by Toomre et.al. Two modal forms are considered - rolls and hexagons. The roll solutions exhibit the odd property that the heat transport increases with increasing viscosity. This is certainly an unstable configuration and subject to shear instability. The hexagonal solutions are tested in two forms - open (upflow in the center) and closed (downflow in the center).

Closed solutions are shown to have a larger convective flux than open solutions. The preference for this solution however, may not be physical. Convection possibly chooses its scale and planform by the nonlinear coupling between separate modes and not on the basis of the transport (Palm 1975). Penetration in the closed solutions is directed mainly into the stellar interior, since the velocity in the cell center has twice the amplitude of the cell edge component. These solutions show penetration with a scale that is greater than the height of the unstable region, and they drive at least one countercell (Figure 5.6). The countercell is evidenced by the

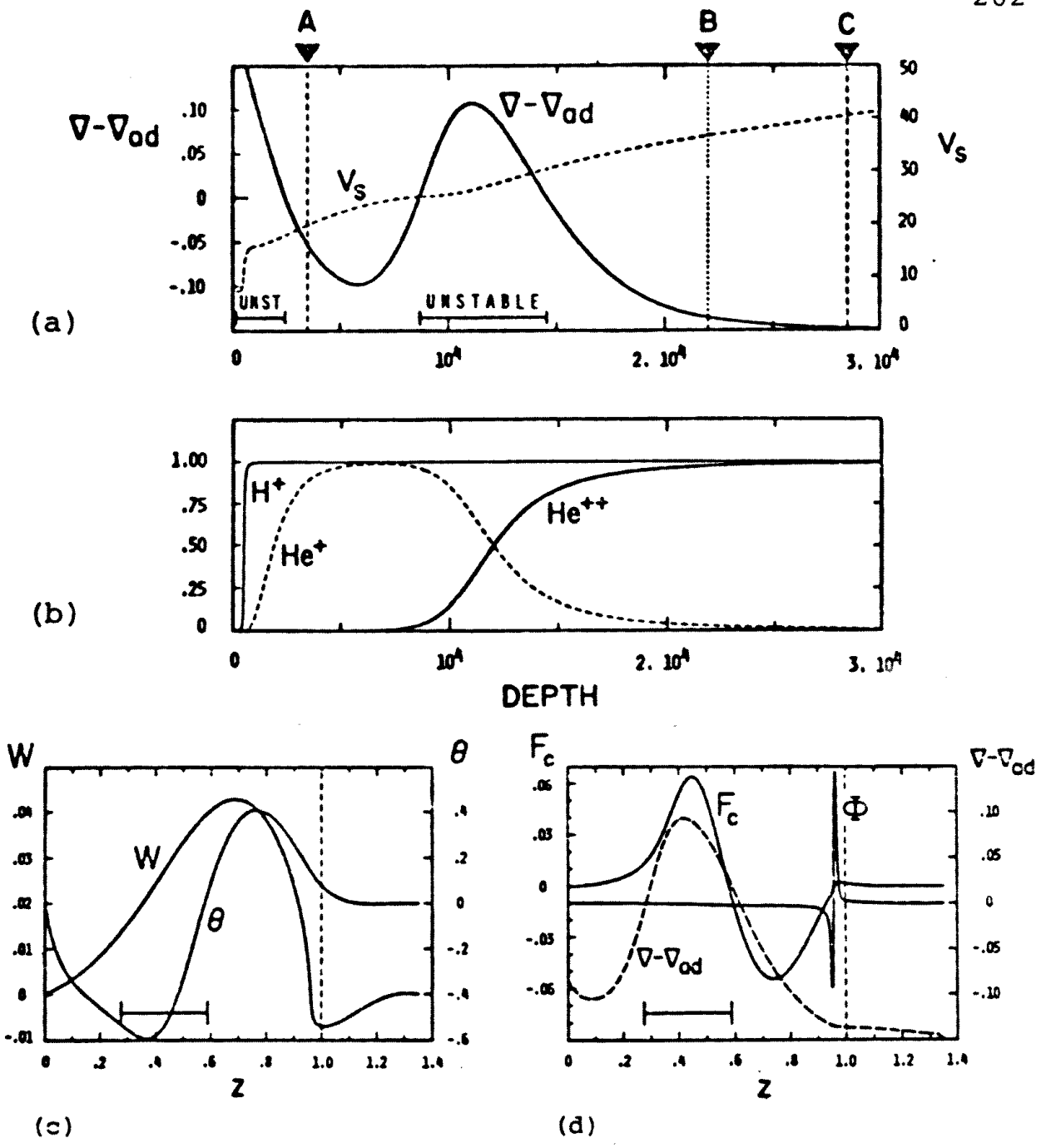

Figure 5.5

Model for an A-type star. This illustrates the results from anelastic modal calculations applied to the He II convection zone in an A-type star from Toomre et.al. (1976). In (a) and (b) conditions in the mean atmosphere are shown as derived from a mixing-length treatment. The superadiabaticity $\nabla - \nabla|_{ad}$ reaches a peak in the unstable He II zone where the motions feel their greatest buoyant driving. The local sound speed V_S decreases as the temperature throughout the zone. Results from the calculations for the vertical flow amplitude in the cell center W, the temperature fluctuations θ, the convective flux F_C, and the flow vorticity ϕ are shown in (c) and (d). The vertical scale extends from depths A to C in (a) with depth B defining the height z= 1.0. These results are for the closed solution which has downflow in the cell center so that there is substantial penetration of the motions into the stellar interior. The penetrating motions drive countercells a evidenced by the reversal in sign of W and by the sharp peak that occurs in ϕ near z= 1.0.

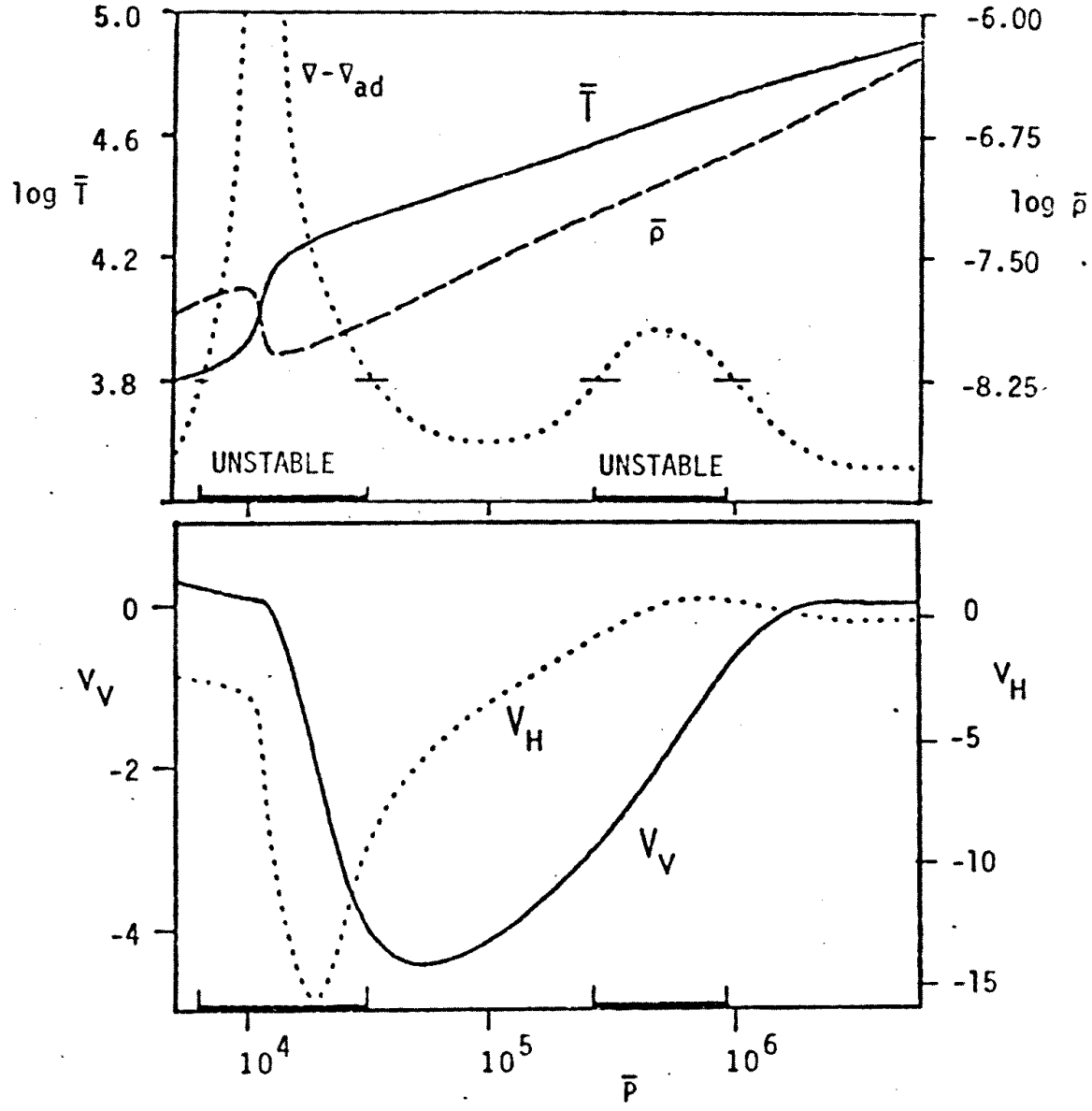

Figure 5.6

A-type star model for open cells. This shows the solution for the open cell convective motions generated in the He II ionization zone as they penetrate into the A star atmosphere from Zahn et.al. (1979). The initial conditions in the atmosphere are illustrated in the upper drawing giving the superadiabatic gradient $\nabla - \nabla_{ad}$, the mean temperature $\bar{T}$, and density $\bar{\rho}$. These are plotted against the mean pressure which emphasizes the H I unstable zone, by considerably expanding the vertical scale near the surface of the star. Results from this anelastic modal calculation for the vertical flow component in the cell center w, and the horizontal flow amplitude in these hexagonal cells u, are shown in the lower drawing. The magnitude of the vertical component rapidly approaches zero in the upper unstable zone indicating that these He II driven flows are very effectively braked in this region. This is evident also since the horizontal component u reaches has a peak in absolute amplitude in this zone. This result is consistent with our observations that show maximum braking of the mesogranular and supergranular flows low in the atmosphere and nearest to the unstable H I ionization zone.

reversal in the sign of W.

Zahn, Toomre, and Latour (1979) have examined the penetration properties into the stellar atmosphere for the open solution in the A-type star. They show that the penetrating motions feel strong braking as they pass through the relatively thin unstable region due to H I ionization. Figure 5.7 shows W(z) and the amplitude of the horizontal component of the velocity which is proportional to dW(z)/dz. The penetrating motions are abruptly turned in the H I ionization zone. Large pressure forces act to turn the large scale motions as they pass through the very thin ionization zone.

This result is indicated in our observations. We see very strong braking of the mesogranular and supergranular motions deep in the photosphere, and it is likely that similarly strong braking is occurring below the visible surface. If this were not the case it would be difficult to understand the small vertical mass flux we see in the photosphere given any reasonable estimate for the flows in the convection zone. Apparently the larger scale of convective motion are abruptly turned as they pass through the realtively thin H I ionization zone.

5.4 Summary of Results and Future Research

The goal of this work has been to determine the height variation of steady flows seen in the solar atmosphere. Our observations were obtained through a program of coordinated measurements with the University of Colorado Ultraviolet Spectrometer on the OSO 8 satellite and the Sacramento Peak Observatory tower telescope diode array. While the OSO 8 satellite could provide velocity measurements in the chromospheric Si II λ1817 line, the SPO diode array was able to make high resolution velocity and intensity measurements in a number of spectral lines. We were generally successful in coordinating these observations as confirmed by comparing the chromospheric intensities as measured in Si II λ1817 with the OSO 8 satellite and Ca II λ8542 (or λ3933) with the SPO diode array.

Our observations at large radius vector show the familiar supergranular horizontal flows in the photosphere. This flow field is clearly cellular and exhibits the relatively large dynamic range of 800 ms^{-1}. Our simultaneous observations in Si II reveal the existence of a steady flow field of similar character in the middle chromosphere. Motions in Si II are seen to persist at least 4.5 hours and vary on a scale of ~32,000 km like those of the photospheric supergranular motions. Unlike

the photospheric motions, however, this flow field shows the much larger dynamic range of ~3000 ms^{-1}. In directly comparing the motion fields at the two heights we recognize many similar features indicating that the flows may be the same seen at the two distinct heights. This comparison is however complicated by the fairly high level of noise and poor spatial resolution in the OSO 8 measurements, and by the presence of the large amplitude of vertical steady motions that exist in the chromosphere as indicated in our disk center observations. Further clarification of the possible connection between the horizontal steady flows seen in the photosphere with those seen in the chromosphere will become possible in the upcoming SMM satellite mission. A modified version of the UV Spectrometer will be operating, enabling higher spatial resolution with increased sensitivity. The instrument has been modified by using multiple detectors at the exit slit of the spectrograph so that both sides of a spectral line can be sampled simultaneously.

We have carried our similar velocity measurements at the center of the sun where we sample the vertical flow component. This is a difficult observation since the supergranular vertical motions are less than 100 ms^{-1}. All previous ground-based programs which have tried to identify the supergranular vertical flows have been severely limited by a) the large component of granulation

signal (~1000 ms^{-1}), b) the oscillatory motions (~500 ms^{-1}), c) contamination by the supergranular horizontal flows, or by d) systematic or statistical noise in the detector. The SPO diode array is well suited for this measurement, being able to sample velocities with 1" resolution over a several arcminute square in less than the Nyquist period of the oscillations. This instrument, however, has been severely limited in its velocity sensitivity due to an uncorrectable drift in the detector gains. We introduce a new technique which is able to recalibrate the diode gains after the data acquisition and find that we can recognize steady flows with amplitudes less than 30 ms^{-1}. This has permitted us to identify downflow sites associated with the enhanced chromospheric intensity seen in Ca II, lesser amplitude downflows loosely correlated with the network, large scale upflows in the cell centers, and a smaller scale of motion that we call mesogranulation. The largest amplitude downflows appear to be magnetically controlled based upon the very good correlation with the Ca II intensity. The lesser amplitude downflows and upflows in the network are probably supergranular in origin.

The most conspicuous feature in these vertical velocity measurements is the mesogranulation that appears superposed on the supergranular motion field. Mesogranules are upflow and downflow features with scales of

6" to 12" and occur both on the supergranular cell boundary and in the cell interior. The same mesogranules are recognized in independent one-half hour averages of the velocity and are present also in both the Mg I and Fe I measurements. Two-dimensional Fourier analysis shows that there is power at these spatial wavelengths comparable to that seen in the supergranulation. Mesogranulation may be the penetrating motions from a scale of convection driven in the He I ionization zone, while granulation and supergranulation originate in the H I and He II zones respectively. This scale of motion may play a role in the generation of acoustic waves since its scale is comparable to that of the observed five-minute oscillation.

In our middle chromospheric Si II velocity measurements obtained at disk center, we identify steady flows that persist for at least nine hours. As in our Mg I and Fe I measurements, the lower resolution Si II observations show a good correlation with the bright network features. Downflow is associated with the bright network and upflow occurs in the dark intercells. These flows exhibit a much greater dynamic range of ~1000 ms^{-1}. Higher resolution Si II observations indicate that considerable spatial substructure exists in these vertical flows. In these measurements we recognize flows that have 3000 ms^{-1} dynamic range and vary on a scale of ~10".

In directly comparing these Si II velocity pictures with those simultaneously obtained in Mg I or Fe I we are unable to identify the same features. This may be due to noise or the limited spatial resolution in the Si II measurements or simply reflect a physical difference in the motion fields at these two heights.

The general character of the steady motion field changes significantly in the 11 density scale heights between the photosphere and middle chromosphere. The photospheric motions that we associate with supergranulation are quite isotropic, having a horizontal flow rms that is nearly 10 times larger than the vertical flow rms. The mesogranulation, on the other hand, has a slightly larger vertical component than the supergranulation. With increasing height in the atmosphere, the flow field tends to increase in amplitude and becomes very nearly isotropic between the vertical and horizontal components. The mass flux carried by these flows very decreases with height, due primarily to the large density drop off. The mechanical flux associated with the steady motions is about 10^6 ergs cm^{-2} s^{-1} at the base of the photosphere and drops rapidly to about 10^3 ergs cm^{-2} s^{-1} at the temperature minimum. The relatively large horizontal motions which we see in this region are evidence for the general turning of the vertical flows and are associated with this dissipation of kinetic energy. In

the chromosphere the kinetic energy flux remains relatively constant as indicated by the more isotropic flow field.

The large kinetic energy flux carried by the mesogranular and supergranular motion fields raises the possibility that these flows may play a significant role in the heating of the chromosphere. Although most of the energy in these flows in dissipated below the chromosphere, it must go into a different form which could act as the direct heating mechanism. Penetrating convective motions are most efficient generators of gravity waves. Gravity waves are difficult to observe and may be able to reach chromospheric levels and so qualify as a good candidate for carrying this energy flux. Further ground-based observations of intensity and velocity fluctuations may serve to identify the actual role that gravity waves play in the solar atmosphere.

The possibility that the mesogranular and supergranular motions are convective in origin is most intriguing: observations of these flows may provide a means for probing the flows at great depth in the sun. The character of the flows low in the photosphere indicates the nature of the flows at the top of the hydrogen ionization zone, which is convectively unstable. Apparently these motions feel strong braking in a region of convective instability and little braking in the stable region

above! From the point of view acquired from laboratory studies of penetrating convective motions, this is a rather surprising property of the flows. In a star however the bounding stable region is the rarified atmosphere which is quite unlike the constant density bounding stable fluid found in laboratory convection experiments. Numerical models of an A-type star (Toomre et.al. 1976, Zahn et.al. 1979) show that large scale convective motions driven in the He II ionization zone feel the most dissipation while penetrating through the very thin unstable ionization precisely in agreement with our observations.

In summary we have found that supergranular flows are able to penetrate much higher into the atmosphere than had previously been supposed. The extent of this penetration is indicated by both the 100 fold increase in amplitude of the supergranular scale steady vertical flows that occurs between the photosphere and middle chromosphere, and by the tendency toward isotropy between the horizontal and vertical motions with increasing height. We feel that our observations of the steady component in the photosphere are the first which show the vertical supergranular component. We see large scale ~50 ms^{-1} downflows associated with the bright Ca II network and comparable relative upflows in the cell centers. In addition these observations show distinct sites of ~100

ms^{-1} material downflow specifically correlated with magnetic fields. Mesogranulation, a 6" to 12" scale of steady motion, is apparent both in the network and in the cells in these disk center velocity measurements. These features persist for at least one hour and are evident in both the Fe I and Mg I observations. It is possible that mesogranules are convective in origin and are driven in the first ionization zone of He. Our OSO 8 chromospheric velocity measurements of the steady vertical component reveal motions with a mesogranular scale but these are near the instrumental resolution limit. These properties of the supergranulation and mesogranulation must be examined in greater detail. In the future new observational programs proposed to be carried out with the SPO diode array and with the SMM satellite may help to clarify and refine the characteristics of these large scale steady flows in the solar atmosphere.

REFERENCES

Adrian, R.J., "Turbulent Convection in Water over Ice", J. Fluid Mech. Vol. 69 (1975), 753-781.

Altrock, R.C., and Canfield R.C., "Analysis of the Solar Magnesium I Spectrum", Astrophys. J. Vol. 194 (1974), 733-741.

Altrock, R.C., November, L.J., Simon, G.W., Milkey, R.W., Worden, S.P., "Heights of Formation of Non-magnetic Solar Lines Suitable for Velocity Studies", Solar Physics Vol. 43 (1975), 33-37.

Ando, H., and Osaki, Y., "Nonadiabatic nonradial Oscillations: An Application to the Five Minute Oscillations of the Sun", Publ. Astron. Soc. Japan Vol. 27 (1975), 581-603.

Ando, H., and Osaki, Y., "The Influence of the Chromosphere and Corona on the Solar Atmospheric Oscillations", Publ. Astron. Soc. Japan Vol. 29 (1977), 221-233.

Athay, R.G., and Canfield, R.C., "Computed Profiles for the Solar Mg b and Na D lines", Astrophys. J. Vol. 156 (1969), 695-706.

Athay, R.G., The Solar Chromosphere and Corona in the Quiet Sun, Dordrecht, Reidel, 1976.

Athay, R.G., and White, O.R., "Chromospheric Oscillations Observed with OSO 8: II. Average Power Spectra for Si II", Astrophys. J. Suppl. Vol. 39 (1979), 333-346.

Babcock, H.W., "The Solar Magnetograph", Astrophys. J. Vol. 118 (1953), 387-396.

Bahng, J.,and Schwarzschild, M., "Lifetime of Solar Granules", Astrophys. J. Vol. 134 (1961), 312-322.

Baker, N., and Kippenhahn, R., "The Pulsation in Models of Cephi Stars", Zeitschrift fur Astrophysik Vol. 54 (1961), 114-151.

Beckers, J.M., "Photospheric Brightness Differences Associated with the Solar Supergranulation", Solar Physics Vol. 5 (1968), 309-322.

Beckers, J.M.,and Morrison, "The Interpretation of

Velocity Filtergrams: III. Velocities inside Solar Granules", Solar Physics Vol. 14 (1970), 280-293.

Beckers, J.M.,and Milkey, R.W., "The Line Response Function of Stellar Atmospheres and the Effective Depth of Line Formation", Solar Physics Vol. 43 (1975), 289-292.

Beckers, J.M.,and Nelson, G.D., "Some Comments on the Limb Shift of Solar Lines: II. The effect of Granular Motions", Solar Physics Vol. 58 (1978), 243-261.

Beckers, J.M., private communication (1978).

Bevington, Data Reduction and Error Analysis in the Physical Sciences, First ed., New York, McGraw Hill, 1969, 336 pp.

Biermann, L., "Untersuchungen uber den inneren Aufbau der Sterne IV Konvektionszonen im Innern der Sterne", Zeitscrift fur Astrophysik Vol. 5 (1932), 117.

Biermann, L., "Uber die Chemische Zusammensetzung der Sonne", Zeitscrift fur Astrophysik Vol. 22 (1943), 244.

Bogart, R., Dynamics of the Solar Convective Envelope, Ph D Thesis, Cornell University, Physics Dept., 1978, 147 pp.

Bohm, K., "Unstable Modes in the Solar Hydrogen Convective Zone", Astrophys. J. Vol. 137 (1963), 881-900.

Bohm, K., "Convective Modes with Turbulent Viscosity and Conductivity", preprint (1979).

Bohm-Vitense, E., "Uber die Wasserstoffkonvektionszone in Sternenverschiedener Effektivtemperaturen und Leuchtkrafte", Zeitscrift fur Astrophysik Vol. 46 (1958), 108.

Bruner, E.C. Jr., Chipman, E.G., Lites, B.W., Rottman, E.G., Shine, R.A., Athay, R.G., White, O.R., "Preliminary Results from the Orbiting Solar Observatory 8: Transition Zone Dynamics over a Sunspot", Astrophys. J. Vol. 210, L97-L101.

Canfield, R.C.,and Mehltretter, "Fluctuations of Brightness and Vertical Velocity at Various Heights in the Photosphere", Solar Physics Vol. 33 (1973), 33-48.

Canfield, R.C.,and Musman, S., "Vertical Phase Variation and Mechanical Flux in the Solar Five Minute

Oscillation", Astrophys. J. Vol. 184 (1973), L131-L136.

Canfield, R.C., "The Height Variation of Granular and Oscillatory Velocities", Solar Physics Vol. 50 (1976), 239-254.

Chipman, E.G., Bruner, E.C. Jr., Shine, R.A., Lites, B.W., Rottman, G.J., Athay, R.G., White, O.R., "Preliminary Results From the Orbiting Solar Observatory 8. Velocities in the Solar Chromosphere Observed in the Si II 1816 Lines", Astrophys. J. Vol. 210 (1976), L103.

Chipman, E.G., "OSO 8 Observations of Wave Propagation in the Solar Chromosphere and Transition Region", Bull. AAS Vol. 9 (1977), 323.

Chipman, E.G., private communication (1978).

Cox, A.N., Brownlee, R.R., and Eilers, D.D., Astrophys. J. Vol. 144 (1966), 1024.

Cox, J.P.,Cox, A.N., Olsen, N.H., King, D.S., and Eilers, D.D., Astrophys. J. Vol. 144 (1966).

Cox, J.P., and Giuli, R.J., Principles of Stellar Structure. Vol. 1 First edition, New York, Gordon and Breach, 1968.

Demarque, P., "The Structure of Population II Stars", Astrophys. J. Vol. 132 (1960), 366-379.

Deubner, F-L.,"Some Properties of Velocity Fields in the Solar Photosphere", Solar Physics Vol. 17 (1971), 6-20.

Deubner, F-L., "Observations of Low Wavenumber Nonradial Eigenmodes of the Sun", Astron. and Astrophys. Vol. 44 (1975), 371-375.

Deubner, F-L., "Photospheric Observations of Solar Pulsations and Other Wave Phenomena", Proc. November 1977 OSO 8 Workshop (1977).

Deubner, F-L., Ulrich, R.K.,and Rhodes, E., "Solar p mode Oscillations as a Tracer of Radial Differential Rotation", Astron. and Astrophys. Vol. 72 (1979), 177-185.

Dunn, R.B., Rust, D.M.,and Spence, G.E., Proceedings: Society for Photo-optical Engineers Vol. 44 (1974), 109.

Eddington, A.S., The Internal Constitution of the Stars, Cambridge, Cambridge University Press, 1926.

Emden, R., Gaskugeln, Berlin, Teubner, 1907.

Evans, J., and Michard R., Communication at Berkeley meeting of IAU Comm. 12, (1961).

Evans, J.,and Michard, R., "Observational Study of Macroscopic Inhomogeneities in the Solar Atmosphere: III. Vertical Oscillatory Motion in the Solar Photosphere", Astrophys. J. Vol. 136 (1962), 493-506.

Finn, G.D.,and McAllister, H.C., "Observed and Theoretical Profiles of the Si II Lines at 1814", Solar Physics Vol. 56 (1978), 263-273.

Frazier, E.N., "An Observational Study of the Hydrodynamics of the Lower Solar Photosphere", Astrophys. J. Vol. 152 (1968a), 557-575.

Frazier, E.N., "A Spatio Temporal Analysis of Velocity Fields in the Solar Photosphere", Zeitscrift fur Astrophysik Vol. 68 (1968b), 345-356.

Frazier, E.N., "Multi-channel Magnetograph Observations", Solar Physics Vol. 14 (1970), 89-111.

Frazier, E.N., "A Velocity Error in Babcock Type Magnetographs", Solar Physics Vol. 38 (1974), 69-72.

Gebbie, K.B., November, L.J., Toomre, J., and Simon, G.W., "The Variation with Height of the Supergranular Velocity Fields", Bull AAS Vol. 10 (1979), p. 672.

Gingerich, O., Noyes, R.W., Kalkofen, W., Cuny, Y., "The Harvard-Smithsonian Reference Atmosphere", Solar Physics Vol. 18 (1971), 347.

Goldreich, P.,and Keeley, D.A., "Solar Seismology: I. The Stability of the Solar p modes", Astrophys. J. Vol. 211 (1977a), 934-942.

Goldreich, P.,and Keeley, D.A., "Solar Seismology: II. The Stochastic Excitation of the Solar p modes by Turbulent Convection", Astrophys. J. Vol. 212 (1977b), 243-251.

Gough, D.O., Spiegel, E.A., Toomre, J., "Modal Equations for Cellular Convection", J. Fluid Mech. Vol. 68 (1975), 695-719.

Gough, D.O., and Weiss, N.O., "The Calibration of Stellar

Convection Theories", Mon. Not. R. astr. Soc. Vol. 176 (1976), 589-607.

Hart, A.B., "Motions in the Sun at the Photospheric Level. IV. The Equatorial Rotation and Possible Velocity Fields in the Photosphere", Mon. Not. Roy. astr. Soc. Vol. 114 (1954), 17-38.

Hart, A.B., "Motions in the Sun at the Photospheric Level. VI. Large Scale Motions in the Equatorial Region", Mon. Not. Roy. astr. Soc. Vol. 116 (1956), 38-55.

Hart, M.N., "Linear Convective Modes and the Energy Transport in Stellar Convection Zones", Astrophys. J. Vol. 184 (1973), 587.

Harvey, J., private communication (1976).

Henyey, L., Vardya, M.S., and Bodenheimer, P., "Studies in Stellar Evolution: III. The Calculation of Model Envelopes", Astrophys. J. Vol. 142 (1965), 841.

Herschel, W., "Observations tending to investigate the nature of the Sun, in order to find causes or symptoms of its variable emission of light and heat; with remarks on the use that may possibility be drawn from solar observations", Phil. Tran. Roy. Soc. 1801 part 1, 265.

Hofmeister, E. Kippenhahn, R., and Wigert, A., "Sternentwicklung I: Ein Programm zur Losung der zeit abhangigen Aufbaugleichungen", Zeitscrift fur Astrophysik Vol. 59 (1964), 215-241.

Huggins, W., "Results of some observations on the bright granules of the solar surface", Mon. Not. R. A. S. Vol. 26 (1866), 260.

Iben, I., Jr., "A Comparison Between Homogeneous Stellar Models and the Observations", Astrophys. J. Vol. 138 (1963), 452-470.

Janssen, J., "Memoire sur la photographic solaire", Ann. Obs. Meudon Vol. 1 (1896), 91.

Keil, S.L.,and Canfield, R.C., "The Height Variation of Velocity and Temperature Fluctuations in the Solar Photosphere", Astron. and Astrophys. Vol. 70 (1978), 169-179.

Keil, S.L., "A New Measurement of the Center to Limb Variation of the rms Granular Contrast", Solar Physics Vol. 53 (1976), 359-368.

Latour, J.,and Zahn, J.-P., "On the Boundary Conditions Imposed by a Stratified Fluid", Geophys. Astrophys. Fluid Dynamics Vol. 10 (1978), 311-318.

Latour, J., Spiegel, E.A., Toomre, J., Zahn, J.-P., "Stellar Convection Theory: I. The Anelastic Modal Equations", Astrophys. J. Vol. 207 (1976), 233-243.

Leighton R.B., "Observations of Solar Magnetic Fields in Plage Regions", Astrophys. J. Vol. 130 (1959), 366-380.

Leighton, R.B., "Preview on Granulation", Il Nuovo Cimento Suppl. Vol. 22 (1961), 321-327.

Leighton, R.B.,Noyes, R.W., and Simon, G.W., "Velocity Fields in the Solar Atmosphere. I. Preliminary Report", Astrophys. J. Vol. 135 (1962), 474-499.

Leighton, R.B., "The Solar Granulation", Ann. Rev. Astro. Astro. 1963, 19-40.

Lighthill, M., Proc. Roy. Soc. A211 (1952), 564.

Linsky, J., and Avrett, E.H., "The Solar H and K Lines", Publ. Astro. Soc. Pacific Vol. 82 (1970), 169-248.

Lites, B.W., Bruner, E.C., Jr., Chipman, E.G., Shine, R.A., Rottman, G.W., White, O.R., Athay, R.G., "Preliminary Results from OSO 8: Persistent Velocity Fields in the Chromosphere and Transition Region", Astrophys. J. Vol. 210 (1976), L111-L113.

Mihalas, B., Internal Gravity Waves in the Solar Atmosphere, Ph.D. Thesis, University of Colorado, Dept. of Astro-geophysics, 1979.

Moore, D.R.,and Weiss, N.O., "Nonlinear Penetrative Convection", J. Fluid Mech. Vol. 61 (1973), 553-581.

Mullan, D.J., "Cellular Convection in Model Stellar Envelopes", Mon. Not. R. astr. Soc. Vol. 154 (1971), 467-489.

Musman, S., "Penetrative Convection", J. Fluid Mech. Vol. 31 (1968), 343-360.

Musman, S., and Rust, D.M., "Vertical Velocities and Horizontal Wave Propagation in the Solar Photosphere", Solar Physics Vol. 13 (1970), 261-286.

Namba, O.,and Diemel, N.E., "A Morphological Study of the Solar Granulation", Solar Physics Vol. 7 (1969), 167-177.

Nelson, G.D.,and Musman, S., "A Dynamical Model of the Solar Granulation", Astrophys. J. Vol. 214 (1977), 912-916.

November, L.J., Toomre, J., Gebbie, K.B., Simon, G.W., Bruner, E.C., Jr., Chipman, E.G., Lites, B.W., Orral, R.Q., Shine, R.A., Athay, R.G., and White, O.R., "Supergranular Velocity Fields Observed in the Solar Transition Region with OSO-8", Bull. AAS Vol. 8 (1976), 311.

November, L.J., Toomre, J., Gebbie, K.B., Simon, G.W., "Vertical and Horizontal Components of Supergranular Velocity Fields Observed with OSO-8", Bull. AAS Vol. 9 (1977a), 337.

November, L.J., Toomre, J., Gebbie, K.B., Simon, G.W., "Supergranular Velocity Fields", Proc. November 1977 OSO 8 Workshop (1977b), 451.

November, L.J., Toomre, J., Gebbie, K.B., Simon, G.W., "The Height Variation of Supergranular Velocity Fields Determined from Simultaneous OSO-8 Satellite and Ground-Based Observations", Astrophys. J. Vol. 227 (1979), 600-613.

Opik, E.J., "Transport of Heat and Matter by Convection in Stars", Mon. Not. R. astr. Soc. Vol. 110 (1950), 559.

Palm, E., "Nonlinear Thermal Convection", Ann. Rev. Fluid Mech. Vol. 7 (1975), 39-61.

Pugh, E.M., and Winslow, G.H., The Analysis of Physical Measurements, Reading Mass., Addison Wesley, 1966.

Rayleigh, Lord, "On Convection Currents in a Horizontal Layer of Fluid When the Higher Temperature is on the Under Side", Phil. Mag. Vol. 32, 529-546.

Reeves, E.M., Foukal, P.V., Huber, M.C.E., Noyes, R.W., Schmahl, E.J., Timothy, J.G., Vernazza, J.E., Withbrow, G.L., "Solar EUV photoelectric Observations from Skylab", IAU Symposium No. 57 (1974), 497-500.

Rhodes, E., Ulrich, R.K., and Simon, G.W., "Observations of Nonradial p mode Oscillations on the Sun", Astrophys. J. Vol. 218 (1977), 901-919.

Roxburgh, I.W., "A Note on the Boundary of Convective Zones in Stars", Mon. Not. R. astr. Soc. Vol. 130 (1965), 223-228.

Schwarzschild, K., Nacr. Kon. Gesellsch. d. Wiss., Gottingen, No. 1. (1906).

Schwarzschild, M., Howard, R., Harm, R., "Inhomogeneous Stellar Models V. A Solar Model with Convective Envelope and Inhomogeneous Interior", Astrophys. J. Vol. 125 (1957),. 233-241.

Schwarzschild, M., Structure and Evolution of the Stars, First edition, New York, Dover Publications, 1958, 296 pp.

Schwarzschild, M.,"Photographs of the Solar Granulation Taken from the Stratosphere", Astrophys. J. Vol. 130 (1959), 345-363.

Secchi, A., Le Soleil, 2nd edition Vol. 1 (Gauthier-Villars, Paris, 1875).

Shaviv, G., and Salpeter, E.E., "Convective Overshoot in Stellar Interior Models", Astrophys. J. Vol. 184 (1973), 191-200.

Siedentopf, H., Astronomische Nachrichten Vol. 247 (1932), 297.

Siedentopf, H., Astronomische Nachrichten Vol. 249 (1933), 53.

Siedentopf, H., Astronomische Nachrichten Vol. 255 (1935), 157.

Simon, G.W., and Leighton, R.B., "Velocity Fields in the Solar Atmosphere: III. Large-Scale Motions, the Chromospheric Network, and Magnetic Fields", Astrophys. J. Vol. 140 (1964), 1120-1147.

Simon, G.W., "Observations of Horizontal Motions in Solar Granulation: The Relation to Supergranulation", Zeitscrift fur Astrophysik Vol. 65 (1967), 345-363.

Simon, G.W., and Weiss, N.O., "Supergranules and the Hydrogen Convection Zone", Zeitscrift fur Astrophysik Vol. 69 (1968), 435.

Skumanich, A., "On Thermal Convection in a Polytropic

Atmosphere", Astrophys. J. Vol. 121 (1955), 408-417.

Skumanich, A., Smythe, C., and Frazier, E.N., "On the Statistical Description of Inhomogeneities in the Quiet Solar Atmosphere. I. Linear Regression Analysis and Absolute Calibration of Multichannel Observations of the Ca+ Emission Network", Astrophys. J. Vol. 200 (1975), 747-464.

Spiegel, E.A., and Veronis, G., "On the Boussinesq Approximation for a Compressible Fluid", Astrophys. J. Vol. 131 (1960), 442-447.

Spiegel, E.A., "A Generalization of the Mixing-Length Theory of Turbulent Convection", Astrophys. J. Vol. 138 (1963), 216-225.

Spiegel, E.A., "Convection in Stars: I. Basic Boussinesq Convection", Ann. Rev. Astro. Astro. 1971, 323-352.

Spiegel, E.A., "Convection in Stars: II. Special Effects", Ann. Rev. Astro. Astro. 1972, 261-304.

Stein, R., "Generation of Acoustic and Gravity Waves by Turbulence in an Isothermal Stratified Atmosphere", Solar Physics Vol. 2 (1967), 385-432.

Stein, R., in progress (1969).

Tanenbaum, A.S., Wilcox, J.M., Frazier, E.N., Howard, R.,"Solar Velocity Fields: 5-Min Oscillations and Supergranulation", Solar Physics Vol. 9 (1969), 238-342.

Toomre, J., Zahn, J.-P., Latour, J., and Spiegel, E.A., "Stellar Convection Theory: II. Single-Mode Study of the Second Convection Zone in an A-Type Star", Astrophys. J. Vol. 207 (1976), 545-563.

Toomre, J., "Overshooting Motions from the Convection Zone and their Role in the Atmospheric Heating", Highlights of Astronomy Vol. 5, ed. P.A. Wayman, Reidel, 1979.

Tousey, R., Bartoe, J.-D.F., Bohlin, J.D., Brueckner, G.E., Purcell, J.D., Scherrer, V.E., Sheeley, N.R., Schumacher, R.J., Vanhoosier, M.E., "A Preliminary Study of the Extreme UV Spectroheliograms from Skylab", Solar Physics Vol. 33 (1973), 265.

Townsend, A.A., "Natural Convection in Water over an Ice Surface", Quart. J. Roy. Met. Soc. Vol. 90 (1964), 248-

259.

Townsend, A.A., "Internal Waves Produced by a Convective Layer", J. Fluid Mech. 24 (1966), 307-319.

Tripp, D.A., Athay, R.G., and Peterson, V.L., "Spectrum Synthesis of Chromospheric Lines of Si II and Si III", Astrophys. J. Vol. 220 (1978), 314-324.

Ulrich, R.K., "Convection Energy Transport in Stellar Atmospheres: I. A Convective Thermal Model", Astrophys. and Space Sci. Vol. 7 (1970a), 71-86.

Ulrich, R.K., "Convective Energy Transport in Stellar Atmospheres: II. Model Atmosphere Calculation", Astrophys. and Space Sci. Vol. 7 (1970b), 183-200.

Ulrich, R.K., "The Five Minute Oscillation of the Solar Surface", Astrophys. J. Vol. 162 (1970c), 993-1002.

Ulrich, R.K., "A Nonlocal Mixing-Length Theory of Convection for use in Numerical Calculations", Astrophys. J. Vol. 207 (1976), 564-573.

Ulrich, R.K., and Rhodes, E., "The Sensitivity of Nonradial p mode Eigenfunctions to the Solar Envelope Structure", Astrophys. J. Vol. 218 (1977), 512-529.

Unsold, A., "Konvektion in der Sonnenatmospare", Zeitscrift fur Astrophysik Vol. 1 (1930), 138.

Worden, S.P., Solar Supergranulation, Ph.D. Thesis, University of Arizona, Dept. of Astronomy, 1975, 156 pp.

Worden, S.P., and Simon, G.W., "A Study of Supergranulation Using a Diode Array Magnetograph", Solar Physics Vol. 46 (1976), 73-91.

Zahn, J.-P., Toomre, J., and Latour, J., "Convection in an A-Type Star", in progress (1979).

APPENDIX A

STABILITY OF THE DIODES

The sensitivity of the diodes at SPO slowly varies in time thus introducing streaks in intensity and velocity images. We apply the correction factor g_i and offset d_i for each diode before further processing of the diode data,

$$I_i' = g_i I_i + d_i \ . \qquad (A.1)$$

Here I_i is a measured intensity for diode i and I_i' is the corrected value.

We determine g_i and d_i in the sample raster assuming that on the average any two points separated by only one arcsecond will have the same intensity. In practice we determine the slope s_i and the zero z_i for intensities measured in diode i plotted against those measured in diode i+1 for the spatial steps j in the sample raster. I_{ij} represents an intensity measurement for diode i, 0 < i N_D, where N_D is the number of diodes, and raster step j, 0 < j < N_X, where N_X is the number of raster steps. The least squares slope s_i and zero z_i are written after

Bevington 1969,

$$s_i = \tan\left[\frac{1}{2}\tan^{-1}\left(\frac{N_X\Sigma_j I_{kj} I_{I+ij} - \Sigma_j I_{ij}\Sigma_j I_{I+ij}}{N_X\Sigma_j I_i{}^2{}_j - (\Sigma_j I_{ij})^2}\right) + \frac{1}{2}\tan^{-1}\left(\frac{N_X\Sigma_j I^2_{i+ij} - (\Sigma_j I_{i+ij})^2}{N_X\Sigma_j I_{ij} I_{i+ij} - \Sigma_j I_{ij}\Sigma_j I_{i+ij}}\right)\right]$$

$$z_i = \frac{1}{N_X}\left(\Sigma_j I_{i+ij} - s_i \Sigma_j I_{ij}\right) . \qquad (A.2)$$

The last diode N_D is compared with the first diode in the subsequent swath to which it is physically adjacent so i= N_D+1 is replaced by i= 1 in (A.2). The intensities measured for diode i+1, I_{i+2}, are thus related to those for diode i, I_i, by the relation,

$$I_{i+1} = s_i I_i + z_i . \qquad (A.3)$$

If the raster has no streaks, and there is no need for a gain and dark current correction, then the intensity I_{ij} will usually be near $I_{i+1,j}$ for all j, and $I_{i+2} = I_i$. If, however, diode i+1 differs from diode i in any systematic (but linear) way then $s_i \neq 1$. and $z_i \neq 0$.

The slopes s_i and zeros z_i are related to the gains g_i and dark currents d_i. We impose the condition that $I_{i+2}' = I_i'$, or that the corrected intensities show no systematic variation over the raster. With this and upon

elimination of I_i and I_{i+2} between equations (A.1) and (A.3) we arrive at this equation in terms of I_i,

$$g_{i+1}s_iI_i + g_{i+1}z_i + d_{i+1} = g_iI_i + d_i \ . \qquad (A.4)$$

Since this must be valid for all values of I_i we can define these $2N_D$ simultaneous equations in g_i and d_i:

$$s_i = \frac{g_{i+1}}{g_i} \ ,$$

$$z_i = \frac{1}{g_{i+1}} (d_i - d_{i+1}) \ , \qquad (A.5)$$

where again $i= N_D+1$ is replaced by $i= 1$. Inversion of this nonlinear system for the desired g_i and d_i is done by a method of successive iteration which we find converges rapidly for the initial guess $g_i= 1$ and $d_i= 0$.

Although this algorithm is fairly complicated and computationally expensive we have found that it has considerable advantages over other methods. Most other techniques for computing gains and dark currents are non-local; that is they assume certain features about the large scale variation of intensity. In this algorithm, diode i is compared only with diode i+1 and no large scale variations are introduced. Solar rotation and limb darkening are accurately reproduced, and artificial brightening around sunspots is avoided. Other methods, like forcing the average of each line to be the same

value, do introduce unrealistic velocity and intensity variations.

APPENDIX B

PROPERTIES OF THE HEXAGONAL PLANFORM FUNCTION

When upward motions in penetrating convection are slowed these motions may dissipate some of their energy flux as they are turned back down. Fluid must be conserved in steady state so that the upward momentum flux ρw_{up} balances the downward momentum flux ρw_{dn} within a cell. Horizontal motion occurs when the vertical flow is so turned. Within a cell, if the area occupied by material upflow differs from that occupied by material downflow an asymmetry results which will may lead to differing kinetic energy in the upward and downward flows, so that $\rho w_{up}^2 \neq \rho w_{dn}^2$. That energy difference results in a local conversion of energy into other forms such as heating by turbulence or generation of acoustic-gravity waves.

The planform function for a hexagon $f(x,y)$ is defined:

$$f(x,y) = \sqrt{2/3}\ \left[2\cos(\sqrt{3}\ ax)\cos(ay) + \cos(2ay)\right] \quad \text{(B.1)}$$

which satisfies the normalization condition:

$$\frac{1}{S}\int_S |f(x,y)|^2 \partial S = 1 \ . \qquad (B.2)$$

Here S is a surface over the hexagon. The cellular scale is π/a. Figure B.1 illustrates the cell planform function with the scale chosen so that a= 1.

i) velocity rms

The vertical velocity in the cell w is defined:

$$w = f(x,y)W(x) \ . \qquad (B.3)$$

The horizontal components u, v must satisfy the continuity equation $\nabla.(\rho\underline{u}) = 0$, and be isotropic in x,y. Horizontal velocity components u, and v satisfying these conditions are,

$$\rho u = \frac{1}{a^2}\frac{\partial f}{\partial x}\frac{\partial}{\partial z}(\rho W) \ ,$$

$$\rho v = \frac{1}{z^2}\frac{\partial f}{\partial y}\frac{\partial}{\partial z}(\rho W) \ . \qquad (B.4)$$

The rms velocities are evaluated as integrals of the square of the velocity component over the cell planform.

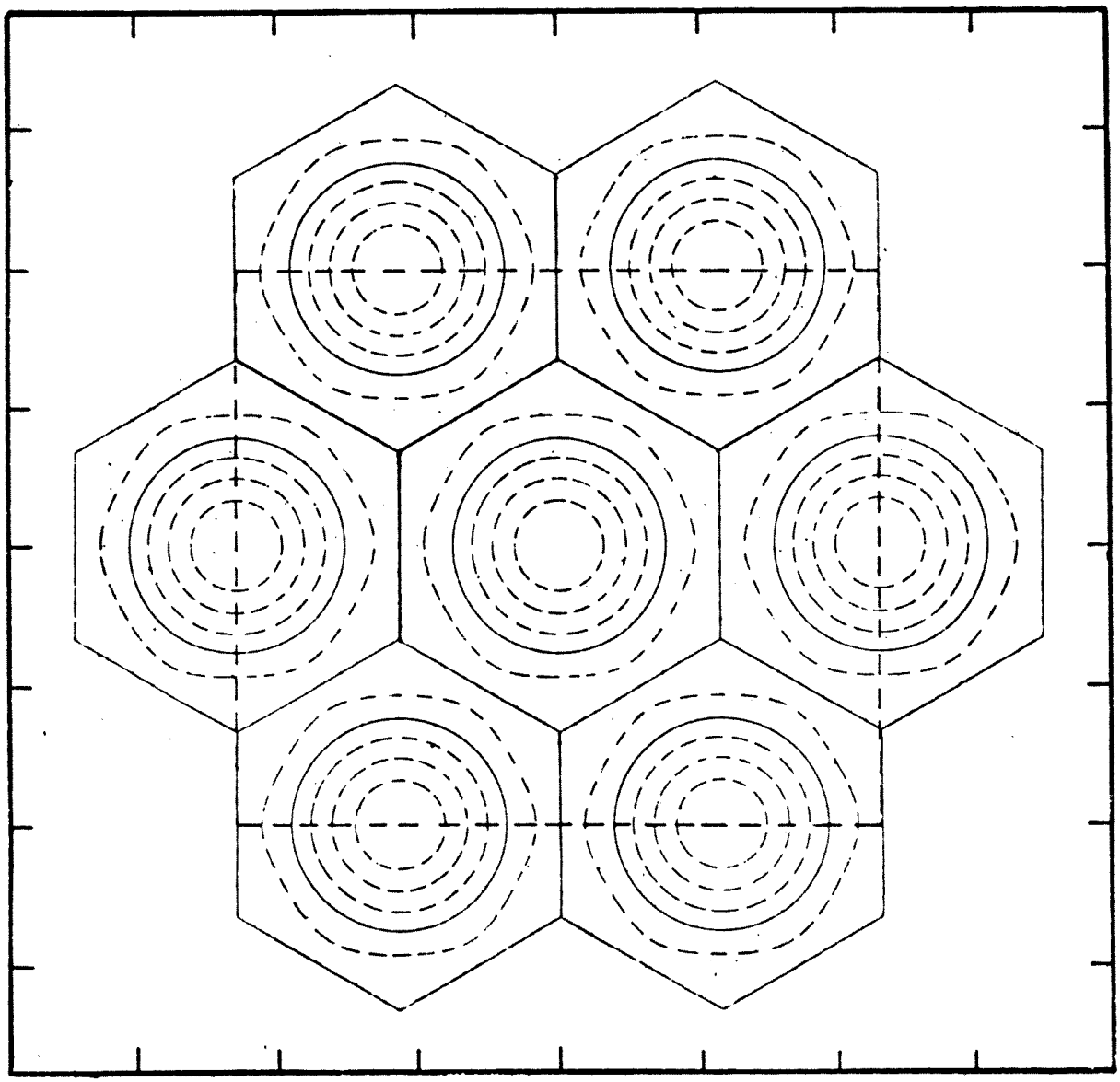

Figure B.1

Hexagonal planform function. This figure illustrates the planform function f(x,y) discussed in the text. This function varies from +1.0 at the center of the cell to -0.5 at each vertice. In the figure contours are drawn at each increment of 0.25 in f and the solid contour corresponds to f= 0. The dashed box encloses four cells and is a convenient surface to use in determining different norms for f. The scale of the hexagon is different in x than in y in this orientation and the surface of integration is therefore rectangular.

$$w_{rms} = \left(\frac{1}{S}\int_S f^2 \partial S\right)^{1/2} W(z) = W(z) \ , \tag{B.5}$$

$$u_{rms} = \frac{1}{a^2}\left[\frac{1}{S}\int_S \left(\frac{\partial f}{\partial x}\right)^2 \partial S\right]^{1/2} \frac{\partial}{\partial z}(\rho W) \ ,$$

$$v_{rms} = \frac{1}{a^2}\left[\frac{1}{S}\int_S \left(\frac{\partial f}{\partial y}\right)^2 \partial S\right]^{1/2} \frac{\partial}{\partial z}(\rho W) \ . \tag{B.6}$$

Evaluating the integral yields,

$$u_{rms} = v_{rms} = \frac{\sqrt{2}}{a}\frac{d}{dz}(\rho W) \ . \tag{B.7}$$

ii) the kinetic energy flux K(z)

The amount of kinetic energy deposited at a level in the atmosphere depends upon dW/dz. The net upward flux K(z) is written in terms of the density $\rho(z)$ as,

$$K = \frac{\rho}{S}\int_S (u^2+v^2+w^2)w \ \partial S \ . \tag{B.8}$$

In terms of the planform function f(x,y) we have,

$$K = \frac{1}{Sa^4}\left\{\int_S \left[\left(\frac{\partial f}{\partial x}\right)^2 + \left(\frac{\partial f}{\partial y}\right)^2\right] f \partial S\right\} \frac{W}{\rho}\left[\frac{\partial(\rho W)}{\partial z}\right]^2$$

$$+ \frac{1}{S}\left(\int_S f^3 \partial S\right) \rho W^3 \ . \tag{B.9}$$

Upon evaluation of the integrals this becomes,

$$K = \sqrt{\frac{2}{3}} \frac{w}{a^2 \rho} \left[\frac{\partial (\rho W)}{\partial z}\right]^2 + \sqrt{\frac{2}{3}} \rho W^3 \quad . \tag{B.10}$$

In terms of u_{rms}, w_{rms} we have,

$$K = \sqrt{\frac{2}{3}} \rho (w_{rms} u_{rms}^2 + w_{rms}^3) \quad . \tag{B.11}$$

The energy deposited per unit height is just -dK/dz. This is readily written in terms of W(z) and ρ(z) from the result (B.10).

APPENDIX C

This appendix contains supplimental observations of the horizontal flow component seen at radius vector 0.8. These observations are used in the discussions of OSO 8 persistence in the raster mode and rms velocity amplitude in the point mode in Chapter 2. By including these data here, we are able to illustrate all the observations without bogging down the reading of the main body of the text.

INTENSITY

VELOCITY

·500 m/s

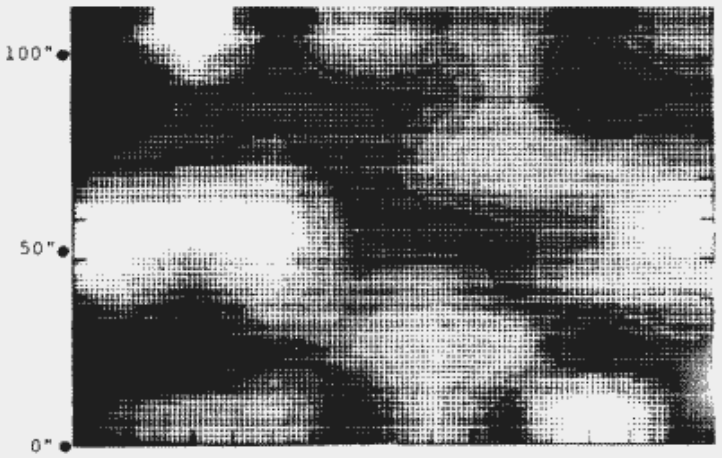

ORBIT
7562

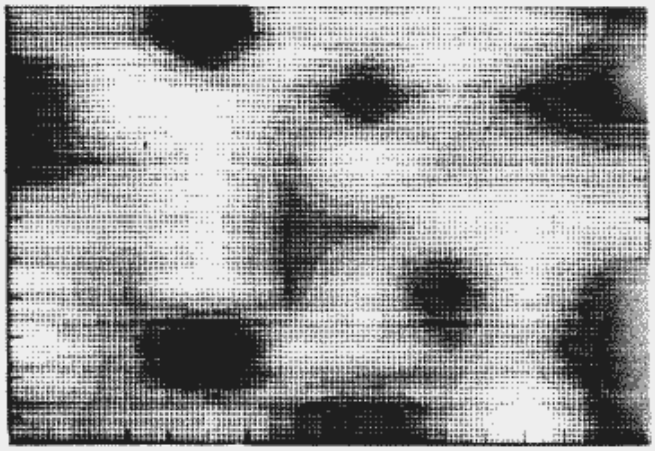

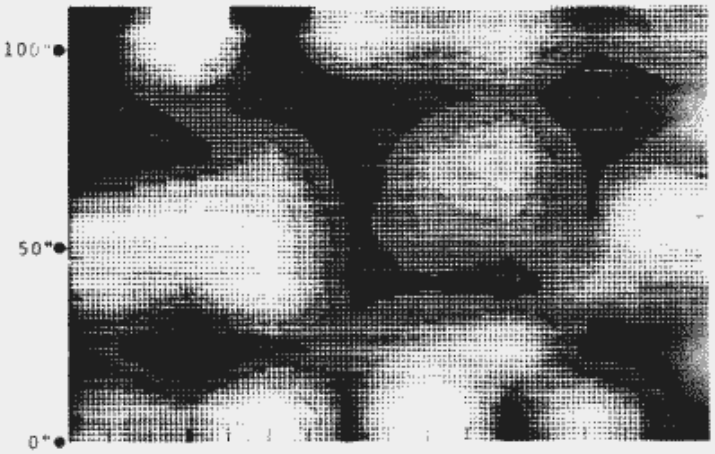

ORBIT
7563

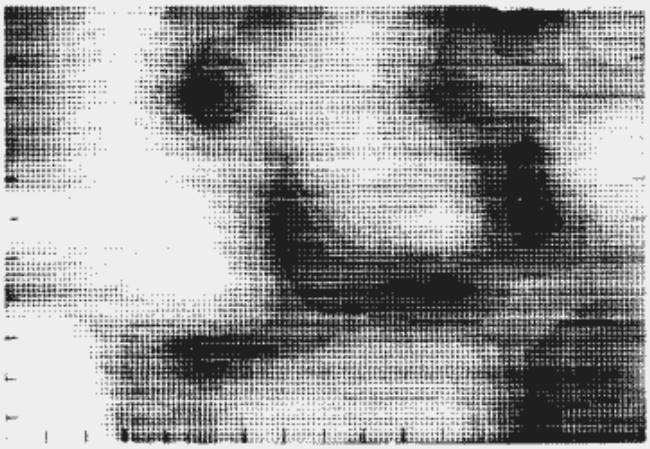

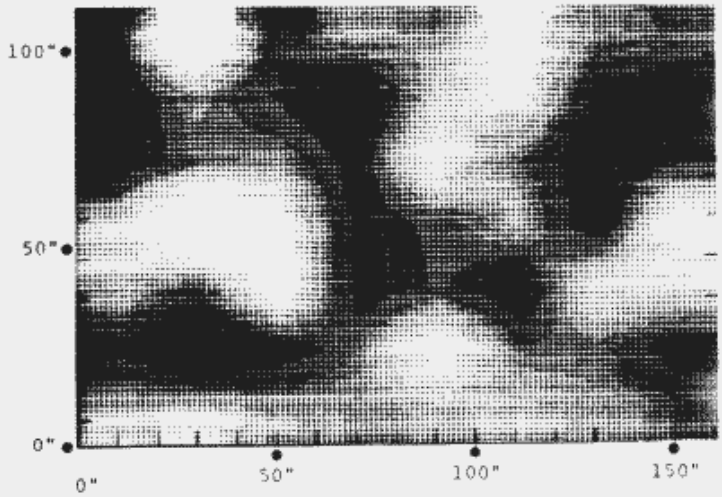

ORBIT
7565

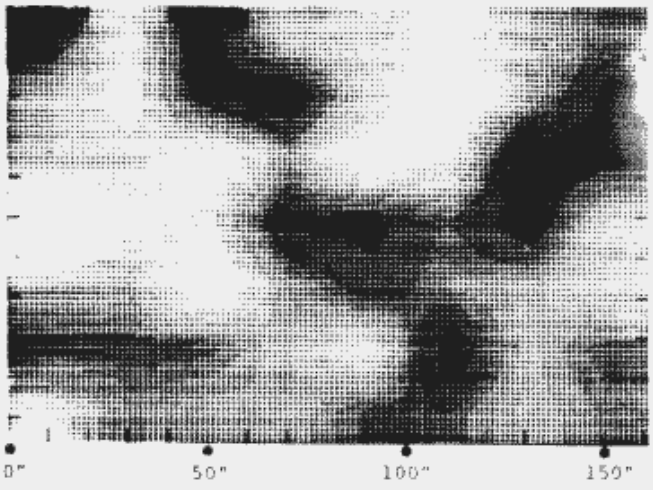

OSO - 8

Si II ·1817

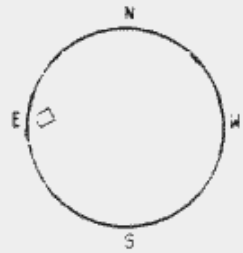

Figure C.1

Persistence in the raster-mode observations on day 6308. These are time-averaged intensity and Doppler velocity images formed from OSO 8 raster-mode observations in Si II 1817. The observations cover an area 132" x 168" at radius vector 0.8 on the quiet Sun near the west limb on day 6308 (3 November 1976). In this set the pointing of the instrument was updated to compensate for the effect of solar rotation. The left side shows the intensity pictures, each an average over one full orbit's observations. The intensity pictures show the same bright features in the three separate images indicating reproducability of the measurements. The velocity averages on the right show persistence of the flows throughout the 5.5 hours of observation.

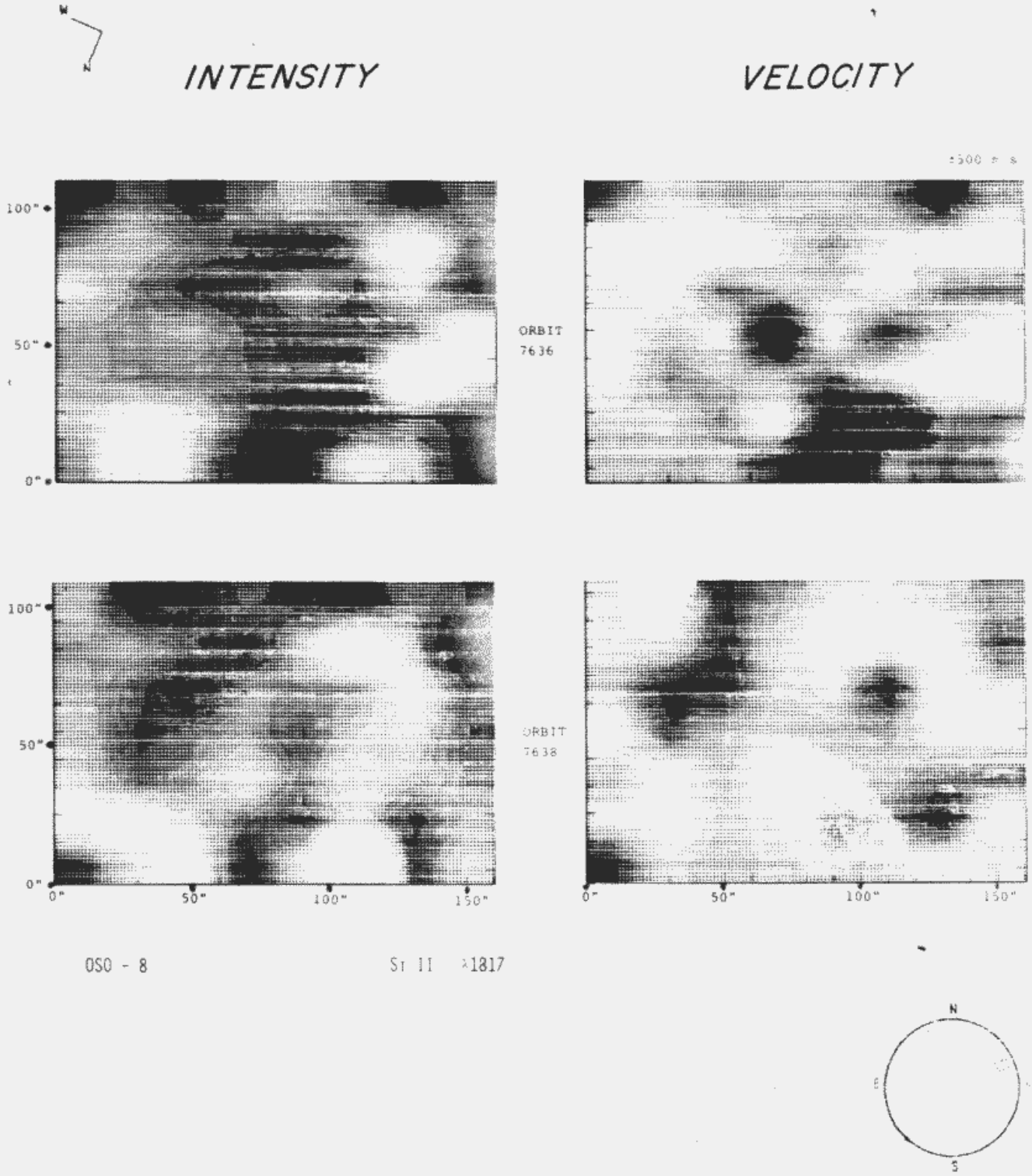

Figure C.2

Persistence in the raster-mode observations on day 6313. These are time-averaged intensity and Doppler velocity images formed from OSO 8 raster-mode observations in Si II λ1817, like those shown in Figure C.1. The observations were made on day 6313 (8 November 1976). In this set the pointing of the instrument was not updated to compensate for the effect of solar rotation, and this has introduced a 24" drift toward the west between the separate images. The intensity pictures show little persistence in the two separate orbits. Persistence in the velocity averages on the right is also somewhat uncertain.

INTENSITY

VELOCITY

±500 m/s

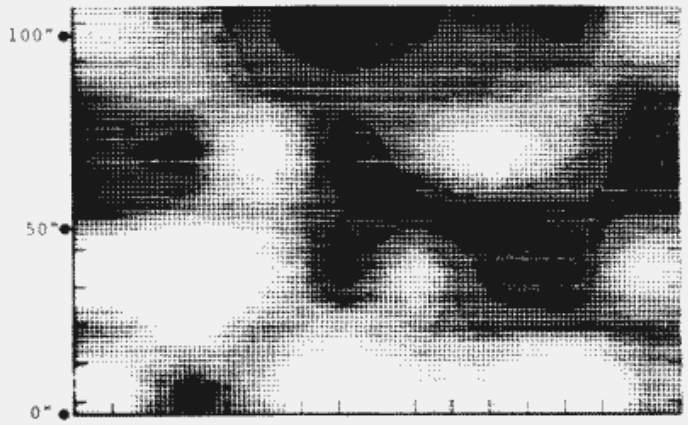

ORBIT 7829

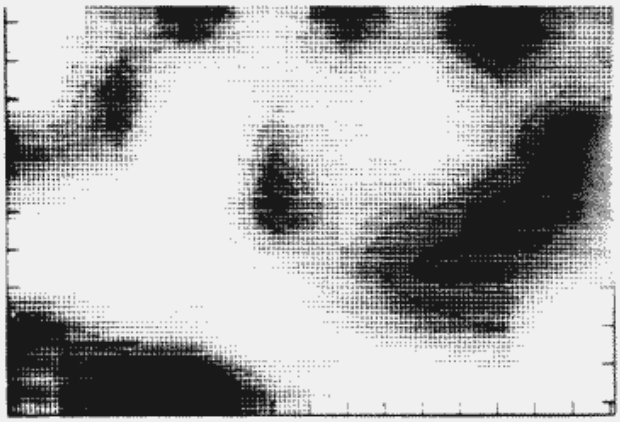

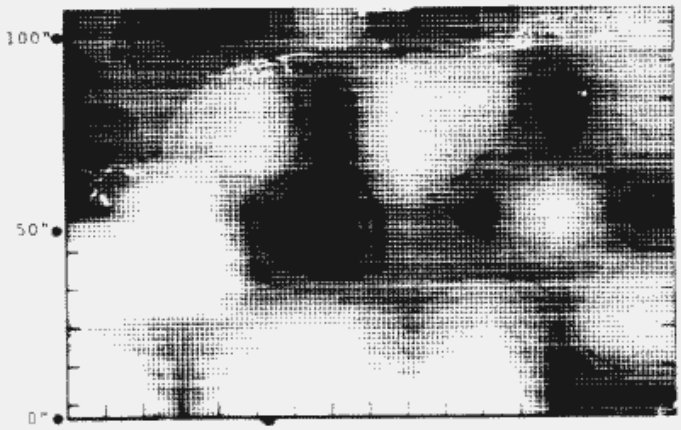

ORBIT 7831

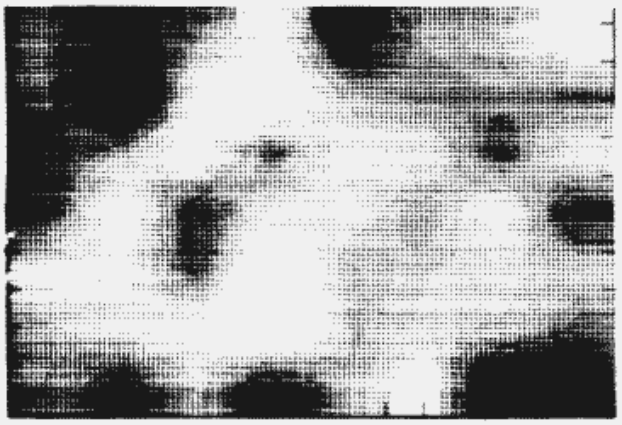

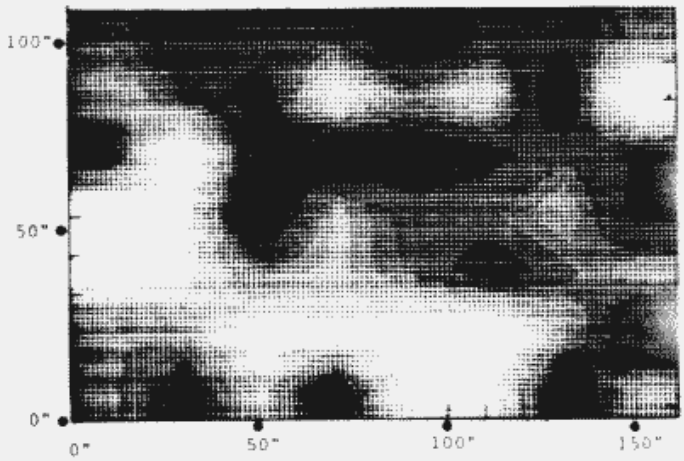

ORBIT 7833

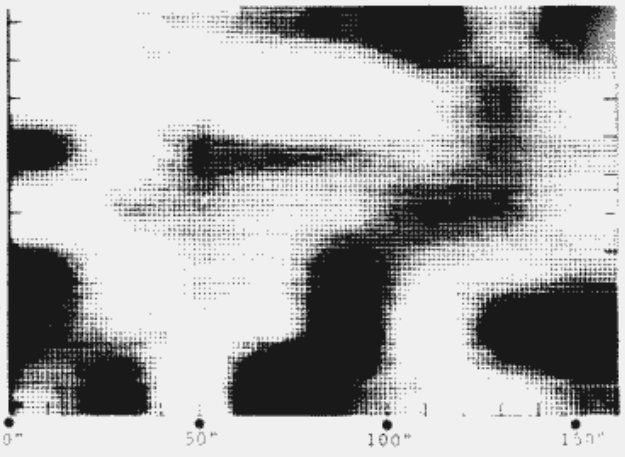

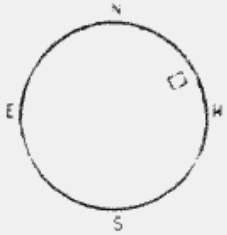

Figure C.3

Persistence in the raster-mode observations on day 6326. These are time-averaged intensity and Doppler velocity images formed from OSO 8 raster-mode observations in Si II λ1817, like those shown in Figures C.1 and C.2. The observations were made on day 6326 (21 November 1976). In this set the pointing of the instrument was not updated to compensate for the effect of solar rotation, and this has introduced a 24" drift toward the west between the separate images. The intensity pictures show the same bright features in all three orbits. In the velocity averages on the right there is some agreement in the sign of the most prominent flows.

INTENSITY

VELOCITY

500 m/s

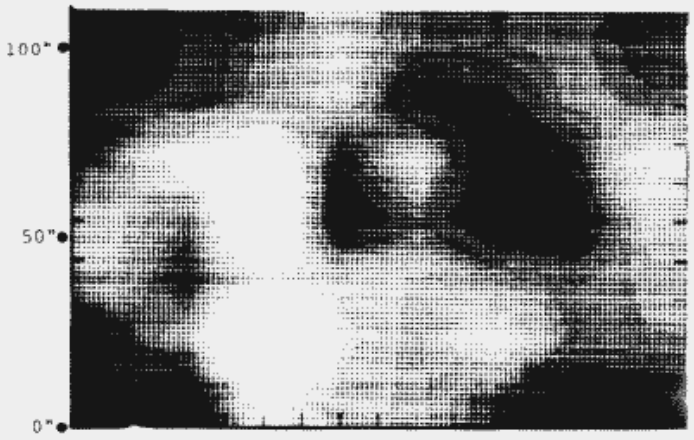

ORBIT 7852

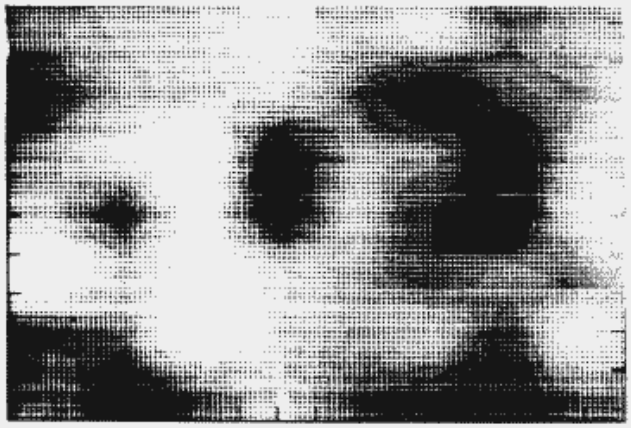

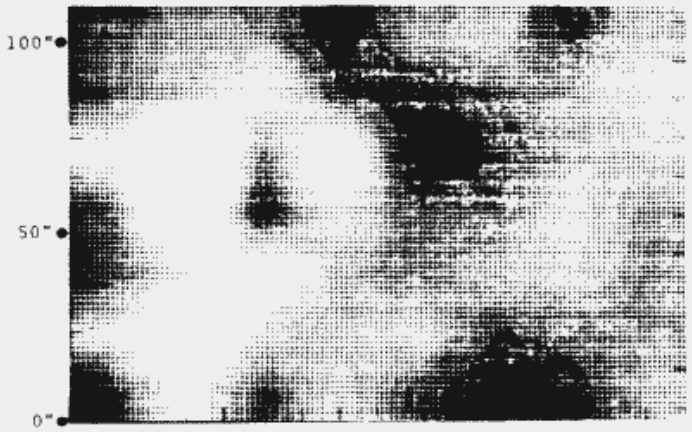

ORBIT 7854

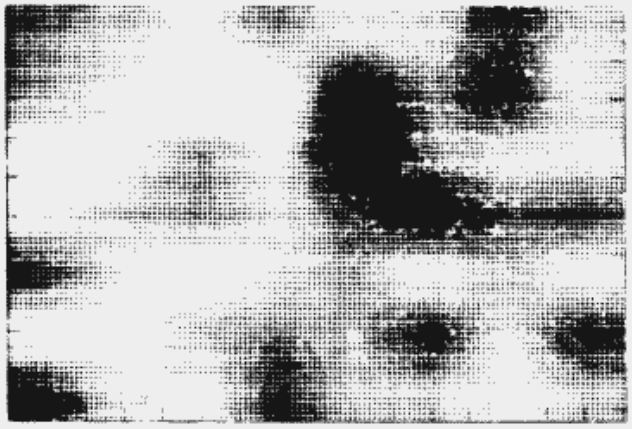

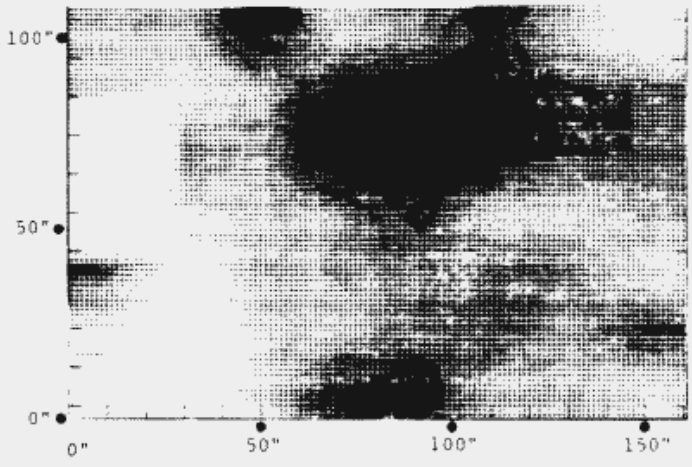

ORBIT 7856

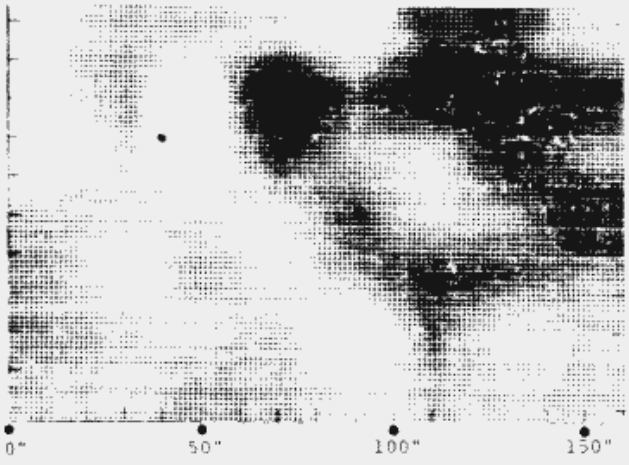

OSO - 8 Si II 1817

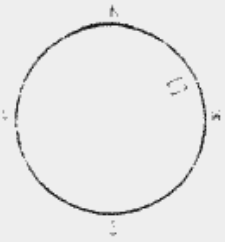

Figure C.4

Persistence in the raster-mode observations on day 6327. These are time-averaged intensity and Doppler velocity images formed from OSO 8 raster-mode observations in Si II λ1817, like those shown in Figures C.1, C.2, and C.3. The observations were made on day 6327 (22 November 1976). In this set the pointing of the instrument was not updated to compensate for the effect of solar rotation, and this has introduced a 24" drift toward the west between the separate images. The intensity pictures show the same bright features in all three orbits after proper compensation is made for the sizable drift of the image toward the west due to solar rotation. In the velocity averages on the right there is good agreement in the most prominent flows, indicating persistence over the 7 hours of observation.

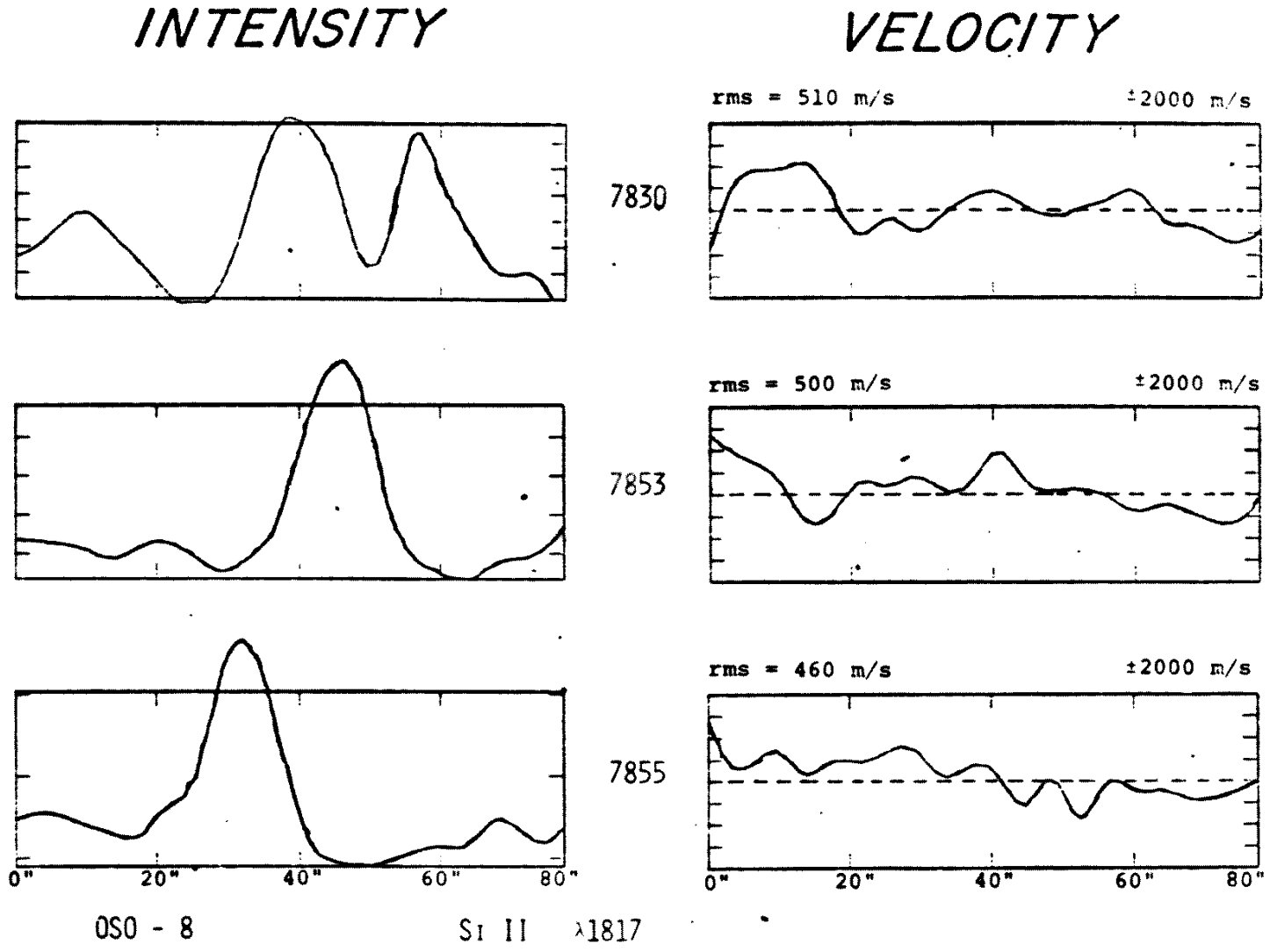

Figure C.5

Examples of OSO 8 higher-resolution point-mode orbits. These are additional examples of point-mode observations in Si II showing the intensity and velocity line drawings. All these orbits were run with the slit oriented perpendicular to the direction toward the limb. The intensities vary on a scale of ~30" corresponding to roughly the scale of the chromospheric network. The velocities show considerably more substructure and vary on a scale of roughly 15". The dynamic range in the velocity in these examples is roughly 1500 ms^{-1} and it shows an rms of about 500 ms^{-1}.

APPENDIX D

Like Appendix C this appendix is included to illustrate additional observations so that all the available data is shown. These observations suppliment the Chapter 4 discussion of the persistence in the vertical steady flows seen with OSO 8.

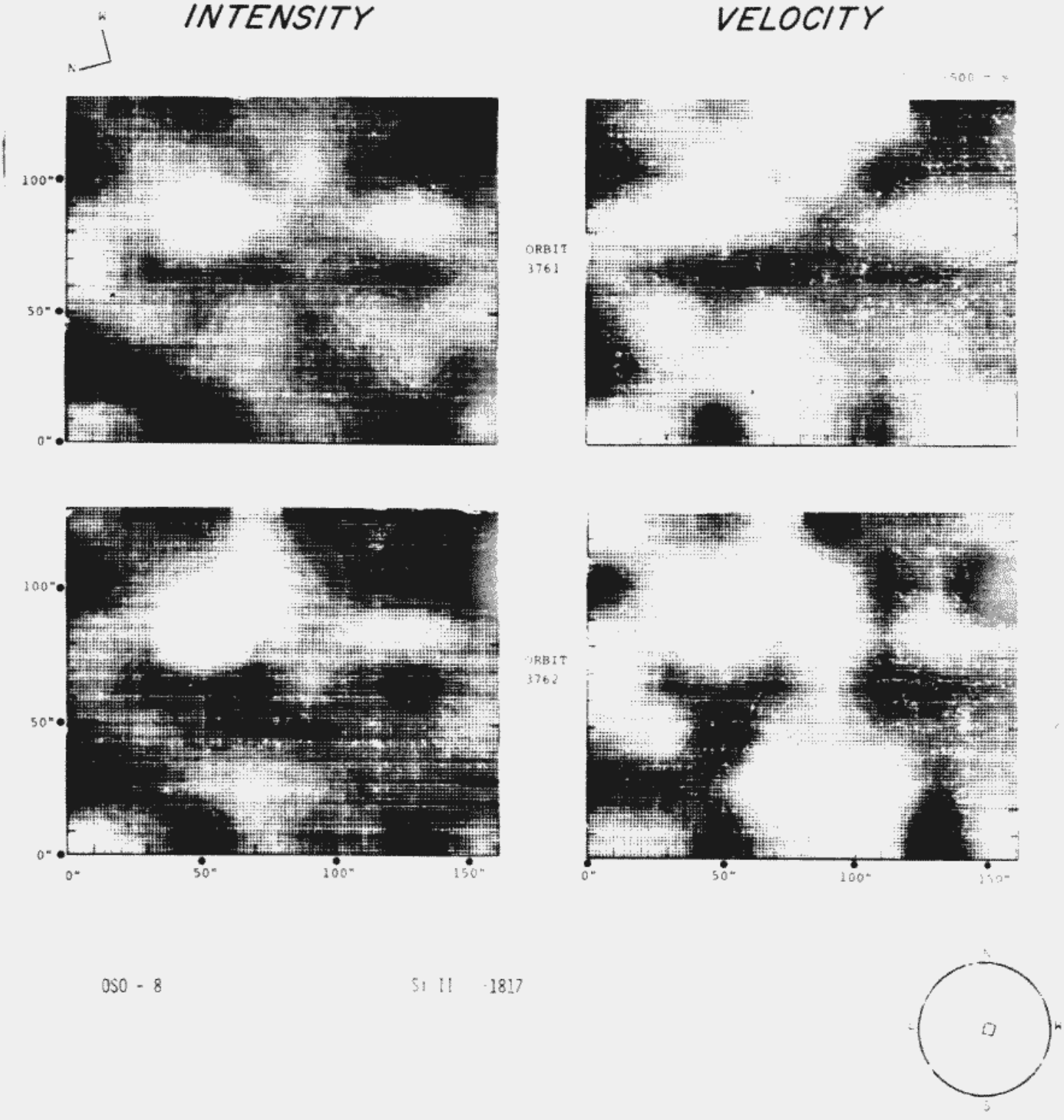

Figure D.1

Persistence in the raster-mode observations on day 6056. This is a sequence of two consecutive orbits showing the time-averaged intensity and Doppler velocity images formed from OSO 8 raster-mode observations with 7 x 8 raster elements. The observations were made at disk center in the quiet Sun on day 6056 (25 February 1976). In this set the pointing of the instrument was updated to compensate for the effect of solar rotation. The intensity images show the same bright features in both orbits. The velocity images also show a correlation among the most prominant features indicating persistence of the flows.

INTENSITY

VELOCITY

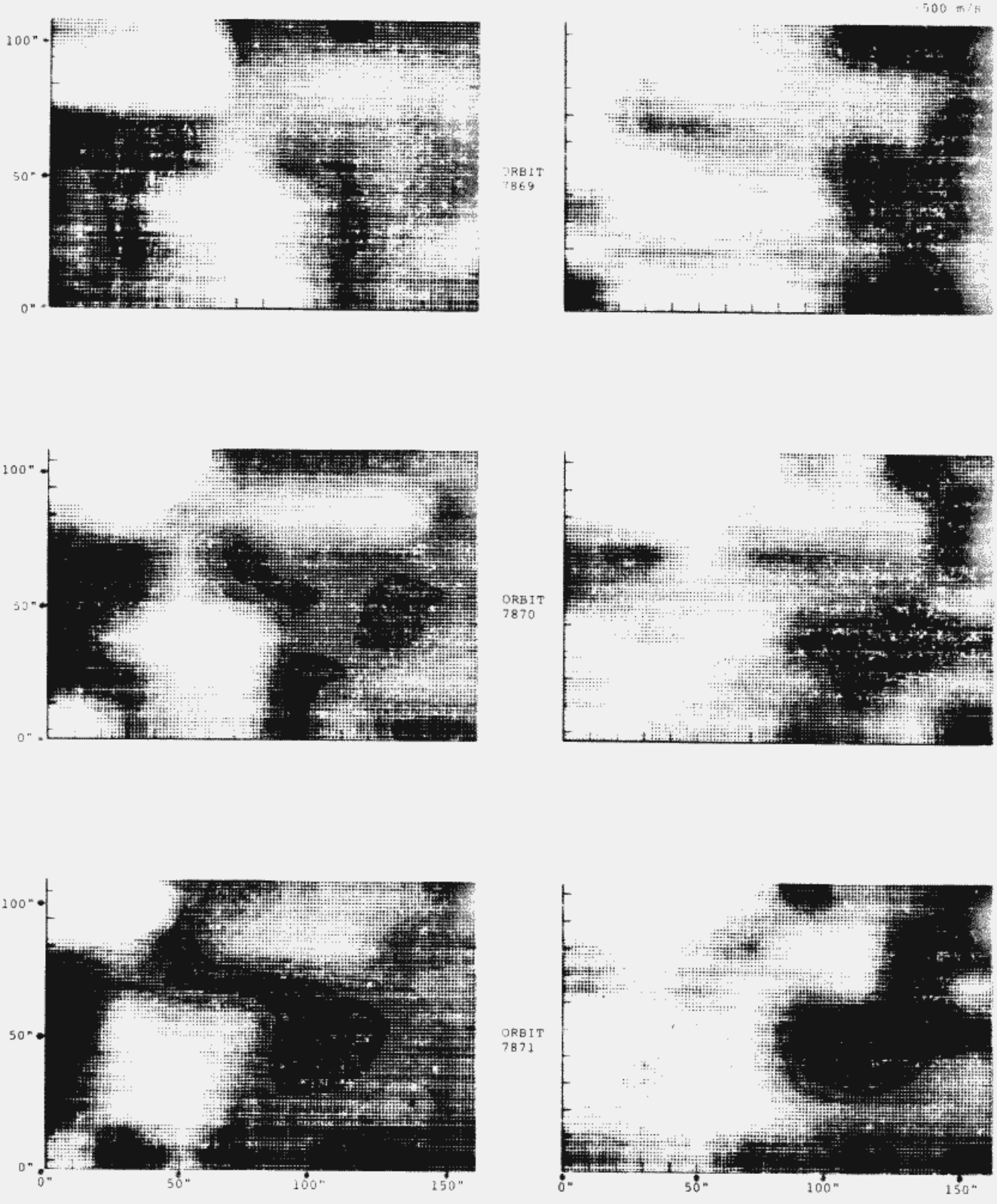

OSO - 8

Si II λ1817

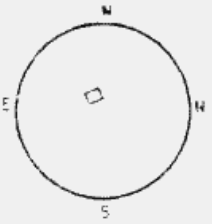

Figure D.2

Persistence in the raster-mode observations on day 6058. This is a sequence of two consecutive orbits showing the time-averaged intensity and Doppler velocity images formed from OSO 8 raster-mode observations with 7 x 8 raster elements. The observations were made at disk center in the quiet Sun on day 6058 (27 February 1976). In this set the pointing of the instrument was updated to compensate for the effect of solar rotation. The intensity images show the same bright features in both orbits. The velocity images also show a correlation among the most prominant features indicating persistence of the flows.